Evaluation of Crack Repair Effectiveness and Thermal Insulation Performance in the Envelope for Enhanced Building Durability

（外気と接する建築部材の耐久性向上に資するひび割れ補修と断熱性能の評価）

2023 年 9 月

李 雨彤 (LI YUTONG)

Contents

Chapter 1 Introduction

1.1. Background

In 2020, COVID-19 pandemic led to a significant decrease in the demand for construction in major economies. The reasons for this could be workplace closures due to the epidemic closure, labor and material shortages, and changes in work patterns. The result is that construction undergoes the sharpest decline in CO_2 emissions in the last decade [1]. However, in 2021, construction activity picked up in most major economies, workplaces reopened, and energy-intensive use of buildings increased. In addition, more emerging economies are increasing the use of fossil fuel gases in buildings. As a result, CO_2 emissions from building operations reach an all-time high of about 10 billion tons. If the estimated 3.6 billion tons of CO_2 emissions from the production of building materials (such as concrete, steel, aluminum, glass and bricks) are included, buildings account for about 37% of global emissions in 2021 [2].
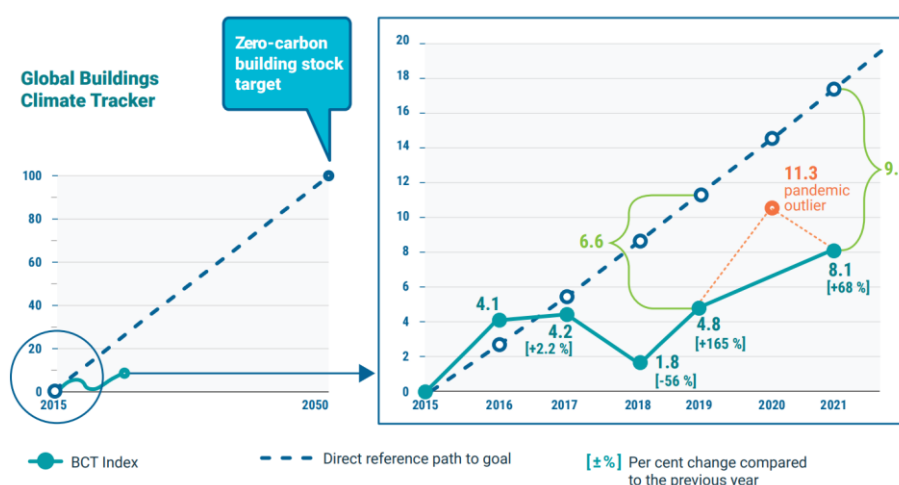
Figure 1–1 Direct reference path to a zero-carbon building stock target in 2050 (left); zoom into the period between 2015 and 2021, comparing the observed Global Buildings Climate Tracker to the reference path (right) [2].

The Global Buildings Climate Tracker monitored the progress of the building construction industry towards the Paris Agreement. The current results indicate a negative rebound in decarbonization of the building sector since 2020. Energy intensity has increased, and emissions have grown. This has led to a growing gap between observed energy efficiency and the reference path pathway, as shown in **Figure 1–1** [2]. By 2060, as the world's economy grows and living standards increase the global consumption of raw materials will almost double, exacerbating the environmental overload we experience today (Organization for Economic Co-operation and Development [OECD] 2019). The International

Resource Panel highlighted that the application of material efficiency strategies throughout the building stock has tremendous potential to reduce greenhouse gas emissions. Measures include reducing building and material requirements, using low carbon materials, operations, methods and design. The most urgent priority must be to increase the longevity of existing and new building stock and reuse existing components whenever possible [2].

In recent years, an increasing number of countries have recognized the importance of the building sector in decarbonization initiatives and have taken active action to introduce and revise various building codes and standards (UN Climate Change Conference 2022). At the same time, various governments are providing financial assistance and support to address building and infrastructure issues, especially in maintenance and improvement of existing buildings. In Japan, for example, the building industry has shifted from "Scrap & Build" to "Storage & Renovation" in the last two decades. As shown in **Figure 1–2**, the rate of maintenance and refurbishment has been increasing year by year and has exceeded 30% in 2020.
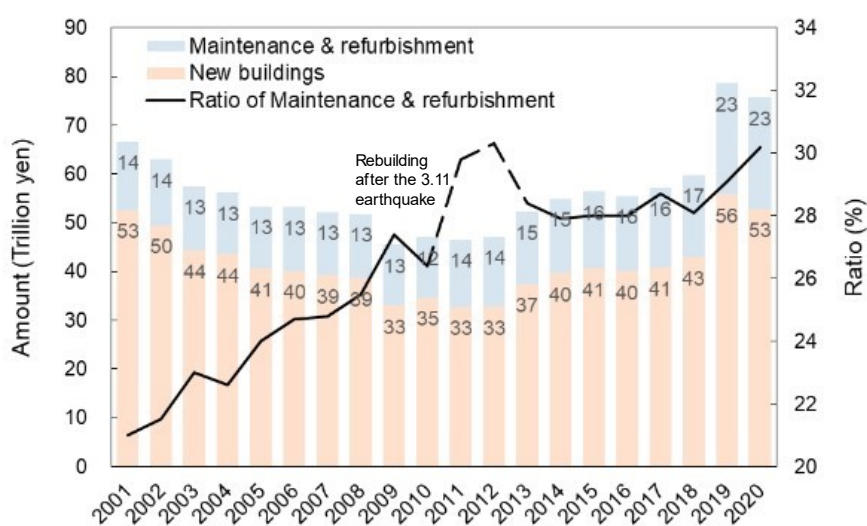
Figure 1–2 Variations of maintenance & renovation in construction works in Japan (data from the Ministry of Land, Infrastructure, Transport (MLIT)).

According to the 2022 Annual Report on Housing Consultation Statistics released by the Dispute Resolution Support Center and Home Renovation (Public Interest Incorporated Foundation) in Japan, the highest-ranking part of renovation work on individual houses is the roof, accounting for 60.5%. In second place is the exterior, accounting for 47.6% [3]. For buildings, the envelope is critical and plays a role in protecting the building interior from the external environment. It is because of the envelope that a building can withstand natural forces such as wind, rain, sunlight and temperature changes. Because of this, the building envelope is also the part of the building that is most susceptible to deterioration. Specifically, the Dispute Resolution Support Center and Home Renovation also reported

the building parts most involved in building deficiencies when tenants consulted with experts, and the statistics are shown in **Figure 1–3**. Exterior walls and roofs accounted for 16.7 % and 12.0 %, respectively. In addition, the statistics of expert consultation according to the type of defects are shown in **Figure 1–4**. Homeowners have the highest concern about cracks, with a mention rate of 17.8%.
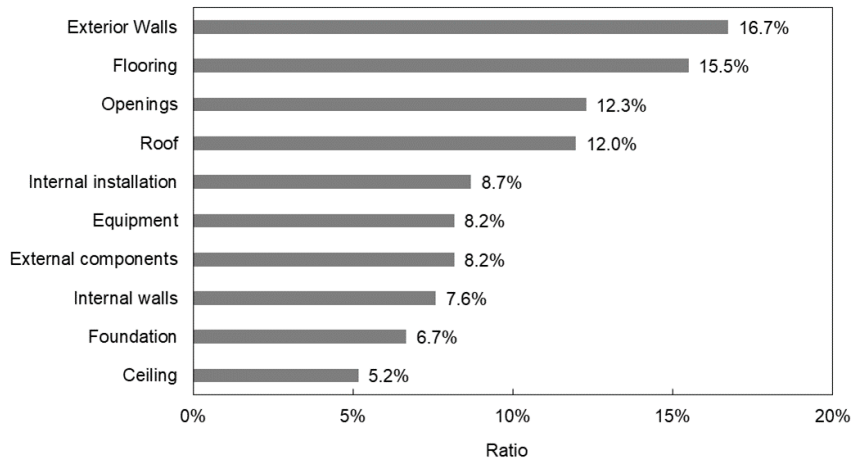
Figure 1–3 Percentage results of construction defective parts in the expert consultations (data from Dispute Resolution Support Center and Home Renovation in Japan).
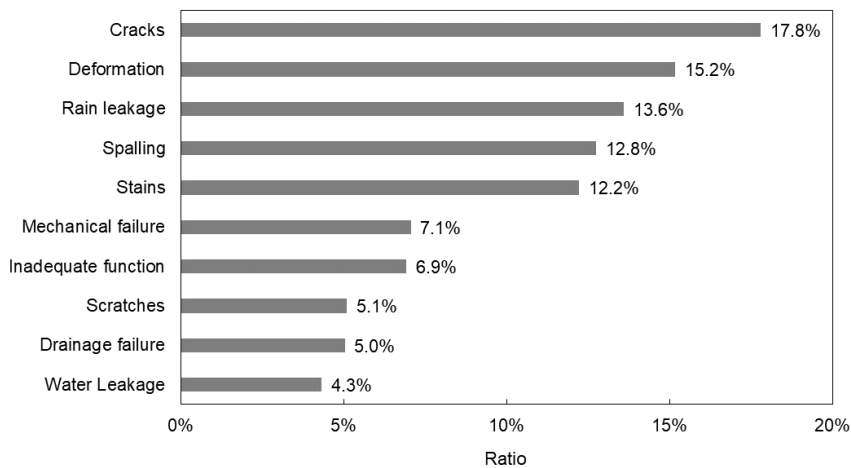
Figure 1–4 Percentage results of types of construction defects in expert consultations (data from Dispute Resolution Support Center and Home Renovation in Japan).

The occurrence of cracks in concrete buildings is a common phenomenon and almost inevitable. It is caused by the properties of concrete and the influence of environmental factors, including shrinkage of concrete, temperature changes, earthquakes or structural loads. Cracks can lead to structural weaknesses and accelerated damage. Therefore, crack repair plays a vital role in the longevity and sustainability of buildings. With timely repair and the use of appropriate repair materials and techniques, we can extend the life of buildings, reduce maintenance costs, and ensure their sustainability on an economic, environmental and social level.

As mentioned above, the building envelope also plays a key role in reducing energy consumption. A well-designed and constructed envelope system can provide insulation and thermal insulation, reducing heat transfer and energy consumption. Owing to its high energy consumption and predominant use of refrigerants with significant global warming potential, space cooling is one of the major contributors to climate change [4]. According to the International Energy Agency, the energy utilization for space cooling has doubled since 2000. The Programme for Energy Efficiency in Buildings reports that the energy needs of space cooling could triple by 2050, particularly in hot and tropical countries. To address this issue, improving the thermal insulation efficiency of buildings and raising public awareness seem to be effective approaches [4].

1.2. Purpose of this study

The building envelope is crucial in the sustainable development of the construction industry. In this paper, the crack repair and thermal insulation renovation issues of the building envelope are studied for the following purposes:

Purpose 1: To establish crack movement simulation experiments for evaluating repair durability.

Proper crack repair can extend the life of a building and contribute to the sustainability of the construction industry. However, premature repair failures have been observed and one of the possible reasons for this is that crack movement has not been adequately considered. In reality, crack repair involves the joint work between two materials, and the difference in their physical properties can greatly affect the durability of the repair. And crack movement can cause this difference to act frequently at the crack leading to failure.

To achieve the evaluation of repair effectiveness against crack movement, it is necessary to establish the corresponding experimental methods. First, the investigation of actual building crack movement needs to be carried out. Although non-through cracks are common, the purpose of this paper is to focus on through-thickness cracks, which are the most harmful. In the exterior walls of buildings, through-thickness cracks occur owing to the drying shrinkage of concrete, which can cause serious deterioration conditions as harmful substances invade the structure along with air and water through the cracks. Starting with the most harmful through-thickness cracks, it is necessary to accumulate a

large amount of measurement data to generalize whether there is a pattern of crack movement. Then, for the recurring specific crack movement pattern, it needs to be reproduced in the laboratory. The key points include reproduction of the deterioration elements and of the influence factors.

Purpose 2: Evaluation of common repair solutions for resistance to crack movement to establish a more appropriate solution selection system

To fully consider the effect of crack movement when selecting a crack repair solution, data on the durability evaluation of common repair solutions against crack movement are needed to support the selection. Common crack repair methods may include injection method, U-groove routing and sealing method, and surface coating method. The materials involved mainly include epoxy resins, polymer cements and waterproofing coatings. Durability can be evaluated by measuring their ability to suppress crack movement and the number of cycles they withstand. In addition, for the results to be widespread, the relationship between their physical properties and durability needs to be clarified so that it can be generalized to similar materials. Moreover, for different climatic conditions and movement conditions through-thickness cracks should also be evaluated to simulate more variables of real buildings.

Purpose 3: To establish a simple thermal insulation performance evaluation method and a prediction formula for heat-flow density

A proper insulation system can reduce a building's energy consumption. Making homeowners aware of the importance of insulation construction and renovation helps the building industry to be sustainable. One of the keys is to use simple evaluation methods and indicators to communicate with the non-expert. To this end, small heat-flow sensors are a possible solution. Different heat transfer experiments should be designed to clarify the effectiveness of heat-flow sensors. Using indoor temperature increment as an evaluation indicator allows everyone to understand the performance of insulation materials, therefore, the relationship between heat flow and temperature increment needs to be clarified. In addition, simulation calculations of full-size building models can help to use the experimental data for more scenarios. A quantitative comparison of common insulation systems on the market should be performed after establishing the experimental approach. This can accumulate experimental data to help establish a correspondence table between heat flow and temperature increment in the future, making the thermal insulation evaluation convenient.

1.3. Scope of this study

The main structure of this paper is shown in **Figure 1–5**. The main contents of each chapter are as follows:
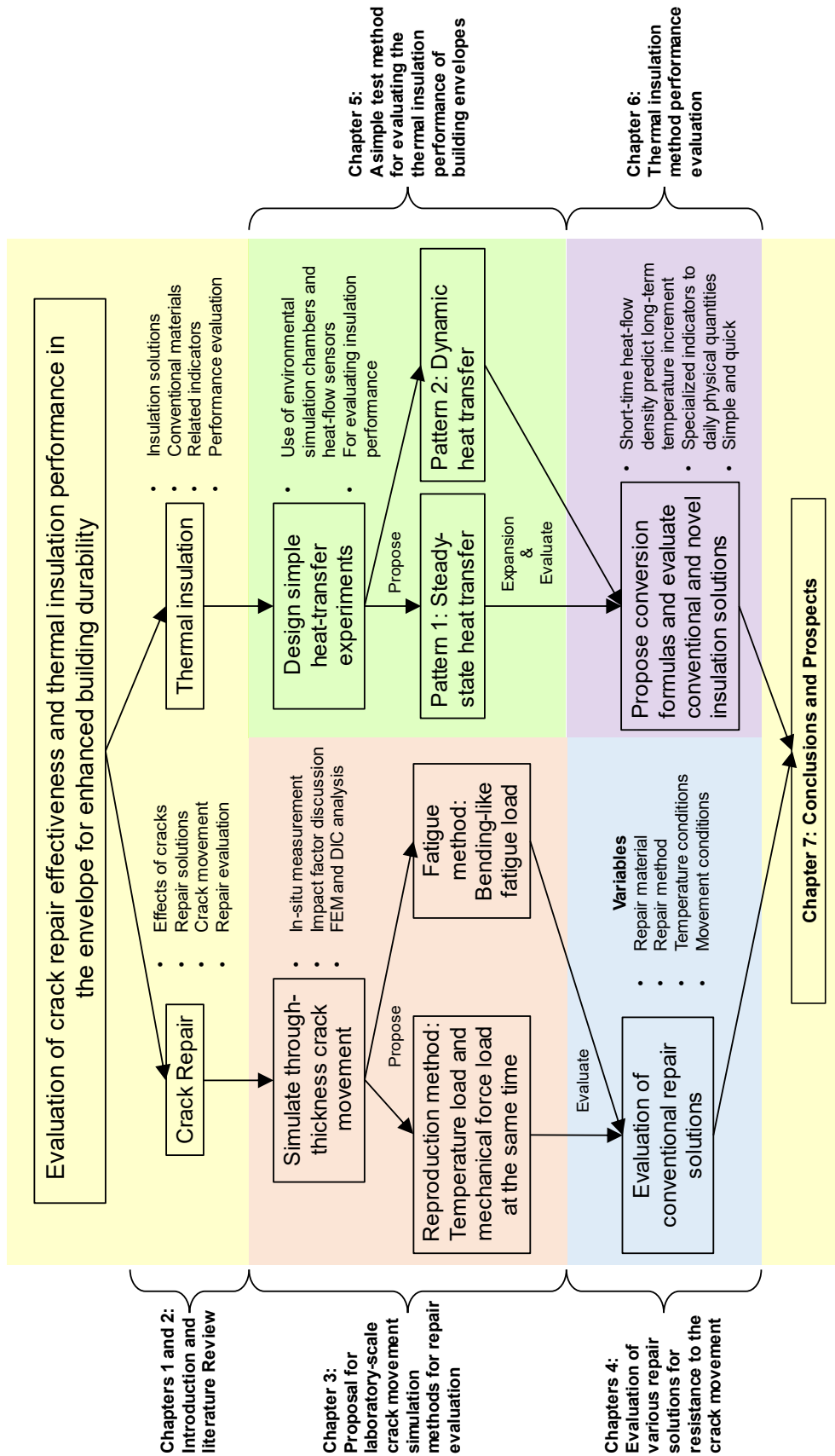
Figure 1–5 The main structure and contents of this paper.

Chapter 1

This chapter provides the background, purpose and main content of the study. The importance of sustainable development in the construction industry is described. It is particularly important to extend the service life of existing buildings and to reduce CO_2 emissions in the construction industry. For this reason, two main research objectives have been chosen for the most deterioration-prone parts of the building envelope: crack repair and thermal insulation construction.

Chapter 2

This chapter addresses a literature review of the building envelope regarding crack repair and insulation construction. The causes of cracks and their effects on buildings were investigated. By measuring the crack width variation, the possible crack movement caused by temperature fluctuations is clarified and the movement is found to be a potential factor affecting the durability of the repair. The current methods for evaluating the effectiveness of crack repair were sorted out, and it was found that the element of bending-like movement has yet to be studied.

In terms of insulation construction, based on a survey of common insulation solutions, the research was conducted on insulation materials that are not restricted by the site and can be easily renovated. In terms of insulation construction, based on a survey of common insulation solutions, the research was conducted on insulation materials that are not restricted by the site and can be easily renovated. By compiling methods for evaluating the effectiveness of insulation, the problem that professional metrics are not conducive to communication with homeowners was identified. Establishing a relationship between everyday physical quantities and professional physical quantities may help homeowners realize the importance of insulation construction and renovation.

Chapter 3

To address the issue that through-thickness crack movement, a degradation factor, has not been adequately studied, two laboratory-scale simulation experimental methods are proposed in this chapter. First, the movement of actual buildings with through-thickness cracks is measured. After clarifying the mechanism of the bending-like movement, it is proposed that the simultaneous application of thermal and mechanical loads to the cracks is the key to the reproduction experiments. A reproduction test method for evaluating the resistance of repair solutions to crack movement was established after the scheme simulation of the constraints of mortar specimens using the finite element method.

In addition, mechanical fatigue experiments simulating bending-like movement can be used to evaluate the durability of crack repair solutions. The effectiveness of the proposed test setup was verified by the digital image correction method. The use of top and bottom symmetrical specimens can produce a force state with bending-like movement where one side is tensioned, and the other side is compressed.

Chapter 4

This chapter evaluates common crack repair methods and materials for resistance to crack movement. Methods covered are injection method, U-groove routing and sealing method, and surface coating method. The materials used include mainly epoxy resin type, polymer cement type and water-based acrylic waterproofing coatings. In the reproduction experimental method, it was found that different repair solutions have different ability to suppress crack movement and may also change the pattern of crack movement by comparing the data before and after repair. The durability of repair materials other than polymer cement was demonstrated for a limited test time. By varying the initial temperature of the experiments, it was found that the change in the physical properties of the repair material may be a key factor in changing the crack movement pattern, and numerical simulations were performed using the finite element method.

In the fatigue tests, specimen deterioration forms, damage rates and strain levels were discussed around injection and surface coating methods. The tendency of hard resins not to be suitable for large movements as well as soft resins not to be suitable for high temperatures was found. For the surface coating method, the effectiveness of water-based acrylic waterproofing coatings in repairing small movements was confirmed. When movement conditions become large, additional crack bridging functional layers are required.

Chapter 5

To address the potential problems of existing insulation performance assessment methods with difficult equipment control and long testing times, this chapter designs a simple laboratory-scale method to evaluate the insulation performance of building components. The effectiveness of the heat-flow sensor is demonstrated in static and dynamic heat transfer experiments. When the boundary conditions are the same, a larger absolute value of the heat-flow sensor implies a better insulation performance. In tests on two roof slab samples with different insulation levels, it was found that the insulation substantially reduced the indoor temperature increment by increasing its own temperature gradient.

Chapter 6

To establish the relationship between heat-flow values and temperature to evaluate the insulation performance of building elements, this chapter conducted static and dynamic heat transfer experiments on two factory roof slab specimens using an environmental simulation chamber and heat-flow sensors. The relationship between heat-flow density with time was proposed. Using this method, in the field, the long-time indoor temperature increment can be roughly predicted from the short-time heat-flow measurements. In addition, the insulation performance of 14 experimental specimens was evaluated, including self-developed and commercial insulation materials and construction methods of factory roof slabs.

Chapter 7

This chapter summarizes the main conclusions, limitations of this study. Recommendations for future research are also listed.

Chapter 2 Literature review

2.1. Cracking and crack movement in reinforced concrete building exterior walls

2.1.1.Concrete cracks: causes, impacts and detection

(1) Causes of cracking

Cracking is one of the most common forms of deterioration in reinforced concrete structures. In Japan, among the various failures of structures, the demand for crack repair is usually the most required service [5]. Cracking occurs whenever the principal tensile stresses of the load or restraint exceed the tensile strength of the concrete, usually caused by shrinkage [6][7], thermal stresses [8], chemical reactions [9][10], etc. In addition, the poor construction practices, loading, unsoundness, and earthquake are also the causes of the cracking of the concrete structures[11][12][13][14].
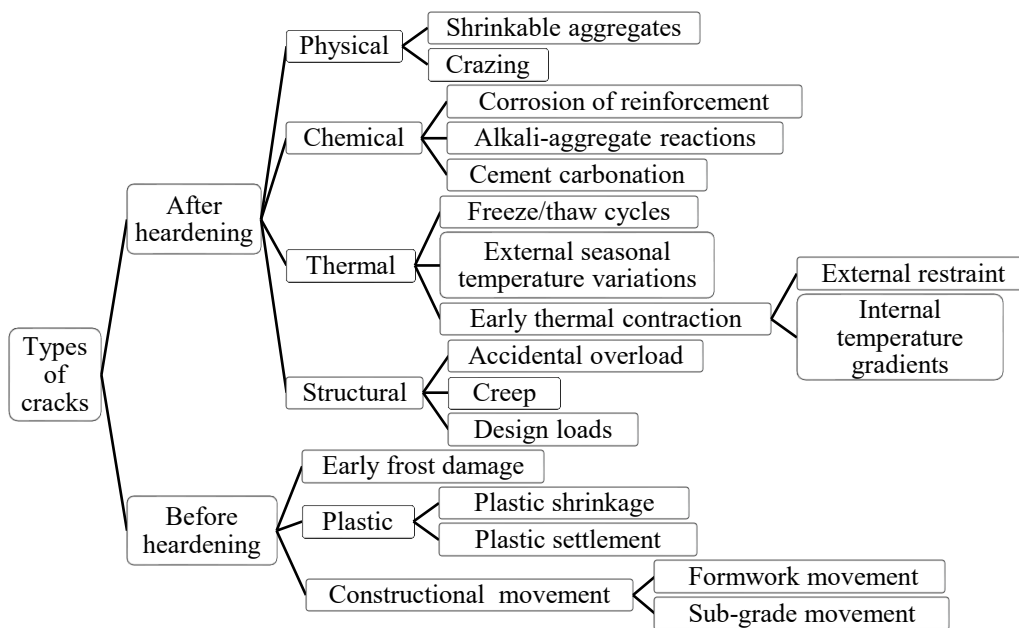
Figure 2–1 Main types of concrete cracks.

The causes of cracks in concrete are classified in the current standards of various countries. Some tend to be classified into material, construction, environment, and external forces, such as standards in Japan. Others like standard in American tend to classify depending on the three phases of the concrete life cycle: plastic (phase while it has still not set), hardening (phase while it is still green), hardened (phase and in service). The types of concrete cracks are roughly summarized in the **Figure 2–1**. Some typical crack patterns are described in the **Figure 2–2** and **Table 2–1** [15].
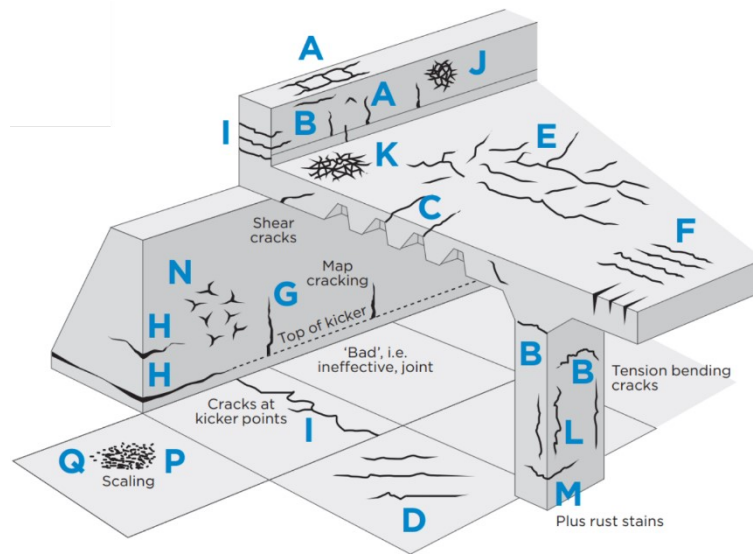
Figure 2–2 Patterns of concrete cracks [15].

Table 2–1 Details of cracks in Figure 2-1 [15].

Letter	Type of Cracking	Subdivision	Most Common Location	Primary Cause (excluding restraint)	Secondary Causes/Factors	Time of Appearance
A	Plastic settlement	Over reinforcement	Deep sections	Excess bleeding	Rapid early drying conditions	Ten minutes to three hours
B		Arching	Top of columns			
C		Change of depth	Trough and waffle slab			
D	Plastic shrinkage	Diagonal	Roads and slabs	Rapid early drying	Low rate of bleeding	Thirty minutes to six hours
E		Random	Reinforced concrete slabs			
F		Over reinforcement	Reinforced concrete slabs	Ditto plus steel near surface		
G	Early thermal contraction	External restraint	Thick walls	Excess heat generation	Rapid cooling	One day or two or three weeks
H		Internal restraint	Thick slabs	Excess temp. gradients		
I	Long-term drying shrinkage		Thin slabs (and walls)	Inefficient joints	Excessive shrinkage inefficient curing	Several weeks or months
J	Crazing	Against formwork	"Fair faced" concrete	Impermeable formwork	Rich mixes	One to seven days, sometimes much later
K		Floated concrete	Slabs	Over troweling	Poor curing	
L	Corrosion of reinforcement	Natural	Columns and beams	Lack of cover	Poor quality concrete	More than two years
M		Calcium chloride	Precast concrete	Excess calcium chloride		
I	Alkali-aggregate reaction		Damp locations	Reactive aggregate plus high-alkali cement		More than five years

For concrete exterior walls, the common causes of cracks may include dry shrinkage, which takes the common form shown in the **Figure 2–3** [11]. Dry shrinkage is the main cause of cracking in hardened concrete. This cracking takes place near the restraints due to volume changes in the concrete. When concrete is exposed to moisture it swells and when it is exposed to air with relatively low humidity it shrinks, such air drawing water out of its cement paste. This cracking is the result of a combination of factors that influence the magnitude of the tensile stresses that cause it. These factors include the amount and rate of shrinkage, the degree of restraint, the modulus of elasticity, and the amount of creep. Additional factors to be aware of include the type of aggregate, water content, binder type, and the concrete's mix proportions and mechanical properties. The amount and type of aggregate and the cement paste are the main influences on the amount of drying shrinkage.
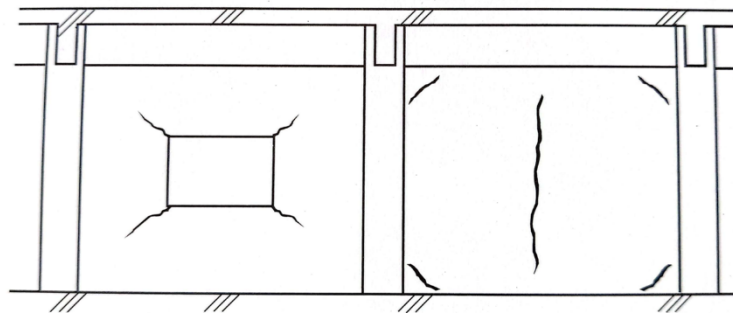
Figure 2–3 Example of dry shrinkage cracks in building exterior walls [11].

Thermal stress can also lead to concrete cracking. The concrete then cracks when the tensile stresses imposed by a change in volume differential exceed that of its tensile strength. Environmental factors such as freezing and thawing, wet and dry, and hot and cold cycles can also cause stress changes in concrete and thus cracking. For concrete exterior walls, drying shrinkage due to changes in ambient humidity, and deformation due to temperature changes caused by sunlight exist. These changes can cause diagonal cracks at the end and top of the exterior wall, cracks at the corners of the openings, and vertical cracks in the restrained sections like the beams as shown in the **Figure 2–4** [11].
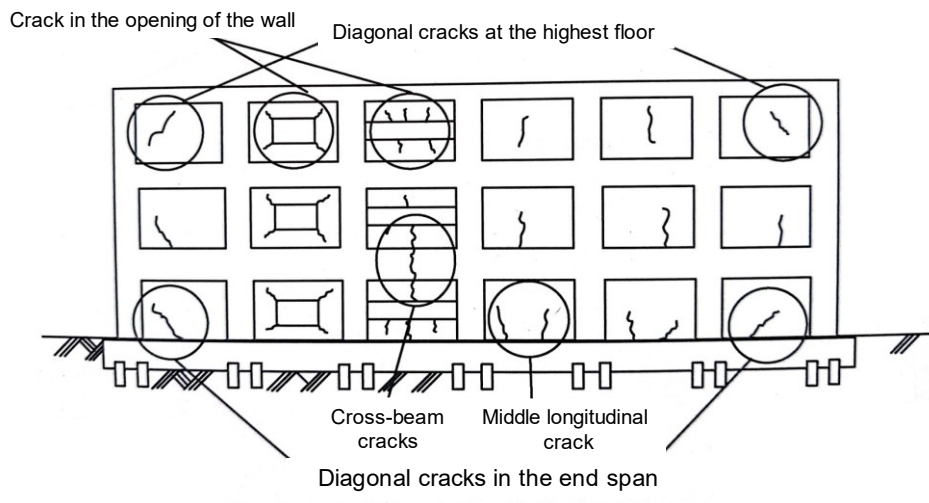
Figure 2–4 Exterior wall crack patterns caused by environmental humidity and temperature changes [11].
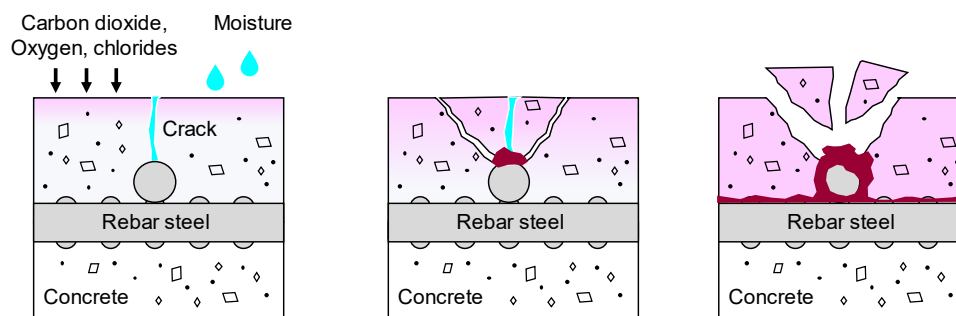
Figure 2–5 Possible serious impact of cracks.

(2) Impact of concrete cracks

Cracks usually lead to aesthetic defects, leakages resulting in corrosion, spalling, and in extreme cases, structural failures [12][13]. Aesthetic defects due to concrete cracks can vary in severity, from small hairline cracks that are barely noticeable to larger cracks that can be seen from a distance. The size and location of the crack can greatly affect its impact on the building's appearance. Aesthetic defects can lower the value of the building and make it unappealing to potential buyers or tenants. Additionally, and more seriously, cracks can allow foreign and aggressive materials to penetrate the concrete (**Figure 2–5**). Chlorides in de-icing salts and sea salts can rapidly reach the reinforcing steel through cracks and initiate corrosion. When the cracks open, carbonation is accelerated and the high pH of the concrete decreases, causing passivation of the reinforcement in the concrete. As steel corrodes, it expands, causing the surrounding concrete to crack and spall. This can weaken the entire structure and potentially lead to a total collapse. In addition, when water is present in the cracks, the moisture content of the concrete increases significantly, which also leads to an increase in the corrosion

rate of the steel. In combination with mechanical effects such as runoff, water can also widen and deepen cracks. In the case of frost, water in the cracks can quickly cause more serious damage.

In addition, our research team measured the micro-vibration of a building. The results indicated that the cracks may also cause abnormal vibrations in the building. The target of the investigation was Building No. 1 of the four buildings of the Former Army Clothing Depot located in Hiroshima Prefecture, Japan. The outline and appearance of the building are shown in **Table 2–2** and **Figure 2–6**, respectively.

Table 2–2 Building outline.

Building name	Former Army Clothing Depot
Location	2–4–60 Deshio, Minami Ward, Hiroshima City
Building area	2340 m^2 (Each building)
Total Floor Area	5289 m^2 (Each building)
Start of construction	Year of 1912
Completion	Year of 1913
Structure	Three floors, reinforced concrete structure, brick exterior walls
Building Experience (Building No. 1)	Obtained by Hiroshima Prefecture from the national government (Ministry of Finance). After being used as a prefectural technical high school, it was rented to a transportation company, and since 1995 it has been completely closed and is now an unused structure.

Figure 2–6 Appearance of the Former Army Clothing Depot (taken in October 2018).

There were many cracks in the building. **Figure 2–7** shows typical cracks in the beam-to-beam cross section. As shown in the figure, the damage was most conspicuous in the inner columns on the

third floor, where ring-shaped cracks were observed along the entire length of the columns (**Figure 2–8**). The average crack width was 2.2 mm, which was significantly larger than typical crack widths. We speculated that these cracks on the third floor were caused by the differential settlement of the building. The settlement in the middle of the building was larger than that in the periphery.

Micro-vibrations in the height direction of the building were measured. A high sensitivity triaxial accelerometer that integrates a wireless communication unit and crystal acceleration detector was used for the measurement. The measurement device uses Bluetooth wireless communication based on long-range communication standards (100 m communication distance). The sensors can be easily installed in places where wiring is difficult, such as under the floor, on the eaves, behind the ceiling, etc. In the measurement of vibration characteristics in the height direction of the building, the sensors were set up in the positions shown in the **Figure 2–9**.
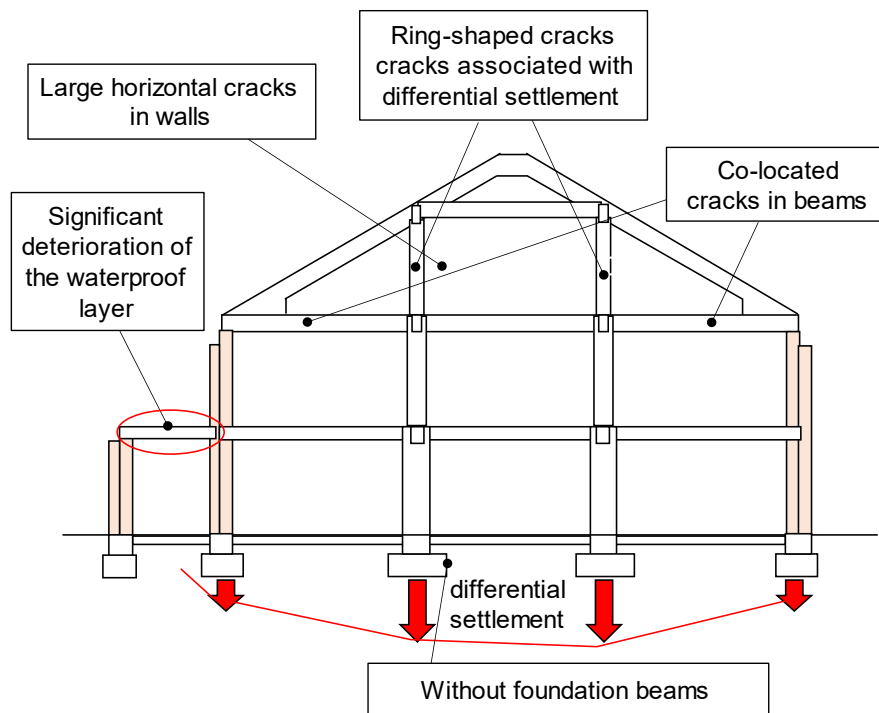
Figure 2–7 Cross-sectional view in beam-to-beam direction.

(a) Third floor with cracked columns

(b) Column with ring-shaped cracks (middle column on the third floor)

(c) Large horizontal cracks in the wall on the third floor

(d) Cracks in the same location on the second-floor beams

Figure 2–8 Typical cracks in the building.

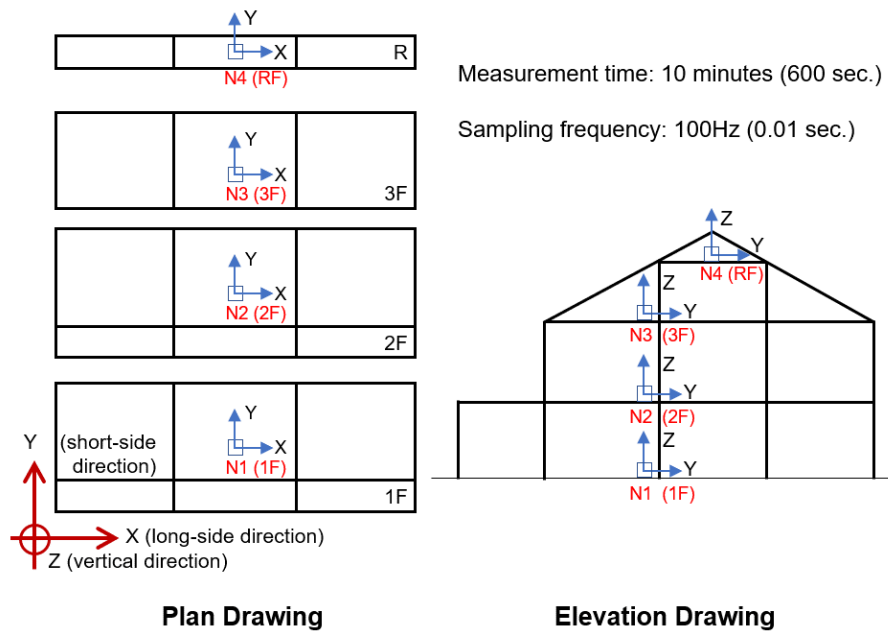**Plan Drawing**   **Elevation Drawing**

Figure 2–9 Sensor location.

Acceleration waves were measured for 10 minutes (600 seconds) with 100 Hz sampling, and the average Fourier spectral was obtained from the measured waves. The 2048 data in the 20.48 s interval were taken as a set, and two adjacent sets of data were overlapped by 50% of the interval. The response ratio of each floor to the first-floor response spectral, i.e., the transfer function, was calculated. **Figure 2–10**, **Figure 2–11** and **Figure 2–12** shows the transfer function in the X direction (long-side direction), Y direction (short-side direction) and Z direction (vertical direction), respectively. Band-pass filtering (target frequency ±0.1 Hz) was performed for each peak period to obtain the average response value of the peak acceleration at each measurement point. The average response values of each layer were concatenated into a vibration mode plot as shown in **Figure 2–13**. In **Figure 2–13**, for the vibration mode in the X direction, the third-floor slab shows a greater response than the top part of the shed beam. In the Y direction, the uppermost floor shows the largest response. This may be explained by the continuous atrium in the long direction shown in the third-floor plan in **Figure 2–9**, in addition to the differential settlement shown in **Figure 2–7**. The third-floor slab of the building had a continuous atrium to ensure ventilation, and the third-floor slab hardly had a rigid floor structure. We believed that the vibration modes shown in **Figure 2–13** and **Figure 2–14** are very dangerous during earthquakes, thus the atrium needs to be reinforced. The first mode natural period of this building was about 0.153 sec. in the X direction and 0.172 sec. in the Y direction.

17
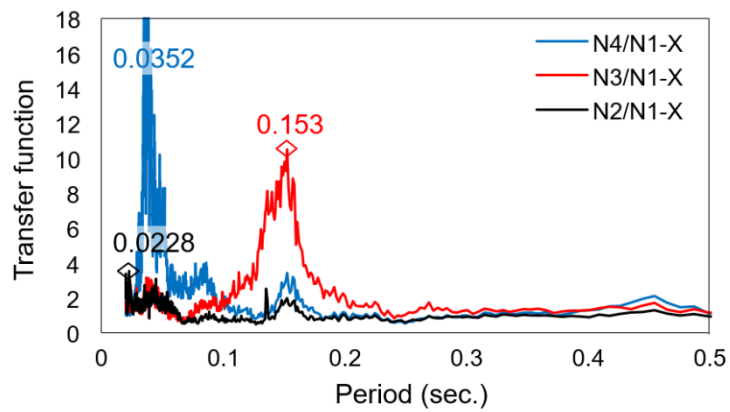
Figure 2–10 Transfer function (X direction).
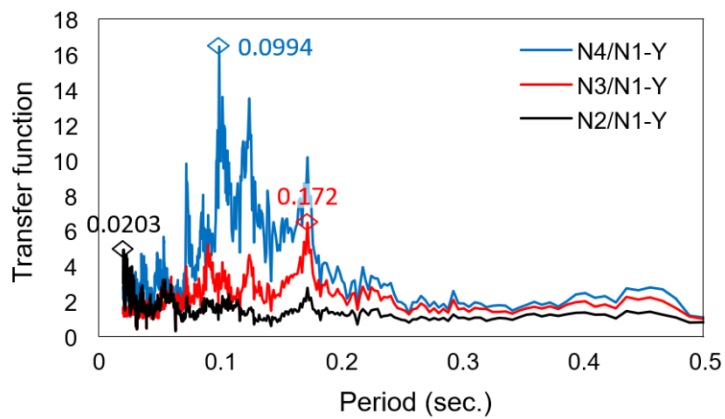
Figure 2–11 Transfer function (Y direction).
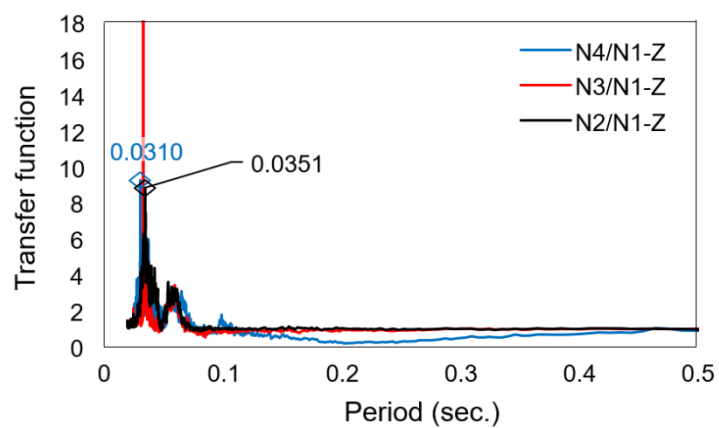
Figure 2–12 Transfer function (Z direction).
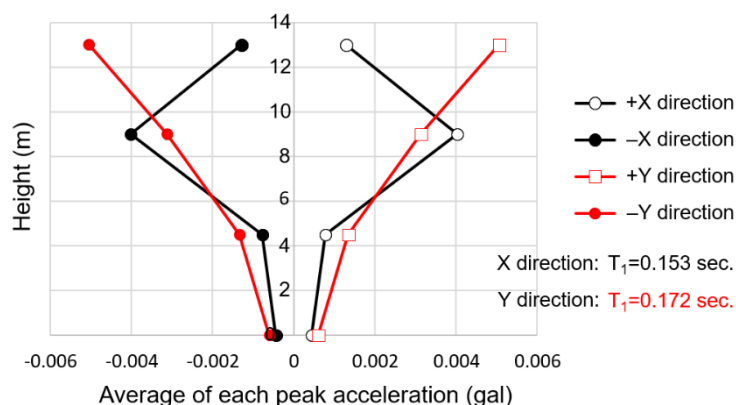
Figure 2–13 Vibration mode (1st order mode).

(a) 0.0352 sec. period
band

(b) 0.153 sec. period
band

(c) 0.172 sec. period
band
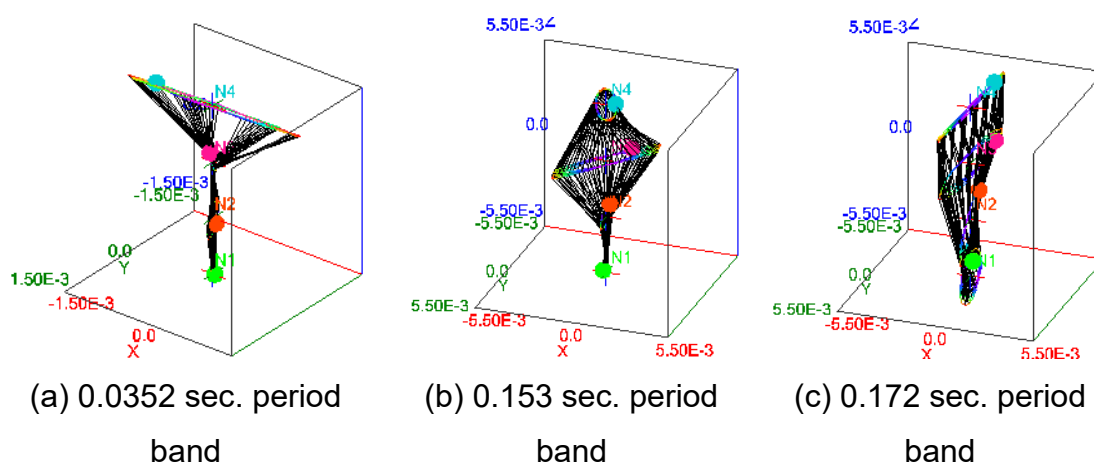
Figure 2–14 Extraction of waveforms in the specific period bands (main
response for 20.48 sec.).

Table 2–3 Natural period and natural frequency of buildings.

Direction	T_1 (sec.)	f_1 (Hz)
X direction (Long-side direction)	0.153	6.54
Y direction (Short-side direction)	0.172	5.81

Table 2–3 summarizes the natural period and natural frequencies of the building. The period in the
X direction (long-side direction) is shorter than that in the Y direction (short side direction). The
measurements were performed at the center of each floor; thus, the obtained period characteristics are
representative of the typical vibration characteristics of the whole building in both long and short

directions. The external surface of the target building was a brick wall structure in the long-side direction. In the short side direction, except for wall structures such as gable walls, the main structural form inside was RC rigid frame structure. Thus, the long-side direction had a structure with higher layer rigidity than the short-side direction.

Figure 2–10 also shows that the vibration characteristics at measurement point N4, which was measured on the beam of the roof truss, has a peak period of 0.0352 sec. on the short-period side. **Figure 2–14** shows a Lissajous drawing of the mode waveforms of the specific period bands (0.0352 sec., 0.153 sec., 0.172 sec.) of the building, including this period band. The peak period of 0.0352 sec. corresponds to the peak period band in the vertical direction of the first floor, as can be seen in **Figure 2–12**. The transfer function in the Y direction shown in **Figure 2–11** does not show any peak in this period band. Therefore, only the vibration characteristics in the X direction of roof truss beam (N4-X) shown in **Figure 2–10** are affected in this period band. This may be caused by the structural difference between the short and long-side directions. In other words, the structure in the short side direction is a triangular truss structure consisting of roof raking beam, a third-floor middle column, and second-floor beam members. Horizontal vibrations caused by excited rocking are less likely to occur in the frame. Conversely, in the long-side direction, the third floor is a rigid frame structure. This structure tends to have a vertical rocking vibration of the middle columns, which causes a horizontal vibration of the plane. In general, cracks can also cause abnormal vibration in buildings.

Therefore, proper crack repair is an important part of extending the service life of a building and ensuring its economic value [14][16]. It is essential to address concrete cracks promptly to prevent these hazards from occurring. Regular inspection and maintenance can help identify and repair cracks before they become a significant issue.

(3) Concrete crack detection

The detection of concrete cracks is crucial for ensuring the structural integrity and safety of a building. Visual inspection is one of the most basic and straightforward methods for detecting cracks in concrete. Aids that can be used typically include crack width ruler, crack width microscope, and tell-tale crack monitor as shown in **Figure 2–15**. Other methods for detecting cracks are shown in the **Figure 2–16** including the use of acoustic and ultrasonic testing [17][18][19][20], ground-penetrating radar [21][22], and infrared thermography [23][24]. Acoustic and ultrasonic testing can detect cracks by analyzing the sound waves or vibrations that are generated when the concrete is struck with a hammer or other instrument. Ground-penetrating radar uses radar waves to detect and map the location of cracks in concrete. Infrared thermography detects cracks by measuring the temperature changes in the concrete surface.

The method used for crack detection depends on various factors, including the size and location of the cracks, the accessibility of the concrete surface, and the budget available for inspection and maintenance.

(a) Crack width ruler

(b) Crack width microscope

(c) Tell-tale crack monitor

Figure 2–15 Some tools for measuring crack width

(a) Ultrasonic testing [20]

(b) Ground-penetrating radar inspection [22]

(c) Thermal infrared image [24]
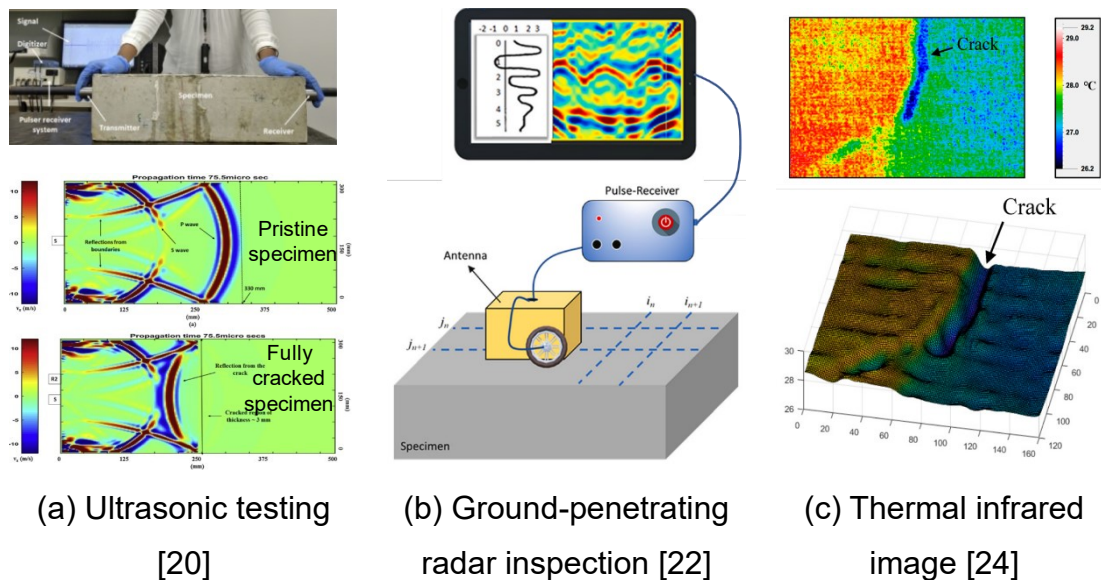
Figure 2–16 Non-destructive crack detection methods.

2.1.2.Crack movement: measurement and pattern

The crack movement involved herein refers to the change in crack width caused by the expansion or contraction of concrete materials under the influence of ambient temperature changes. These daily crack movements of approximately 0.02 mm to 0.2 mm have been reported in bridge [25], pavement (**Figure 2–17**) [26][27], track [28], beam [29], and wall [30] concrete elements (excluding traffic factors). Furthermore, the magnitude of daily crack movement may be influenced by temperature [26] and structural constraints [28]. This crack movement occurs almost every day, and although the movement becomes smaller after the crack has been repaired, it still exists as shown in **Figure 2–18**

[31]; this could be explained by the difference in thermal expansion or contraction between the repair material and the concrete substrate. In other words, crack movement exists throughout the entire life cycle of a building.

The movement generates repeated cycles of tensile and compressive stresses in the repair area, which may cause fatigue failure of the material [32]. In the case of insufficient strength of concrete substrate and repair material, or the lack of adhesion between the two, it leads to repair failure with re-cracking or debonding [33][34][35]. Most importantly, crack movement occurs in conjunction with temperature changes. This is true for components such as exterior walls exposed to a wide range of temperatures, from sub-zero to temperatures as high as 40 ∘C or 50 ∘C. Cyclic temperature changes are a highly adverse degradation condition, especially for polymeric repair materials, which are extremely sensitive to temperature for both mechanical properties [36][37] and adhesion to concrete substrates [38][39]. Thus, it is argued that external mechanical forces coupled with temperature loading expose the repair area to more complex deterioration conditions, which is why crack movement can be considered to affect the durability of the repair.
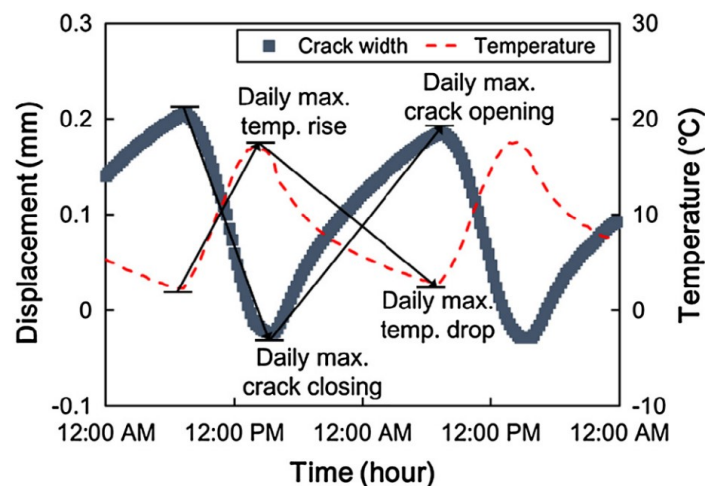

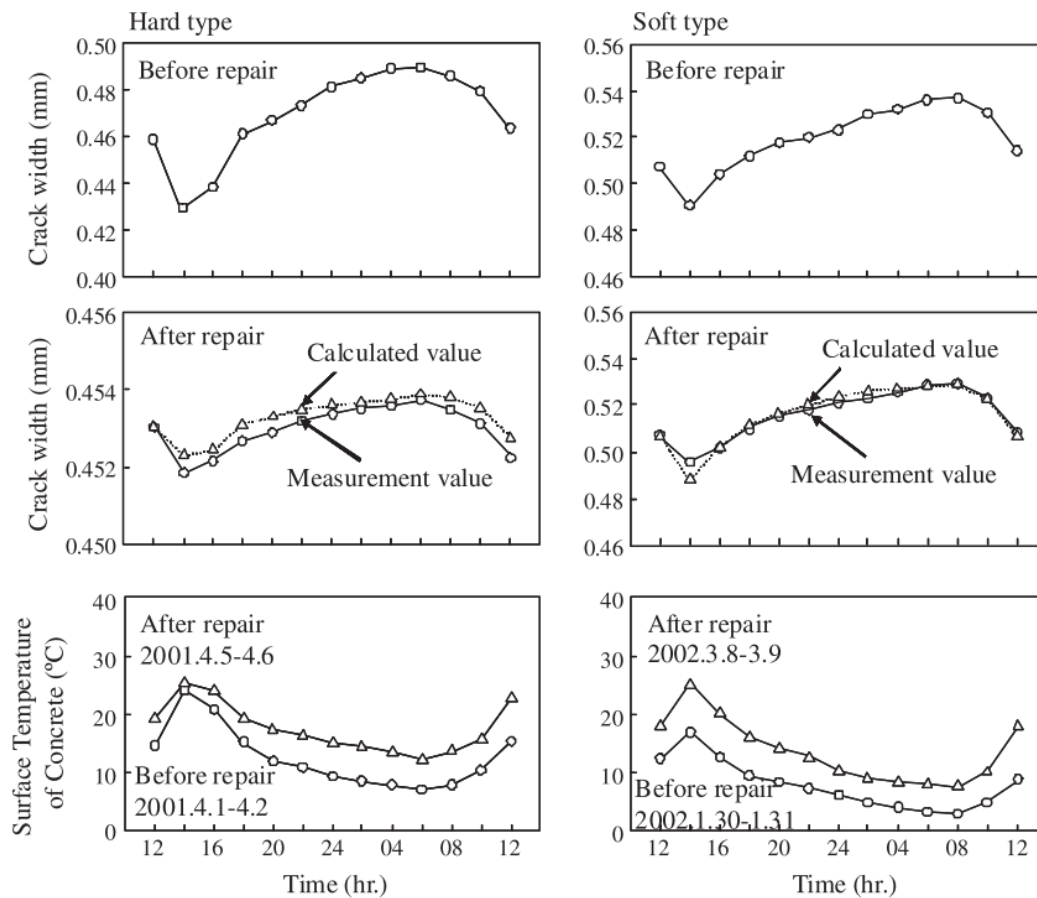Figure 2–17 Crack width and temperature [26].

Figure 2–18 Measurement and calculated value of crack movement before and after injecting epoxy resin [31].

Additionally, our research team noticed a new possible crack opening and closing movement pattern when measuring the crack movement in actual building walls in the Hiroshima [40], Aichi [41], and Hokkaido regions [30][42]. As an example, the measurement results of the exterior wall of a building located in Aichi Prefecture is shown in the **Figure 2–19**. When the measurements were made on cracks that penetrated the thickness of the wall (through-thickness cracks), the change of crack widths on the indoor side and the outdoor side were in opposite directions, showing a bending-like movement (**Figure 2–20**): as the outdoor temperature increased, the outdoor crack widths became smaller, while the indoor crack widths became larger. In this case, the repair material is no longer subjected to pure axial compression or tension during the work, but to compression on one side and tension on the other side, depending on the position in the cross-section of the wall. Moreover, the change in crack width occurred simultaneously and cyclically with temperature changes. This movement pattern of through-thickness cracks can also have an impact on the durability of the repair and can even place demand on the timing and location of the repair. The timing of the repair refers to whether the repair is done when the crack width is large or when the crack width is small, which determines how the repair material

should be stressed in the future. The location of the repair may refer to the injection method being used either on the outdoor side of the wall, or both on the outdoor and indoor side. However, there is no test method that can satisfy the special opening and closing pattern of through-thickness cracks to evaluate the durability of the repair.
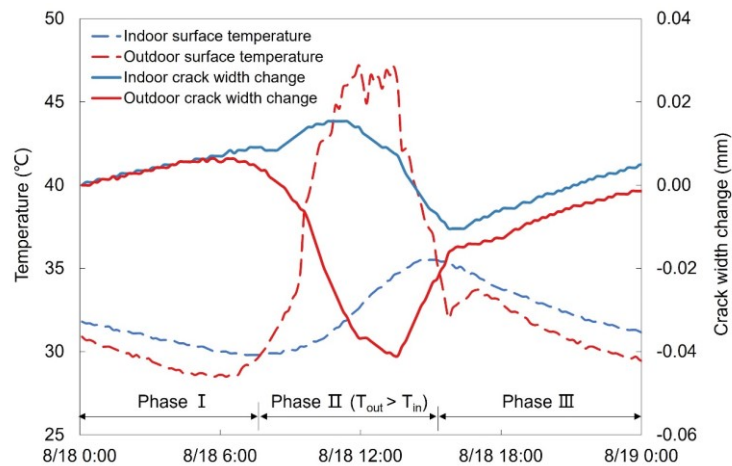
Figure 2–19 Wall surface temperature and crack width change over time on August 18, 2019 (Chubu University, Aichi Prefecture, Japan).
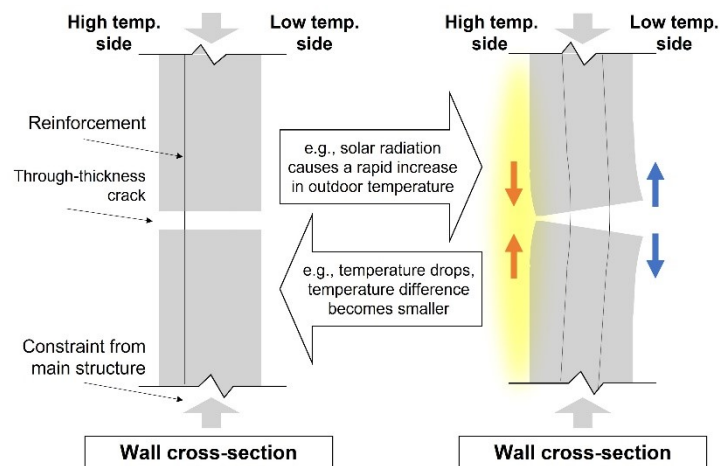

Figure 2–20 One pattern of opening and closing movement of through-thickness cracks under influence of temperature gradient.

2.2. Crack repair technologies and evaluations

2.2.1. Crack repair solutions and requirements

Concrete crack repair is a necessary maintenance task for concrete structures to prevent further

damage and ensure their durability. Various methods are available, such as epoxy injection, routing and sealing, and grouting. A variety of crack repair guidelines are available in various countries, the more commonly used being ACI 224.1R-07 [43], which is a technical report published by the American Concrete Institute (ACI) that provides guidance on the cause, evaluation and repair of cracks in concrete structures. The report covers 13 types of repair methods including injection, drilling and plugging, and stitching, among others, as shown in the **Figure 2–21**. It provides detailed guidance on the selection of appropriate repair materials and methods based on the type of crack and structural requirements.
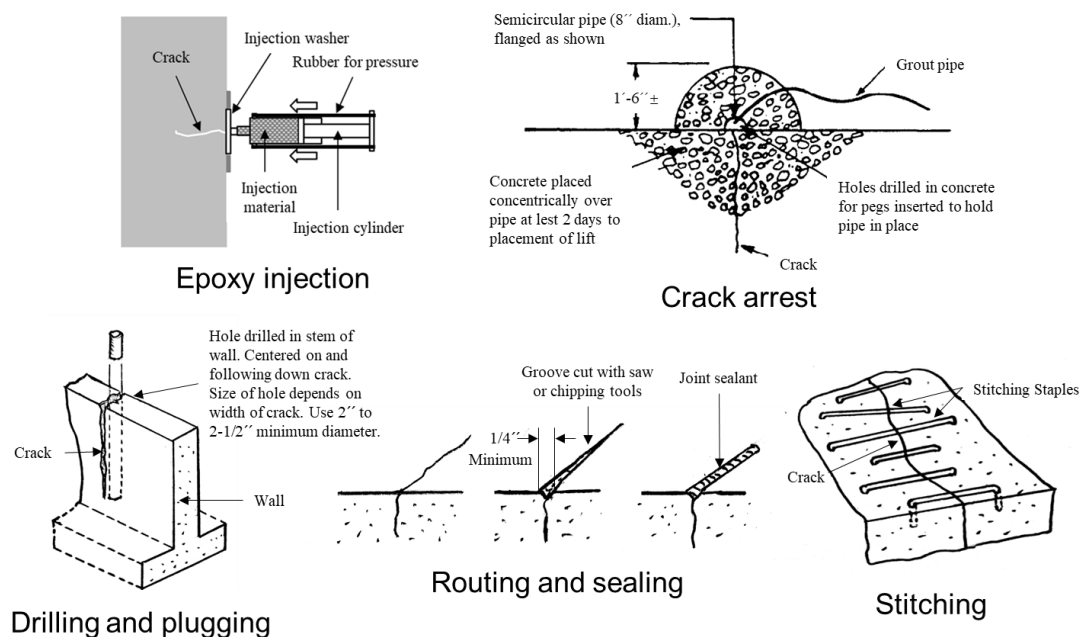
Figure 2–21 Some typical crack repair methods [43][44].

In addition, the European standard BS EN 1504 is an important reference guide for crack repair. First, it selects methods for dealing with concrete defects based on six main principles: 1. Protect against ingress; 2. Moisture control; 3. Concrete restoration; 4. Structural strengthening; 5. Physical resistance; 6. Resistance o chemicals. Next, based on the above principles, structural and non-structural repairs such as impregnation, coating, filling, injection, electrochemical treatment, and replacement are recommended for selection. In subsequent sections of BS EN 1504, the requirements of the desired materials are made explicit for the selection of suitable commercially available products.

In general, according to the required performance, crack repair materials can be divided into injection materials and filling materials. Alternatively, the repair materials can also be classified depending on the main components into cement-based and resin-based repair materials. These materials should focus on satisfying strength, followability (elastic resilience), fluidity, etc. Specifically, ACI 224.1R-07 [43] and [45] provide details on crack repair materials, which include,

but are not limited to: 1. Epoxy resin; 2. Urethane resins; 3. Polyurethane chemical grouts; 4. Polyurethane sealant; 5. Silicone sealant; 6. Methacrylates; 7. Polymer grout; 8. Polymer-cement grout; 9. Cement grout.

There are many researchers who have conducted various studies on concrete crack repair materials. By replacing the cement binder of the concrete mixture by polymer partially, polymer modified cementitious (PMC) repair materials can be obtained. Coalescence of the polymer occurs as the cement hydrates, resulting in a co-matrix of hydrated cement and polymer film throughout the concrete. The modified repair material has improved mechanical properties, bond strength, abrasion resistance and impermeability [46][47]. Polymer concrete (PC) is a type of concrete in which a polymer binder, such as epoxy or polyester resin, is used instead of Portland cement as the binding agent. This results in a high-strength material that is resistant to chemical attack and has low permeability. PC has a higher initial cost than traditional materials and is typically used in applications that require high strength and durability, such as bridge decks and pavements [48][49]. In addition, geopolymer concretes (GPC) is considered a relatively new sustainable construction material due to its incorporation of industrial waste materials into its composition. They are cement-free alternative materials produced by the chemical action between alumino-silicate materials such as fly ash, metakaolin and/or granulated blast furnace slag and an alkali activator, often a mixture of sodium hydroxide (NaOH) and sodium silicate solution (Na_2SiO_3) [50]. GPC also has good durability, adhesion characterization and resistance to chemical attack, making it suitable for use in harsh environments such as wastewater treatment plants, chemical storage facilities, and marine structures [51][52][46]. Moreover, in the last two decades, various fiber-reinforced polymer (FRP) composites have gained attention for strengthening and repairing concrete facilities. FRPs are high-strength, durable, easy to install, and can be selected from a wide variety of fibers that balance functionality with environmental friendliness [53]. The fibers can both enhance the shear strength initially and also act as a bridge to control the crack width after the cracks appear. In this case, the use of high-performance fiber-reinforced cementitious composites can provide additional benefits for self-healing concrete [46][53].

Regarding the selection of repair solutions, in majority of the specifications related to crack repair, the scale of the crack (width, depth, density), progression of the crack (change in width, also known as crack movement), and environment in which the crack is located (temperature and humidity) are the main selection criteria [11][54][45]. In actual engineering applications, while data such as crack width and ambient temperatures are easily obtained for repairing cracks, data on crack movement is hardly obtainable due to the high cost of service, equipment, and continuous monitoring time [55]. As a result, crack repair solutions are usually chosen based on visual inspection or human experience instead of quantitative data [55][56]. Coupled with multiple and complex deterioration conditions, failures such as re-cracking, sealant peeling, and other repair failures often occur prematurely after crack repair [57][44][58][33].

2.2.2.The evaluation of crack repair

Currently, the main subjects of experimental evaluation of concrete crack repair performance include the physical and mechanical properties of the repair material and its compatibility with the concrete substrate. For instance, the filling condition [59][60], compressive strength [61][62], tensile shear strength [62], flexural toughness [63], and bonding behavior with concrete substrate [64][65][66] are utilized in many studies to evaluate the performance of repair materials. In addition, water resistance [67][68], chemical corrosion stability [69][70], and resistance to freeze-thaw cycles [70][46] are also important test objects for evaluating the durability of various repair systems.

Specifically, the repair of cracks often involves covering the existing concrete substrate with a new layer of material. However, owing to the mismatch of material properties, additional stresses are generated at the new-old interface, i.e., it is the weakest part of the system. Therefore, it is important to assess the integrity of the interfacial bond. **Figure 2–22** shows the test methods that can be used to measure the bond strength at the interface. These methods are mainly divided into direct tension tests, indirect tension tests (including splitting tests and flexure tests), pure shear tests and combined shear-compression tests [71]. Direct tension testing ((a) and (b)) are the most effective and direct in situ test methods, which have been developed as standard test procedures and are widely used to characterize the interface bond strength. A potential drawback may be the dependence on the test sampling location. Moreover, the results of this type of test tend to be on the conservative side. Regarding the indirect tension tests, they are popular because they can be performed using standard compression test machines. Specifically, the flexure tests ((s) to (w)) evaluate the bond strength by bending elongated specimens. The advantage is the simple operation, and the disadvantage is the low efficiency caused by the smaller test surface-to-volume ratio. Splitting tests ((c) and (d)) are performed using application of compressive load and Poisson effect to generate tensile stresses on the bonding surface. They offer a higher surface-to-volume ratio than flexure tests and are the most widely used type of indirect tension tests. Shear tests ((e) to (m)) are test methods in which torsion or direct shear forces are applied at the interface. Possible disadvantages are the failure to achieve pure shear owing to the presence of bending moments, and stress concentrations at the edge areas. The combined shear-compression tests ((e) to (m)) are test methods that have been developed to reduce this stress concentration. One of the most frequently applied is the slant shear test. The lower the angle of inclination, the lower the shear bonding strength. However, since friction is more prominent in these tests, it leads to a tendency to measure larger shear strength.
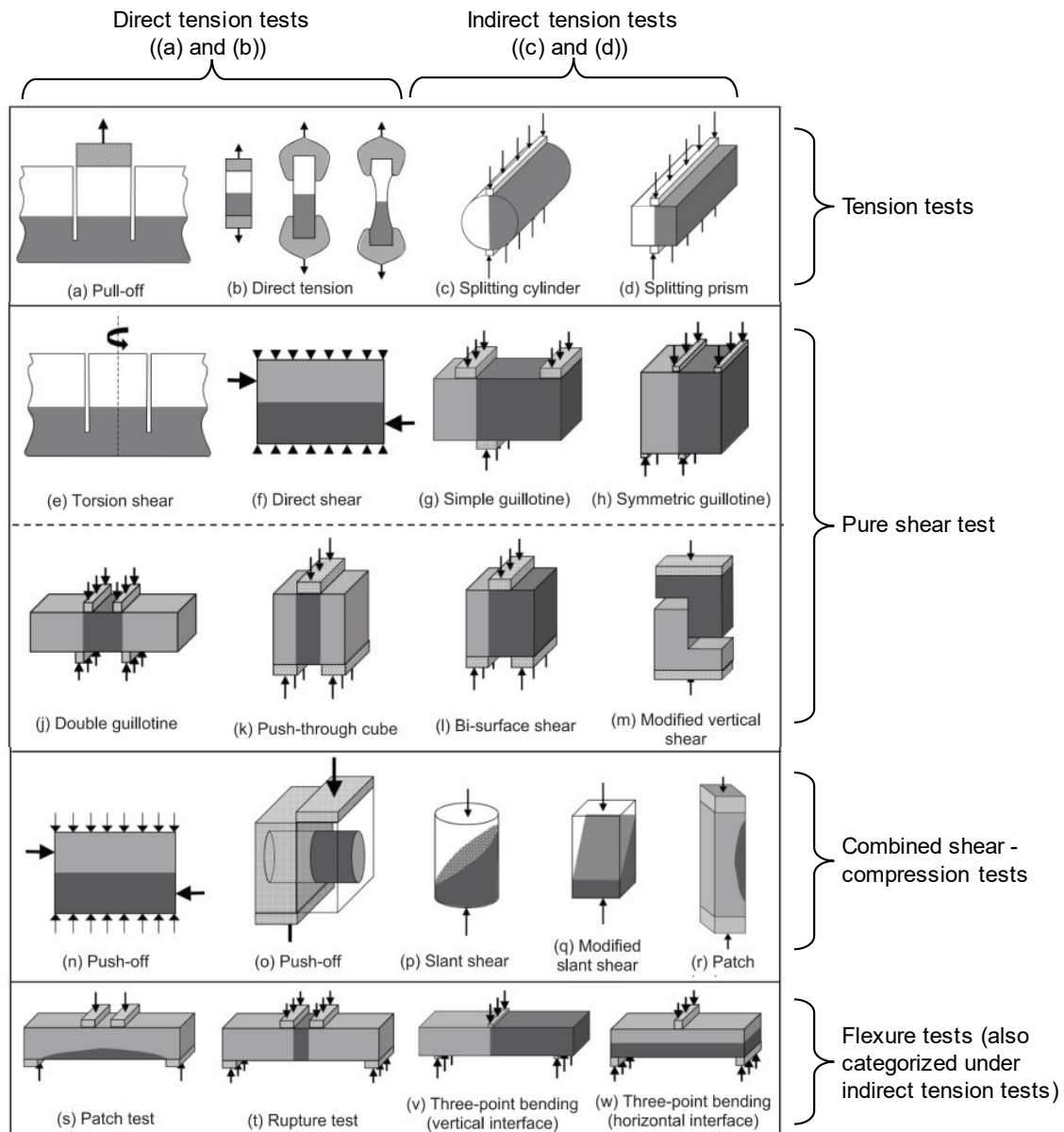
Figure 2–22 Tests for assessing bond strength [71].

However, there are many deterioration conditions in the field, and therefore, there are many crack repair evaluation methods that consider multiple factors. Jiang et al identified six complex forms of degradation factors ("thermal stress, chemical corrosion, erosion due to ground water flow, hydrostatic pressure, substrate movement, and humidity on concrete surface") to evaluate the performance of various types of grout-injection materials and presented a new comprehensive evaluation system that allows for quantitative comparisons [72]. Rashid et al studied the interface between concrete and polymer cement mortar (PCM) under a variety of hygrothermal conditions and observed that the interfacial strength decreased significantly with increasing temperature, while the effect of moisture was minimal [73]. Meanwhile, discussing the effect of continuous and cyclic temperature durations

on PCM-concrete interface, Rashid et al pointed out that temperature cycling conditions have the most detrimental influence on the mechanical behavior compared to other conditions [74]. In terms of test methods involving crack movement, Delucchi et al conducted a series of experiments on the crack bridging ability (CBA) of coatings (the test method is summarized in EN 1062-7 [75]) and highlighted that temperature would affect the CBA values by changing the mechanical properties of the material [76]. Tanaka et al developed a deterioration machine that can apply axial movements to the repair area based on measurements of crack movements in actual building walls and beams, and experimental results showed that repeated movements as small as 2 μm can lead to rupture [29]. Shin et al from the same research team, also investigated the effect of actual weather deterioration on the fatigue resistance of the epoxy resin injection repair area, and after comparing the results of laboratory deterioration experiments, they suggested that complex deterioration conditions in accelerated deterioration tests were needed [77]. Since then, that team has performed further fatigue tests under various conditions and highlighted those large movements and high temperatures, lead to a lower fatigue resistance of the repair area [78][31].

2.3. Building envelope insulation methods and materials

2.3.1. Common insulation solutions

The building envelope is the physical barrier between the indoor and outdoor environments of a building. Ensuring the good insulation performance of building envelopes is important for improving their energy efficiency and reducing structural deterioration factors [79][80][81]. During summers, 50% to 70% of the total energy may penetrate building structures from roof elements [82][83][84], as they are highly exposed to solar radiation for extended periods. Therefore, the use of insulation solutions on roof elements can limit the entry of heat into a building's interior space, thereby reducing the thermal load and, consequently, the demand for refrigeration equipment to provide comfort to occupants.

From this perspective, at the structural level, possible solutions to address this issue are:

1. Green roofs [85][86][87][88] in **Figure 2–23**;
2. Reflective systems [89][90][91] in **Figure 2–24**;
3. Radiant barrier configurations [92][93][94][95] in **Figure 2–25**.

Alternatively, at the material level, there are:

4. Various thermal insulation materials in **Figure 2–26**.

The insulation materials are not limited by building type and offer the advantages of low cost, high flexibility, and high compatibility.
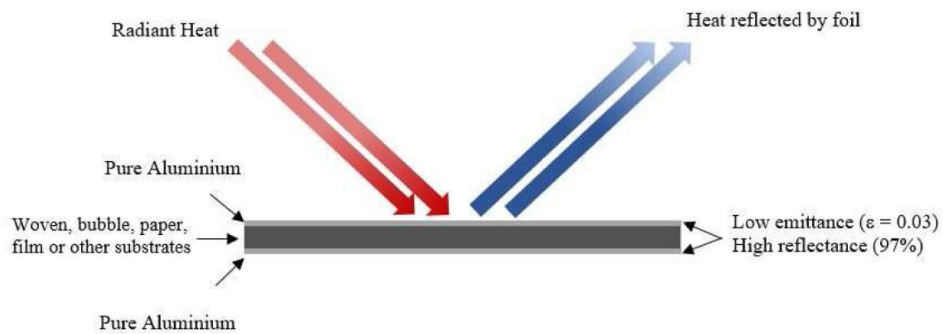
Figure 2–23 Classification of green roofs [85].

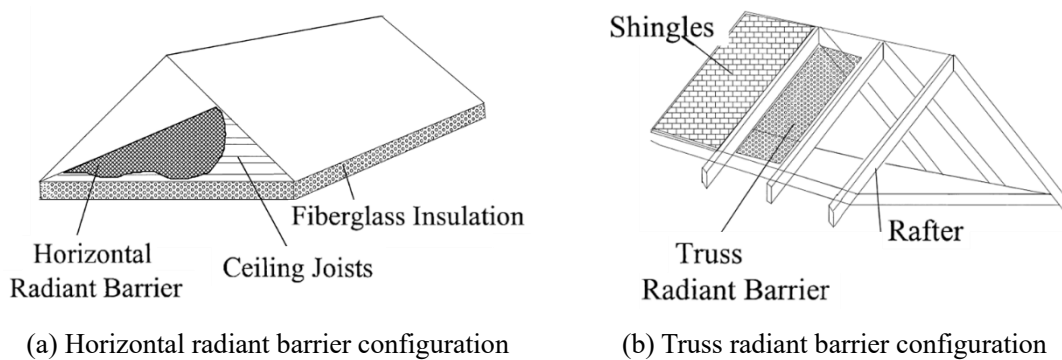Figure 2–24 Mechanism of reflective material [91].

(a) Horizontal radiant barrier configuration　　(b) Truss radiant barrier configuration

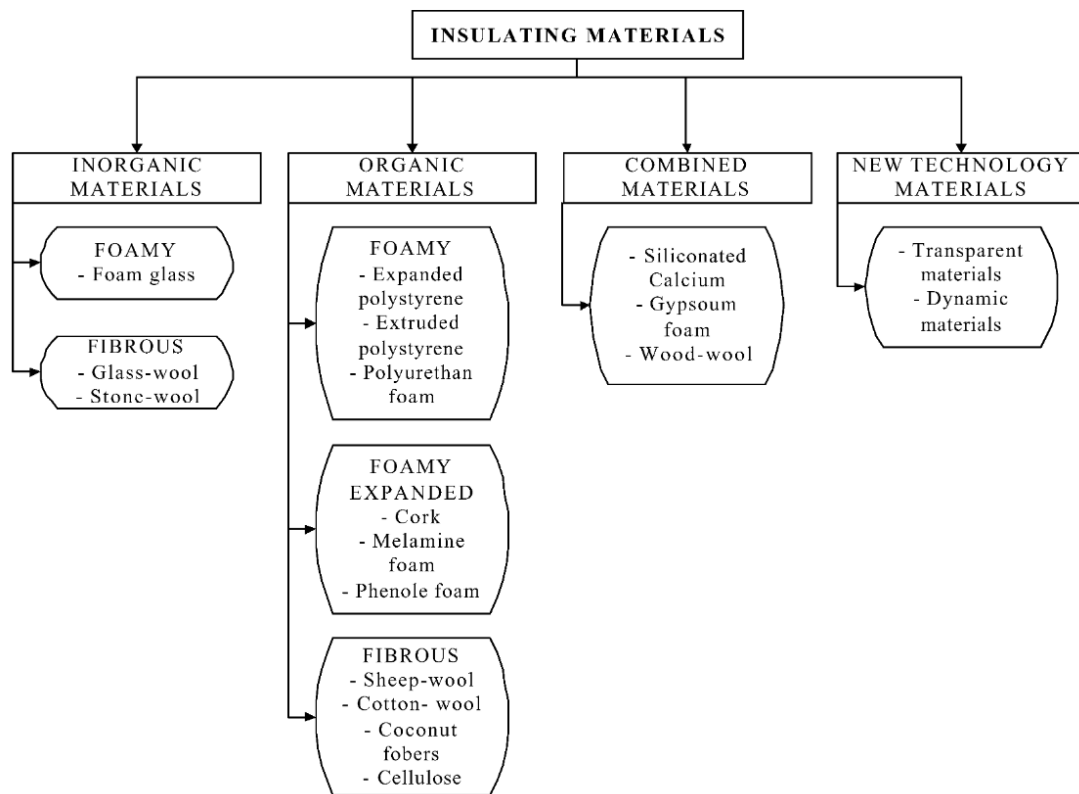Figure 2–25 Radiant barrier configurations [92].

Figure 2–26 Classification of the most used insulating materials [96].

2.3.2. The conventional insulation materials involved in this study

Notably, good insulation materials can maintain thermal comfort inside a housing environment and prevent heat exchange with the surrounding environment. Conventional insulation materials are available in a range of options to suit different applications. Each insulation material has its own advantages and disadvantages, and it is necessary to choose the right one for the specific situation. The next space will be devoted only to the insulation materials involved in this study.

(1) Polyurethane

Polyurethane (PUR or PU) is produced through an exothermic reaction between di- or polyisocyanate with a polyether polyol [80]. Thermal conductivity varies from 0.022 to 0.040 W/m·K, density from 15 to 45 kg/m^3 and specific heat is between 1.3 and 1.45 kJ/kg·K [80][97]. Thermal conductivity is influenced by the cell size and decreases when the cell size decreases [98]. Polyurethane can be used to produce panels and pipe sections (the following type A), or it can be expanded in the building site as a foam (the following type B).

Type A: Rigid polyurethane foam (PUF). PUF is made into boards at the plant and cut into various sizes in situ as needed. It is lightweight and easy to install, making it a popular choice for many construction projects. It is cost effective and durable. However, the joints between the panels may

require extra attention to maintain air tightness and thermal insulation.

Type B: Sprayed polyurethane foam (SPF). SPF is applied to surfaces as a liquid, which then expands and hardens into a foam. It is typically applied using a spray gun, and it can be used to insulate a wide range of surfaces, including roofs, walls, floors, and attics. The major advantages of SPF insulation are that it can be applied to irregularly shaped surfaces and can easily conform to the shape of the surface it is applied to.

(2) Extruded polystyrene

The extruded polystyrene (XPS) is produced by melting the polyester grains into an extruder, with the addition of a blowing agent. It has a thermal conductivity of 0.031 to 0.037 W/m·K, a density of 15 to 75 kg/m^3, and a specific heat between 1.3 and 1.7 kJ/kg·K [80][99]. High humidity can reduce its insulation performance [100]. Since the material is easily flammable and burning releases dangerous gases, a fire retardant is often added in the manufacturing process.

2.4. Thermal insulation performance: evaluation indicators and measurement methods

Currently, indicators for evaluating the performance of insulation materials include the thermal conductivity (K-value) and thermal resistance (R-value). Thermal conductivity measures the rate at which heat flows through the material, with a lower K-value indicating better insulation. R-value is a measure of the resistance of the material to heat flow, with a higher R-value indicating better insulation performance. These values can be measured using several different methods. The most accurate method for measuring thermal conductivity is the guarded heat plate method (GHP) according to standards ISO 8302 [101] as shown in **Figure 2–27** [102], which involves sandwiching the insulation material between two plates and measuring the rate of heat transfer through the material. Another method for measuring thermal conductivity is the heat flow method according to standards ISO 8301 [103] as shown in **Figure 2–28** [102], which measures the rate of heat flow through a small sample of insulation material. R-value can be calculated by dividing the thickness of the insulation material by its thermal conductivity. These methods are commonly used to determine the effectiveness of insulation materials and to ensure that buildings are properly insulated to improve energy efficiency and occupant comfort.
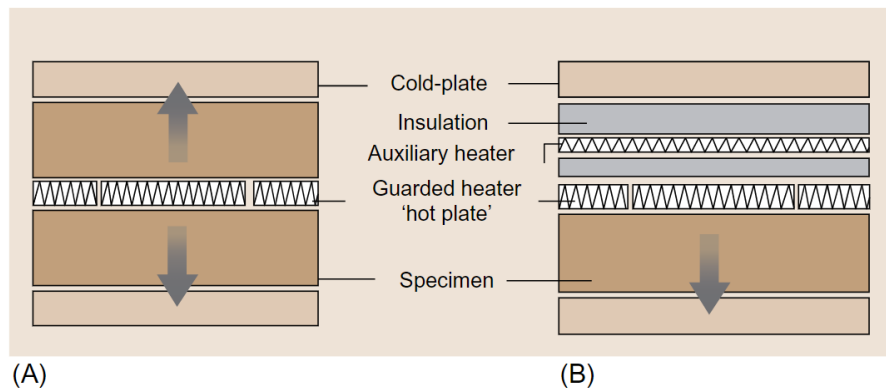
Figure 2–27 Principle of the guarded heat plate method (GHP) with a two-specimen apparatus (A) and a single-specimen apparatus (B) [102].
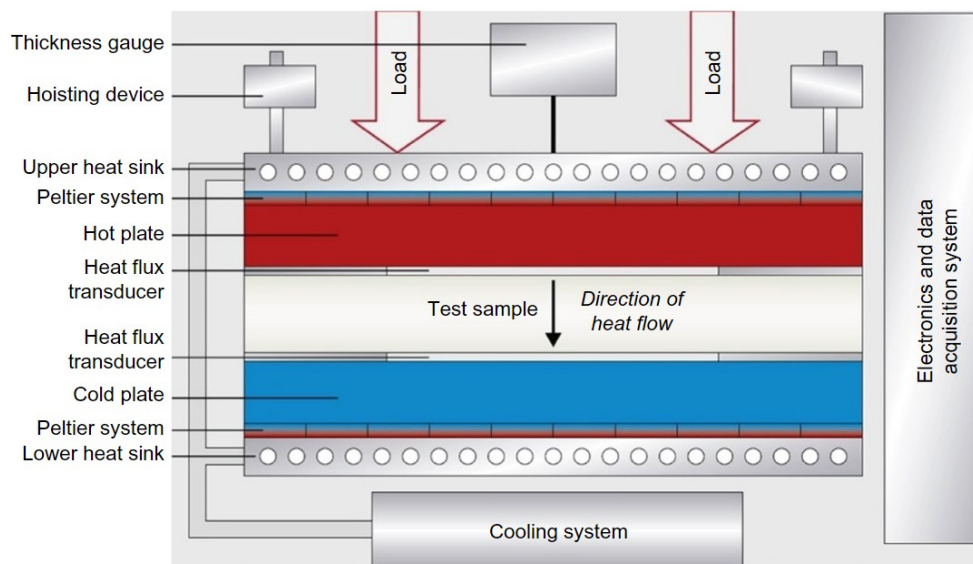

Figure 2–28 Heat flow method [102] for measuring thermal conductivity.

However, in the field, a typical building envelope may consist of multiple layers such as the substrate, insulation, and decorative layers, which makes it difficult to determine the physical properties of each layer of the element. Therefore, in actual practice, the indicators for evaluating the thermal insulation performance of building elements generally include the total thermal resistance and thermal transmittance (U-value) determined in ISO 6946 [104]. A lower U-value indicates better insulation performance and means that less heat can flow through the component. Additionally, the common measurement methods for the U-value include the Calibrated Hot Box (CHB) and Guarded Hot Box (GHB) method according to ISO 8990 (**Figure 2–29**) [105], heat flow meter method (HFM) based on ISO 9869-1 (**Figure 2–30**) [106], infrared thermography method (IRT) (**Figure 2–31(a)**) [107][108], and temperature-based method (TBM) (**Figure 2–31(b)**) [107][109][110]. The

comparison of various U-value measurement methods is summarized in **Table 2–4**.However, most of these measurements must satisfy the approximate steady-state heat-transfer conditions for large temperature differences. Therefore, in situ measurements over at least 72 h in specific seasons are usually required to obtain reliable data [104][111]. Alternatively, it is necessary to filter the data [112] or use dynamic theory to consider the fluctuations, hysteresis, and decay of the heat-flow density and temperature [113][114][115].
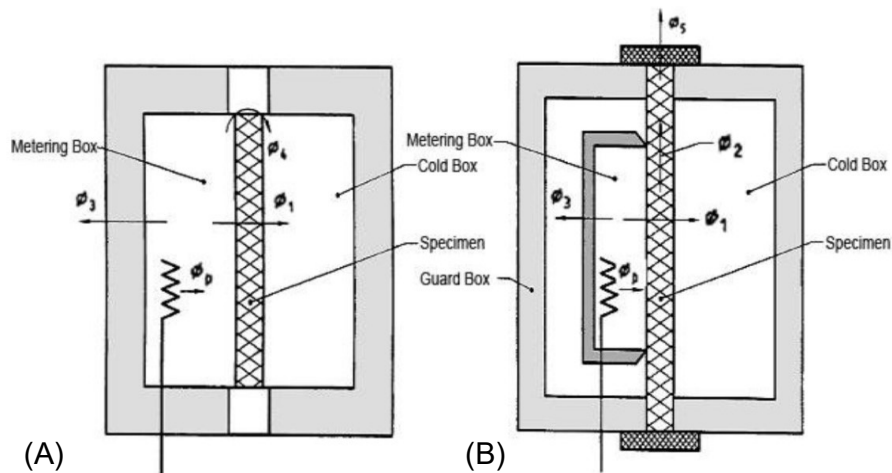

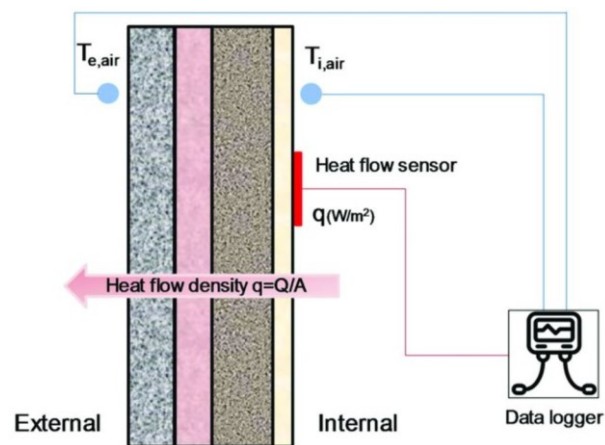Figure 2–29 (A): Calibrated Hot Box (CHB) and (B): Guarded Hot Box (GHB) method [105].

Figure 2–30 Heat flow meter method (HFM) for measuring U-value [106].

(a) Infrared thermography method
(IRT)

(b) Temperature-based method
(TBM)
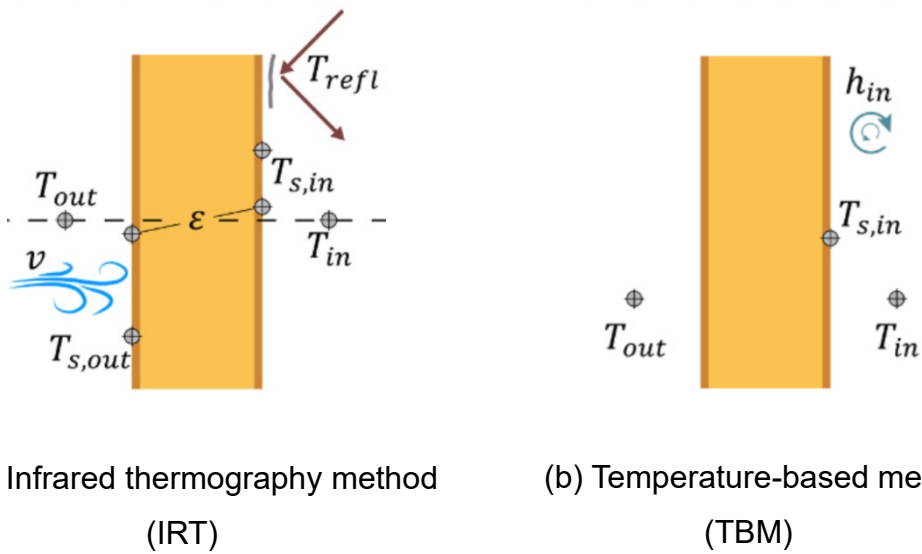
Figure 2–31 Other common U-value measurement methods [107].

Table 2–4 Comparison of U-value measurement methods [107][116][111][117].

Method	CHB GHB	HFM	IRT	TBM
Accuracy Range [%]	n.a.	Winter: 0–163 Avg. 24 Summer:45–142 Avg. 90	Winter: 0–162 Avg. 19 Summer:1–286 Avg. 55	Winter: 4–37 Summer:2–62
Cost	High	High	High	Low
Time	n.a.	Min. 3 days	Less than1 day	Min. 3 days

Advantages	CHB: Apparatus is simpler in design and operation than the GHB; Allows testing of larger specimens. GHB: Does not need to have a calibration factor for the flanking loss of the metering box, due to the existence of the guard box; Simpler to calibrate than the CHB.	Non-invasive method; The higher the temperature gradient, the more reliable the results are; Internationally recognized and most widely used; Lightweight and easy to carry equipment; Both in laboratory and in-situ.	Non-destructive method; Large number of applications, can detect multiple pathologies; No direct contact and can be used over long distances; Lightweight, short time and in real time.	A relatively new method; Simple and economical equipment; Non-destructive method; Simple calculation.
Drawbacks	CHB: Flanking loss between the metering chamber and the climatic chamber through the specimen frame; The lab temperature must be controlled to avoid corrections in the calibration factor. GHB: The measuring area is limited to the size of the metering box; More challenging to analyze inhomogeneous specimens due to the size of the metering box.	The measurement is local; Require direct contact; For homogenous object; Lightweight construction elements and the presence of multi-layered air spaces lead to questionable results; Highly dependent on the calibration and the equipment.	Very high price for the equipment; Qualified person to analyze the results and to operate the IR camera; Highly dependent on climatic conditions; Misreading information is taken by the camera when temperatures have very close range.	Non-standardized method; The transfer coefficients used in the calculations represent estimates only and are not necessarily the actual values between the environment and the wall; The accuracy of the measurement results depends on environmental conditions, such as temperature differences and temperature fluctuations;

2.5. Research cases and challenges in building insulation

So far, based on these indicators, the effectiveness of various insulation materials has been evaluated in several studies. Su et al. designed and fabricated basalt fiber-reinforced plastic roof panels with core materials of extruded polystyrene, polyurethane, and rock wool. They conducted a series of investigations on the thermal conductivity, U-values, and thermal bridge effects of these experimental specimens by means of GHP and CHB experiments and Abaqus software analysis [118]. Geoola et al. designed a guarded hot box wherein the use of a thermal screen could reduce the U-value by approximately 30% at different wind speeds and temperature differences [119]. Pasupathy et al. performed experimental investigations and numerical simulations on the thermal behavior of a residential roof using phase-change materials (PCMs) [120]. In a transient analysis, Prakash et al. demonstrated that the use of PCMs can reduce the heat entering a room by 13% [121]. Costantine et al. conducted experimental and numerical investigations on the temperature, humidity, and heat flux in an office with hemp-lime insulation [122]. The ability of natural mesoporous materials to reduce surface temperatures was validated based on both steady-state and periodic experiments by Rahman et al. [123]. Altin et al. built three full-scale buildings and conducted temperature, moisture, and sound tests on boron-doped sheep wool, expanded polystyrene, and rock wool insulation [124]. Yin et al. carried out in situ tests on the thermal performance of a double-layered dome with aerogel-glass wool insulation and provided numerical analysis data for the design of the combination of insulation materials [125]. Hasan et al. investigated roof insulation in Iraq and discovered that certain combinations of insulation could reduce the heat flow by more than 79% [126]. Kuma et al. measured the thermal conductivity of insulation materials available in the Indian market using an automatic guarded hot plate apparatus and computed the thermal resistance and thermal transmittance of 112 wall and roof sectors [127]. Zhao et al. evaluated the bulk density, thermal conductivity, water absorption, and compressive strength of a large number of environment-friendly building insulation materials. They also selected seven of the most competitive insulation materials using the city of Harbin, China, as an example, by life-cycle cost [128].

To better address the energy management problems encountered by building owners, the economic aspects and applications of common building insulation materials, in addition to their performance characteristics, were also discussed by Al-Hamoud and Aditya et al. [129][97]. Halwatura et al. investigated the impact of insulated roof slabs on air-conditioning loads and estimated their life-cycle cost benefits [130]. Papadopoulos discussed various aspects of insulation materials, including their environmental and public health impacts, within the framework of legislation and the market [96]. Notably, in most cases, the evaluation indicators are targeted toward practitioners in the building industry. However, for owners, it is sometimes difficult to intuitively predict the insulation performance. We believe that establishing a connection between professional evaluation indicators and temperature, a common physical quantity, may be a solution to this issue.

2.6. Conclusions

This chapter addresses a literature review of the building envelope regarding crack repair and insulation construction. The main findings are as follows:

1. Cracks are the most common form of deterioration in reinforced concrete buildings. Harmful substances can invade the interior of the structure through cracks, and untimely treatment can accelerate the serious consequences. Measurements of actual buildings have shown that cracks also cause abnormal vibrations in the structure. Proper repair of cracks can extend the life of a building.

2. Daily temperature fluctuations cause changes in crack width, i.e., crack movement. This means that crack movement occurs almost every day. In addition, because the physical properties of the repair material and the concrete material are different, the crack movement still exists after the repair. The movement affects the durability of the repair effect. For the through-thickness cracks, when the outdoor surface temperature rises, the outdoor cracks close and the indoor cracks open, producing a bending-like movement.

3. Current crack repair evaluations include filling conditions, physical strength, chemical resistance, etc. Experiments that simulate realistic coupling of multiple deterioration conditions usually include temperature conditions, hydrostatic pressure, etc. The degradation conditions of bending-like cyclic movement have not been studied. Such deterioration is in the form of simultaneous thermal and mechanical loading, for which there is no corresponding experimental method.

4. Among the various building insulation solutions, insulation materials are popular because of the lack of site restrictions and the variety of choices. The index of thermal insulation performance is clearly defined and measured in the codes of various countries. However, in the laboratory, the huge equipment and complicated calibration process are the main difficulties. In field measurements, long time monitoring is a must. When evaluating the effectiveness of insulation construction, common physical quantities rather than specialized indicators might improve the efficiency of communication with the building owner.

Chapter 3

Proposal for laboratory-scale crack movement simulation methods for repair evaluation

3.1. Purpose

This chapter mainly proposed two lab-scale test methods for reproducing the movement of through-thickness cracks. The test method in this chapter can provide an accessible way to evaluate the effectiveness and durability of various repair solutions under the influence of crack movement.

To this end, this chapter gave measurements of through-thickness crack movement on actual buildings, and their movement mechanism diagrams. The factors that may affect the movement amplitude were also discussed and summarized to provide a basis for the establishment of the test methods. After the practicality and stability of the proposed test methods were verified, an application example for the effect of specimen temperature reduction on the crack movement was also given. We believe that the optimum crack repair solution can be selected by establishing the test methods that simulate the opening and closing of cracks at the laboratory scale.

3.2. Movement of through-thickness cracks in actual buildings

3.2.1. Monitoring of crack movement

To exclude the influence of individual cases and to improve the representation of the measurement results, our team conducted measurements of cracks on actual buildings at different latitudes in Japan: Hokkaido (higher latitude, colder region), Hiroshima Prefecture (lower latitude, warmer region), and Aichi Prefecture area (central region of Japan). This paper reports the measurement results of through-thickness cracks in Hiroshima Prefecture.

The measurement object was a pharmaceutical warehouse building located at Hiroshima University in Hiroshima Prefecture, Japan. The through-thickness crack was located on the exterior wall of the reinforced concrete structure, as shown in **Figure 3–1**. The wall surface temperature and change in crack width were measured by Type T Thermocouples and KG-2 A Crack Displacement Transducers respectively. Displacement transducers were mounted across the cracks on the concrete surface to continuously monitor the change in the crack width over time. Its waterproof structure allows this transducer to make stable measurements outdoors over a long period of time, with sensitivity and capacity of 1500×10^{-6} strain/mm and ± 2 mm, respectively. The effect of temperature variations on this sensor is negligible. The specifications of the displacement transducers used in this work for the

continuous monitoring of the crack width change are listed in **Table 3–1**. The preparation before the monitoring is the same for two types of transducers, taking the PI-2-50 as an example, and the procedure is shown in **Figure 3–2**. The data recording interval is 10 minutes.
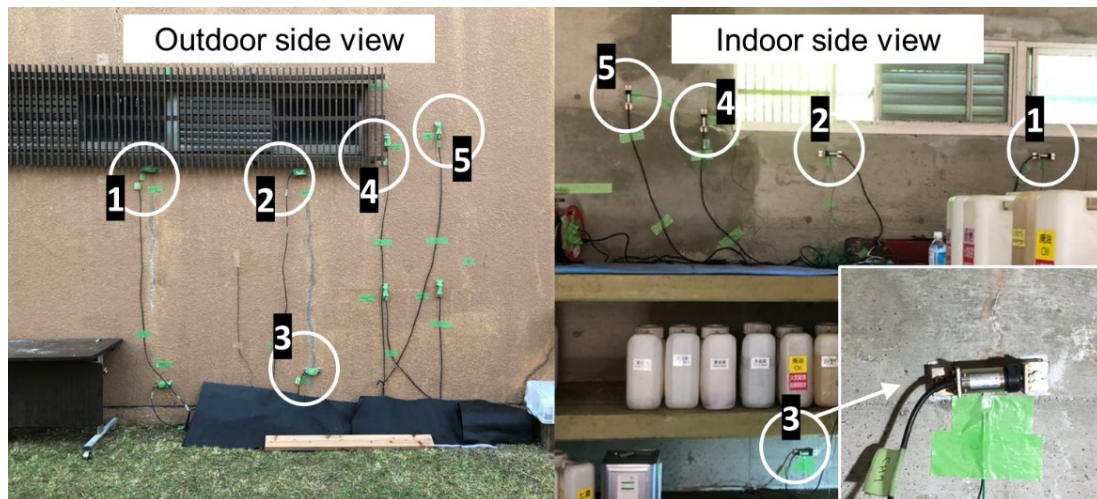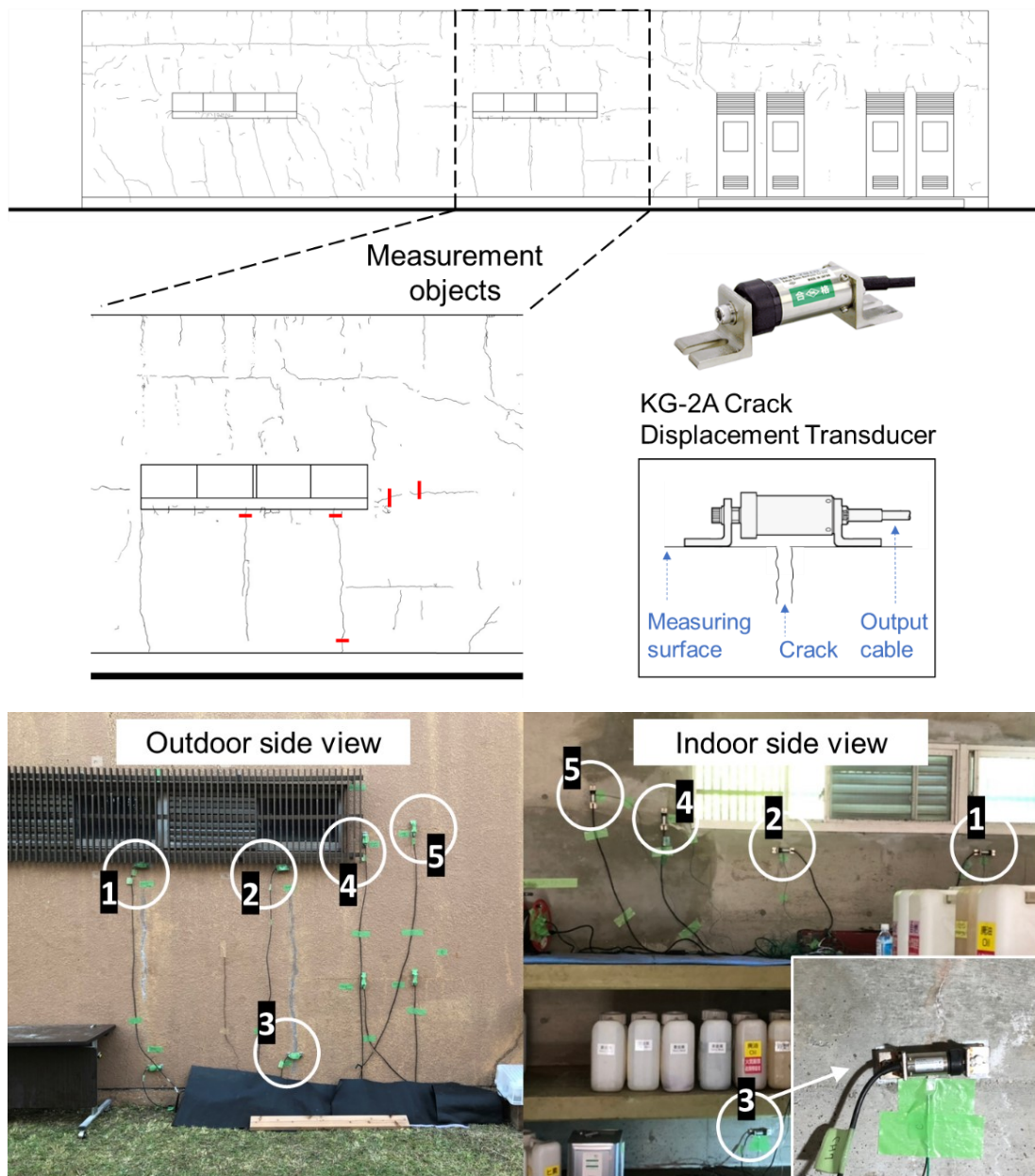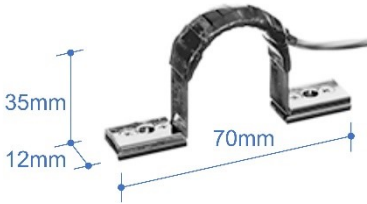

Figure 3–1 Measurement object appearance (Hiroshima University, Hiroshima Prefecture, Japan).

Table 3–1 Information on transducers.

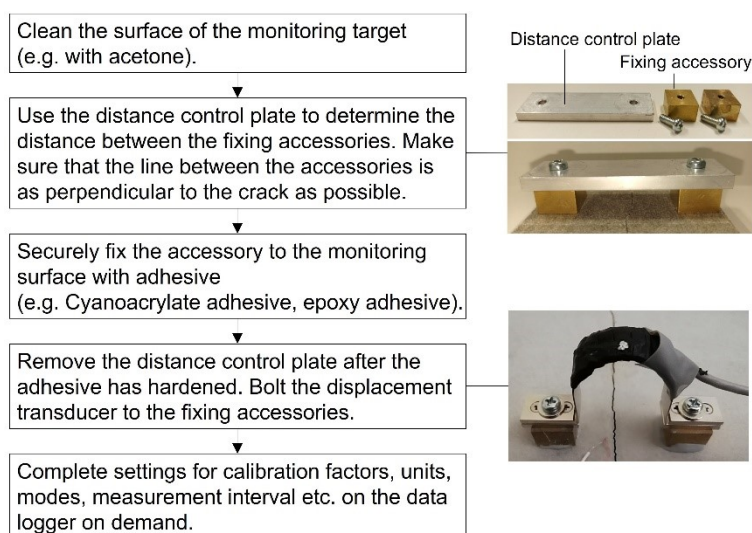| Type	KG-2A Crack Displacement Transducer	PI-2-50 Pi-shape Displacement Transducer
Dimensions		
Capacity	±2 mm	±2 mm
Sensitivity	1500×10^{-6} strain/mm	2000×10^{-6} strain/mm
Allowed temperature range	-20 ∘C – 60 ∘C	0 ∘C – 60 ∘C
Weight	180 g	40 g

Figure 3–2 Preparation procedures for monitoring (data such as temperature calibration factors and temperature characteristic equations for each sensor are provided by the manufacturer).

The results of the wall surface temperature are shown in **Figure 3–3**. Among them, the results for the outdoor side are from October 28 to November 1 (Period I). However, the indoor side measurement results for the same period could not be obtained because of an instrument malfunction, thus the graph shows the temperature results from November 3 to 7 (Period II). In addition, the air temperature data for Period I to Period II were all available, as shown in **Figure 3–4**. Excluding the gray area periods

in the **Figure 3–4**, the air temperatures of Period I and Period II are approximately the same, and according to the local weather station data, the daylight hours on these days were approximately the same, which means that the climatic conditions were approximately the same. Therefore, in the subsequent discussion, the gray time domain in **Figure 3–4** is discarded and the indoor side wall surface temperature of Period II is used to represent that of Period I.
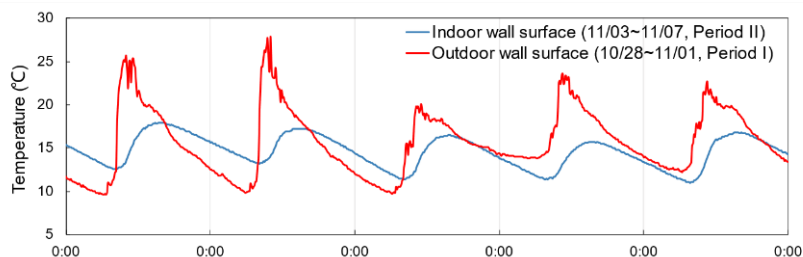

Figure 3–3 Wall surface temperature over time (Hiroshima University, Hiroshima Prefecture, Japan, 2021).
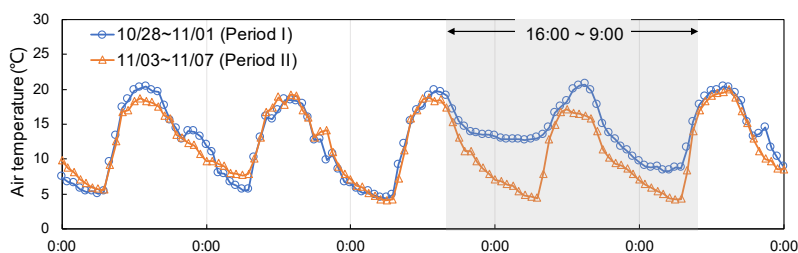

Figure 3–4 Air temperature over time (Hiroshima University, Hiroshima Prefecture, Japan, 2021).

The changes in crack width are shown in **Figure 3–5**. The curves were obtained by considering the initial crack width as zero, with larger values indicating crack opening and smaller values indicating closing. Here, the trend of crack width change showed a strong correlation with temperature change. When the temperature increased in the daytime, the outdoor side cracks were closed, while the indoor side cracks were opened. Subsequently, after the temperature recovered at night, the crack width returned to its initial state. This may be related to the inconsistent temperature variation of the indoor and outdoor surfaces during that period, that is, the existence of a temperature gradient in the cross-section of the wall.
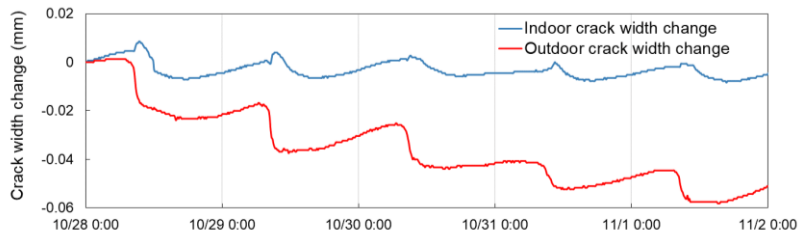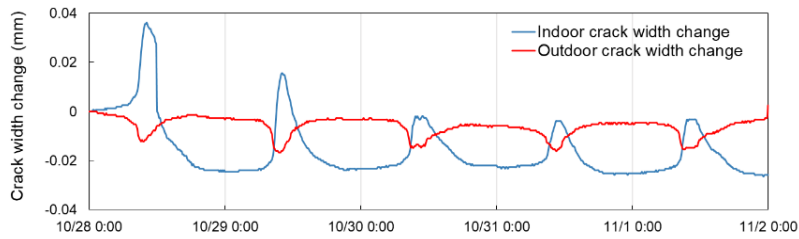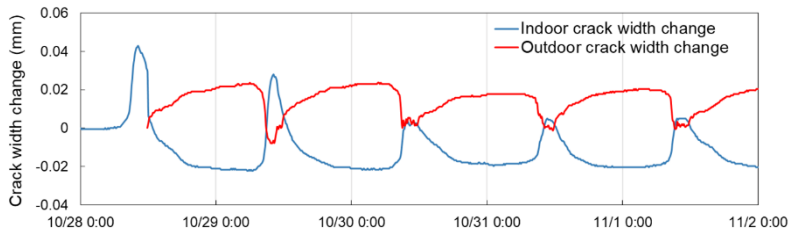
(a) Crack 1
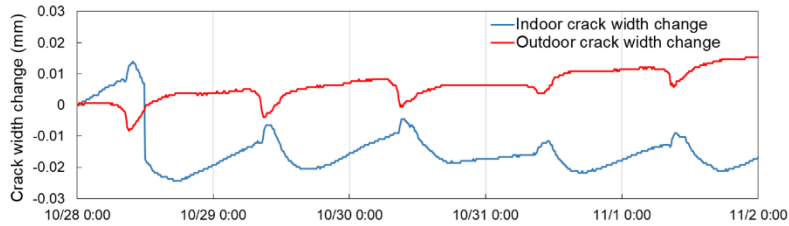
(b) Crack 2
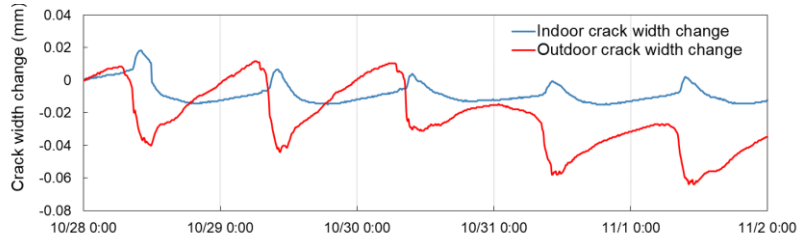
(c) Crack 3

(d) Crack 4

(e) Crack 5

Figure 3–5 Crack width change over time (Hiroshima University, Hiroshima Prefecture, Japan, 2021).

Overall, based on measurements in actual buildings, it was found that a particular pattern of movement of through-thickness cracks can be monitored when a large temperature difference exists between the indoor and outdoor sides. When the outdoor temperature rises, expansion stresses are generated on the outdoor surface of the wall. There is no thermal expansion on the indoor surface at this time, which leads to a stress imbalance in the cross-section of the wall. In addition, the through-thickness crack makes the wall structure non-integral, and under this stress state, a characteristic bending-like movement occurs. In this case, the indoor crack is represented as an opening movement. The outdoor crack is represented as a closing movement in the in-plane direction of the wall, once the temperature expansion component is greater than the reduction caused by bending. Afterwards, when the temperature difference decreases, the driving force of the movement becomes smaller, and the crack width returns to its original equilibrium state.

3.2.2. Discussions of factors that may affect the crack movement

In this subsection, we discuss the relationship between crack movement and three variables: the temperature difference between the indoor and outdoor surfaces of the wall, the strength of restraining force from the main structure, and the initial width of the crack. Although other variables may also affect the crack movement, the currently available measurement data demonstrate only the relationship between crack movement and these three variables; therefore, the other variables will not be discussed in this paper. The definition of the terms and the calculations involved in the discussions are shown in **Figure 3–6**. To exclude the effect of concrete shrinkage behavior as much as possible, the crack widths were set to zero at 0:00 each day during data processing.

$$f'(t) = f(t) - f(t_0) \quad \text{(a)}$$
$$g'(t) = g(t) - g(t_0) \quad \text{(b)}$$
$$h(t) = f'(t) - g'(t) \quad \text{(c)}$$
$$F = f(t_1) - f(t_0) \quad \text{(d)}$$
$$G = |g(t_2) - g(t_0)| \quad \text{(e)}$$
$$H = \max\{h(t)\} \quad \text{(f)}$$

$f(t)$: Indoor crack width change
$g(t)$: Outdoor crack width change
$h(t)$: Crack movement amplitude
F: Max. indoor side crack width change
G: Max. outdoor side crack width change
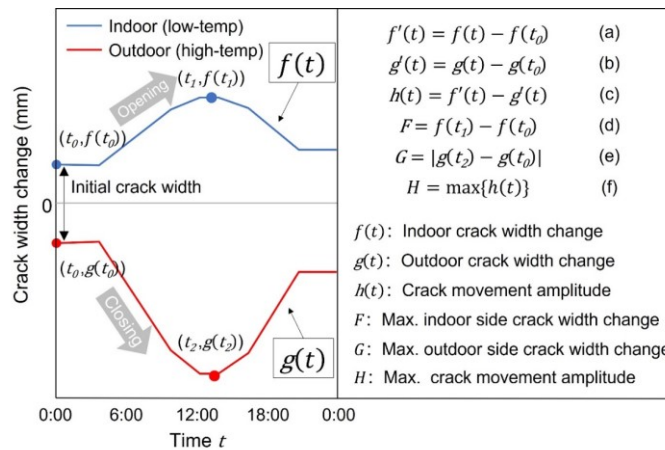H: Max. crack movement amplitude

Figure 3–6 Terms and the calculations involved in the discussions.

(1)　Temperature conditions

As previously mentioned, the presence of temperature difference leads to a characteristic opening and closing movement of the through-thickness cracks. Therefore, the measured temperature difference versus movement amplitude for five days is plotted. The crack movement amplitude here was the difference between the crack width change on the two surfaces, which was taken to indicate the level of crack movement in this study. A larger value means that the difference in stress on the repair material or concrete at different locations in the wall cross-section is greater. In other words, the greater the movement amplitude, the more likely or earlier repair failure would occur. To get more positive values, the crack movement amplitude is calculated by subtracting the value of the crack width change on the high-temperature side from that on the low-temperature side.

In this section, cracks in Hiroshima (**Figure 3–7**), Aichi (**Figure 3–8**) and Hokkaido (**Figure 3–9**) are discussed. These data contain both warm weather in summer and cold weather conditions in winter. As shown in **Figure 3–8(a)**, the measurement object located in Aichi Prefecture was a through-thickness crack that occurred in a reinforced concrete exterior wall on the first floor. The measurement object in Hokkaido was a through-thickness crack occurring in the cantilevered wall of a five-story reinforced concrete building. The dry shrinkage crack penetrated through the wall from south to north, and the east side of the wall was restrained by its connection to the main building structure, as shown in **Figure 3–9(a)**.
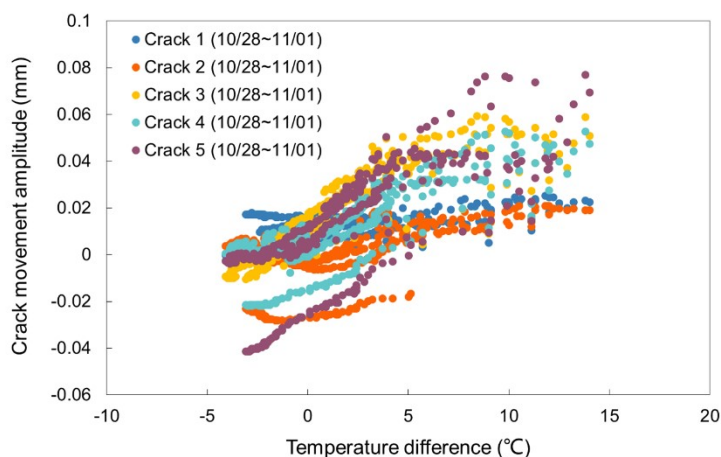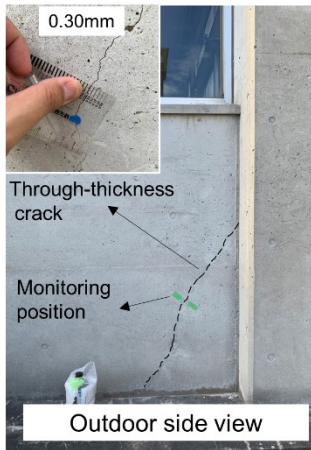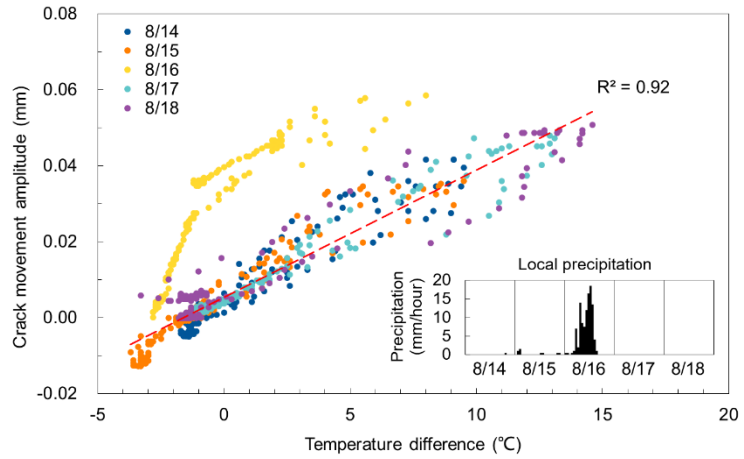

Figure 3–7 Relationship between temperature difference and crack movement amplitude in five cracks over five days (Hiroshima University, Hiroshima Prefecture, Japan, 2021).
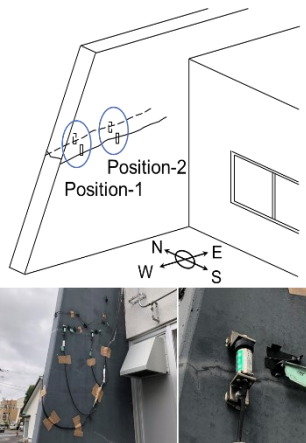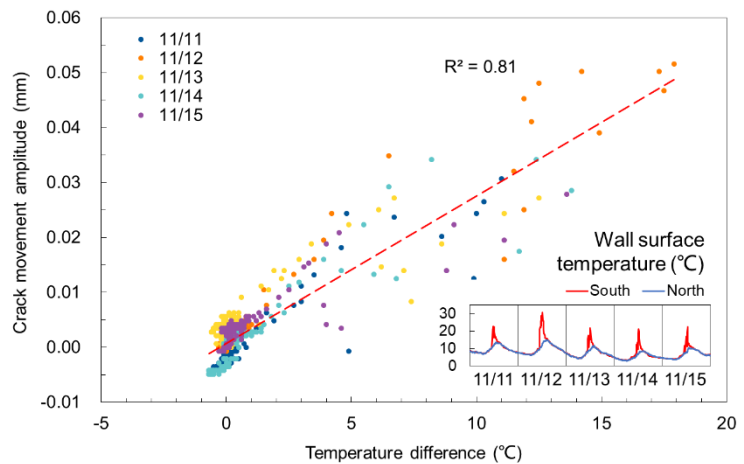
(a) Measurement
appearance

(b) Warm days in summer

Figure 3–8 Relationship between temperature difference and crack width
change in five days (Chubu University, Aichi Prefecture, Japan, 2019).

(a) Measurement
appearance

(b) Cold days in winter

Figure 3–9 Relationship between temperature difference and crack width
change in five days (Sapporo, Hokkaido, Japan, 2018).

In **Figure 3–7**, the greater the temperature difference, the greater the crack movement amplitude tends to be. All five cracks roughly conform to this pattern, except that the slope of each differs. From **Figure 3–8(b)**, on days with a large temperature difference, the crack movement amplitude is also large, and there is a linear correlation. However, the data on August 16 had a significant deviation. In fact, the local precipitation for that day changed dramatically because of a typhoon. Concrete manifests

wet expansion deformation when the moisture content of concrete increases via the seeping of water into the pores of the concrete [131][132]. In addition, the shrinkage of concrete can be greatly inhibited by rainfall and the loss of solar radiation [133][134]. These factors could explain the deviation of the crack movement on August 16. In this case, because the focus is only on the effect of temperature difference, a linear relationship is simulated for the data of the other four days, and a coefficient of determination of 0.92 is obtained. In addition, **Figure 3–9(b)** shows an example of the relationship between temperature difference and movement amplitude during cold days. The temperature difference existed for a shorter period, and the data points in the big temperature difference part are more dispersed; thus, the coefficient of determination is 0.81.

In general, the temperature difference between the two surfaces of the wall is considered to have a strong linear relationship with the opening and closing movement of the through-thickness cracks; the greater the temperature difference, the larger the movement amplitude.

(2)   Restraining force conditions

A numerical simulation analysis of the effect of member constraint conditions on crack movement has been reported in previous research, but analysis of data measured from actual buildings has not been done. In this subsection, the data measured by our team in Hokkaido are utilized for discussion. Data for the days with the approximate maximum temperature differences between the two surfaces of the wall throughout the year are chosen as the subject of the present discussion. The selected data period is from October 18 to 22, 2018. As shown in **Figure 3–9(a)**, measurement was done at two points on each of the north and south sides, such that Position-1 was located at the end, and Position-2 was placed closer to the main structure. Position-2 was subjected to greater restraint than Position-1.

Figure 3–10 shows the graph of the temperature difference versus movement amplitude for two positions over five days. When the temperature conditions at the two positions are almost the same, there was a difference in the crack movement amplitude, implying that the restraining force can affect the crack movement. The approximation curve of Position-1 (0.0031) has a larger slope value than that of Position-2 (0.0025). Therefore, it implies that the smaller the restraining force, the larger the movement amplitude of the through-thickness cracks. In this example, the crack occurred in a cantilevered wall where the external restraint was primarily from the main structure. In a typical building exterior wall, the external constraints may be from beams and columns. It is hypothesized that the amplitude of the crack movement may be smaller near the beams and columns, and the amplitude of the cracks at the window and door openings may be larger.
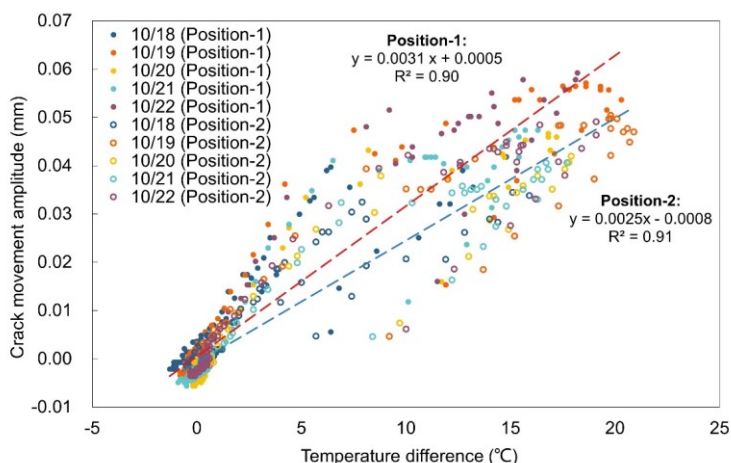
Figure 3–10 Relationship between temperature difference and crack width change in five days for Position-1 and Position-2 (Sapporo, Hokkaido, Japan,2018).

(3) Initial crack width

The crack width is a very important indicator for selecting a repair solution; thus, the relationship between crack width and crack movement is chosen for discussion. Nine cracks are selected, and the crack width of the objects at night, without solar radiation, is considered as the initial crack width. The details of the target cracks are listed in **Table 3–2**. However, the movement amplitudes of all cracks could not be provided because of missing data. Considering that the movement of the through-thickness cracks is characterized by the changes in temperature, the outdoor cracks are closed, and the indoor cracks are opened. Normally, during the daytime when temperatures are rising, cracks should be closed owing to concrete expansions. If the indoor side cracks are opened during this time, then this may represent a characteristic opening and closing movement of the through-thickness cracks taking place. Following this idea, the maximum value of the indoor crack width change during daytime hours is considered in the discussion of the relationship with the initial crack width. Although a larger indoor crack width change does not represent a larger crack movement amplitude, this is regarded as a reasonable application of the currently available data. Moreover, to exclude the effect of temperature difference as a driving force of the movement, data with a temperature difference of around 10 ∘C are utilized as much as possible. For those cracks for which temperature data were not available, the data for the day that had the largest crack width change during the measurement periods (about a week) were used.

Table 3–2 Information on object cracks.

No.	Initial crack width (mm)*1	Object crack description	Temperature			Daily crack movement			Time of the data
			Indoor side surface temperature (°C)	Outdoor side surface temperature (°C)	Temperature difference (°C)	Maximum indoor side crack width change (mm)*2	Maximum outdoor side crack width change (mm)*3	Maximum Movement amplitude (mm)	
1	0.05 (indoor)	Crack in the cold joint on the south wall of the eighth floor	30.9	—	—	0.051	—	—	2006/8/15
2	0.15 (indoor)	Crack in the diagonal direction at the opening of the wall on the north side of the sixth floor	30.9	—	—	0.018	—	—	2006/8/15
3	0.15 (indoor)	Dry shrinkage crack in the cantilever wall on the first floor	20.9	30.5	9.6	0.008	0.021	0.029	2018/9/19
4	0.30 (outdoor)	Dry shrinkage crack in the first floor walls	33.4	42.9	9.5	0.006	0.033	0.040	2019/8/14
5	0.35 (indoor)	Crack in the diagonal direction at the opening of the wall on the south side of the sixth floor	30.3	—	—	0.056	—	—	2006/8/15
6	0.45 (indoor)	Crack in the diagonal direction at the opening of the wall on the south side of the third floor	24.8	35.0	10.2	0.043	0.040	0.083	2007/9/27
7	0.45 (indoor)	Dry shrinkage crack in the middle of the narrow wall of the second floor in the longitudinal direction	25.6	34.3	8.7	0.029	—	—	2007/9/26
8	0.60 (indoor)	Dry shrinkage crack at the end of the eighth-floor wall in diagonal direction	—	—	—	0.056	—	—	2005/9/22
9	2.00 (indoor)	Crack in the diagonal direction at the opening of the wall on the north side of the sixth floor	—	—	—	0.023	—	—	2005/9/8
10	0.25 (indoor) 0.60 (outdoor)	Dry shrinkage cracks in the vertical direction at the opening of the wall	—	27.9	—	0.008	0.016	0.023	2021/10/29
11	0.40 (indoor) 0.50 (outdoor)	Dry shrinkage cracks in the vertical direction at the opening of the wall	—	27.9	—	0.013	0.006	0.019	2021/10/29
12	0.15 (indoor) 0.35 (outdoor)	Dry shrinkage cracks in diagonal direction at the opening of the wall	—	27.9	—	0.019	0.040	0.059	2021/10/29
13	0.20 (indoor) 0.35 (outdoor)	Dry shrinkage cracks in diagonal direction at the opening of the wall	—	27.9	—	0.040	0.013	0.053	2021/10/29
14	0.30 (indoor) 0.35 (outdoor)	Dry shrinkage cracks in vertical direction near the foundation beam of the wall	—	27.9	—	0.048	0.029	0.077	2021/10/29

*1 For the cases where the entire crack was not consistent in width, the local crack width at the monitoring point has been noted.

*2 The crack movement on the indoor side was the opening movement.

*3 The crack movement on the outdoor side was the closing movement.

The relationship between the initial crack width (using the width of indoor side, except for No.4 crack) and the daily maximum value of the indoor side crack width change is summarized in **Figure 3–11**. The magnitude of the crack movement seems to be unrelated to the initial crack width. Considering the limitations of the data, it is not completely certain that there is no influence relationship between the two, but it is certain that the influence coefficient of crack width is extremely small. It is indicated that narrow cracks may also undergo large opening and closing movements like wide cracks. This needs to be considered when selecting crack repair solutions.
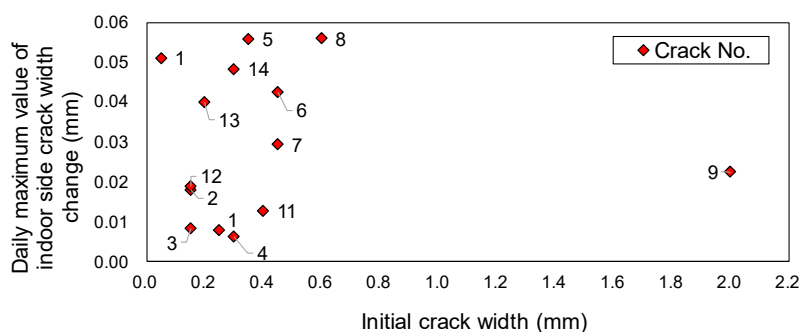

Figure 3–11 Relationship between initial crack width and maximum indoor side crack width change for each crack.

3.3.   A lab-scale test method for reproducing the movement of through-thickness cracks

3.3.1. A proposal of crack movement reproduction test method

(1) Experimental specimens

Commercially available ready-mixed mortar conforming to JASS 15 (bulk density: 1737 kg/m^3) was utilized. The ratio of fine aggregate to cement was 3:1 and the water-to-cement ratio was 0.6. The 28-day compressive strength was 30.7 N/mm^2 (testing method: JIS R 5201). These mortar mix proportions are only an example and are not a mandatory condition for this test method.

First, considering the versatility of the test method, commercially available styrene square boxes were utilized as molds for mortar specimens; therefore, the specimen dimensions here are of no particular significance and are considered feasible even with slight changes. To ensure that the specimens with through-thickness cracks remain whole, two 5 mm diameter threaded rods were pre-embedded. Cracks were induced by greased metal or resin sheets of appropriate thickness. The mortar was then mixed and poured into the mold. Next, after the initial setting of the mortar, the sheets used to generate the crack were pulled out towards the upside and downside, respectively. Finally, specimens were cured at 20 ∘C, RH 60% for 28 days. Examples of mold and specimen dimensions are shown in **Figure 3–12(a)** and **Figure 3–12(b)**, respectively.
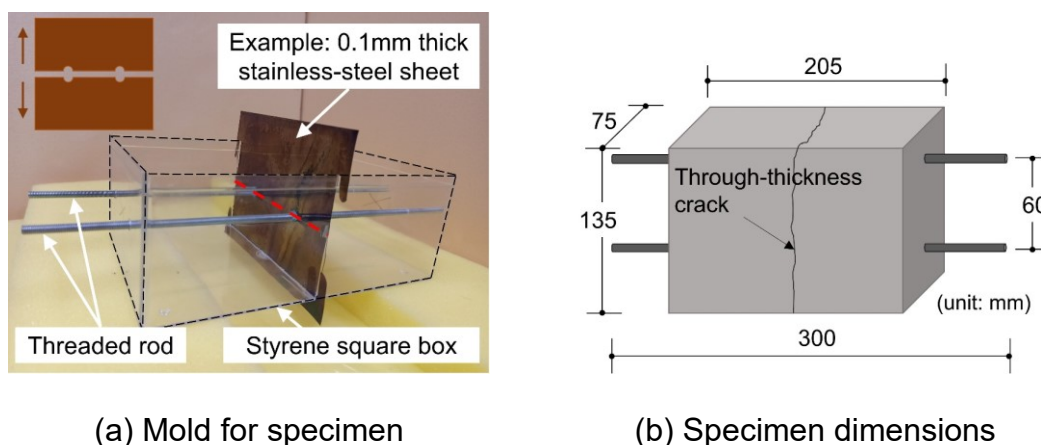
(a) Mold for specimen   (b) Specimen dimensions

Figure 3–12 Mold for making through-thickness crack specimens and
dimensions of experimental specimens.

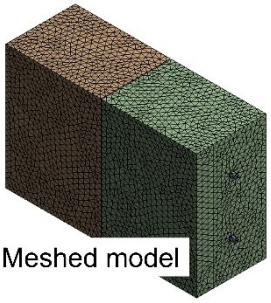**(2) Proposals for experimental setup based on numerical simulations**

As previously discussed, temperature difference is the driving force for the opening and closing movement of through-thickness cracks. When reproducing it on a lab-scale, the thermal load is not difficult to achieve; however, the challenge is to retrain the experimental specimen. For this reason, the Finite Element Method (FEM) analysis is employed to simulate the experimental state to give a reference for the development of the experimental setup. Note that the numerical simulations involved here are a highly simplified model and are only a reference for simulating the restraining approach.

The analysis was carried out using the 3D FEM program, ANSYS Workbench. The dimensions of the numerical model are shown in **Figure 3–12(b)**, and the material properties are shown in **Table 3–3**. The threaded rod was simulated using the ''structural steel'' unit that comes with the system. One side of the model was assumed to be the outdoor surface of the wall, and a heating operation was performed on it. The opposite side of this surface was assumed to be the indoor surface. To correspond with the measurement results of the displacement sensor during the actual building measurement, the deformation in the X-direction at the cracks was observed here. The settings for analysis are shown in **Table 3–4**. In the thermal loading of the assumed outdoor surface, a total of 6 sub-steps were set, and the sub-step end time was 6 s. ''Transient Thermal'' and ''Transient Structural'' analysis systems were utilized. The link between the analysis systems is shown in **Figure 3–13**. This numerical simulation is a highly simplified model for the reference of constraint conceptions selection only.

Table 3–3 Material properties for FEM analysis.

Property		Mortar	Threaded rod	Unit
Density		2100	7800	kg/m^3
Isotropic Secant Coefficient of Thermal Expansion	Coefficient of Thermal Expansion	1.5E−0.5	1.2E−05	1/K
Isotropic Elasticity	Young's Modulus	2E+10	2E+11	Pa
	Poisson's Ratio	0.2	0.3	—
Isotropic Thermal Conductivity		1.51	60.5	W/(m K)
Specific Heat, C_p		700	434	J/(kg K)

Table 3–4 Details of settings.

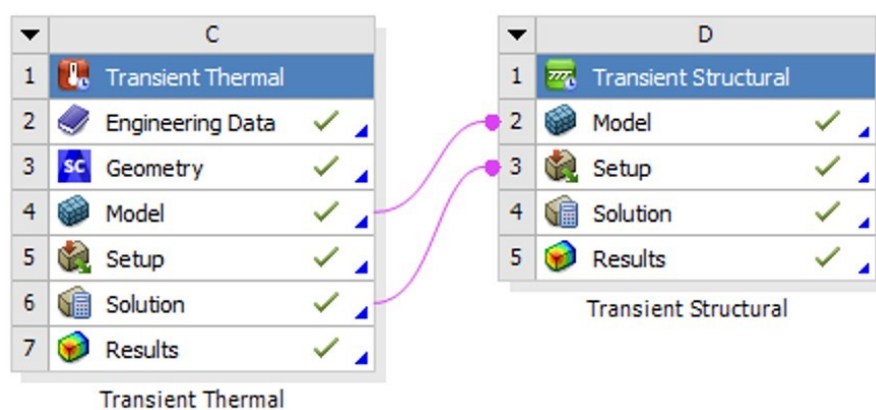| Mesh method	Tetrahedrons
Body sizing	5 mm
Nodes	205922
Elements	144316
Contact type	Bonded
Step controls	Defined by substeps

Meshed model

Figure 3–13 Analysis systems and their links.

The first conception was to screw the threaded rod to fix the specimen to a device. The applied force corresponding to the FEM model is represented in **Figure 3–14(a)**. The deformation at the highest temperature is shown in **Figure 3–14(b)**. The changes in temperature and crack width for the full substeps are shown in **Figure 3–14(c)**. Thermal expansion can be seen to have occurred on the outdoor

surface, but because this was a free surface, most of the deformation was concentrated at the ends rather than at the crack. Coupled with the fact that cracks on both indoor and outdoor sides are opening movements under thermal history, this concept is considered unworkable.
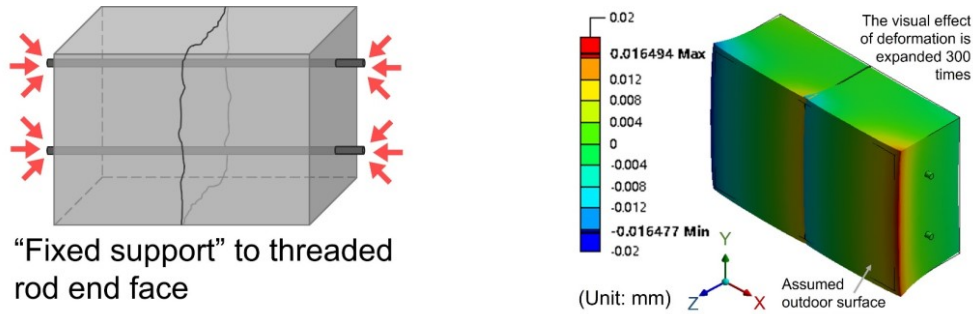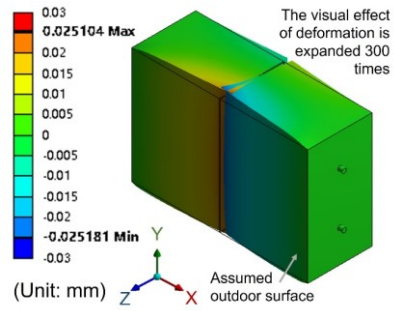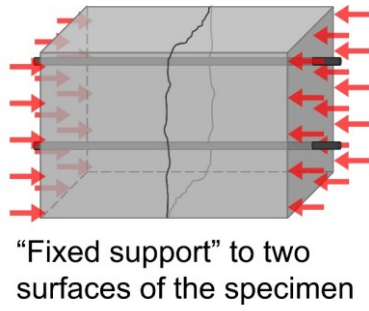

(a) Schematic diagram of fixing method

(b) Deformation in X-direction of sub-step 6
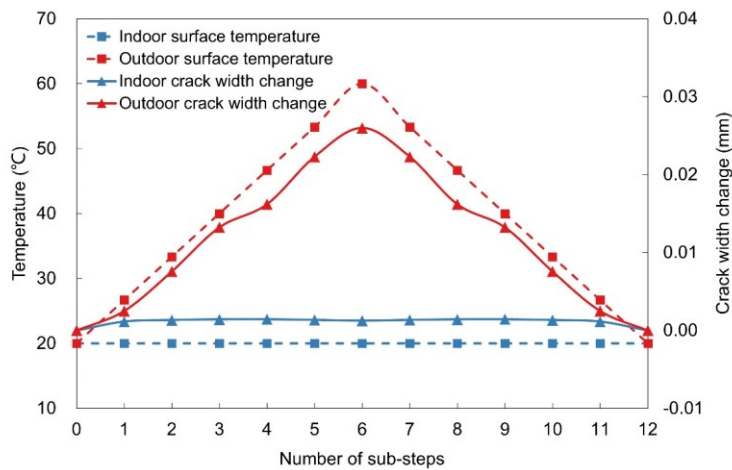
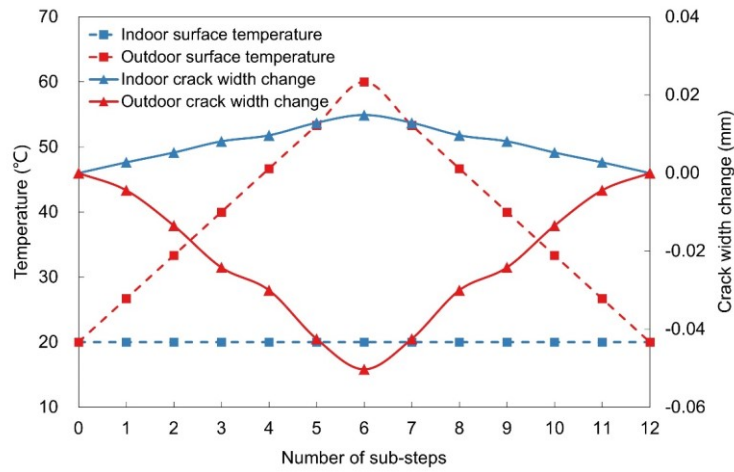(c) Results of temperature and crack width change for each sub-step

Figure 3–14 Numerical simulation to fix specimen: Conception one.

Based on this, the second conception was to strengthen the constraint at both the ends of the specimen to make the deformation more concentrated at the cracks (**Figure 3–15(a)**). From the deformation results in **Figure 3–15(b)**, the amount of expansion on the assumed outdoor side mostly occurred at the cracks. With increasing temperature, the model showed the expected movement pattern of the outdoor cracks closing and the indoor cracks opening. However, the crack width change in the full sub-steps (**Figure 3–15(c)**) revealed that the indoor side cracks were opened by approximately 0.01 mm in a small order of magnitude, possibly because the constraints were too strong; therefore, Conception two was considered to have room for improvement.
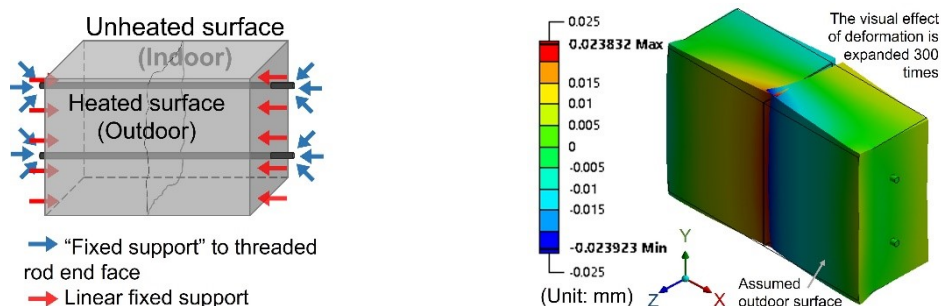
(a) Schematic diagram of fixing method

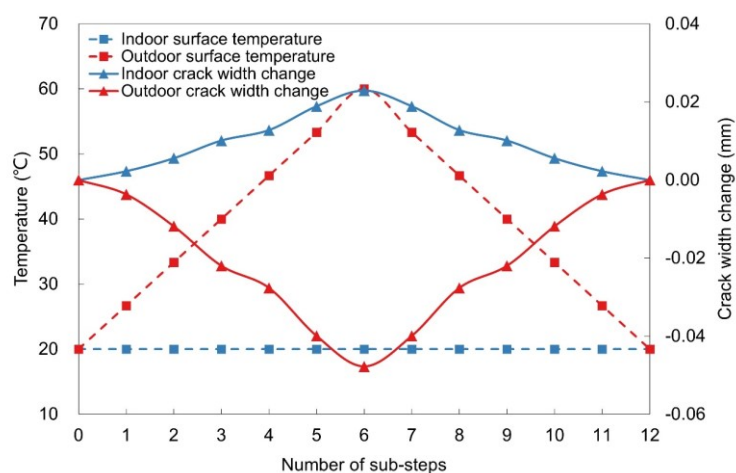(b) Deformation in X-direction of sub-step 6

(c) Results of temperature and crack width change for each sub-step

Figure 3–15 Numerical simulation to fix specimen: Conception two.

Thus, Conception three was to weaken the restraining force on the indoor side (**Figure 3–16(a)**). In this case, **Figure 3–16(b)** was obtained, and the characteristic opening and closing movement of the through-thickness crack was still satisfied. Moreover, as shown in **Figure 3–16(c)**, the crack width changes on the indoor and outdoor sides were of the same order of magnitude.

(a) Schematic diagram of fixing method

(b) Deformation in X-direction of sub-step 6

(c) Results of temperature and crack width change for each sub-step

Figure 3–16 Numerical simulation to fix specimen: Conception three.

In summary, it was inferred that asymmetric forms of restraining force on the indoor and outdoor sides may be the key to reproduce the crack movement at lab-scale, which provides an approach for the development of a test method. Note that symmetric restraint can also reproduce the bending-like movement; however, the asymmetric restraint is chosen to be closer to the movement pattern of the onsite buildings. This can be explained by the fact that the larger the amplitude available in the experiment, the more variables can be adjusted, and more cracks can be reproduced.

(3) Experimental setup and procedure

The experimental setup was designed according to Conception three described in the above section. As illustrated by **Figure 3–17(a)**, the restraining device contained three parallel stainless-steel plates and four support rods. The two plates that had contact with the experimental specimen were designed with notches to facilitate fixing the specimen. The threaded rods were held by nuts and washers to provide the end surface-fixed support displayed in **Figure 3–16(a)**. Two round steel rods were placed

in the notches such that they were sandwiched between the specimen and the device to supply the linear fixed support shown in **Figure 3–16(a)**. A photo of the experimental setup is shown in **Figure 3–17(b)**. An infrared lamp was used for thermal loading. The irradiated side was assumed to be the outdoor side, and the opposite unirradiated side was the indoor side.
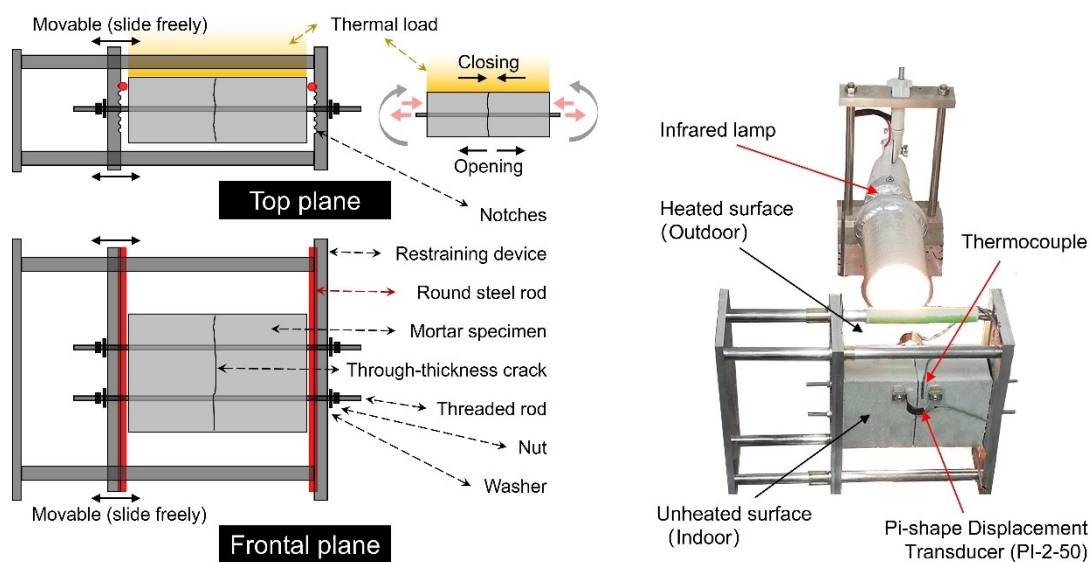
(a) Sketch of experimental setup   (b) Photo of experimental setup

Figure 3–17 Lab-scale crack movement reproduction experimental setup.

The experimental procedure was irradiated for one hour, followed by natural cooling at 20 ◦C. The distance between the infrared lamp and experimental specimen was 100 mm. For measurements, two PI2-50 Pi-shape Displacement Transducers were placed on the indoor and outdoor surfaces of the experimental specimen, and two Type T Thermocouples were placed in the same position as the displacement transducers. The transducer could be easily accessed at the laboratory scale owing to its simple structure, with sensitivity and capacity of 2000×10^{-6} strain/mm and ± 2 mm, respectively. The effect of temperature variations on this sensor is negligible. Further details on displacement transducers and monitoring preparation are presented in **Table 3–1** and **Figure 3–2**, respectively. During the experiment, all parts other than the specimens were shielded with plasterboard or insulating material to avoid direct radiation and unwanted thermal expansion. In addition, the transducers were ensured to be within the specified allowed temperature range.

(4) Experimental results

An example of the result for crack movement reproduction experiment is shown in **Figure 3–18**. The maximum outdoor surface temperature was 54.2 ◦C, while the maximum indoor surface temperature, delayed by 14 min, was 32.1 ◦C; these were reasonable temperatures that could occur. In

addition, when the temperature increased, the crack width on the indoor and outdoor sides went in the opposite directions. The outdoor side crack closed, and the indoor side crack opened by approximately 0.039 mm and 0.031 mm, respectively. The change on the indoor side is slightly smaller than that on the outdoor side, consistent with the measured trend of the actual building. Furthermore, when the temperature decreased, and the temperature gradient disappeared, the crack width returned to its initial state. Therefore, it is confirmed that the proposed test method can reproduce the same opening and closing movement pattern of through-thickness cracks as in reality.
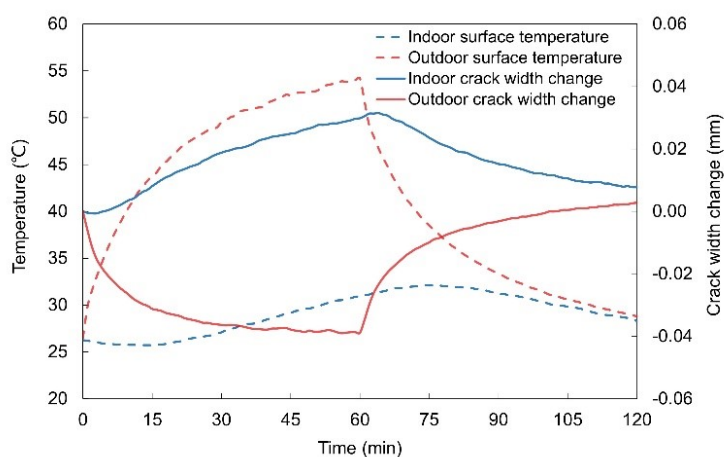

Figure 3–18 Temperature and crack width change over time in lab-scale reproduction test method.

3.3.2. Discussions on the practicality of the test method

Practicality refers to the ability of the proposed test method to reproduce a wide range of crack movements consistent with actual buildings. Through-thickness cracks may be affected by temperature, restraining forces, etc., producing a wide variety of movement amplitudes. Thus, experiments on the reproduction of these experimental variables were performed.

(1) Influence of temperature conditions

It is known that for the same crack, the amount of crack width change is strongly correlated with the temperature difference. To reproduce this relationship, five groups of experiments were carried out on the same experimental specimen. The distance between the infrared lamp and specimen was adjusted to obtain different values of temperature difference. The distance ranged from 100 mm to 300 mm, with 50 mm adjustment in each group. The results of crack width change for each experimental group after one hour of thermal load are shown in **Figure 3–19**.
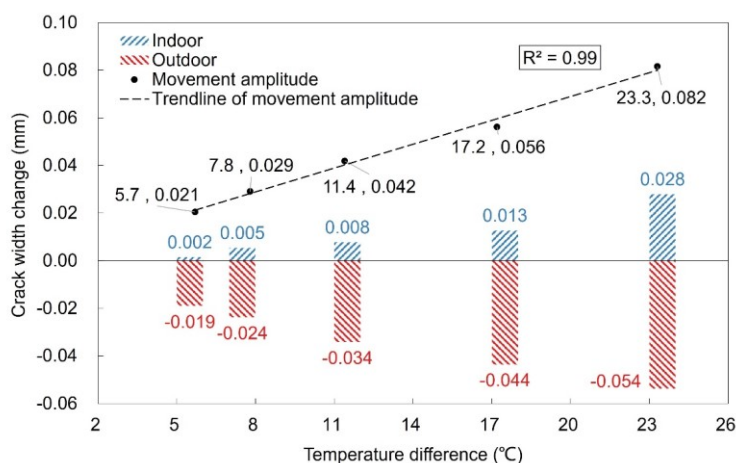
Figure 3–19 Relationship between temperature difference and crack width change in the reproduction experiment.

From the results, the higher the temperature difference, the greater the crack width change. The results show a strong linear correlation between them. Therefore, it could be proven that the main driving force for the crack opening and closing movement in this reproduction experiment, same as in reality, is the temperature difference. Additionally, different crack movement amplitudes can be obtained by adjusting the distance between the lamp and specimen. A variety of experimental variables can be provided in the future evaluation of crack repair effectiveness, which can be considered as the advantage of this test method.

(2) Influence of restraining force conditions

It is demonstrated that the restraining force from the main structure affects the crack movement amplitude. As introduced, the experiment was performed using washers and nuts to hold the specimen to the device. Thus, an adjustable break torque wrench was employed to achieve different restraining forces by quantificationally adjusting the torque. Three experiment groups were performed with the torque of 1.0 N·m, 2.0 N·m, and 3.0 N·m, respectively.

As seen in **Figure 3–20**, the greater the torque, the smaller the crack opening and closing movement. This means that when the temperature, driving force of the movement, and other conditions are the same, if the external force becomes larger, then the crack movement becomes smaller. Therefore, it is possible to reproduce the law of restraining force on crack movement at lab-scale, and the fact that it was achieved by various experimental groups having different movement amplitudes by adjusting the torque, illustrates the operability of this experimental method.
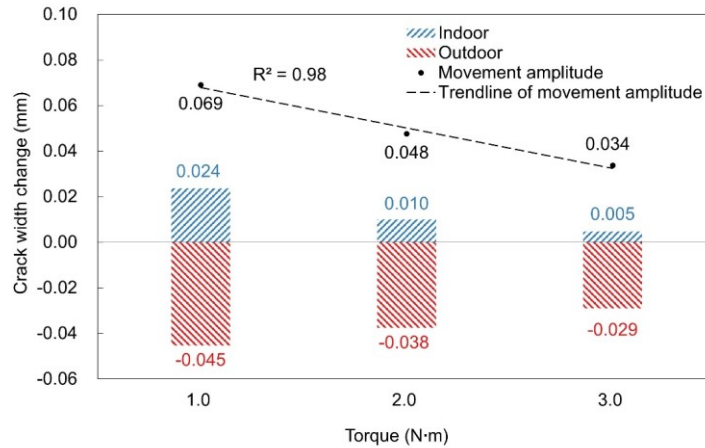
Figure 3–20 Relationship between torque and crack width change in the reproduction experiment.

(3) Influence of initial crack width

The initial crack width is not correlated with the crack movement amplitude in actual buildings. To test this, reproduction experiments were also carried out at lab-scale. Multiple specimens with different initial crack widths were prepared by adjusting the thickness of the metal or resin sheets in the mold (**Figure 3–12(a)**), and the accurate initial crack width of the finished specimens was measured using a microscope. These experimental groups were performed under the same conditions as described in **Section 3.3.1**. To correspond to the data measured in the actual building, only the maximum value of the indoor crack width change was selected. The results are shown in **Figure 3–21**.
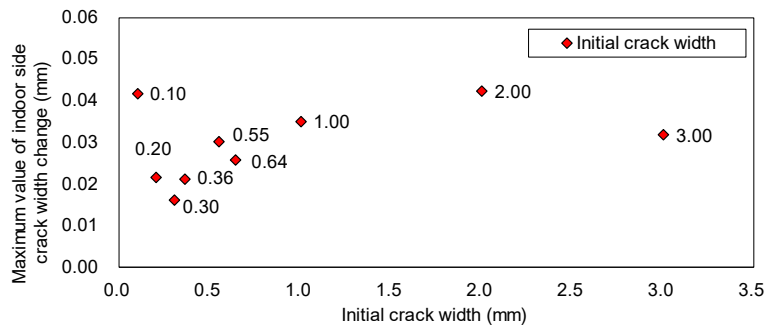

Figure 3–21 Relationship between initial crack width and maximum indoor side crack width change in reproduction experiment.

In **Figure 3–21**, the data points of crack width change versus initial crack width show irregular distribution. On the one hand, the correlation between the two may indeed be very small, which still requires more investigation of on-site data. On the other hand, in this experiment, there are other experimental factors besides temperature difference and torque that may affect the crack movement,

thus leading to deviations. Note that the experimental specimens in the figure were not made in the same period of research. Thus, there are some slight differences between specimens: the position of the inside threaded rods, the cutout shapes of the metal or resin sheets used to make cracks, and the adhesive position of the displacement transducer in the experiment. In addition, for narrow crack, when there is a local lump inside the crack owing to poor fabrication, the movement may be obstructed to affect the movement amplitude thus causing errors. More on the human operation error of the experiment is presented in the next subsection. In general, it is currently confirmed that small cracks can also display large movement amplitudes. The proposed test method enables reproduction at lab-scale, making it possible to evaluate the effectiveness of crack repair for various crack widths and movement amplitudes.

3.3.3. Discussions on the stability of the test method

The stability of the proposed test method is discussed by error analysis in this subsection. One mortar experimental specimen (1 mm initial crack width) was performed ten times in reproduction experiments (named 1st–10th) by different persons. The experimental procedure was as described in **Section 3.3.1**, except that the cooling time was extended to six hours so that the specimens could cool down to the initial ambient temperature. The temperature conditions here were the same, thus only the curves of the crack width change are presented.

As seen from **Figure 3–22**, all ten experimental groups were able to reproduce the phenomenon of through-thickness crack movement by the proposed test method. The opening and closing of the indoor and outdoor surfaces of each group differed, but the group with a large movement amplitude also had larger residual values after cooling. Thus, it was also implying that in future experiments, the difference between the crack width change at the end point of cooling and the end point of heating should be considered as the movement amplitude for each experiment. The average amplitude of these ten experimental groups was about 0.095 mm, and the coefficient of variation was 7.73%, which proved that the error caused by human operation during the experimental setup was small, and the test method had good stability and universality. Note that the cause of the error could be a slight movement of the experimental specimen. The diameter of the threaded rods in the specimen is 5 mm, while the diameter of the pre-drilled holes in the experimental device is 12 mm. This spatial difference could lead to a shift in the geometric center or a twisting of the central axis of the specimen during each experiment. Thus, a more precise specimen placement needs to be specified in advance to reduce this error when using this experimental method.
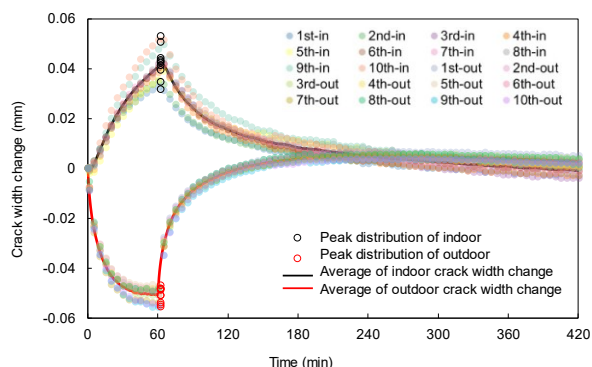
Figure 3–22 Results of one experimental specimen repeated ten times.

3.3.4. Efficiency of lowing temperature on reducing crack movement

It has been shown that temperature is the main driving force for crack movement and this movement will inevitably result in structural weakness. This means that in practical applications, reducing the temperature gradient may also be an important part of the crack repair work. Thus, the specific effect of reducing the temperature gradient on the crack movement is the subject of the experiments in this section.

(1)   Experimental procedure

First, a crack movement reproduction experiment was conducted on the mortar specimens, and the proposed lab-scale reproduction test method was employed (**Figure 3–17**). Mortar specimens with 1 mm through-thickness cracks were prepared. The distance between the infrared lamp and specimen was set to 100 mm, and the torque of the nut for fixing the specimen was controlled at $1.0 \, \mathrm{N \cdot m}$. The experiments were performed at a constant temperature of $20 \, \circ$C. The heating procedure was one hour of infrared irradiation followed by six hours of natural cooling to ensure that the specimens returned to ambient temperature. For measurements, the displacement transducer and thermocouple were still set at the position shown in **Figure 3–17**, which is the upper part of the specimen surface (named "up"). In addition, two more temperature measurement points were set at the geometric centers of the indoor and outdoor surfaces of the specimens (named "mid") to capture the maximum temperature of the irradiated center.

The next step was to apply various waterproof coatings to reduce the temperature gradient. The specimens were kept in a fixed state on the device, and the outdoor surface was coated. After coating, two more temperature measurement points were set at the same positions ("up" and "mid") on the coating surface.

Finally, a crack movement reproduction test was conducted again under the same experimental conditions. The effectiveness of the crack repair is discussed by comparing the measured values of

temperature and crack movement before and after coating.

(2) Experimental material variables

Four types of water-based acrylic waterproof coatings (JIS A6021) were considered in this experiment. These coatings can be classified according to the thermal insulation property (thermal insulation coatings (named T) and non-insulated coatings (named N)), and according to the top coating color (color A (named CA) and color B (named CB)). Each coating was applied on three specimens (named 1, 2, and 3), and the dosage, operation and other details were based on the manufacturer's coating instructions. Photos of the coating process are shown in **Figure 3–23**.

Figure 3–23 Photos of waterproof coating process.

(3) Results

The results of the experimental specimen T-CA-1, as a representative, after being irradiated for one hour are shown in **Figure 3–24**. The temperature at the same position on the mortar surface significantly decreased after coating, with the largest reduction of 11.3 ∘C in the center of the outdoor surface. As the temperature decreased, the temperature difference between the indoor and outdoor surfaces of the specimen also became smaller, leading to less driving force for the crack opening and closing movement; thus, the crack width change and movement amplitude are also significantly reduced.
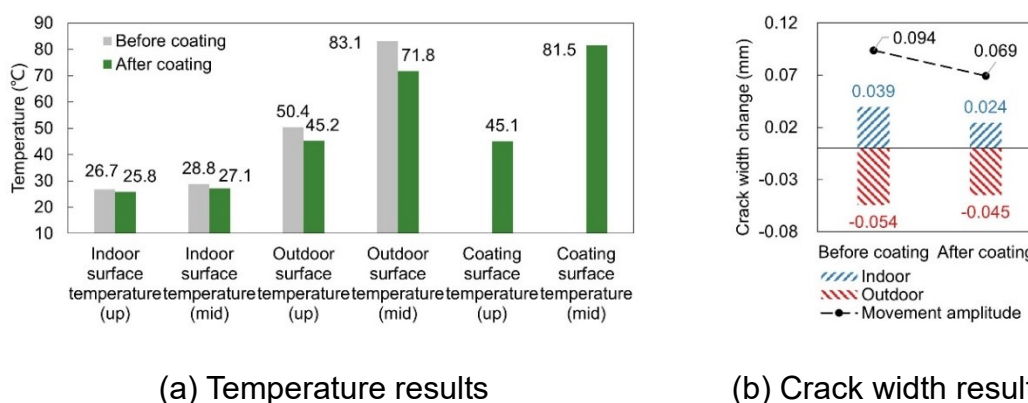

(a) Temperature results

(b) Crack width results

Figure 3–24 Reproduction experimental results before and after coating under same thermal load.

(4) Discussions

To quantitatively evaluate the reduction effect of coating on temperature and crack movement, the T ratio is proposed:

$$\gamma = \frac{A}{B} \tag{3 − 1}$$

where γ is the ratio of "after repair to before repair", which indicates the reduction capacity of coatings. A and B are the values of temperature or crack width change after and before coating, respectively. The smaller the ratio γ, the better the coating's ability to reduce temperature and crack movement. When γ is greater than 1.0, it implies that there is no reduction effect. The average values of three experimental specimens for each coating were calculated and plotted in **Figure 3–25**.
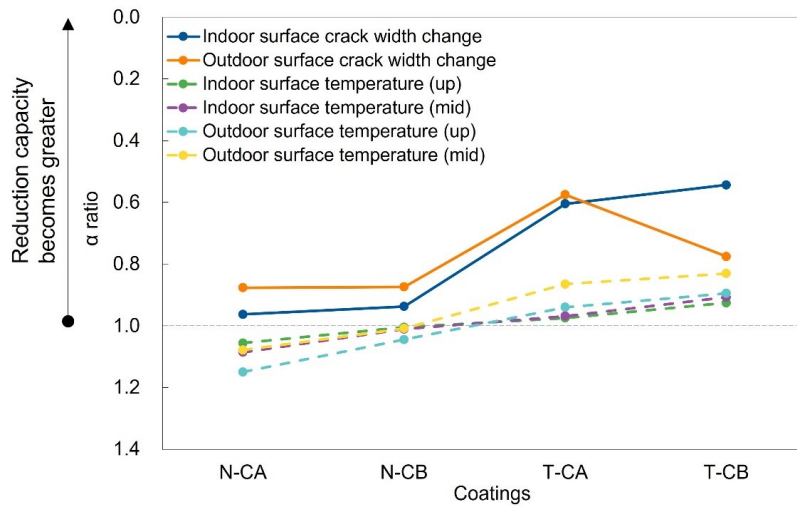

Figure 3–25 γ ratios of temperature and crack movement for each coating.

For the specimens coated with non-insulated performance coatings (N), the temperature did not decrease, which may be explained by the reduced heat convection on the mortar surface caused by the coating cover, resulting in a tendency of heat storage. Nevertheless, the non-insulated coatings (N) still exhibited the ability to inhibit crack movement. This may indicate that the mechanical properties of the coating itself or the adhesion to the mortar dispersed the stresses and thus could reduce the crack movement.

For the thermal insulation coatings (T), the reduction in temperature led to a very significant reduction in crack movement. However, the T-CB specimens with the best temperature reduction capacity did not have the best ability to reduce crack movement. This could happen because more reduction capacity was acting on the crack movement on the indoor side, while the inhibition of the outdoor crack movement by the coating may have a limiting value or, more likely, an experimental error. Additional validation and discussion on this point including increasing the number of specimens

and experimental variables, is required.

The experiment which proves that lowering the specimen surface temperature can reduce the crack movement amplitude was conducted and validated. For future crack repair operations, reducing the temperature may be considered an efficient way to improve repair effectiveness and durability.

3.4. Fatigue test method for simulating bending-like movements of cracks

3.4.1. Experimental apparatus

The fatigue experimental apparatus for simulating the bending-like movement of cracks is shown in **Figure 3–26**. The dimensional drawing of the main part of the apparatus is shown in **Figure 3–27**. The mechanism of the apparatus to achieve the bending-like movement is shown in **Figure 3–28**.
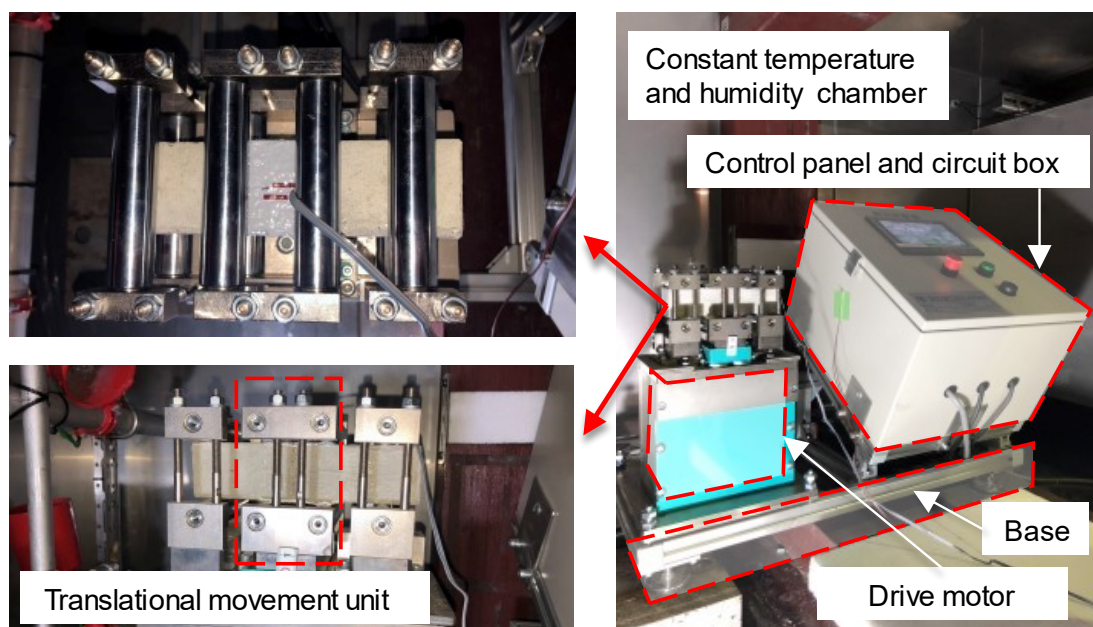

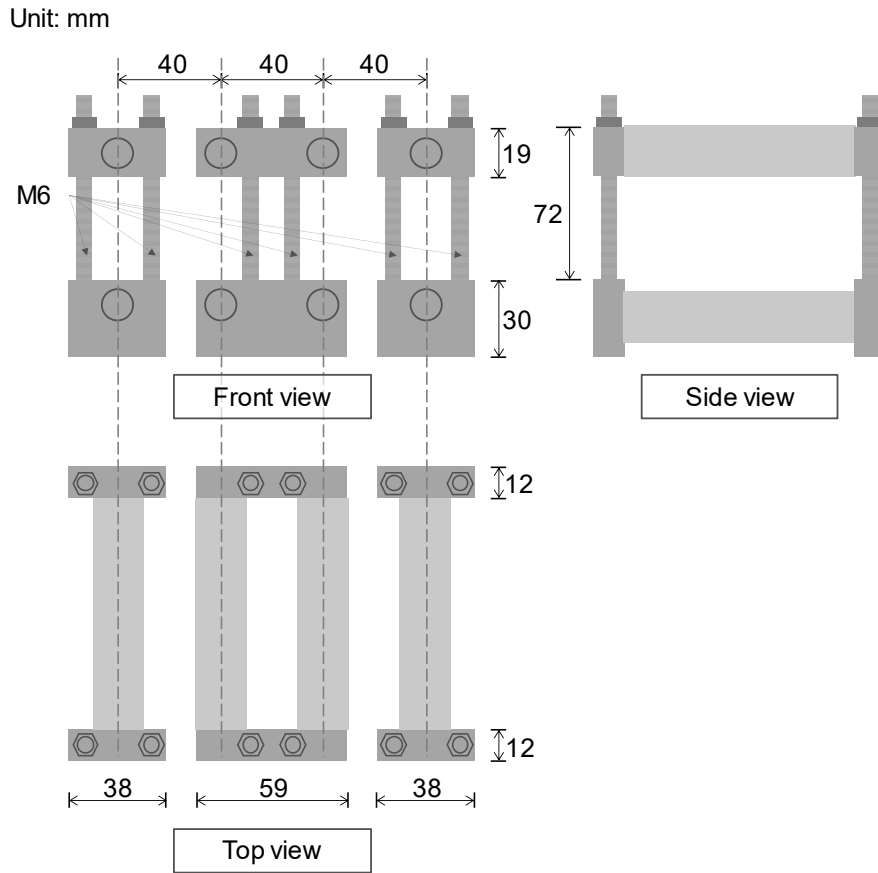Figure 3–26 Crack movement fatigue experimental apparatus.

Unit: mm

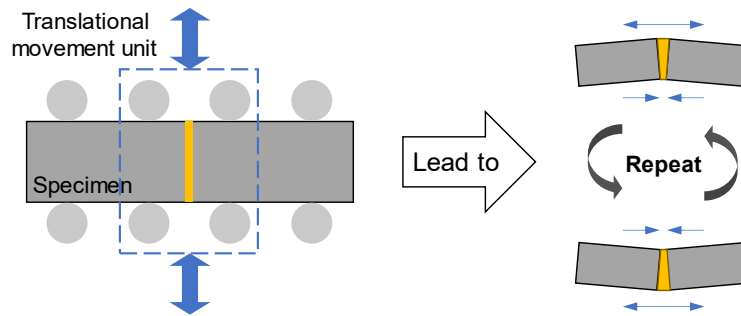Figure 3–27 dimensional drawing of the main part of the apparatus.

Figure 3–28 Mechanism for achieving bending-like movement.

The unit in the middle of the apparatus can be controlled by a hydraulic press to perform an up-and-down translational movement. This movement allows the specimen to produce the same type bending-like movement at the cracks as the building exterior wall, thus enabling durability evaluation of the repair solutions. The unit's pan has a range to ±2.0 mm and can be controlled with an accuracy of 0.001 mm. In addition, this device has the advantage that the cycle time is controllable and can be measured in seconds to accelerate the experiment period. A cycle is the time it takes for the

translational movement unit to complete an upward plus a downward movement. Moreover, the whole device can be placed in a constant temperature and humidity chamber to evaluate repair solutions under various climates.

3.4.2. Experimental specimens

The experimental specimens were commercially available mortar blocks conforming to JIS R 5021. The specimen size was 40 × 40 × 160 mm. Two as a pair for making specimens to simulate crack repair. Photos of the specimen preparation are shown in **Figure 3–29**. As shown in **Figure 3–30**, the crack width was 0.5 mm. The specimen surface was cleaned with acetone only, left as cast. Two repair methods, injection and surface coating, are discussed in this section. The respective specimen preparation procedures are as follows:

Injection method:

1. Seal and fix the two mortar blocks using adhesive tape ensuring a crack width of 0.5 mm;
2. Prepare a hole for epoxy resin injection at the central position at the top of the specimen. Prepare small holes on both sides at the bottom of the specimen for air discharge;
3. Secure the syringe base with sealant and wait for the sealant to fully cure;
4. Install the syringe and inject the epoxy until the cracks are completely filled;
5. Remove the syringe kit and tape.

Surface coating method:

1. Sandwich the pre-prepared acrylic card between two mortar blocks to ensure that the crack width is 0.5 mm. Use C-clamp vise to fix the specimen;
2. Control the coating width to 30 mm. Apply masking tape around the coating area;
3. Apply the coating layer by layer according to the manufacturer's instructions;
4. Remove the masking tape, C-clamp vise, and width control card.
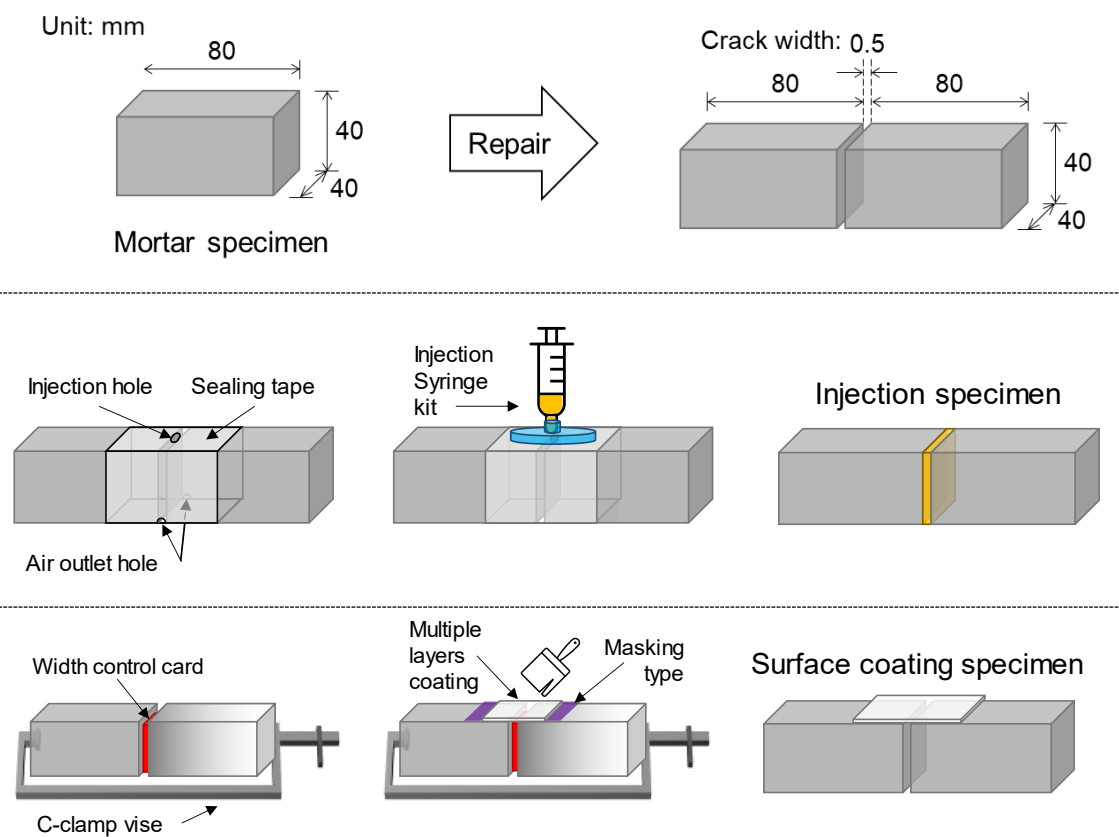

Figure 3–29 Specimen preparation photos.

Figure 3–30 Experimental specimen preparation.

3.4.3. Validation of experimental methods based on digital image correlation (DIC)

To discuss the effectiveness of the fatigue apparatus, a simple experiment based on the digital image correlation (DIC) method is designed in this section. The DIC method is to take two digital images of the specimen before and after deformation and obtain the strain information of the area of interest (AOI) by correlation calculation.

The experimental setup is shown in **Figure 3–31**. During the experiment, the light source intensity and camera position were kept consistent throughout the experiment. Each frame of the captured image is 1920 × 1080 pixels. Image processing was performed using the Vic-2D software from Correlated Solutions, with a computational subset of 40 × 40 pixels and an accuracy of 0.020 pixels.
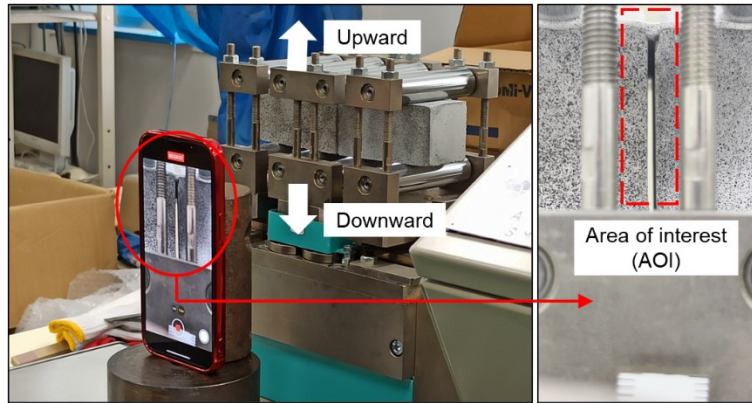
Figure 3–31 The look of the DIC method experiment.

The experimental setup for the injection method specimens was a translational unit movement of ±0.4 mm with a period of 30 s. The DIC results for the upward and downward arrival vertices are shown in **Figure 3–32**. As shown in the figure, the specimen produced a half-tensioned and half-compressed strain state at the crack under the effect of the fatigue apparatus. As shown in the figure, the specimen produced a half-tensioned and half-compressed strain state at the crack under the effect of the fatigue apparatus. In other words, the bending-like movement stress state of the actual building through-thickness cracks was reproduced by this experimental method.
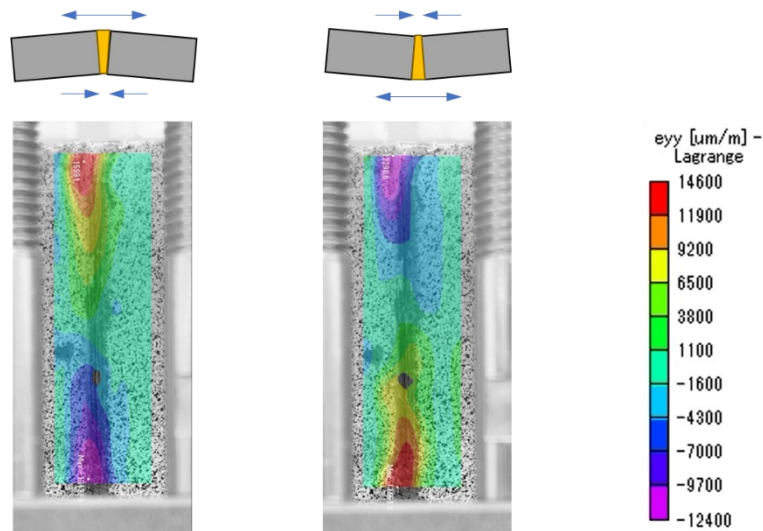

Figure 3–32 Injection repair specimens DIC results.

For surface coating method specimens, the experimental setup was a translational unit movement of ±1.0 mm with a period of 30 s. The DIC results for the upward and downward arrival vertices are shown in **Figure 3–33**. As can be seen from the figure, the coating is subjected to compressive stresses as the unit travels upward, reproducing the situation of the actual building. However, when the unit travels downward, the lack of binding force at the bottom of the specimen caused the strain to be

concentrated at the lower crack apex. This resulted in the coating not being subjected to compressive stresses of the same magnitude as the tensile stresses. This inevitably affects the validity of the material evaluation. Therefore, we believe that in future experiments, the same surface coating should be applied to both the upper and lower surfaces of the specimen to ensure a reasonable distribution of strain.
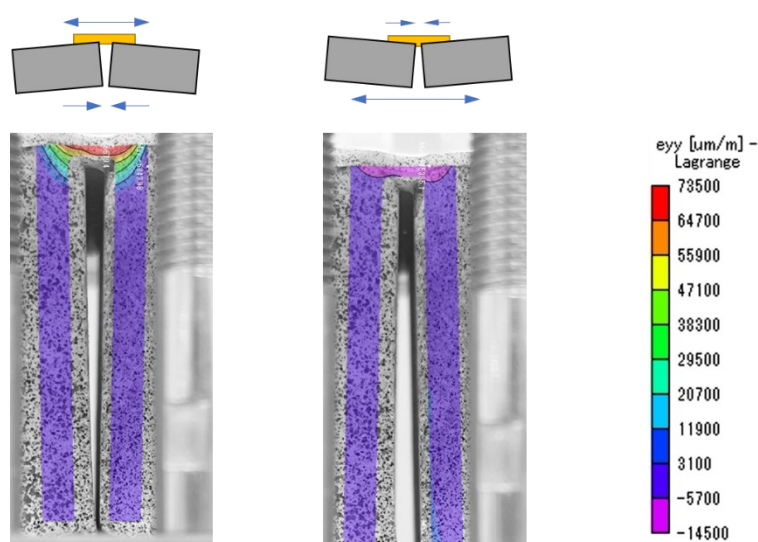

Figure 3–33 Surface coating repair specimens DIC results.

3.5. Air leakage test for crack detection

3.5.1. Air leakage test method

Currently the harmfulness of cracks in buildings and the choice of repair methods are mainly based on the width of the cracks. In addition, to obtain information about the development inside the crack, complex equipment such as ultrasonic and radar may be required. For this purpose, our team proposed a simple experimental set for crack detection.

This air pressure sensor-based experimental set can determine the state of the crack based on the change rate of the air pressure inside the negative pressure chamber. The mechanism diagram of the experimental set is shown in **Figure 3–34**. Cracks can be the path for substances such as air and water to ingress into the concrete, causing corrosion, spalling and other problems. Therefore, it is reasonable to assess the harmfulness of cracks by evaluating the condition of air leakage. The air in the chamber was manually pumped to a certain negative air pressure, and then the suction cup was placed on the measured surface. After the valve was opened, the crack condition of the measured surface could be determined by evaluating the air pressure in the air chamber. The air pressure sensor can record up to 1000 data per second. The advantage of this experiment set is that it is lightweight, small, and portable. Simple operation allows anyone to detect cracks quickly and quantitatively.
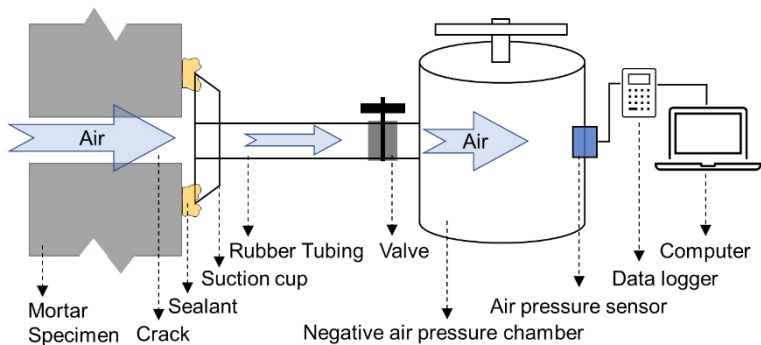
Figure 3–34 Air leakage experiment set mechanism.

3.5.2. Laboratory validation experiment

Our team conducted a simple validation experiment of this test method. The experimental photo is shown in **Figure 3–35**. A 10 × 10 × 40 cm concrete specimen was bent until it fractured, creating a natural shape through-thickness crack. The ends of the specimens were clamped using a C vise clamp. The clamp was adjusted to add torque to obtain different widths of the through-thickness cracks. The widths of these crack were measured using a microscope. Air leakage experiments were performed for these widths of cracks and the results are shown in **Figure 3–36**.
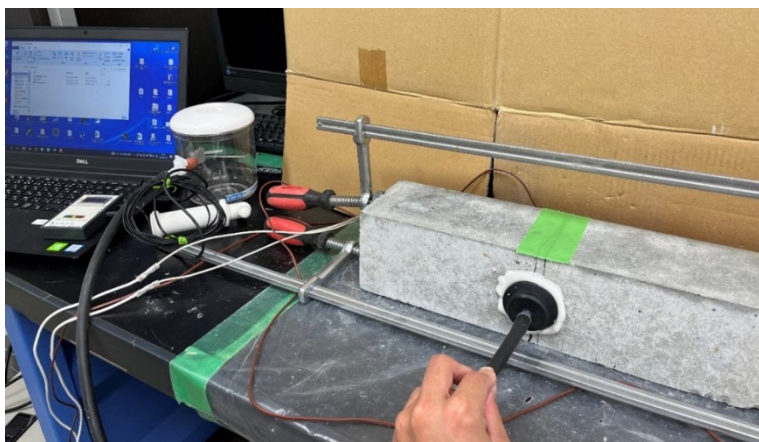

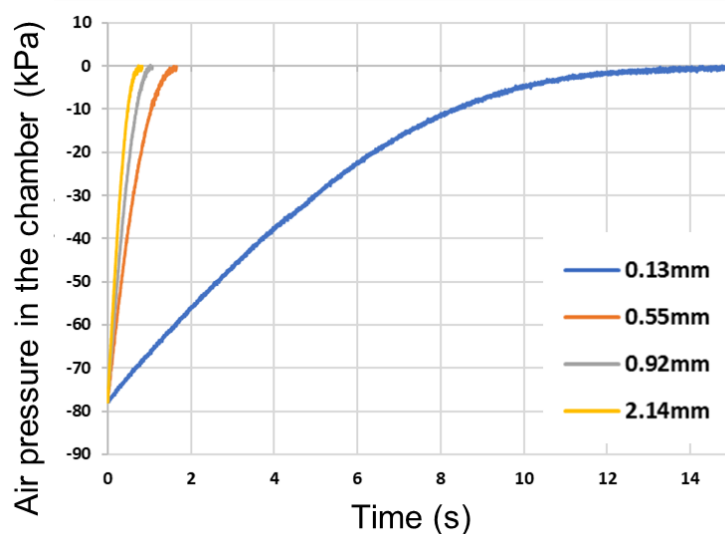Figure 3–35 A simple validation experiment of air leakage test method.

Figure 3–36 Results of air leakage experiments in the laboratory.

In **Figure 3–36**, the air pressure inside the negative air chamber varies with time and approaches standard atmospheric pressure. Note that the standard atmospheric pressure is zeroed in this experiment. For through-thickness cracks with the same internal shape, the larger the width, the faster the change in air pressure. This makes it possible to evaluate the harmfulness of the crack quantitatively. Moreover, extending the experiment time, the test can detect very small cracks.

3.5.3. Survey of actual buildings

Our team also conducted air leakage tests on the exterior walls of the actual building (same building as **Section 3.2.1**). The measurements included through-thickness cracks (Cracks A, C and D), surface crack (Crack B), and non-cracked areas, and the results are shown in **Figure 3–37**. Note that the crack surface width was measured using a crack width ruler. In the results, the difference in air leakage rate between various measurement locations is very obvious, indicating that the air leakage experiment can be used to detect the harmfulness of cracks. It was also found that observing only the surface width of the crack may underestimate the harmfulness of the crack, for example, at 0.1 mm of crack C.
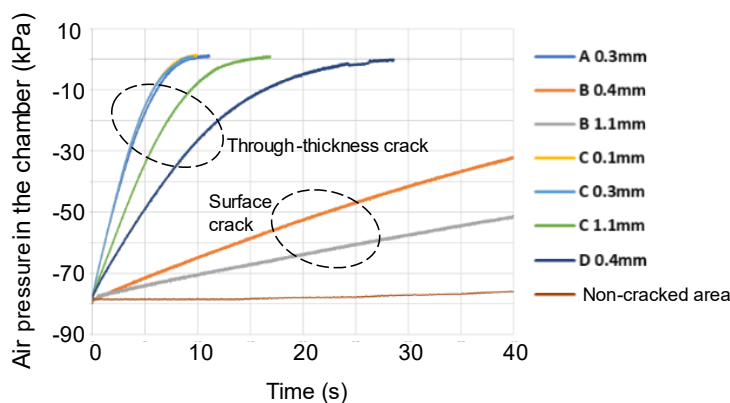
Figure 3–37 Results of air leakage from cracks in the exterior walls of an actual building.

3.6. Conclusions

This chapter aims to establish test methods for the simulating of through-thickness crack movements to make lab-scale evaluation experiments possible. The main conclusions of this chapter are as follows:

1. In most cases, the temperature difference in wall cross-sections causes the through-thickness cracks to undergo a bending-like movement: when the temperature changes, cracks on the high-temperature side close and cracks on the low-temperature side open. This movement is a form of combined temperature and mechanical load deterioration that acts almost daily on the crack repair area.

2. The daily movement amplitude of the through-thickness crack is proportional to the temperature gradient of the wall cross-section, inversely proportional to the strength of the restraining force applied, and not significantly related to the initial crack width.

3. FEM numerical simulations reveal that imposing asymmetric restraining forces on the high and low temperature sides of the experimental specimen may be a more optimal solution for reproducing the bending-like movement of through-thickness cracks at the lab-scale.

4. The proposed experimental setup was verified to be effective in simulating the characteristic movement patterns of through-thickness cracks and satisfying the deterioration form of the combined temperature and mechanical loading. The proposed test method reproduced the crack movement that satisfies the relationship between the movement amplitude and temperature difference, restraining force, and initial crack width in real buildings. In addition, this method can achieve a wide variety of experimental groups by adjusting parameters such as the infrared lamp intensity, wrench torque, and crack width; this method has excellent general applicability and stability. In the crack repair solution selection system given by the Ministry of Land, Infrastructure, Transportation and Tourism of Japan, before the repair, the measurement of crack

movement is required. Using this method, a reasonable reproduction and evaluation can be realized by knowing the specific conditions of the target cracks.

5. Lab-scale reproduction experiments have demonstrated that reducing the specimen surface temperature can effectively reduce the crack movement amplitude as a deterioration factor. On one hand, we verified that the driving force of crack movement in this test method is the temperature difference; on the other hand, a crack repair method that reduces the wall surface temperature can be expected to be more durable due to reduced movement amplitude is informative for practical engineering applications.

6. This chapter also proposed an efficient fatigue apparatus for bending-like movement. The method can simulate the mechanical fatigue of the repair area, and together with the constant temperature and humidity chamber can also simulate the fatigue evaluation in multiple climates. The advantages are controllable movement and period, easy to increase the experimental variables and accelerate the degradation process to shorten the test period.

7. However, this chapter has the following limitations. First, there are many forms of crack movements in on-site buildings. This work applies only to the reproduction of the bending-like movement of through-thickness cracks. Second, only three factors that may affect the crack movement amplitude have been discussed so far. Third, in the future, more on-site building measurements as well as crack repair work needs to be monitored and summarized to overcome the above limitations. In addition, too fast heating rates in reproduction experiments may lead to underestimation of the durability of the repair solution. An experimental cycle does not necessarily represent an actual day. In the future, after data accumulation, it may be a feasible solution to relate the number of cycles in the experiment to the number of days in the actual environment.

Chapter 4

Evaluation of various repair solutions for resistance to the crack movement

4.1. Purpose

The main objective of this chapter is to evaluate the durability of various common crack repair solutions for crack movement. The evaluation methods were two approaches, the crack movement reproduction test method, and the mechanical fatigue test method, which were proposed in the Chapter 3. The repair solutions evaluated mainly include the injection method, the U-groove routing and sealing method and the surface coating method. The repair materials involved include epoxy resin, polymer cement and waterborne acrylic waterproof coating, etc. In the reproduction experiments, we focused on the crack movement pattern before and after the repair, and the progress of deterioration. The feasibility of the heat-flow sensor and air leakage tests in detecting the defect areas and judging the extent of defects was also confirmed. In the fatigue test, the durability of various repair solutions under different amplitude and temperature environments was discussed.

4.2. Evaluation of repair solutions based on reproduction experiments

4.2.1. Materials and methods

(1) Repair solutions

Seven common crack repair solutions were evaluated in this section, as shown in **Table 4–1**.

The injection method included three materials: hard epoxy resin (HE), soft epoxy resin (SE) and polymer cement (PC), and their properties are shown in **Table 4–2**, **Table 4–3** and **Table 4–4**, respectively.
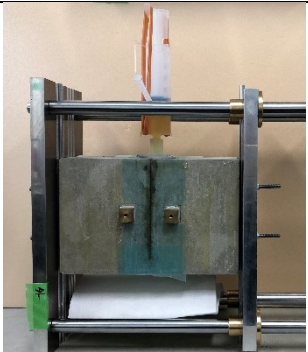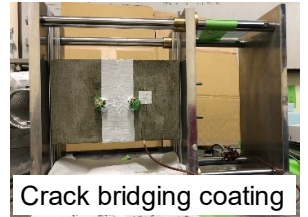
The U-groove routing and sealing method is also a commonly used crack repair method because of its simplicity of operation. The properties of the grouting materials used in this experiment are shown in **Table 4–5**.

The surface coating method (SC) covered three materials, A, B, and C. SCA is a membrane waterproofing material that meets the requirements of JIS A 6021. SCB is a type with an additional layer of crack bridging material applied versus SCA. Specific information and coating procedures for these two surface coatings are shown in **Table 4–6** and **Table 4–7**, respectively. The tensile properties of SCA are shown in **Table 4–8** and **Figure 4–1**. Regarding the crack bridging coating in the SCB

repair method, according to the Japan outer wall waterproofing association (NBK), it refers to a class of products that meet the corresponding specifications. The specific quality requirements are shown in **Table 4–9**. SCA and SCB simultaneously realize crack repair and full-surface waterproof coating effect. Simpler process and better aesthetics than the injection method. In addition, for the previous partial coating and covering method, after the cracks were partially coated, covering the entire wall with finishing coating again was desired. In contrast, SCA and SCB only need to be applied once to the entire wall. Certainly, applying SCA and SCB only partially to the cracks is acceptable if the homeowner is not concerned about aesthetic issues. However, the SCA and SCB used in this paper can only be used directly for the repair of cracks with an initial width of 1 mm or less, and cases larger than 1 mm need to be supplemented with a U-groove routing and sealing method.

In addition, surface coating C (SCC) is a building waterproof finishing coating that meets JIS A 6909, and its coating procedure is shown in **Table 4–10**.

Table 4–1 List of repair solutions for reproduction tests.

Notation	Material	Method	Solution process	Photos
HE	Hard epoxy resin	Injection method	· Surface preparation · Crack sealing · Epoxy preparation · Epoxy injection · Curing and drying · Finishing	
SE	Soft epoxy resin			
PC	Polymer cement			
UC	Flexible epoxy resin	U-groove routing and sealing method	· Crack preparation · Routing · Cleaning, priming · Sealant application · Tooling · Curing and drying	
SCA	Waterborne acrylic waterproof coating conforming to JIS A 6021	Surface coating method	· Crack preparation · Surface priming · Crack bridging coating (In the case of SCB only) · Multiple coat application (The waterproof coating is	Crack bridging coating
SCB	SCA with crack bridging			

	coating	divided into two (SCC) to three (SCA and SCB) coats, and the top coating is divided into two coats)
SCC	Finishing waterproof material conforming to JIS A 6909	· Curing and drying

Table 4–2 Hard epoxy resin properties (According to product provider).

	Main agent	Epoxy resin
Principal components	Hardener	Polyamine
Mixing ratio (mass)		Main agent: hardener = 2: 1
Available time		Approx. 40 min (30 °C, 500 g)
Specific gravity		1.15 ± 0.05
Viscosity (mPa·s)		12000
Bond strength (method a of JIS A 6024) (MPa) (23°C ± 2°C)		8.5
Tensile properties (method A of JIS A 6024) (23°C ± 2°C)	Tensile strength (MPa)	38.9
	Elongation at break (%)	6
Curing shrinkage (%)		2

Table 4–3 Soft epoxy resin properties (According to product provider).

	Main agent	Epoxy resin
Principal components	Hardener	Modified alicyclic polyamine, modified aliphatic polyamine, polyamidoamine
Mixing ratio (mass)		Main agent: hardener = 2: 1
Available time		Approx. 30 ± 10 min (20 °C, 500 g)
Specific gravity		1.15 ± 0.10
Viscosity (mPa·s) (23°C ± 2°C)		5340
Bond strength (method a of JIS A 6024) (MPa) (23°C ± 2°C)		13.5

Tensile properties (method B of JIS A 6024) (23°C±2°C)	Tensile strength (MPa)	4.7
	Elongation at break (%)	106
Curing shrinkage (%)		2.6

Table 4–4 Polymer cement properties (According to product provider).

Principal components	Slurry powder: Utrafine cement	True specific gravity	3.0 ± 0.1
		Powder degree	Approx. 9000 cm^2/g
	Slurry mixture: SBR latex	Specific gravity (20 °C)	1.00 ± 0.1
		Viscosity (mPa·s) (20°C)	< 50
		PH	9.5 ± 1.0
Mixing ratio (mass)		Powder: latex = 5: 3	
Shrinkage (%) (NSKS-003 4.7)		1.9	
Bond strength (N/mm^2) (NSKS-003 4.8)		4.1	
Bending strength (N/mm^2) (NSKS-003 4.9)		4.5	
Water absorption (%)		3.0	

Table 4–5 Flexible epoxy resin for U-groove routing and sealing method (According to product provider).

Principal components		Modified silicone resin, epoxy resin, ketimine
Surface tack-free time		Approx. 3.5 h (23 °C, 50%)
Tensile bond strength (JIS A 6024) (MPa) (23°C ± 2°C)	Tensile strength (MPa)	1.2
	Elongation at break (%)	62
Tensile properties (method C of JIS A 6024) (23°C ± 2°C)	Tensile strength (MPa)	2.0
	Elongation (%)	77

Table 4–6 Information on the main coatings of SCA and SCB (According to product provider).

Materials	Common name	Physical state	Ingredient	Concentration	Chemical formula	CAS number

Priming coating (emulsion: powder = 1: 5) (mass)	Synthetic resin emulsion coating	Liquid (viscous liquid), milky white	Water	80%~90%	H_2O	7732-18-5
			Other	10%~20%	—	—
			Propylene glycol monomethyl ether	< 5%	$C_4H_{10}O_2$	107-98-2
	Cement additives	Solid (powder), ray	Portland cement, alumina cement, slag cement, super sulphate cement, hydraulic cement	> 90%	—	65997-15-1
			Hydrated silicic acid	< 5%	SiO_2	7631-86-9
			Other	< 5%	—	—
Waterproof coating	Synthetic resin emulsion coating	Liquid (viscous liquid), white	Other	50%~60%	—	—
			Water	30%~40%	H_2O	7732-18-5
			Titanium oxide (IV)	1%~10%	TiO_2	13463-67-7
			Methanol	< 5%	CH_3OH	67-56-1
			Zinc oxide	< 5%	ZnO	1314-13-2
Top coating	Synthetic resin emulsion coating	Liquid (viscous liquid)	Water	40%~50%	H_2O	7732-18-5
			Other	30%~40%	—	—
			Titanium oxide (IV)	1%~10%	TiO_2	13463-67-7
			2-Butoxy ethanol	< 5%	$C_4H_9OCH_2CH_2OH$	111-76-2
			Chromium oxide	< 5%	Cr_2O_3	1308-38-9
			Cobalt blue	< 5%	—	1345-16-0

Table 4–7 Coating procedure for SCA and SCB.

Primer coating		0.1 kg/m²
※Crack bridge coating		35 g/m (50 mm width)
Waterproof coating	First time	0.5 kg/m²

|		
	Second time	0.5 kg/m^2
	Third time	0.6 kg/m^2
Top coating	First time	0.15 kg/m^2
	Second time	0.15 kg/m^2

Note: ※Crack bridging coating is only applied to SCB.

Table 4–8 Tensile properties of the coating of the waterproof functional layer of SCA and SCB specimens.

	-20°C	7.9
	-10°C	6.4
Tensile strength (N/mm^2)	0°C	4.8
	23°C	2.4
	60°C	1.7
Elongation at break (%)	467	
	-20°C	142
	-10°C	206
Grip-to-grip elongation at break (%)	0°C	238
	23°C	287
	60°C	192

Note:
- Sample Preparation: Following the JIS A 6021 standard, the waterproof material was uniformly applied to the mold to ensure the absence of air bubbles. After curing for 24 h at 23°C and 50% humidity, followed by an additional 24 h of curing at 40°C, the coating was inverted and subjected to further curing for 48 h at 40°C, and then allowed to cure for a minimum of 4 h at 23°C and 50% humidity.
- Tensile Strength: A dumbbell-shaped No. 3 specimen with a grip-to-grip distance of 60 mm was subjected to a tensile test at a speed of 200 mm/min. The maximum tensile force at the point of coating failure was recorded and used for calculation.
- Elongation at Break: The elongation at break was calculated based on the displacement of 20 mm between the reference marks during the test.
- Grip-to-Grip Elongation at Break: The grip-to-grip elongation at break was calculated based on the displacement of 60 mm between the grips during the test.
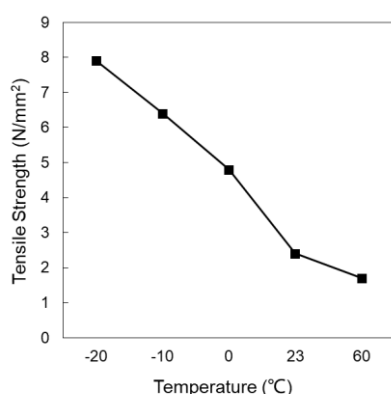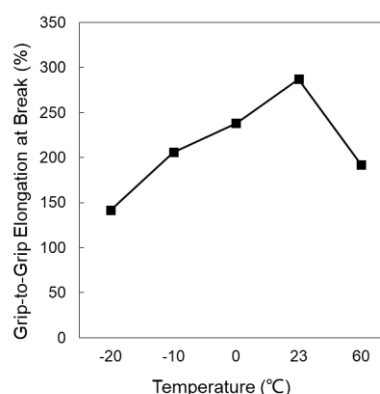
(a) Tensile strength   (b) Grip-to-grip elongation at break

Figure 4–1 Tensile properties of the coating of the waterproof functional layer of SCA and SCB specimens.

Table 4–9 Specific quality requirements for crack bridge coating (According toNBKS-002：2022).

Item		Quality
Material		Base material is acrylic rubber, mixed with mineral fillers and additives.
Tensile performance (JIS A 6021: 2022 7.6.1)	Tensile strength (N/mm²)	> 0.20
	Elongation at break (%)	> 400
Tensile performance after heat treatment (JIS A 6021: 2022 7.9)	Tensile strength ratio (%)	> 100
	Elongation (%)	> 400
Adhesion performance (JIS A 6021: 2022 7.11)	Adhesion strength (N/mm²)	> 0.30, and the sum of the interfacial failure rate※ of the interface between the primer and the crack bridge material and the interface between crack bridge material and the waterproofing material is less than 50%.
Solid content (%) (JIS A 6021: 2022 7.14)		Display value ± 3.0
Cured material specific gravity (JIS A 6021:		Display value ± 0.1

2022 7.15)		

Table 4–10 Coating procedure for SCC.

Primer coating		0.1 kg/m^2
Waterproof coating (Add 3% water to dilute for use. The mass of water is not included in the coating amount)	First time	1.1 kg/m^2
	Second time	1.1 kg/m^2
Top coating	First time	0.15 kg/m^2
	Second time	0.15 kg/m^2

(2)   Experimental settings

The experiments were performed using the reproduced test method presented in Chapter 3. The experimental photos are shown in **Figure 4–2**. Note that rubber heaters were used as the heat source in this section. The procedure for the thermal load is shown in **Figure 4–3**. The initial temperature was 20°C and heated to 60°C in 1 h. After 3 h of natural cooling a second cycle was followed. After 1000 cycles, the entire unit was moved to a room with 5°C ambient, keeping the temperature increment constant as 40°C and continuing the heat load cycle. The purpose of this setup is to verify whether the specimens deteriorate after many cycles and the effect of repair material properties on crack movement at different temperatures.
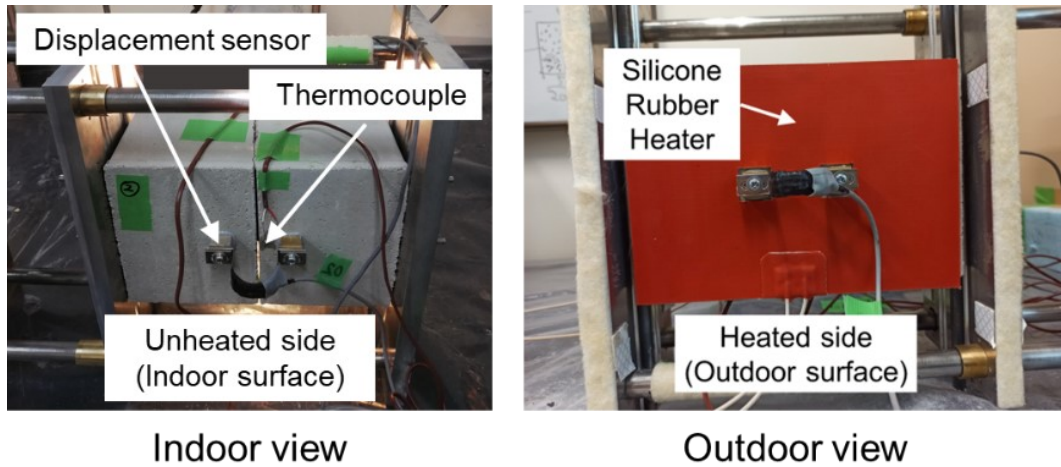
Figure 4–2 Photos of the reproduction experiment using rubber heaters.
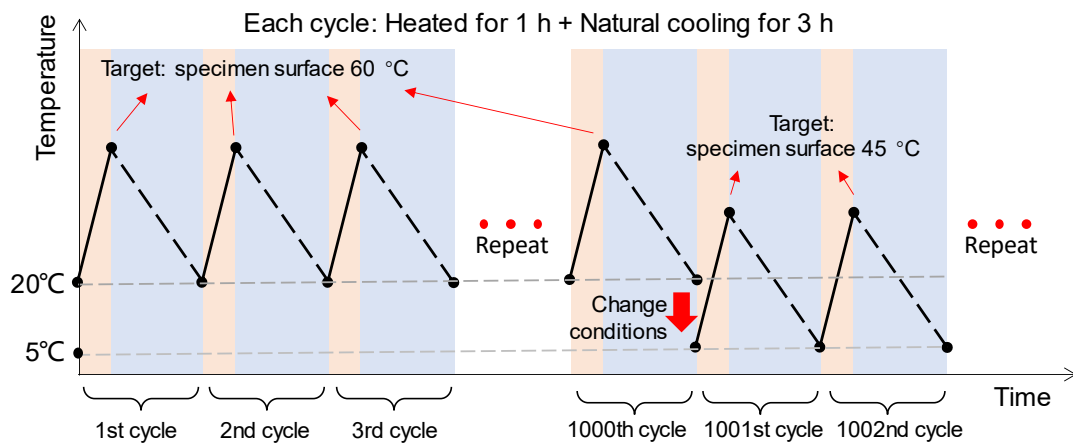
Figure 4–3 Procedure of thermal load cycle.

In the experiment, the sensors were set up in the positions shown in **Figure 4–4**. For the specimens before repair, Pi-shape displacement sensors were set at the cracks on assumed indoor and outdoor surfaces, respectively. T-type thermocouples were set below the displacement sensors. Two heat-flow sensors were attached to the indoor surface of the specimen to measure the heat-flow density at the cracks and at the mortar, respectively. After the repair was finished, all sensors were set in the same position as before the repair. Note that in the case of the surface coating method, additional thermocouples were required on the coating surface. In the experiment, the data loggers were recorded at 10 min intervals.
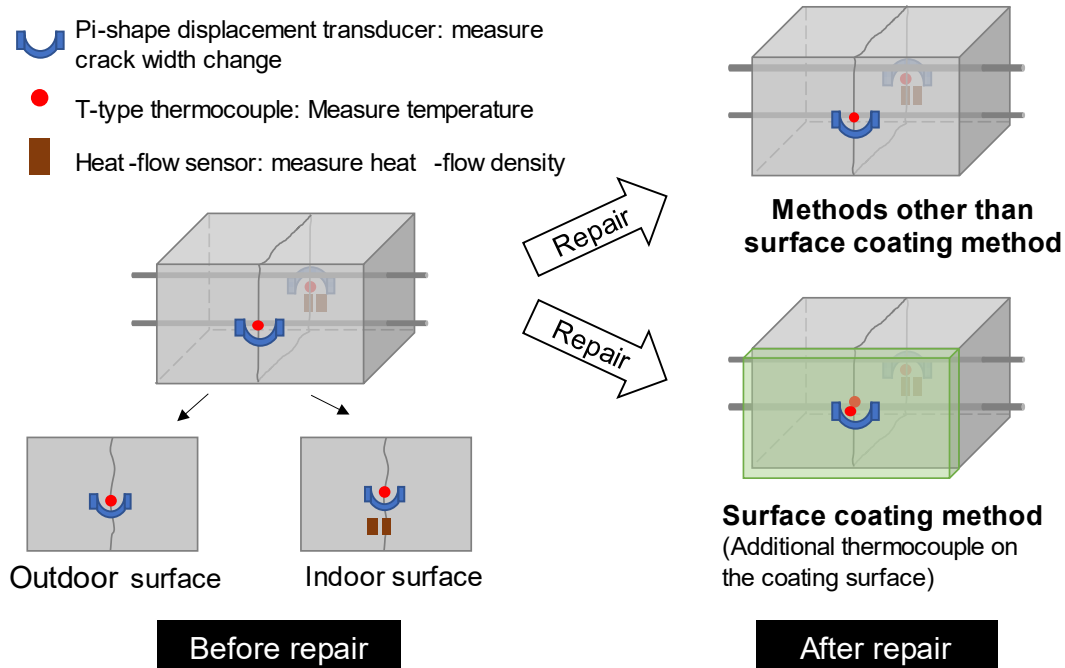
Figure 4–4 Setting positions of sensors in reproduction experiment.

4.2.2.Results and discussions

(1) Hard epoxy resin (HE)

The results of crack movements of HE specimen before and after the repair are shown in **Figure 4–5**. Before repair, the specimen showed bending-like movement: the assumed indoor crack opened, the movement extreme value was 0.054 mm. The assumed outdoor crack closed, the movement extreme value was 0.075 mm. After repair, the crack movement became significantly smaller, and the extreme values of the indoor and outdoor cracks became 0.10 mm and 0.005 mm, respectively. In addition, the cracks on both sides were closing movement. The reason is that the cracked specimens become a whole again after epoxy injection, hence the movement pattern is changed.
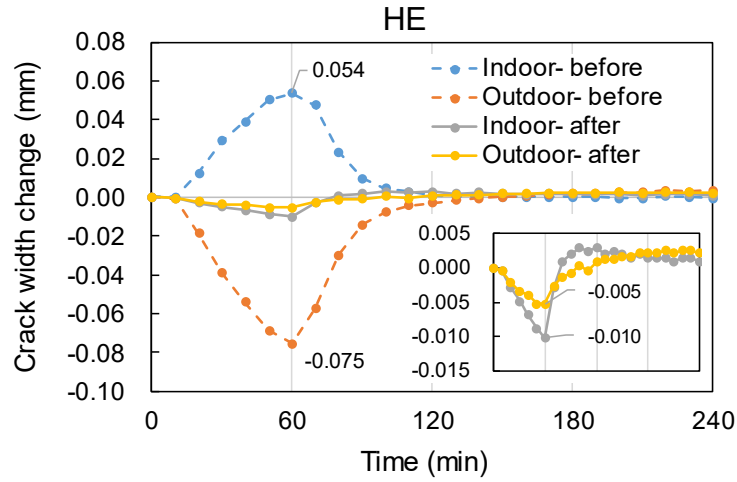
Figure 4–5 Results of crack movement before and after repair of HE specimen.

After repair, the HE specimen was subjected to 1000 cycles of crack movement deterioration in a 20°C environment. Owing to time limit, subsequent experiments in 5°C environment were performed for only 20 cycles. The results of crack movement for all cycles are shown in **Figure 4–6**. The fluctuations in the graph are caused by room temperature fluctuations and rubber heater errors as shown in **Figure 4–7**.
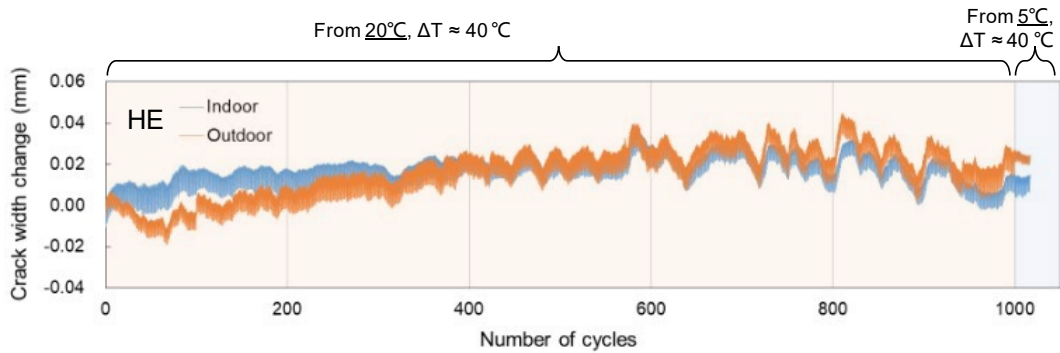
Figure 4–6 Crack movement for all cycles of HE specimens after repair.
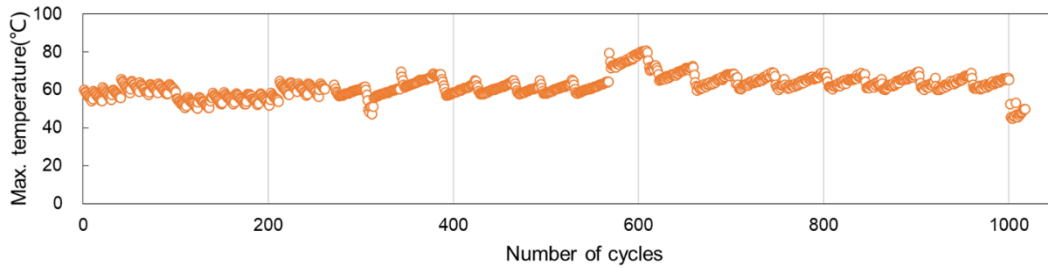
Figure 4–7 Maximum value of temperature on the outdoor surface for each
cycle of HE specimen.

To exclude the effect of temperature fluctuations, only cycles with identical temperature conditions were selected to discuss the change in crack movement. 20°C experiments were selected at the same maximum temperature as before the HE repaired (61.6°C ± 1°C). Experiments at 5°C were selected with the same temperature increment for the cycles (maximum temperature = 46.6°C ± 1°C). The results of the extreme values of the cycles for the same temperature conditions of HE specimens are shown in **Figure 4–8**. In general, the trend of crack movement is generally stable, indicating that the experimental apparatus is providing a steady constraint for the specimen. Noted that the outdoor movement was significantly reduced when the experiment changed from a 20°C environment to 5°C. As the temperature becomes lower, the most likely changes that HE would undergo are a larger Young's modulus and a smaller coefficient of thermal expansion. In other words, the physical properties of the injection material can affect the crack movement after the repair.
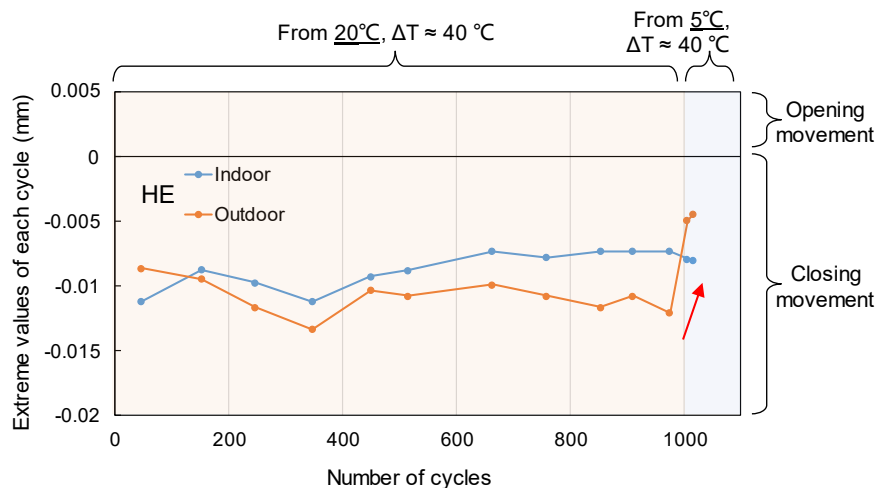
Figure 4–8 Crack movement extreme values of the cycles for the same
temperature condition of HE specimen.

Heat-flow density can be used to determine the thermal properties of the object under test. Under the same boundary conditions, the greater the thermal conductivity of the region under test, the greater

the heat-flow density at that location. **Figure 4–9** shows the heat-flow results for the HE specimen at the mortar and the crack for 1000 cycles at 20°C. As can be seen in the figure, the slope of the approximation curve is 1.07, which is greater than 1.0. This can be explained by the fact that the thermal conductivity of HE is small compared to mortar. This indicates that the heat-flow sensor can be used to determine the defective part of the wall. However, since the differences in the measured values are small, the precondition must be to ensure a sufficient number of samples. A short period of measurement data does not ensure credibility.
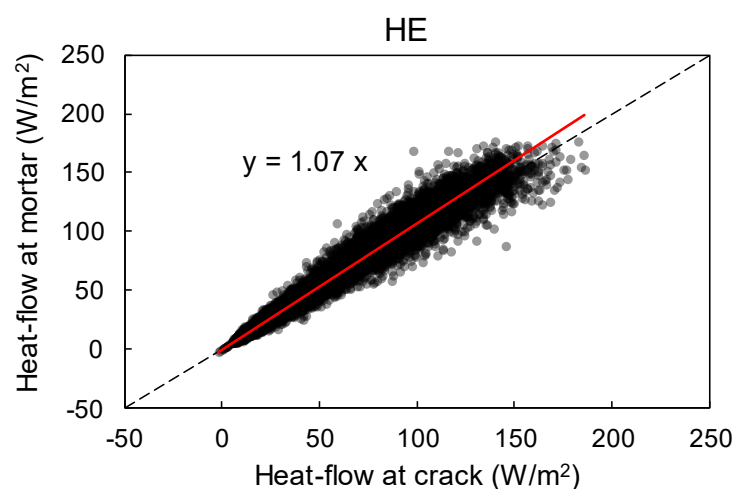
Figure 4–9 Heat-flow density at mortar and crack of HE specimen in relation to their indoor temperature.

(2) Soft epoxy resin (SE)

The crack movement results of the SE specimen before and after repair are shown in **Figure 4–10**. After the repair, a reverse bending-like movement occurred at the crack: indoor closed by 0.012 mm and outdoor opened by 0.006 mm. In addition, after SE repair, the crack movement is greater compared to that of HE specimens. This indicates that the physical properties of the injection material affect not only the crack movement pattern but also the magnitude of the crack movement.
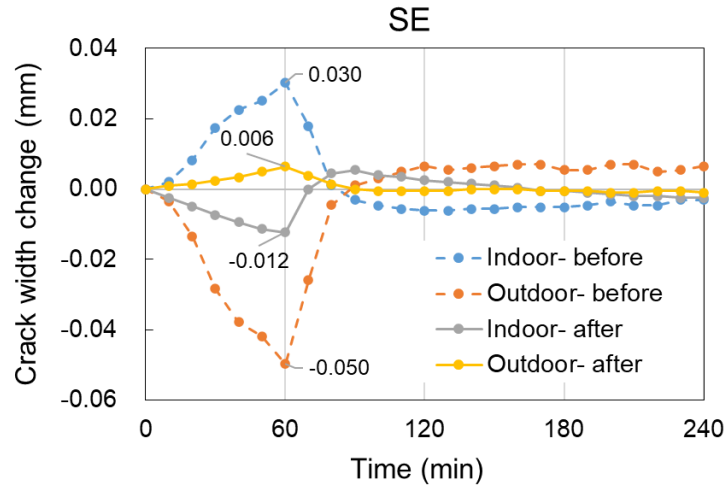
Figure 4–10 Results of crack movement before and after repair of SE specimen.

SE specimens were performed at 20°C and 5°C for 1000 and 500 and cycles, respectively, and the crack movement results are shown in **Figure 4–11**. As can be seen from the figure, the indoor and outdoor cracks change in the direction of opening and closing, respectively. In other words, the crack width does not return to the original position after each cycle, but movement residues exist. This is assumed to be caused by the experimental device. To reproduce the bending-like movement of through-thickness crack, the outdoor side was equipped with a round steel rod. As shown in **Figure 4–12**, when the forces of the round steel rod and the threaded rod are not balanced, movement remains at the indoor and outdoor cracks over time. The SE specimen should correspond to Case 2.
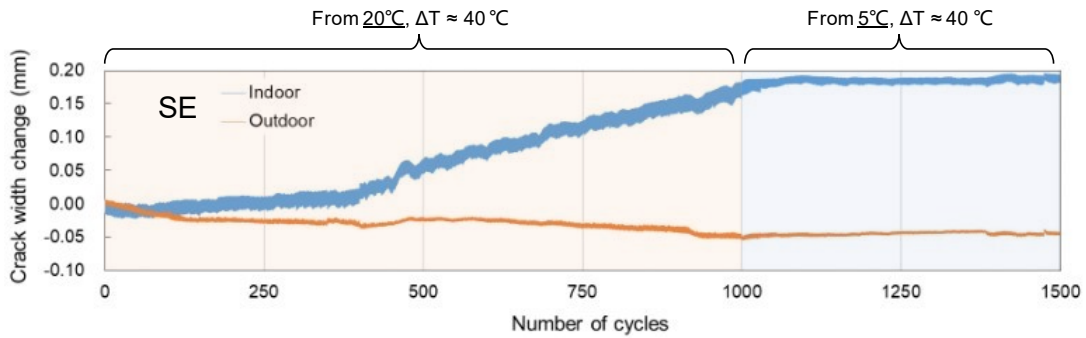
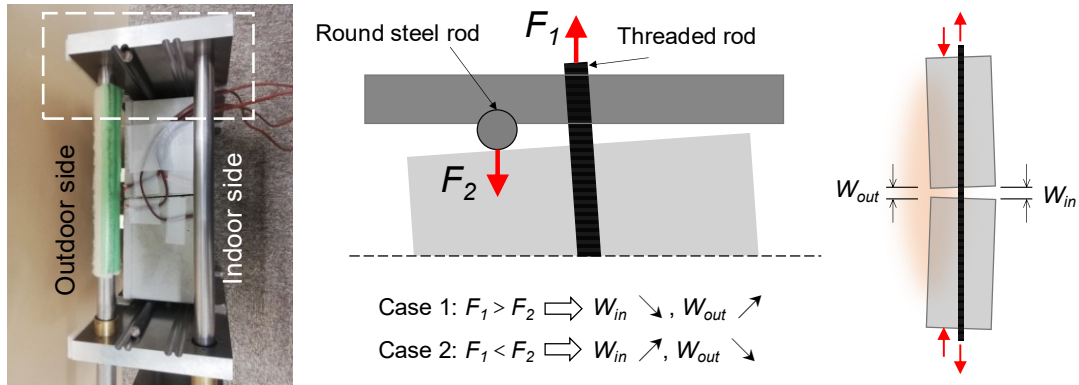Figure 4–11 Crack movement for all cycles of SE specimens after repair.

Figure 4–12 Mechanism of crack width change owing to the device.

Cycles with the same temperature conditions were selected and their extreme values of crack movement are drawn in **Figure 4–13**. The same temperature conditions as before the repair were selected for the 20°C experiment, i.e., a maximum temperature of 61.5°C ± 1°C. The experiment for the 5°C environment selected cycles with a maximum temperature of 46.5°C ± 1°C. In the figure, there is no significant change in crack movement when the temperature environment is constant, and the specimens show no signs of deterioration. The indoor crack movement became significantly smaller when changing the ambient temperature. This is because the Young's modulus of SE becomes larger and the structural stiffness increases, which suppresses the crack movement. The outdoor crack changes from an opening movement to a closing movement. This makes the SE's movement pattern the same as HE's. Therefore, it is presumed that the epoxy resin injection material may cause the repaired cracks to have a movement of closing on both indoor and outdoor sides at low temperatures.
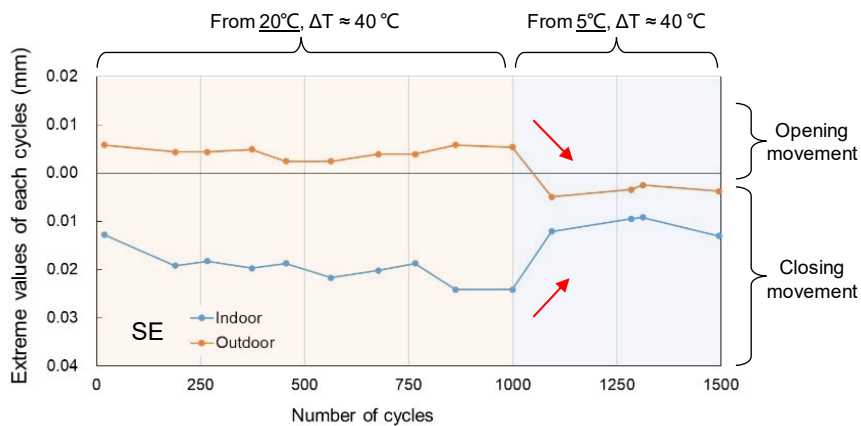

Figure 4–13 Crack movement extreme values of the cycles for the same temperature condition of SE specimen.

The results of heat flow comparison at the mortar and crack are shown in **Figure 4–14**. The thermal conductivity of SE is lower than that of mortar, thus the heat flow at cracks is smaller under the same

boundary conditions. The conclusion is the same as that of the HE specimen. The slope of the approximate line in the figure is 1.08.
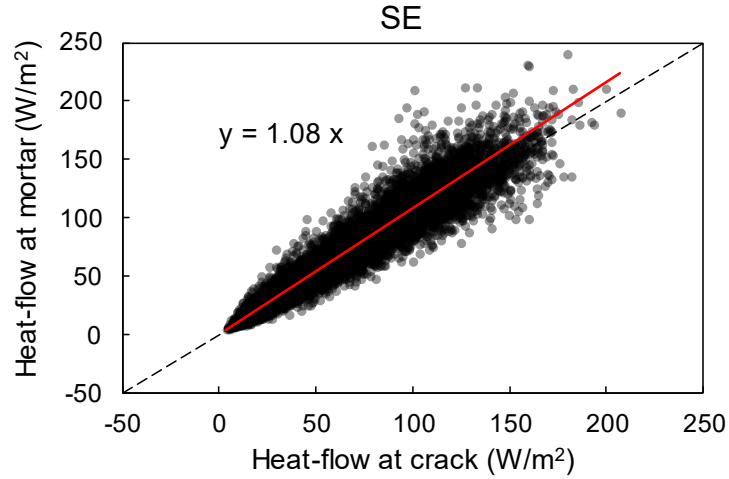

Figure 4–14 Heat-flow density at mortar and crack of SE specimen in relation to their indoor temperature.

(3) Polymer cement (PC)

The results of the crack movement of the PC specimens before and after the repair are shown in **Figure 4–15**. After the repair, the crack movement was significantly reduced, and both were in the direction of closing. The extreme values of the movement on the indoor and outdoor sides were 0.010 mm and 0.003 mm, respectively.
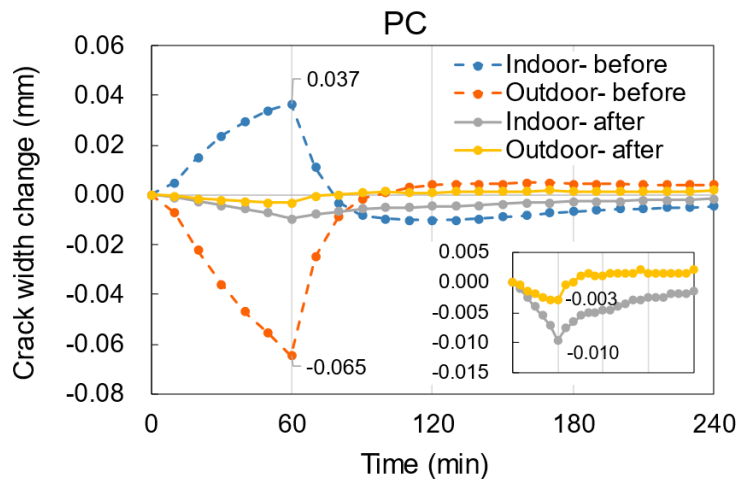
Figure 4–15 Results of crack movement before and after repair of PC specimen.

Because the PC specimen had already deteriorated when it underwent the cycling experiment at

20°C, there was no experiment at 5°C. The results of the crack movement of the PC specimen for 500 cycles at 20°C are shown in **Figure 4–16**. In the figure, the indoor cracks accumulate a closing movement residue, and the outdoor cracks accumulate an opening movement residue. The force state of this specimen may be Case 1 in **Figure 4–12**.
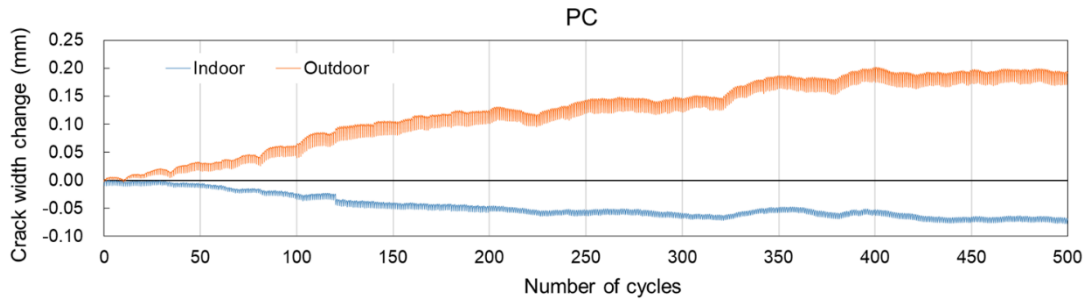

Figure 4–16 Crack movement for all cycles of PC specimens after repair.

The extreme value of crack movement of PC specimen under the same temperature conditions (maximum temperature = 51.8°C ± 1°C) changes as shown in **Figure 4–17**. The indoor crack variation was stable; however, the outdoor movement had a tendency of getting larger in absolute value. This could be because deterioration has occurred, causing the crack movement to become larger again.
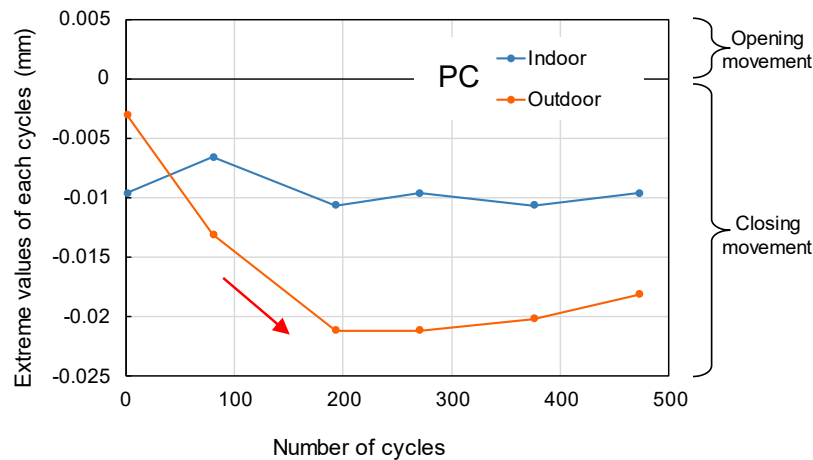

Figure 4–17 Crack movement extreme values of the cycles for the same temperature condition of PC specimen.

Regarding the development of the degradation process, air leakage experiments were performed every few cycles. Taking the data of PC specimen before the repair, after the repair and after 60 cycles of deterioration, the results of the air leakage experiment are shown in **Figure 4–18**. Before the repair, the specimen had a through-thickness crack, thus the air pressure in the negative pressure air chamber changed rapidly. After the repair, the specimen was intact, and the air pressure remained the same. When the specimen was cracked again, the air pressure also changed. In other words, the smaller the

absolute value of air pressure after a certain time, the greater the deterioration of the specimen. The results of air leakage experiments at 30 s for PC specimens at each cycle are shown in **Figure 4–19**. For the indoor surface, no signs of deterioration were detected. This result is the same as the conclusion drawn from the extreme value results of the crack movement. For the outer surface, deterioration could be detected as early as 60 cycles. As the number of cycles increased, the deterioration became progressively more severe. However, at 500 cycles, the air leakage experiment detected less degradation than before. This is because the slimes used repeatedly in the experiment were not cleaned up and covered some cracks. A microscope was used to confirm these indications, as shown in **Figure 4–20**. On the outdoor surface, cracks caused by drying shrinkage of the polymer mortar occurred at a very early stage. The re-cracking position was in the PC repair zone. The crack width gradually increased under the thermal loading. Together with the continuous crack movement, the crack apex moved continuously under stress and the cracks became longer and wider.
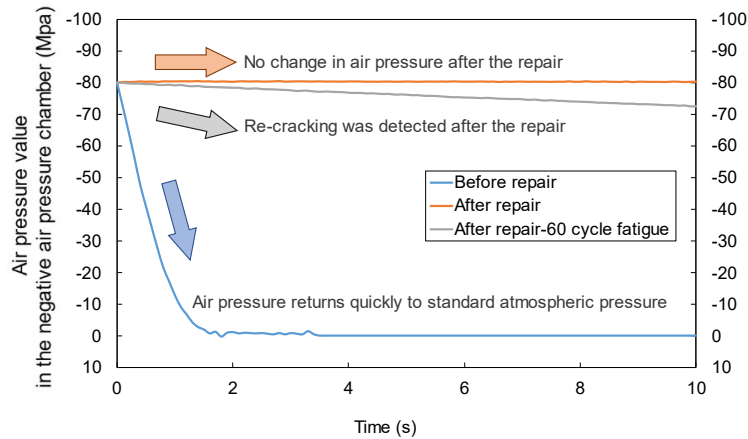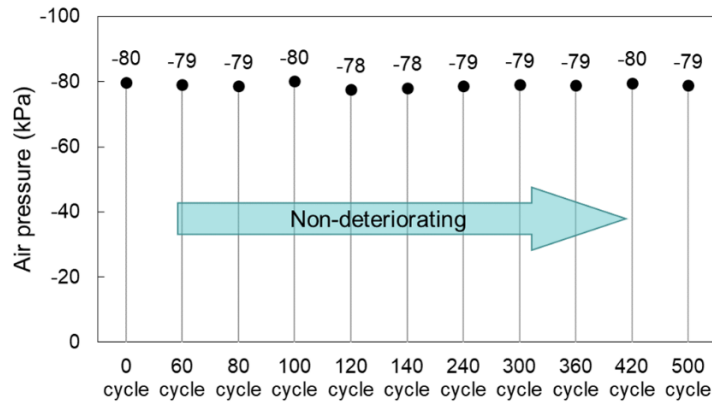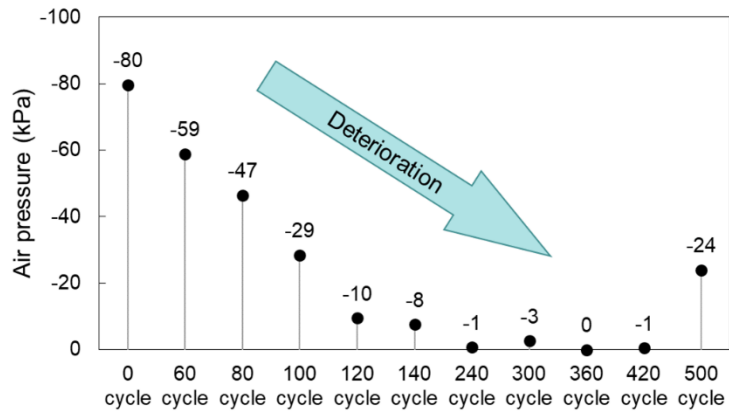

Figure 4–18 Description of the results of the air leakage experiments with PC specimens as an example.

(a) Indoor surface

(b) Outdoor surface

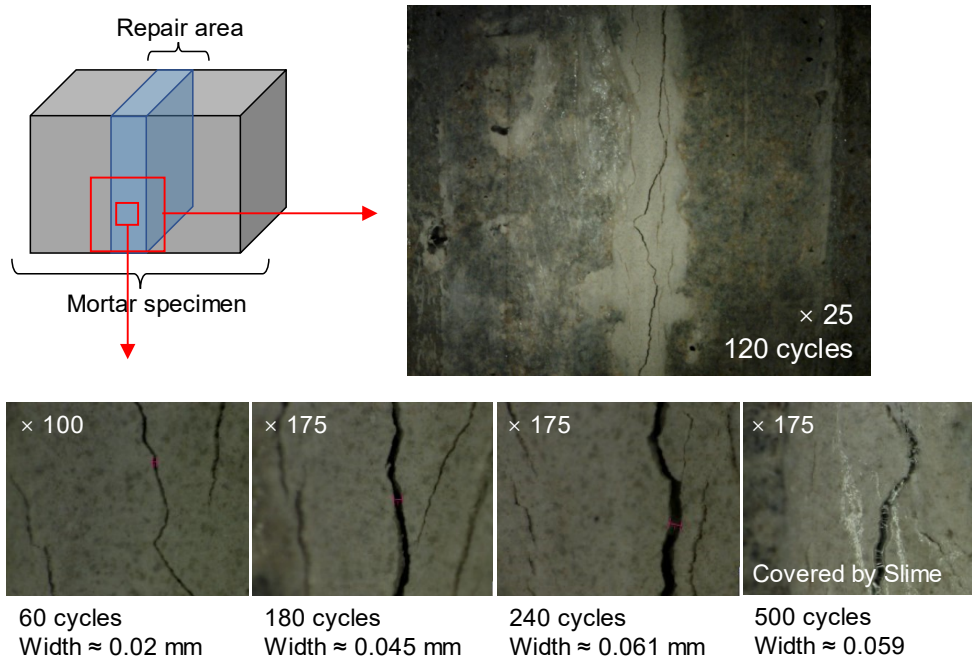Figure 4–19 Results of the air leakage experiment at 30 s for the PC specimen.

Figure 4–20 Re-cracking of the outdoor surface of the PC specimen.

(4) U-groove routing and sealing (UC)

The results of the crack movement of the UC specimen before and after the repair are shown in **Figure 4–21**. Before the repair, the extreme values of the indoor and outdoor crack movements were 0.044 mm and 0.074 mm, respectively. After the repair, both the indoor and outdoor crack movement extremes became smaller, 0.043 mm and 0.032 mm, respectively. Note that after the repair, the crack

showed a reverse bending-like movement, which is the same as the SE specimen. However, the crack movement suppression effect of UC is not as great as that of SE.
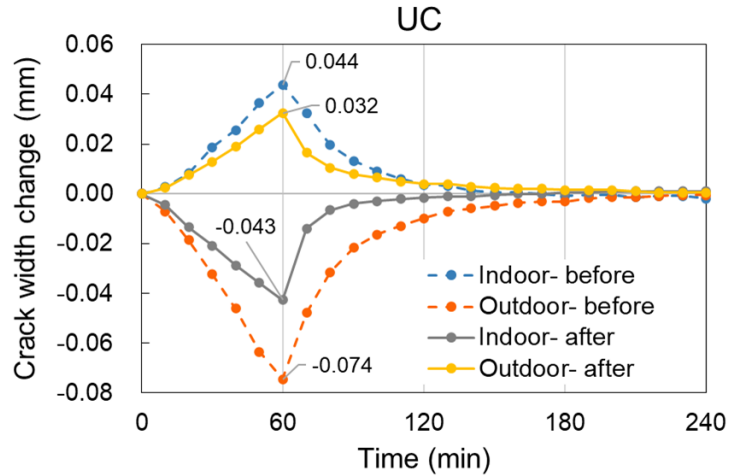

Figure 4–21 Results of crack movement before and after repair of UC specimen.

UC specimens were subjected to 1000 and 800 cycles of reproduction experiments at 20°C and 5°C, respectively. The results of crack movement for all cycles are shown in **Figure 4–22**. As with the SE specimen, the indoor crack of the UC specimen gradually opened up and the outdoor crack gradually closed. This crack width variation is caused by Case 2 in **Figure 4–12**.
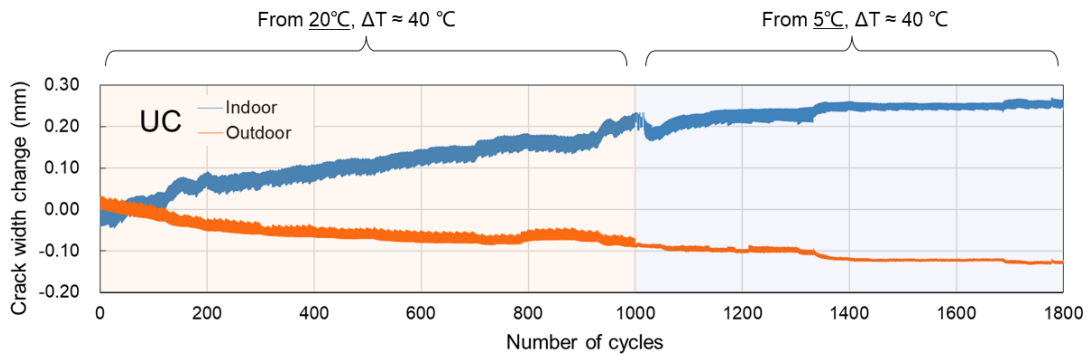

Figure 4–22 Crack movement for all cycles of UC specimens after repair.

The cycles with the same highest temperature were selected and their extreme results of crack movement are shown in **Figure 4–23**. The maximum temperature for the 20°C ambient experiment is 57.7°C ± 1°C, and the maximum temperature for the 5°C ambient experiment is 42.7°C ± 1°C. As can be seen from the figure, the change in ambient temperature did not change the form of the crack movement of the UC specimens, which remained the reverse bending-like movement. In addition, for

the same temperature increment, the initial temperature decrease reduces the crack movement.
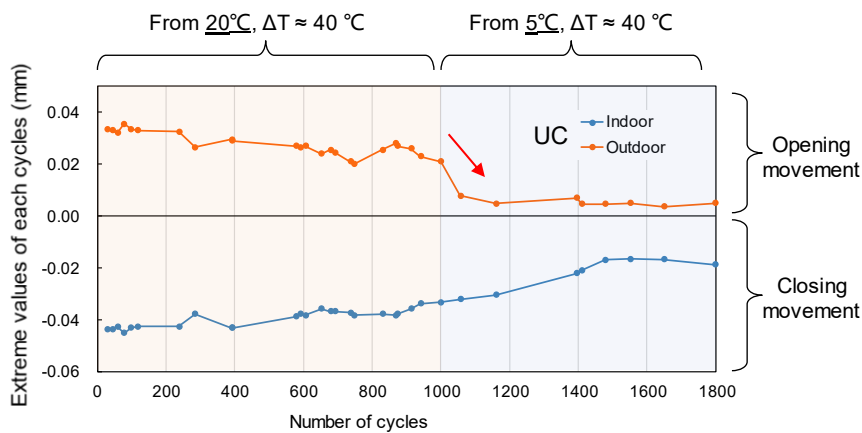

Figure 4–23 Crack movement extreme values of the cycles for the same temperature condition of UC specimen.

(5) Surface Coating A (SCA)

The results of crack movement before and after repair of the SCA specimen are shown in Figure 1. After the repair, the crack movement remained the same bending-like movement, only the movement amplitude became smaller. The indoor crack movement changed from 0.042 mm to 0.010 mm. The outdoor crack movement changed from 0.069 mm to 0.035 mm. The crack movement amplitude after the repair was about 40.5% of that before the repair.
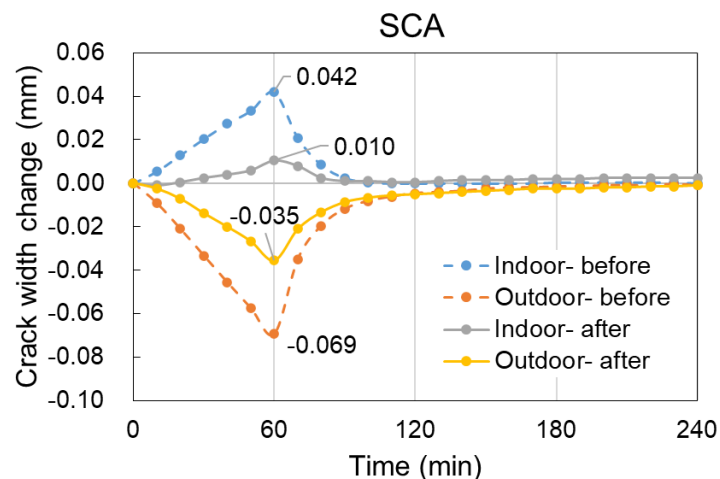

Figure 4–24 Results of crack movement before and after repair of SCA specimen.

Because of time limit, the SCA specimen was subjected to only 500 and 22 movement cycles at 20 °C and 5 °C environments, respectively. The crack movement results of these cycles are shown in

Figure 4–25. The fluctuation of the curves in the figure is mainly caused by the ambient temperature variation and the instability of the rubber heater. The constraint of the experimental device was relatively stable. Moreover, the outdoor movement is significantly larger than the indoor movement.
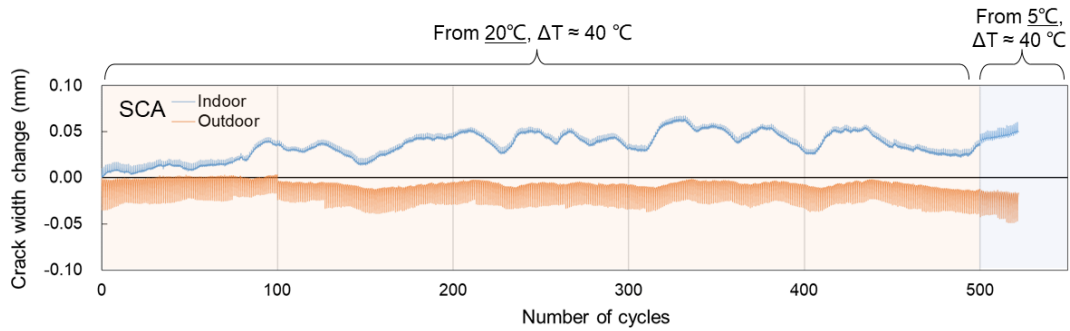

Figure 4–25 Crack movement for all cycles of SCA specimens after repair.

The maximum temperature of the SCA specimen in the cycle before the repair was 62.8 °C. Therefore, the cycles after the repair having the same temperature increment were selected and their crack movement extreme values are plotted in **Figure 4–26**. In the figure, the crack movement becomes larger when the starting temperature becomes lower, which is the opposite result from the previous specimens. There might be errors in the data owing to the small total number of cycles.
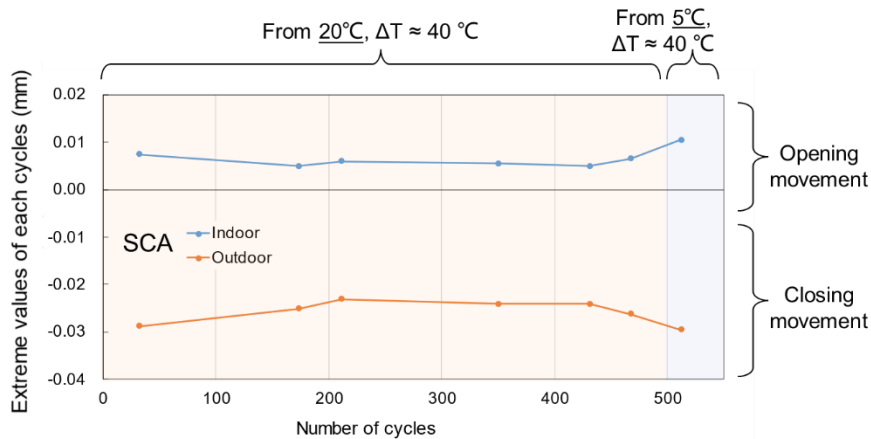

Figure 4–26 Crack movement extreme values of the cycles for the same temperature condition of SCA specimen.

For the SCA specimens, the use of heat-flow sensors was also discussed. After the repair, the crack on the indoor surface remained open. The heat-flow density at this location was compared with that at the nearby mortar, and the results are shown in **Figure 4–27**. The slope of the approximation line is 1.20. This is because the crack is equivalent to a thin layer of air and acts as an insulator. Moreover, the difference between the two locations is greater than that in the case of HE and SE injection methods. This also makes it possible for the heat-flow sensor to determine the presence of cracks.
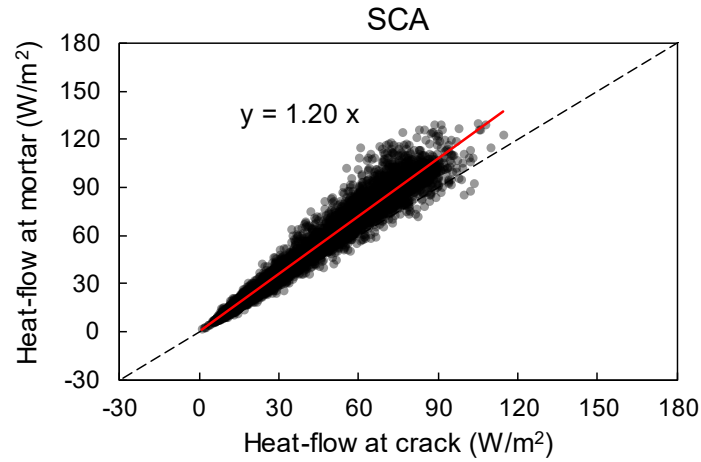
Figure 4–27 Heat-flow density at mortar and crack of SCA specimen in relation to their indoor temperature.

(6) Surface Coating B (SCB)

A comparison of the crack movement of the SCB specimen before and after the repair is shown in Figure 1. As with SCA, the coating of SCB did not change the bending-like movement pattern of the crack, but only reduced the amplitude of the movement. The amplitude of crack movement after repair was about 77.4% of that before repair. SCB applied an additional layer of crack bridging coating than SCA, but the ability to suppress crack movement did not increase. In a waterproofing system, the crack bridging coating is the softest functional layer, thus it works more to follow the crack movement than to suppress it. Certainly, an increase in the number of specimens is needed to get a definite conclusion.
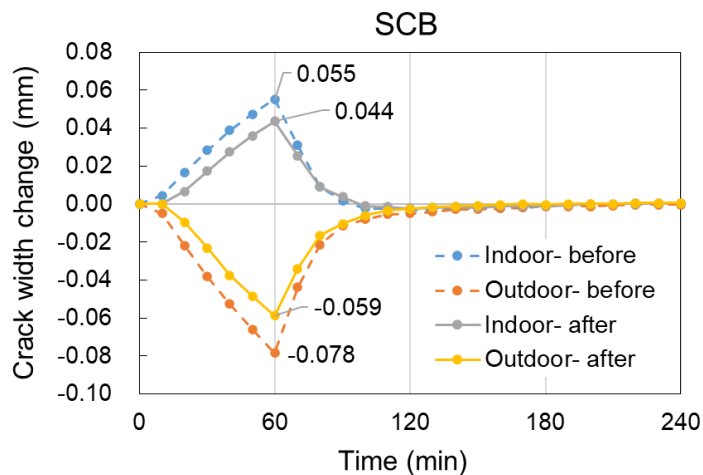

Figure 4–28 Results of crack movement before and after repair of SCB specimen.

The SCB was subjected to 1,000 cycles at 20 °C, followed by 22 cycles at 5 °C. The crack movement results are shown in **Figure 4–29**. During the experiment, both indoor and outdoor cracks had some tendency to open up. This may be caused by the loosening of the experimental device at the nut and the overall constraint force becomes smaller.
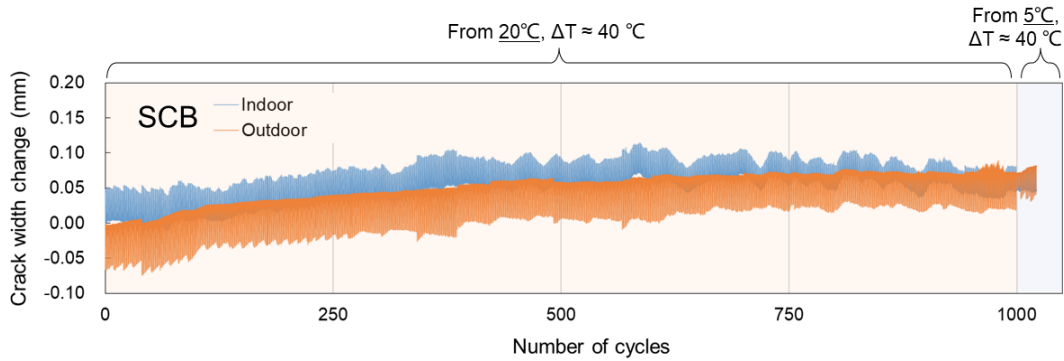
Figure 4–29 Crack movement for all cycles of SCB specimens after repair.

The SCB specimen cycles with maximum outdoor surface temperature of 62.9 °C ± 1 °C (for 20 °C) and 47.9 °C ± 1 °C (for 20 °C) were selected, and their extreme values of crack movement results are shown in **Figure 4–30**. It was found that the amplitude of crack movement was reduced by lowering the ambient temperature. The temperature decreased, the elongation of the waterproof coating decreased, and the tensile strength became greater, thus suppressing the crack movement.
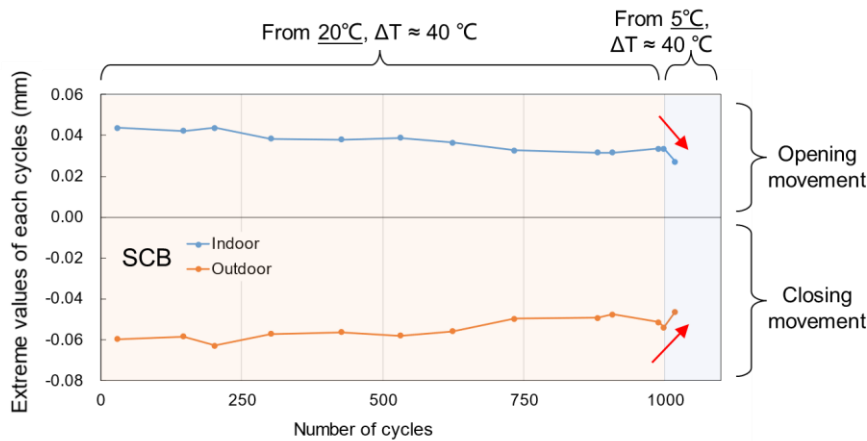
Figure 4–30 Crack movement extreme values of the cycles for the same temperature condition of SCB specimen.

(7) Surface Coating C (SCC)

The crack movement results of the SCC specimen before and after the repair are shown in **Figure 4–31**. Note that the SCC served as a surface coating but changed the movement pattern of the crack. The repaired crack showed a reversed bending-like movement similar to that of the UC specimen.

Because SCC flows very well, during the repair process, the coating flows into the outdoor side of the crack. This partial filling effect creates a force state like the U-groove routing and sealing method.
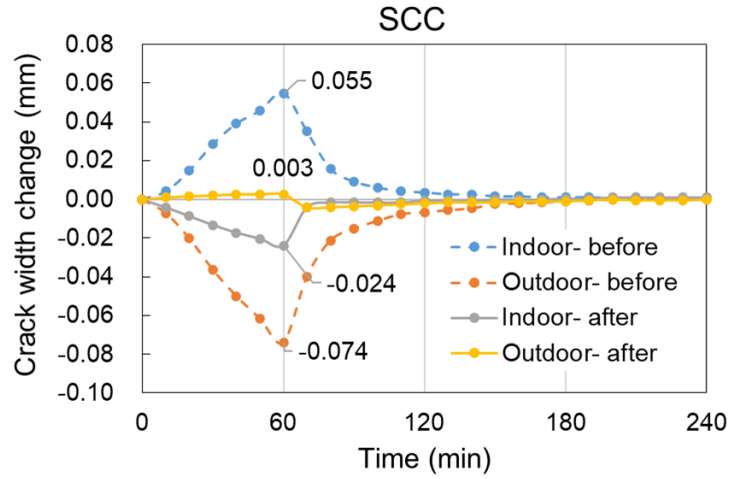
Figure 4–31 Results of crack movement before and after repair of SCC specimen.

The SCC specimens were moved to a 5°C environment after only 467 cycles in a 20°C environment owing to time constraints. The results of crack movement for all cycles of SCC are shown in **Figure 4–32**. The cycles with a temperature increment of 42.3 °C ± 1 °C for 2 two temperature environments were filtered out and plotted in **Figure 4–33**. In the figure, the crack movement becomes smaller when the ambient temperature decreases, especially the indoor crack.

Figure 4–32 Crack movement for all cycles of SCC specimens after repair.

Figure 4–33 Crack movement extreme values of the cycles for the same temperature condition of SCC specimen.

4.2.3. Numerical simulation of crack movement after repair in reproduction experiments

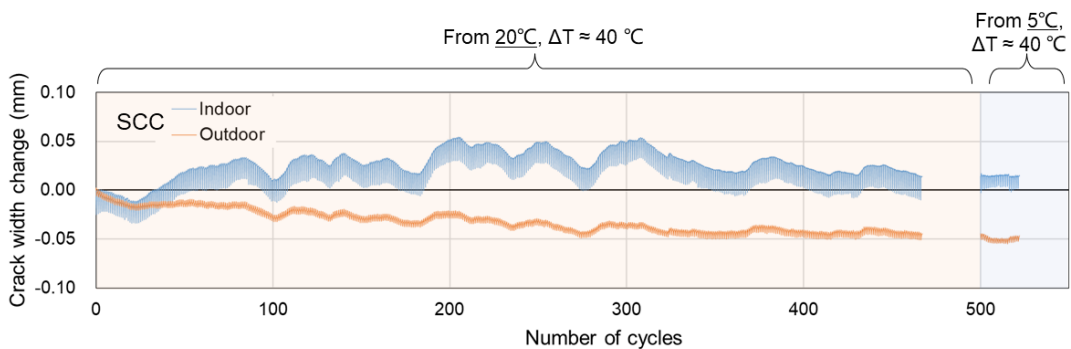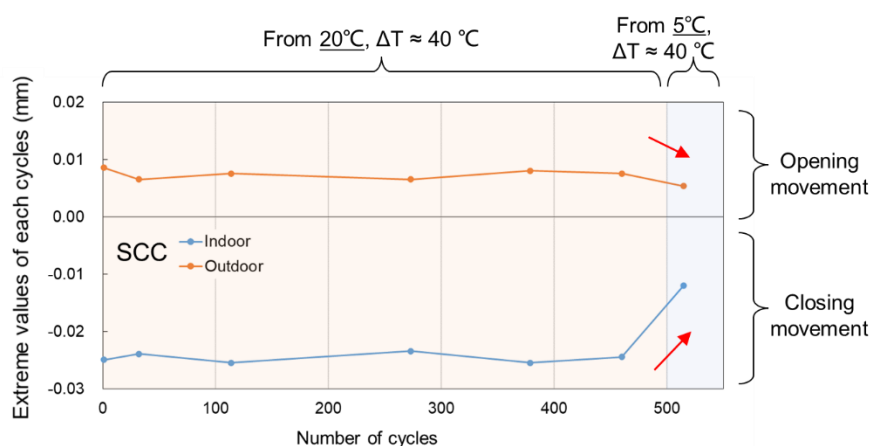As discussed above, the through-thickness cracks show different movement patterns after repair under different repair solutions. The possible crack movements under the injection method, U-groove routing and sealing method and surface coating method are summarized in **Figure 4–34**. Among them, the injection method can produce multiple opening and closing patterns owing to the physical properties and temperature of the material, thus it is not indicated in the figure. In this section, numerical simulations of each of these movements are performed using finite element methods. In the simulation, the properties of each material are shown in **Table 4–11**. The mortar model was the same as in Chapter 3. The analysis system was the static-state thermal and static structural module. The initial temperature was 20 °C. The final temperature of the outdoor surface was 60 °C. The contact surfaces of the materials were all set to "bonded".

(a) Before repair

(b) Injection

(c) U-groove routing and sealing

(d) Surface coating
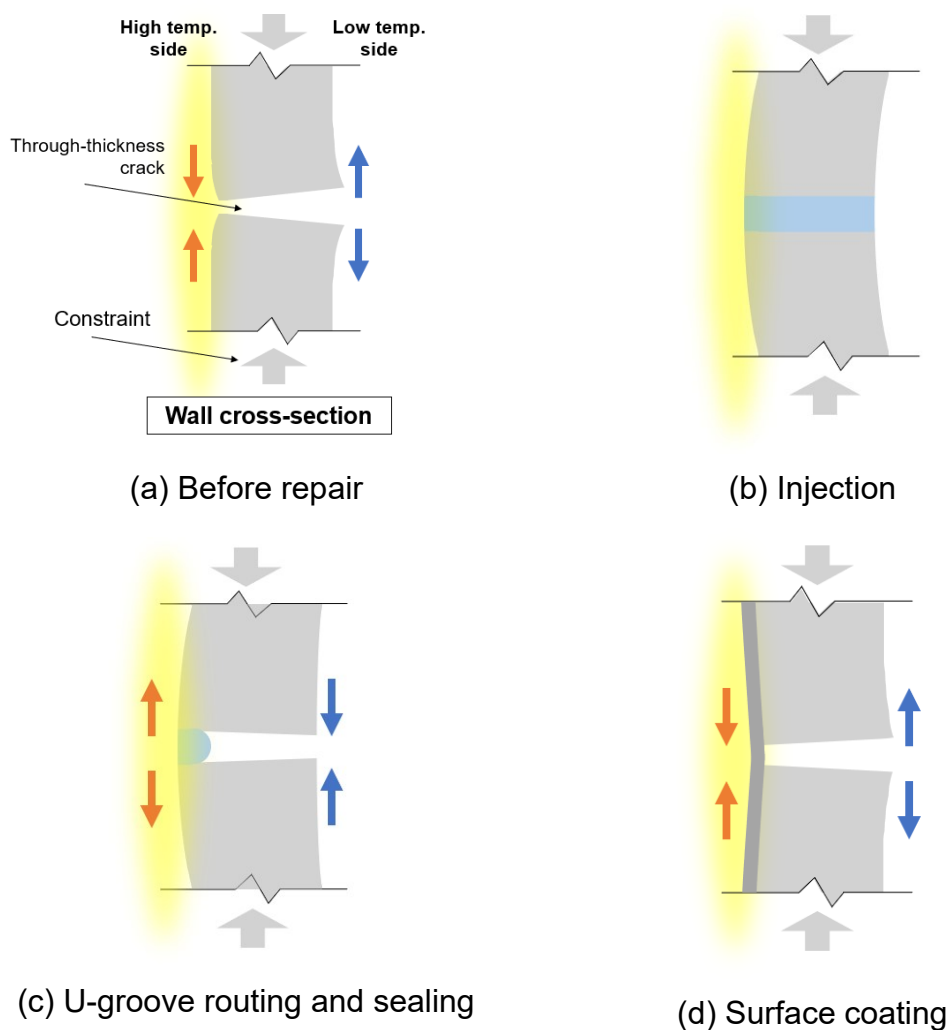
Figure 4–34 Possible crack movement under various repair solutions.

Table 4–11 Properties of materials in numerical simulation of crack movement after repair.

Property	Mortar	Threaded rod	Materials for injection	Epoxy resin for U-groove	Surface coating	Unit
Density	2100	7800	1850	1850	1300	kg/m³
Coefficient of thermal expansion	1.5E–05	1.2E–05	1E–05 ~ 1E–04	6E–05	6E–05	1/K
Young's modulus	2E+10	2E+11	1E+9 ~ 3E+10	5E+9	1E+8	Pa
Poisson's ratio	0.2	0.3	0.3	0.3	0.4	—

Isotropic thermal conductivity	1.51	60.5	0.2	0.2	0.2	W/(m·K)
Specific heat, C_p	700	434	1500	1500	1500	J/(kg·K)

(1) Injection method

Common materials used for injection methods are resin and cement type material. The main factors affecting crack movement include material type and temperature. Temperature affects crack movement by changing the coefficient of thermal expansion and Young's modulus of the material. Therefore, numerical simulations were performed in this section for five coefficients of thermal expansion and four Young's moduli of materials, as shown in **Table 4–12** and **Table 4–13**. Common cement and resin type material properties can be included.

Table 4–12 Coefficient of thermal expansion of injected materials for numerical simulation.

No.	1	2	3	4	5	Unit
Value	10	40	60	80	100	$\times 10^{-6}$ 1/K

Table 4–13 Young's modulus of injection material for numerical simulation.

No.	1	2	3	4	Unit
Value	1	5	15	30	GPa

The simulation results are discussed mainly around the opening and closing movement at the crack. As shown in **Figure 4–35**, an increase in the crack width after the temperature rise on the outdoor surface compared to the width before the rise indicates an opening movement, and vice versa. The results of the numerical simulation are shown in **Figure 4–36**. The different properties of the injection material do cause different opening and closing movements. For example, an injection material with a coefficient of thermal expansion of 10×10^{-6} /K and a Young's modulus of 30 GPa causes a closing movement of both indoor and outdoor cracks. As the coefficient of thermal expansion increases and the Young's modulus decreases, the cracks on both the indoor and outdoor surfaces may move in an opening movement. For epoxy resins, an increase in temperature means an increase in its coefficient of thermal expansion and a decrease in its Young's modulus. In this case, indoor cracks may change from closing to opening and outdoor cracks may change from opening to closing. This is also consistent with the conclusion in the previous section that changing the ambient temperature may change the crack movement pattern after repair.
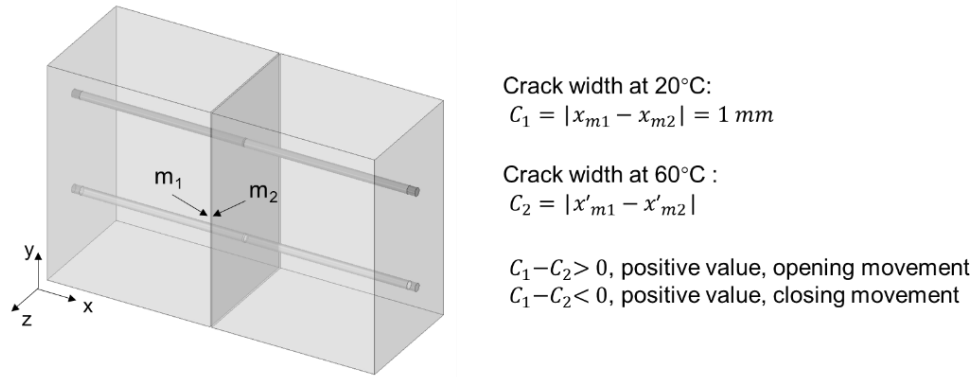
Crack width at 20°C:
$$C_1 = |x_{m1} - x_{m2}| = 1 \, mm$$

Crack width at 60°C :
$$C_2 = |x'_{m1} - x'_{m2}|$$

$C_1 - C_2 > 0$, positive value, opening movement
$C_1 - C_2 < 0$, positive value, closing movement

Figure 4–35 Crack opening and closing movement in numerical simulation.

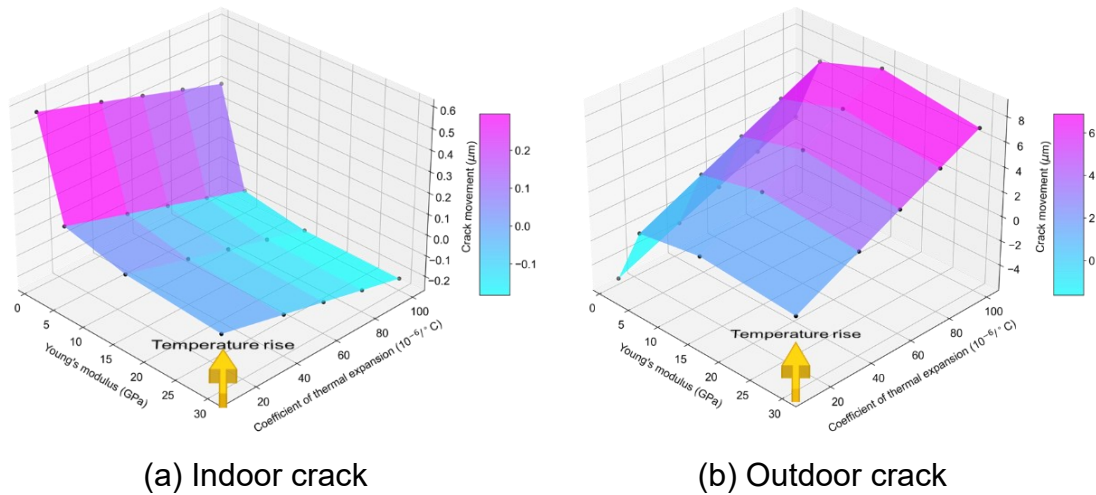(a) Indoor crack

(b) Outdoor crack

Figure 4–36 Possible crack movement in the injection method (positive values are opening, negative values are closing).

(2) U-groove routing and sealing method

The details of the simulation model of the U-groove method are shown in **Figure 4–37**. The deformation results in the X-direction are shown in **Figure 4–38**. After the repair, the indoor crack is closed by 0.058 mm and the outdoor crack is opened by 0.015 mm. This movement is caused mainly by the fact that the repair method fills only the outdoor side.
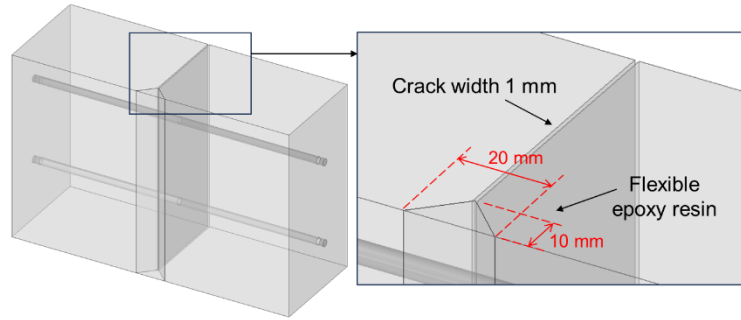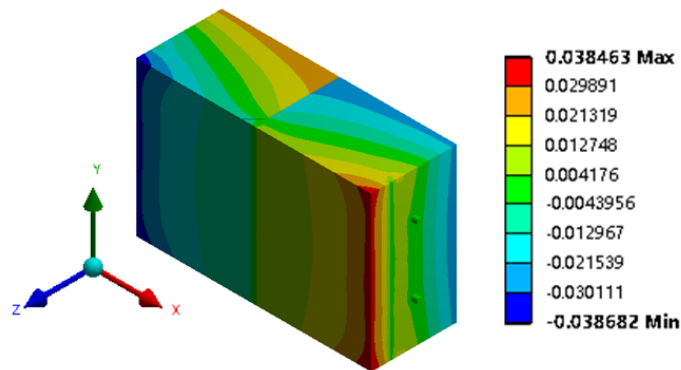
Figure 4–37 The details of the simulation model of the U-groove routing and sealing method.

(a) All bodies

(b) Indoor closing 0.058 mm (at crack)

(c) Outdoor opening 0.015 mm (at crack)

Figure 4–38 The deformation results of the U-groove routing and sealing method in the X-direction.

(3) Surface coating method

The details of the simulation model of the surface coating method are shown in **Figure 4–39**. The deformation results in the X-direction are shown in **Figure 4–40**. After the repair, the indoor crack is opened by 0.045 mm and the outdoor crack is closing by 0.079 mm. This movement is mainly owing to the fact that the Young's modulus of the coating is much smaller than that of the mortar.
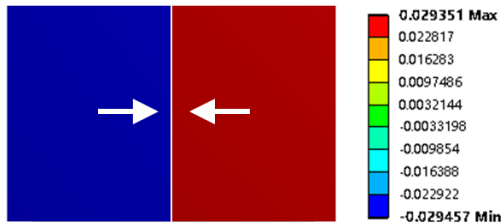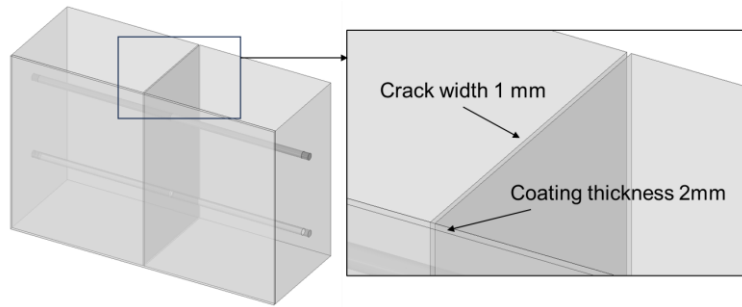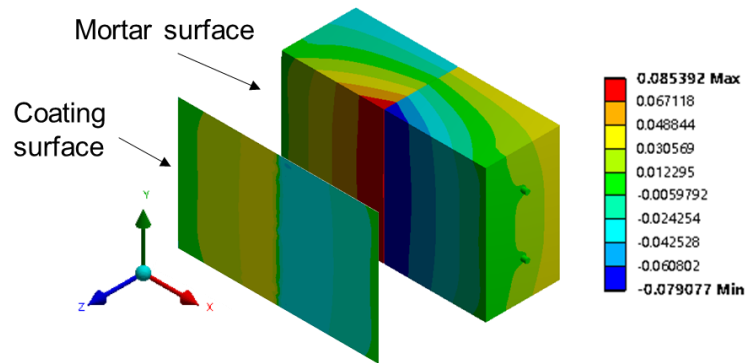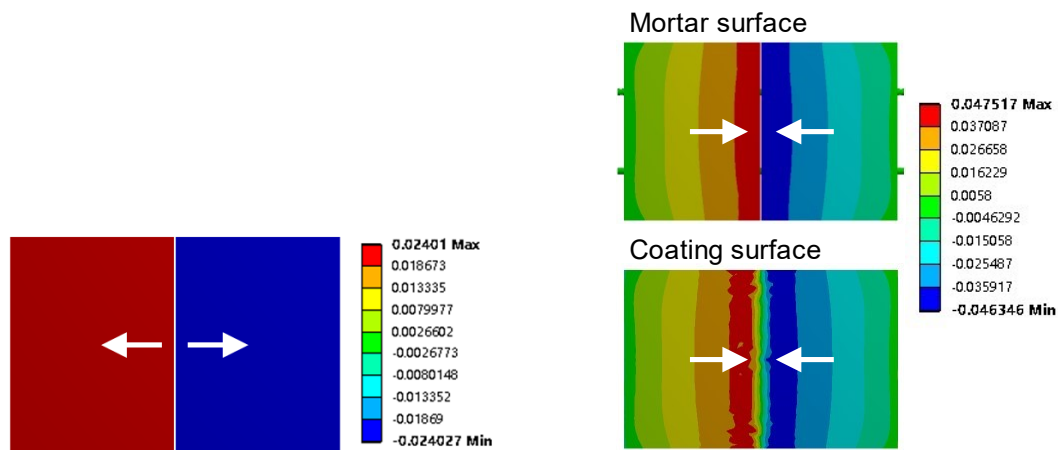
103

Figure 4–39 The details of the simulation model of the surface coating method.

(a) All bodies

(b) Indoor opening 0.045 mm (at crack)

(c) Outdoor closing 0.079 mm (at crack)

Figure 4–40 The deformation results of surface coating method in the X-direction.

104

4.3. Evaluation of repair solutions based on fatigue of bending-like movement

4.3.1.Materials and methods

(1) Repair solutions

Four common crack repair solutions were evaluated in this section, as shown in **Table 4–14**. Note that the materials used were the same as in the previous section.

Table 4–14 List of repair solutions for fatigue tests.

Notation	Method		Solution process	Photos
HE	Hard epoxy resin	Injection method	・ Surface preparation ・ Crack sealing ・ Epoxy preparation ・ Epoxy injection ・ Curing and drying ・ Finishing	
SE	Soft epoxy resin			
SCA	Waterborne Acrylic Waterproof Coating conforming to JIS A 6021	Surface coating method	・ Crack preparation ・ Surface priming ・ Crack bridging coating (In the case of SCB only) ・ Multiple coating application ・ Curing and drying	
SCB	SCA with crack bridging coating			

(2) Experimental settings

This experiment was performed using the fatigue apparatus presented in Chapter 3. The specimen setup is shown in **Figure 4–41**. The torque of each nut was controlled to 1 N·m using an adjustable wrench. A FLKB-6-11 strain gauge from Tokyo Measuring Instruments was attached to the center of the specimen. The strain limit was 5% (50,000 strain). The strain gauge bonding adhesive is CN-E adhesive from the same company. A T-type thermocouple was setup near the specimen for strain value calibration.
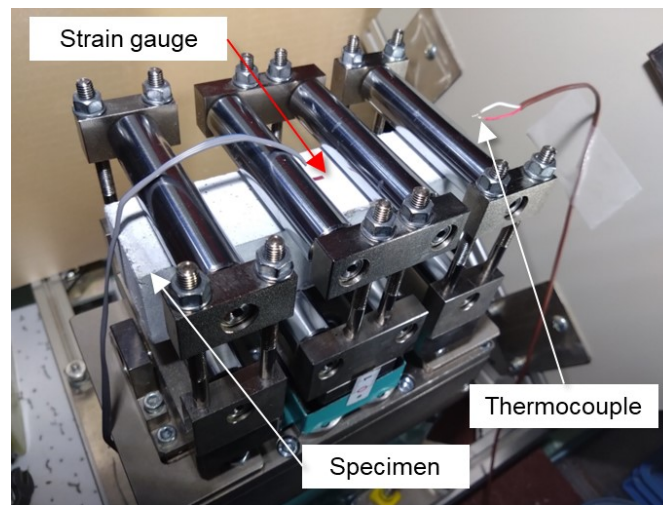
Figure 4–41 Experimental settings of fatigue test.

The concept of the experiment is shown in **Figure 4–42**. When the translational unit of the fatigue apparatus moves, the strain gauge monitors a waveform like a sine curve. The amplitude, length, and other information of the waveform can be used to evaluate the repair solution. Based on the previous test, the balance of specimen damage rate, strain gauge limit, and experimental time was considered, and the movement was set between ± 0.3 mm and ± 0.7 mm (Too small displacements do not deteriorate the specimen. Too large displacements result in a too high rate of specimen damage.), the duration of each cycle was set at 8 s, and the data recording interval was 1 s.
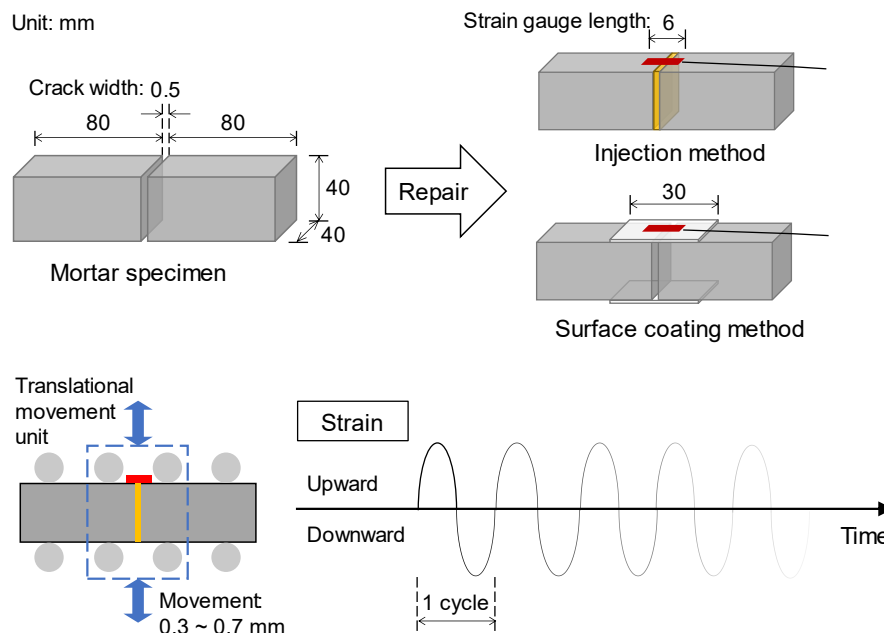
Figure 4–42 Conception of the experiment.

(3) Variables and numbers

In the experiment, the amplitude of the up and down shift of the middle part of the fatigue device was divided into three levels: 0.3 mm, 0,5 mm, and 0.7 mm. The experiments were conducted in a constant temperature and humidity chamber throughout. The humidity was adjusted to 50% RH. The temperature was divided into three levels: 5°C, 20°C and 35°C. This allowed for the evaluation of each repair solution with 9 different sets of variables. The notation of experimental specimens under each variable is shown in the **Table 4–15**. The damage condition of the specimens was recorded after each set of experiments. The relevant symbols used, and their representations are described in the **Table 4–16**. The basic number of specimens for each set of experiments is 5. However, depending on the damage, adjustments were made. The exact execution process is shown in the **Figure 4–43**.

Table 4–15 The notation of specimens under each variable.

Notation		5°C	20°C	35°C
Hard epoxy resin	0.3 mm	HE-5-0.3	HE-20-0.3	HE-35-0.3
	0.5 mm	HE-5-0.5	HE-20-0.5	HE-35-0.5
	0.7 mm	HE-5-0.7	HE-20-0.7	HE-35-0.7
Soft epoxy resin	0.3 mm	SE-5-0.3	SE-20-0.3	SE-35-0.3
	0.5 mm	SE-5-0.5	SE-20-0.5	SE-35-0.5
	0.7 mm	SE-5-0.7	SE-20-0.7	SE-35-0.7
Coating SCA	0.3 mm	SCA-5-0.3	SCA-20-0.3	SCA-35-0.3
	0.5 mm	SCA-5-0.5	SCA-20-0.5	SCA-35-0.5
	0.7 mm	SCA-5-0.7	SCA-20-0.7	SCA-35-0.7
Coating SCB	0.3 mm	SCB-5-0.3	SCB-20-0.3	SCB-35-0.3
	0.5 mm	SCB-5-0.5	SCB-20-0.5	SCB-35-0.5
	0.7 mm	SCB-5-0.7	SCB-20-0.7	SCB-35-0.7

Table 4–16 Symbols describing the damage of the specimen.

Symbol	Injection method	Surface coating method
○	Intact	Intact
△	—	Surface damage but no loss of function
×	broken	Hole damage
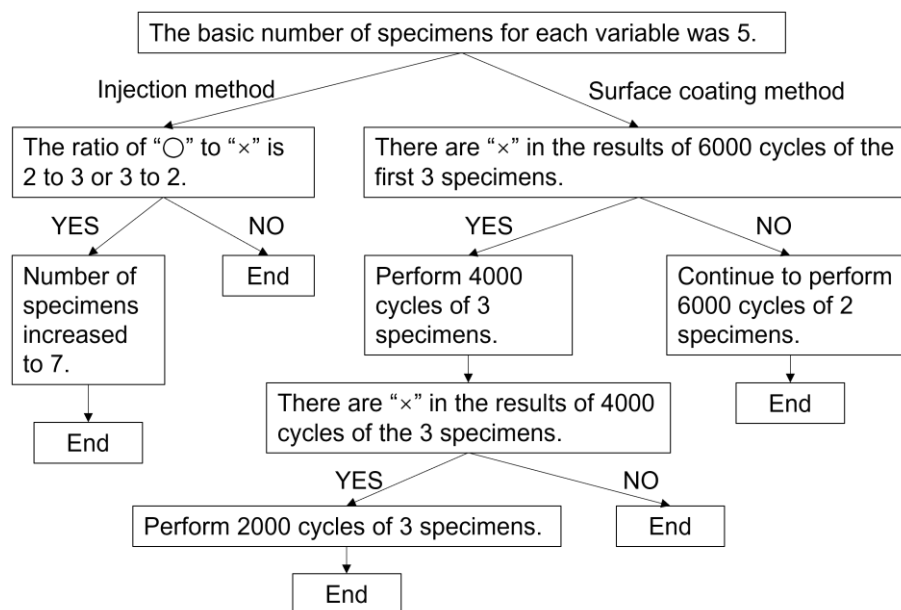
Figure 4–43 The approach flow for deciding the number of specimens.

4.3.2. Results and discussions

(1) Specimen damage results

The results of the experimental specimen damage are summarized in the **Table 4–17**. The damage rate of specimens for injection methods is summarized in **Figure 4–44** and **Figure 4–45**. The ratios in the figures are obtained by dividing the number of specimens with "×" and "○" by the total number of specimens, respectively. Notably, to ensure comparability, only the first five specimens of each group were used to calculate the ratio, i.e., the total number of specimens was 5. Moreover, the typical patterns of damage for each repair solution are shown in **Figure 4–46** through **Figure 4–49**.

Table 4–17 Specimen damage results.

		5°C	20°C	35°C
HE	0.3 mm	○○○○○	○○○○○	×××○○○○
	0.5 mm	×××○○○○	○×○○×○×	××○○×××
	0.7 mm	×××××	××××○	××○××
SE	0.3 mm	○○○○○	○○○○○	×○×○×○○
	0.5 mm	○○○○○	○○○○×	×××××
	0.7 mm	○×○○○	×○×××	×××××
SCA	0.3 mm	6000: ○○○○○	6000: ○○○○○	6000: ○△○○○
		2000: △△△		

	0.5 mm	4000: △×△	4000: △△△	
		6000: ×△×	6000: ×△△	6000: △△△△○
		2000: △△△	2000: ×△×	2000: ××△
	0.7 mm	4000: △××	4000: ×××	4000: ×××
		6000: ×××	6000: ×××	6000: ×××
	0.3 mm	○○○○○	○○○○○	○△○○○
SCB	0.5 mm	△△△△△	△△△△△	○○△△○
	0.7 mm	△△△△△	△△△△△	△△△△△

Note:	Symbol	Injection method	Surface coating method
	○	Intact	Intact
	△	—	Surface damage but no loss of function
	×	broken	Hole damage
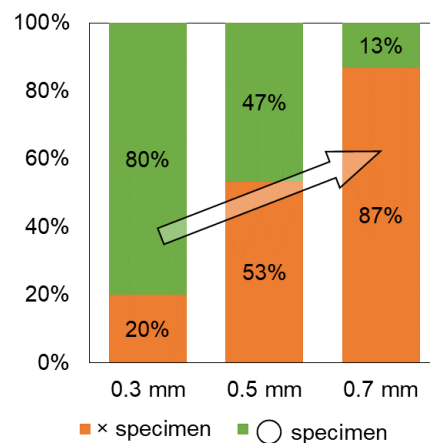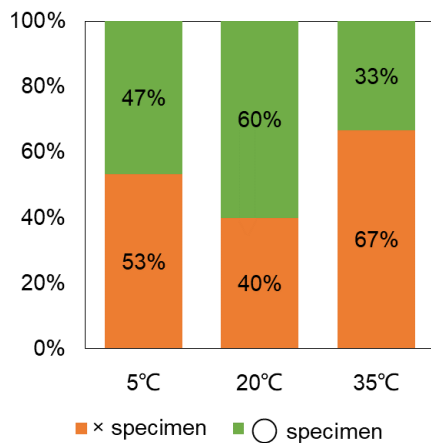
(a) Damage rate versus temperature

(b) Damage rate versus movement

Figure 4–44 HE specimen damage rate (The first five specimens were used for each group).
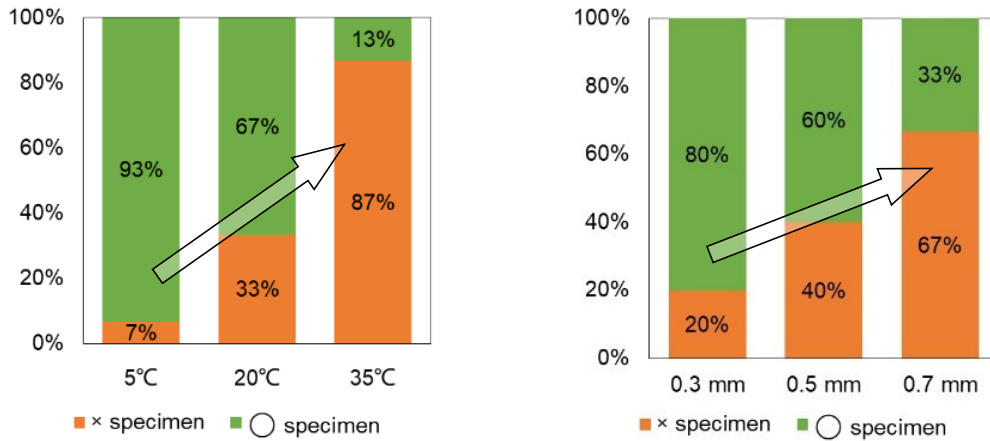
(a) Damage rate versus temperature   (b) Damage rate versus movement

Figure 4–45 SE specimen damage rate (The first five specimens were used for each group).

Figure 4–46 Typical damage pattern of HE specimens: Fracture.
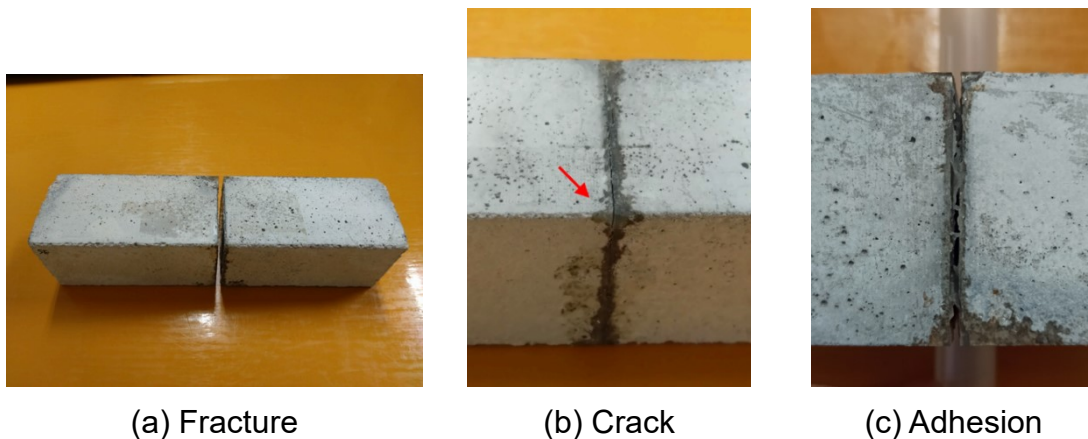
(a) Fracture   (b) Crack   (c) Adhesion

Figure 4–47 Typical damage patterns of SE specimens.

(a) Photo area

(b) Surface crack

(c) Hole damage

(d) Long hole damage
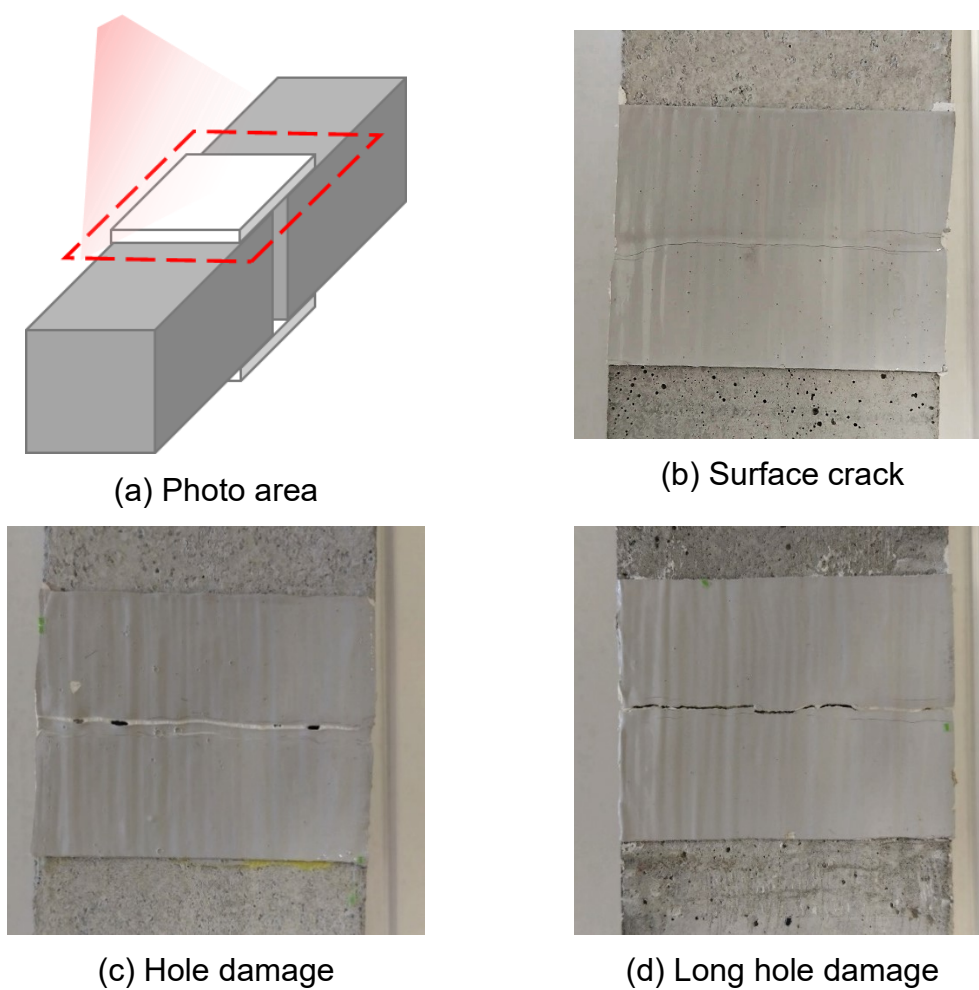
Figure 4–48 Typical damage patterns of SCA specimens.

(a) Surface crack

(b) Crack or peel along strain gauge

Figure 4–49 Typical damage patterns of SCB specimens.

For HE specimens, specimens at low temperatures and small movements were intact. However, when the ambient temperature increased to 35°C, even crack movements with a small movement of 0.3 mm could not be followed and nearly half of the broken specimens occurred. In addition, the relationship between HE specimen damage rate and temperature could be clarified in **Figure 4–44(a)**. However, the damage rate is positively correlated with movement in **Figure 4–44(b)**. The typical damage pattern of HE was fracture (**Figure 4–46**), independent of both temperature and movement conditions.

For SE specimens, the experimental groups in the low-temperature domain all had good resistance to movement fatigue. However, at 35°C, almost no specimens completed the full 6000 cycles. Similarly, it can be seen in **Figure 4–45** that the damage rate of SE specimens showed a significant positive correlation with both temperature and movement. The typical damage patterns of SE were fracture, crack and adhesion, which were mainly related to the temperature environment. Under low temperature environment, the SE material with high Young's modulus showed the same fracture damage as the HE specimens (**Figure 4–47(a)**). When the temperature increased, SE softened, and ductility became better. The damage process was no longer a brittle fracture but an accumulation of processes. With small movements, SE specimen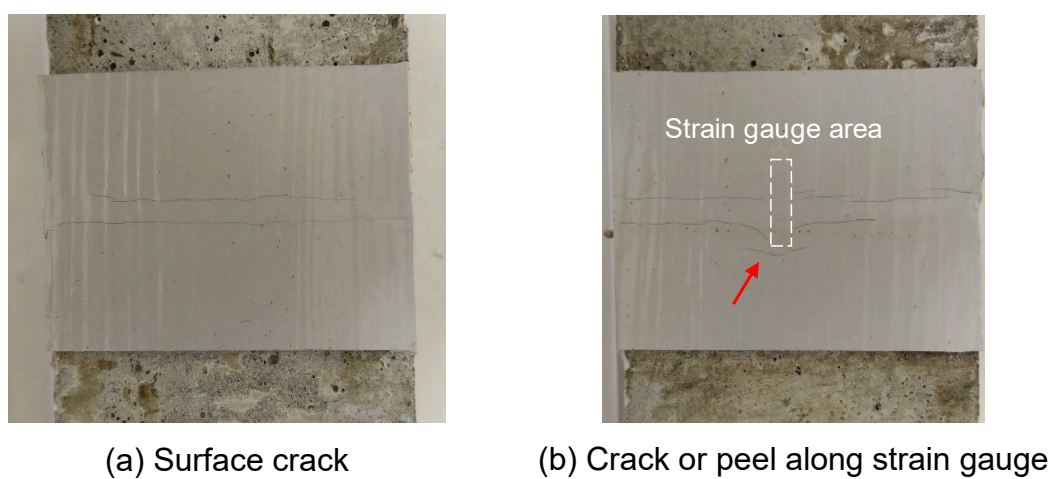s showed cracking as a damage pattern (**Figure 4–47(b)**). As the movement increased, the interlayer stress increased, and the crack depth intensified. However, the crack tip did not occur only at the mortar and epoxy interface but would penetrate the epoxy. Combined with the stickiness of the epoxy resin, the final pattern presented is cracked but adhered (**Figure 4–47(c)**). The specimens of this damage pattern maintained their integrity, but the cracks again allowed the intrusion of harmful substances. Therefore, it is a repair failure.

For SCA specimens, when the movement was 0.3 mm, the specimens showed good workability regardless of the temperature environment. This phase is presumed to be the elastic phase of the coating. However, as the movement increased, the damage rate of the specimens increased. At a movement of 0.5 mm, the external force may reach the yield strength of the coating, causing it to enter the damage phase. Therefore, the elongation properties of the material dominate the damage at this stage. The grip-to-grip elongation at break of the material at 5 °C is the smallest, thus the highest damage rate. Because low temperatures can cause the coating to transition from a cohesive and flexible material to a rigid and brittle one. Almost no specimens could resist fatigue for more than 4000 cycles when the movement was increased to 0.7 mm. The coating was pulled off beyond the necking period when the movement was 0.7 mm. The external force at this point is very likely to exceed the ultimate strength of the coating, thus the damage of the material is dominated by the tensile strength. At 5 °C the tensile strength of the coating is higher than that of the other two temperatures, hence the damage rate is lower. According to the severity, there were mainly three damage modes: surface crack, hole damage and long hole damage (**Figure 4–48**). The degree of damage was mainly correlated with the movement. The greater the movement, the more severe the damage. No correlation between damage

pattern and temperature was found.

For SCB, all specimens were undamaged or only surface damaged after 6000 cycles, therefore experiments with fewer cycles were not performed. In other words, SCB might be the best of the four repair solutions. It can maintain the effect of sealing cracks to stop the intrusion of harmful substances into the structure under all nine conditions. In addition, the intact rate of the specimens at 35°C was greater than the other two groups. The typical damage pattern of SCB specimens was surface cracks (**Figure 4–49(a)**). Although it affected the aesthetics, it could still maintain the sealing at the crack after 6000 cycles and was therefore considered as an effective repair. In addition, some specimens showed damage in the form of surface cracks or peeling along the strain gauges. This damage could cause the measured strain to be smaller than the true value. The treatment of this error will be described again at the amplitude results section.

Overall, for the injection repair solution, the fatigue resistance of the SE specimens may be better than that of the HE specimens, especially in the low-temperature domain. At high temperatures, injection repair solutions tend to fail prematurely. This may be caused by the fact that the Young's modulus of the resin becomes smaller, and the expansion coefficient becomes larger at higher temperatures, causing greater interlayer stresses. For surface coating method, For the surface coating method, it is not very sensitive to the temperature environment, i.e., it may be suitable for crack repair in many climates. Moreover, SCA can guarantee the repair effect during small movements. Additional crack bridging layer is required when the movement becomes large, i.e., SCB solution should be used to ensure the repair effect.

(2) Damage cycles results

The number of cycles when specimens undergo damage is plotted in **Figure 4–50**. For the injection method, information can be obtained from the value of the strain gauge when damage to the specimen occurs. This is because either cracks or fractures cause a sudden increase in the strain value. The cycle in which this value is located is then considered as the number of damage cycles. However, for the surface coating method, the damage cycle is not completely determined by the strain gauge data. This is because the deteriorated area was not necessarily covered by strain gauges. Moreover, both surface cracks and hole deterioration show large strains and cannot be distinguished from each other. Therefore, this section only discusses the damage cycle results of the injection method.
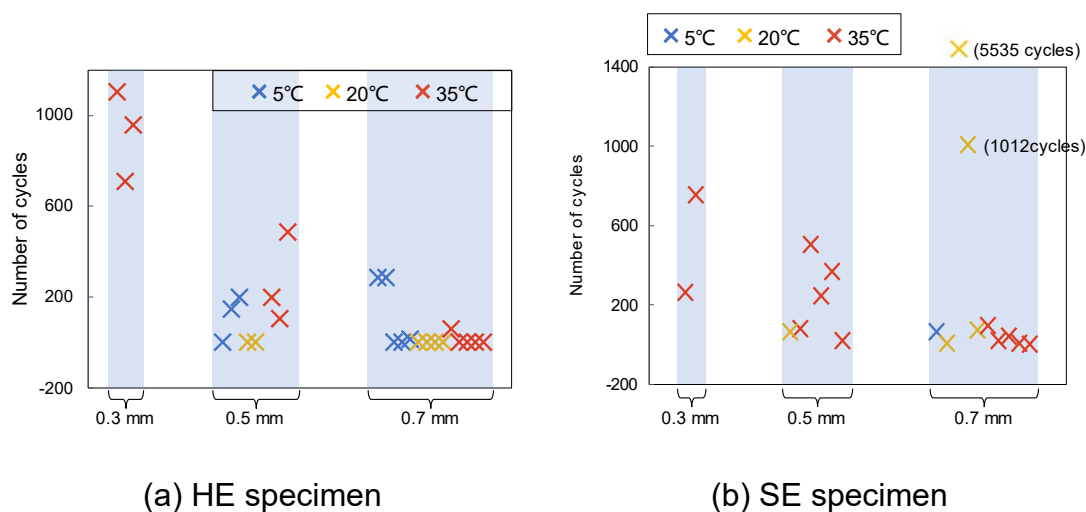
(a) HE specimen　　　　　　　(b) SE specimen

Figure 4–50 Number of cycles when the specimen damaged (The first five specimens were used for each group).

In **Figure 4–50**, each marked point represents a damaged specimen. The first five specimens were used for each group; thus, the blue block width can represent the number of damaged specimens under that movement. In **Figure 4–50(a)**, the number of damage cycles of HE specimens decreases as the movement increases. Moreover, the larger the movement, the more specimens are damaged. This indicates that movement not only causes high damage rate of specimens but also causes premature repair failure. In **Figure 4–50(b)**, no relationship between the number of damage cycles and the movement of SE specimens was found. However, SE specimens are sensitive to temperature based on the phenomenon that the number of red marks is the highest. An increase in temperature is very likely to lead to repair failure.

(3) Typical strain waveform results

The typical strain waveform results for an intact specimen of HE-20-0.7, for example, are shown in **Figure 4–51**. During the experiment, the parts with strain gauges were repeatedly tensioned and compressed. The intact specimens provided continuous fatigue resistance for a continuous 6000 cycles. However, there were only eight data collection points per cycle, thus there was a periodic failure to collect peaks. This showed up as a local variation of the extreme values in the waveform graph. Specifically, the difference between the maximum and minimum values of each cycle is defined as the amplitude. 6000 cycles result in 6000 amplitude values. In this example, the coefficient of variation of these 6000 amplitude values is 5.4%. In other words, the local miss-recording of extreme values is acceptable. In addition, all other intact specimens had an amplitude coefficient of variation of less than 7.0%.
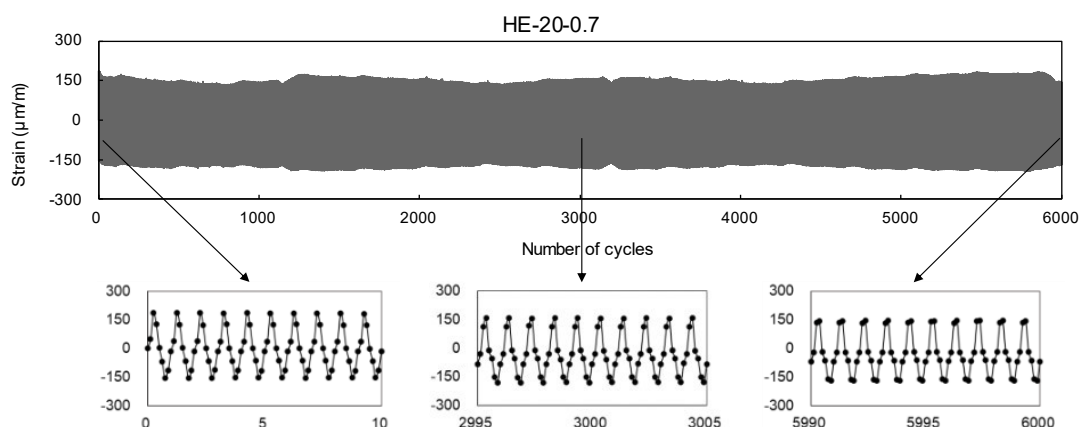
Figure 4–51 Typical strain waveform results of intact specimens (HE-20-0.7 as an example).

Taking HE-35-0.7 as an example, the typical strain results corresponding to the fracture occurring in the specimen are shown in **Figure 4–52**. Before fracture, the strain amplitude was almost constant for each cycle, but was shifted upward or downward (in this example, downward) overall. The direction might be random, as it depends on which part of the specimen is weaker, the upper or lower part. At the end of each cycle, residual strain was slowly accumulated in the weaker half. The specimen fractured when the absolute value of the strain was greater than the maximum value that the specimen could withstand.
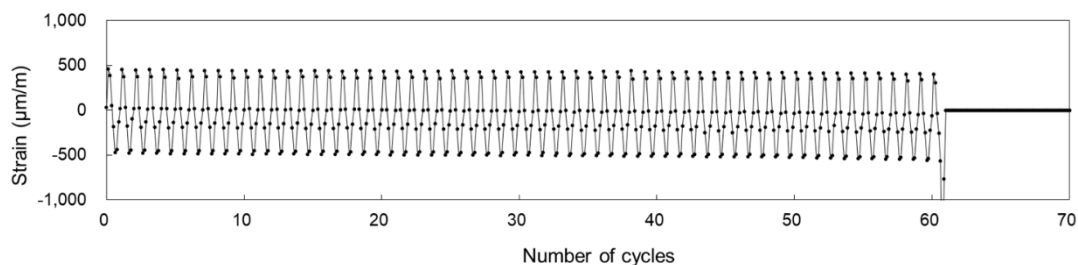
Figure 4–52 Fracture damage strain results of injection method specimen (HE-35-0.7 as an example).

Taking SE-20-0.7 as an example, the typical strain results when the SE specimen is not fractured are shown in **Figure 4–53**. In the figure, the strain amplitude is gradually getting larger for each cycle, indicating that the specimen is gradually losing resistance to movement fatigue. Although higher elongation of SE can follow the movement when the temperature increases, the loss of bonding properties leads to peeling of the resin-mortar interface. Moreover, the strain also tends to be shifted toward the weaker half side. In this example, the residue of the lower part is larger. The specimen was also cracked in the downward process when it was damaged.
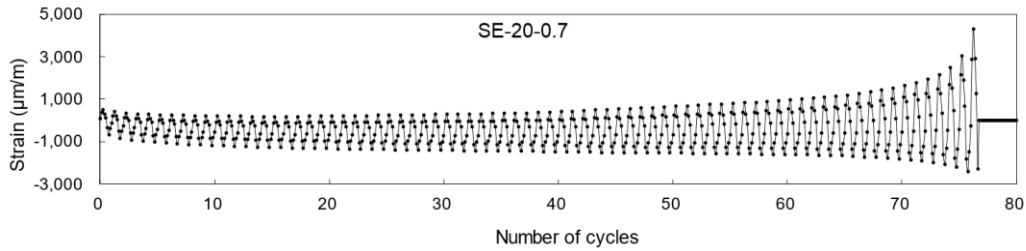
Figure 4–53 Typical strain results for SE specimens except for fracture (SE-20-0.7 as an example).

For the surface coating method, a typical strain waveform plot for a specimen that remains intact after fatigue cycles is of the same form as that of the injection method, which can be referred to in **Figure 4–51**. However, the strain waveform may differ from the injection method when the surface coating specimen deteriorates. Taking SCA-5-0.7 as an example, the typical strain when the surface coating specimen is cracked is shown in **Figure 4–54**. In the initial phase, the strain response of the coating had a decreasing phase before stabilizing. This may be explained that the bonding forces between molecules may change when repeatedly tensile and compressive, and the strain in the material accumulates inside the coating. Another factor contributing to the decrease could be the occurrence of deterioration, as this phenomenon occurred less in the experimental group with small movements. When the coating undergoes minor deterioration, the strain tends to concentrate near the point of deterioration, resulting in a smaller measured value of the strain gauge. As the number of cycles increases, the coating surface cracks and the strain increases significantly, even out of range. However, the degree of deterioration on the upper and lower surfaces of the specimens was not always identical and tended to accumulate on the weaker side. Strain gauges are only set on the upper surface. Therefore, it should be noted that the strain results cannot be used completely to judge the integrity of the specimen.
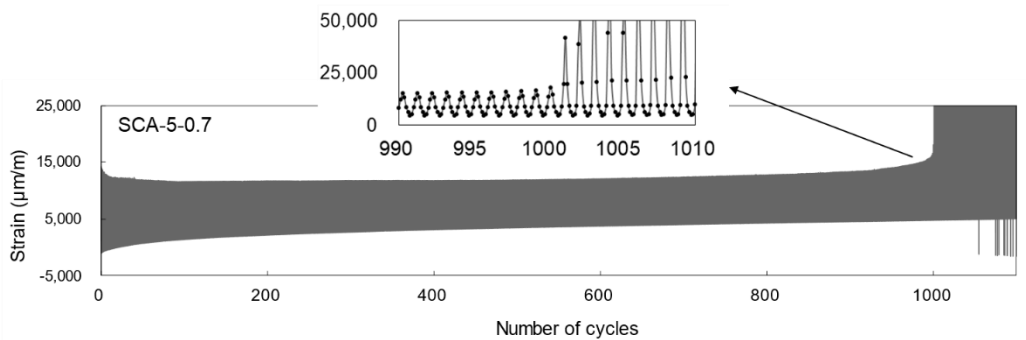

Figure 4–54 Typical strain waveform of surface coating specimens when cracking (SCA-5-0.7 as an example).

Furthermore, abnormal strain results can be caused when the degradation zone does not reach the strain gauge area. For example, in the case of **Figure 4–55**, the strain gauge adhesive locally reinforced the coating surface causing peeling along the edge of the strain gauge. For such strain results, we refer to strain amplitudes of intact specimens to select confidence intervals. As mentioned above, the strain amplitude coefficient of variation of 6000 cycles for intact specimens was below 7.0%. Therefore, for specimens with abnormal strain results, only the previous cycles with a coefficient of variation of less than 7.0% were intercepted and used for the average calculation.
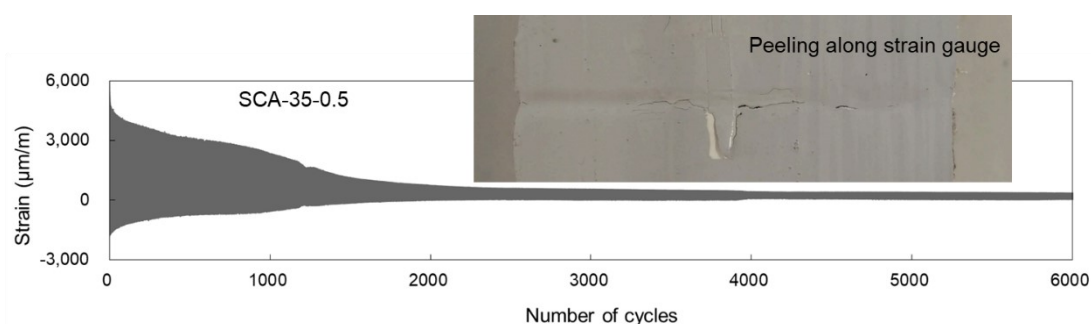
Figure 4–55 Strain waveform results of the coating peeling along the strain gauge (SCA-35-0.5 as an example).

(4) Amplitude results

The amplitude is the difference between the minimum and maximum strain values for each cycle. The results of strain amplitudes for all specimens are shown in **Figure 4–56**, **Figure 4–57**, **Figure 4–58**, and **Figure 4–59**. Notably, the amplitudes above 20,000 strains are not plotted in the figure, considering the performance of the strain gauges. The average values of strain amplitudes for each group of specimens are shown in **Figure 4–60**. The calculation procedure was to calculate the average value of amplitude for each specimen firstly. The intact specimens were averaged using the amplitudes of all cycles. Cracked, fractured such specimens were taken only a certain number of cycles preceding for average calculation. The selection criterion was to ensure that the coefficient of variation was less than 7.0%. Then, specimens with the same temperature and movement were the same experimental group, and these average values were averaged again within the group. The average and standard deviation obtained at the end are the values in **Figure 4–60**.

117

Figure 4–56 HE specimen strain amplitude results.
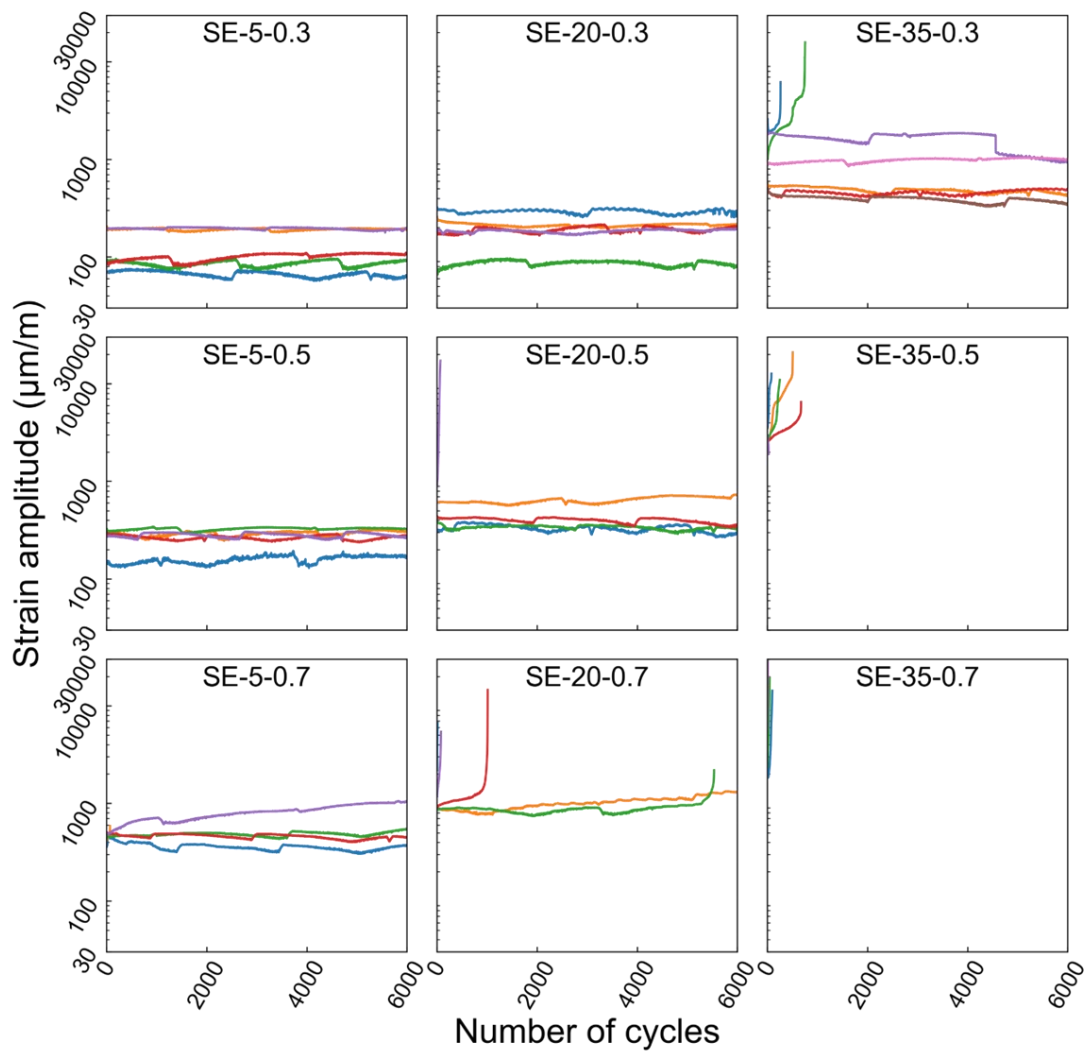
Figure 4–57 SE specimen strain amplitude results.
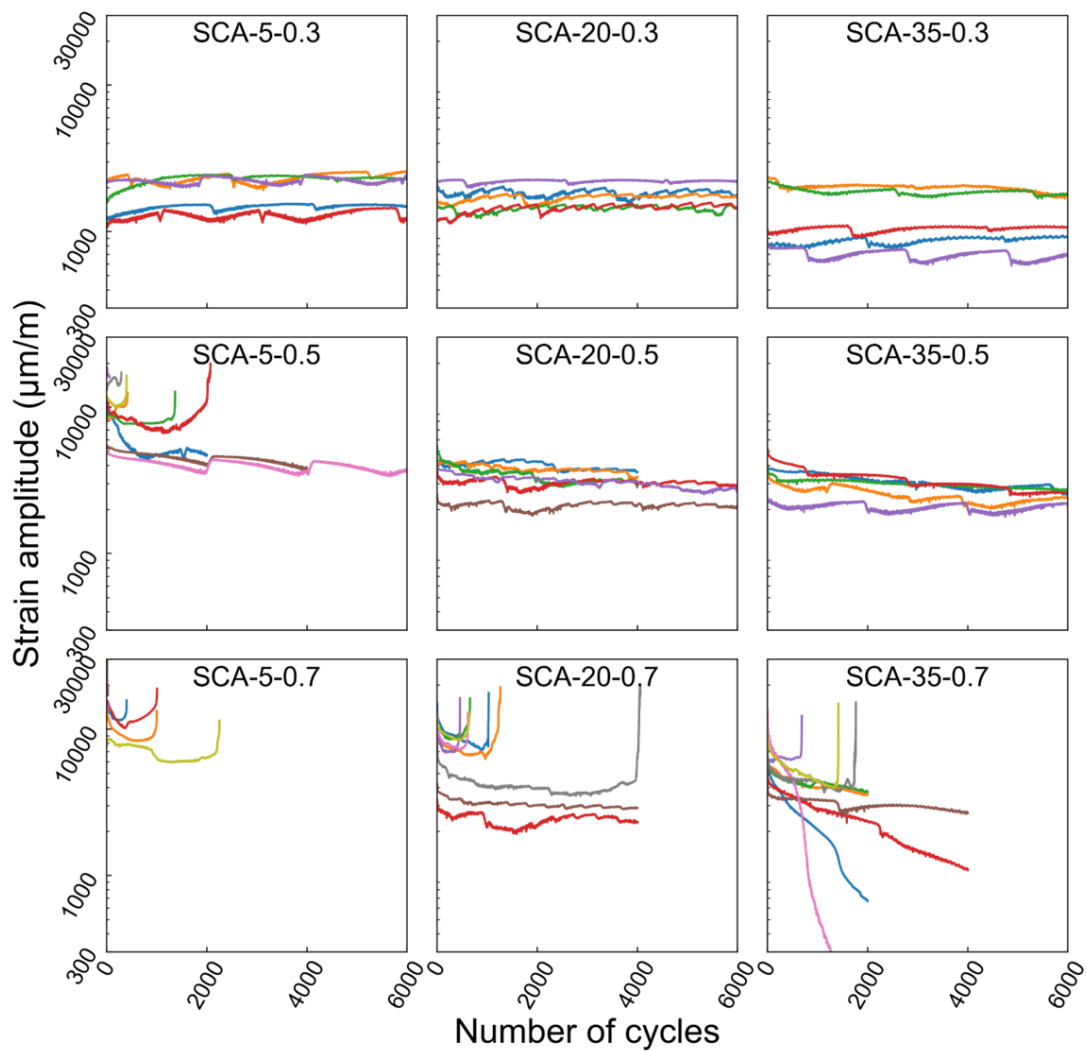
Figure 4–58 SCA specimen strain amplitude results.
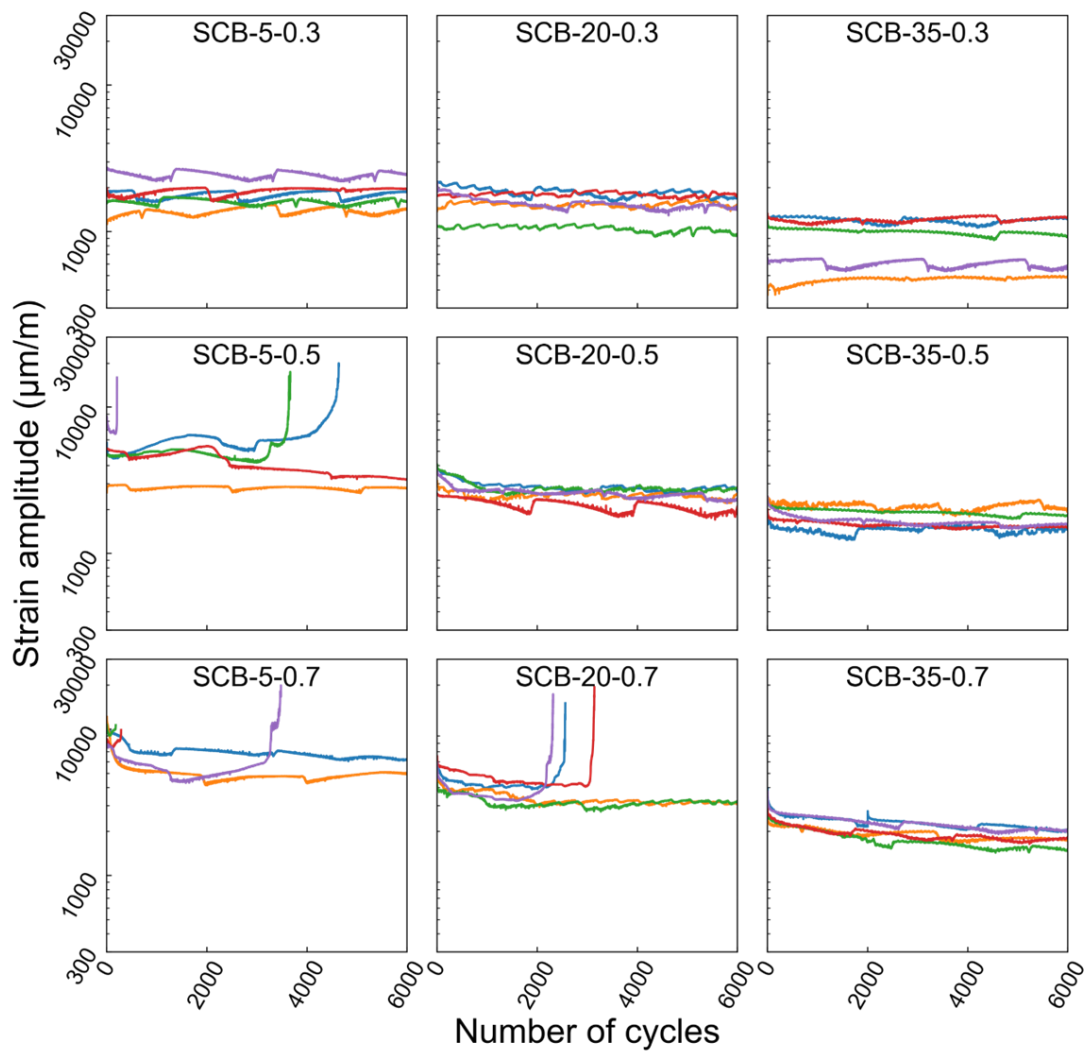
Figure 4–59 SCB specimen strain amplitude results.

(a) HE specimen

(b) SE specimen

(c) SCA specimen

(d) SCB specimen
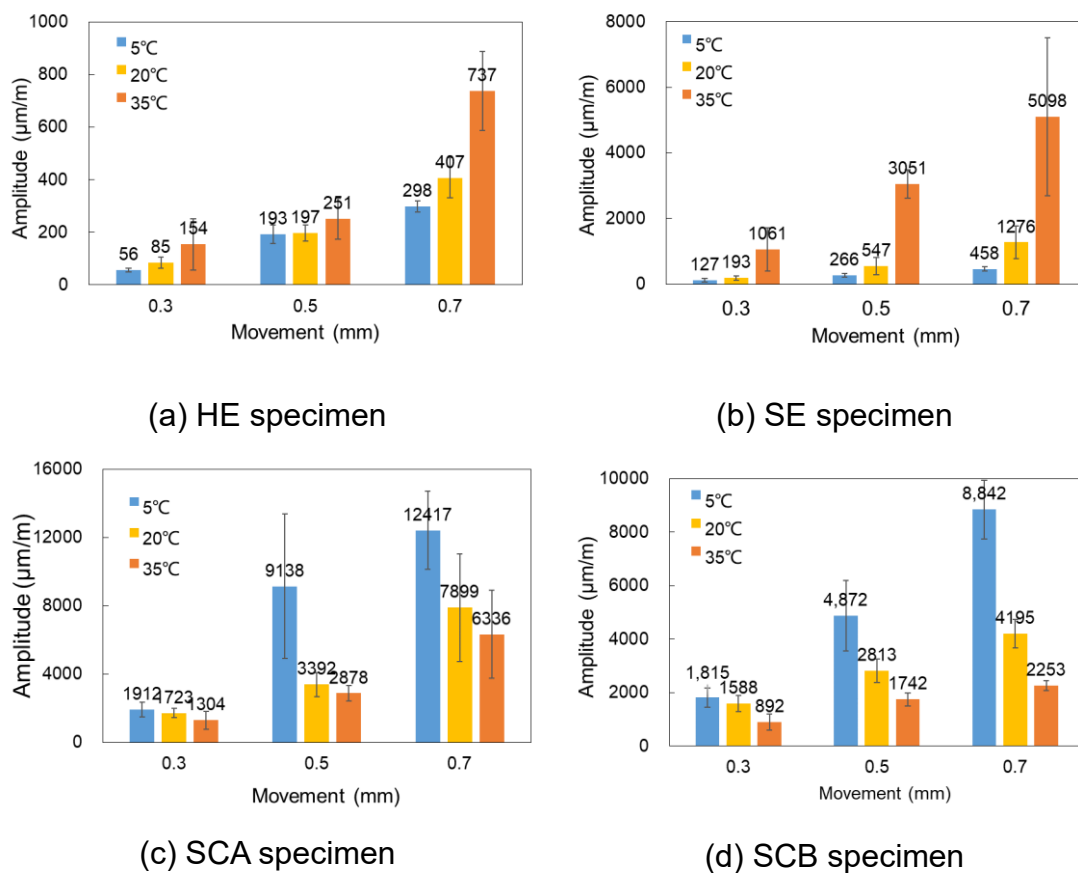
Figure 4–60 Average value of strain amplitude.

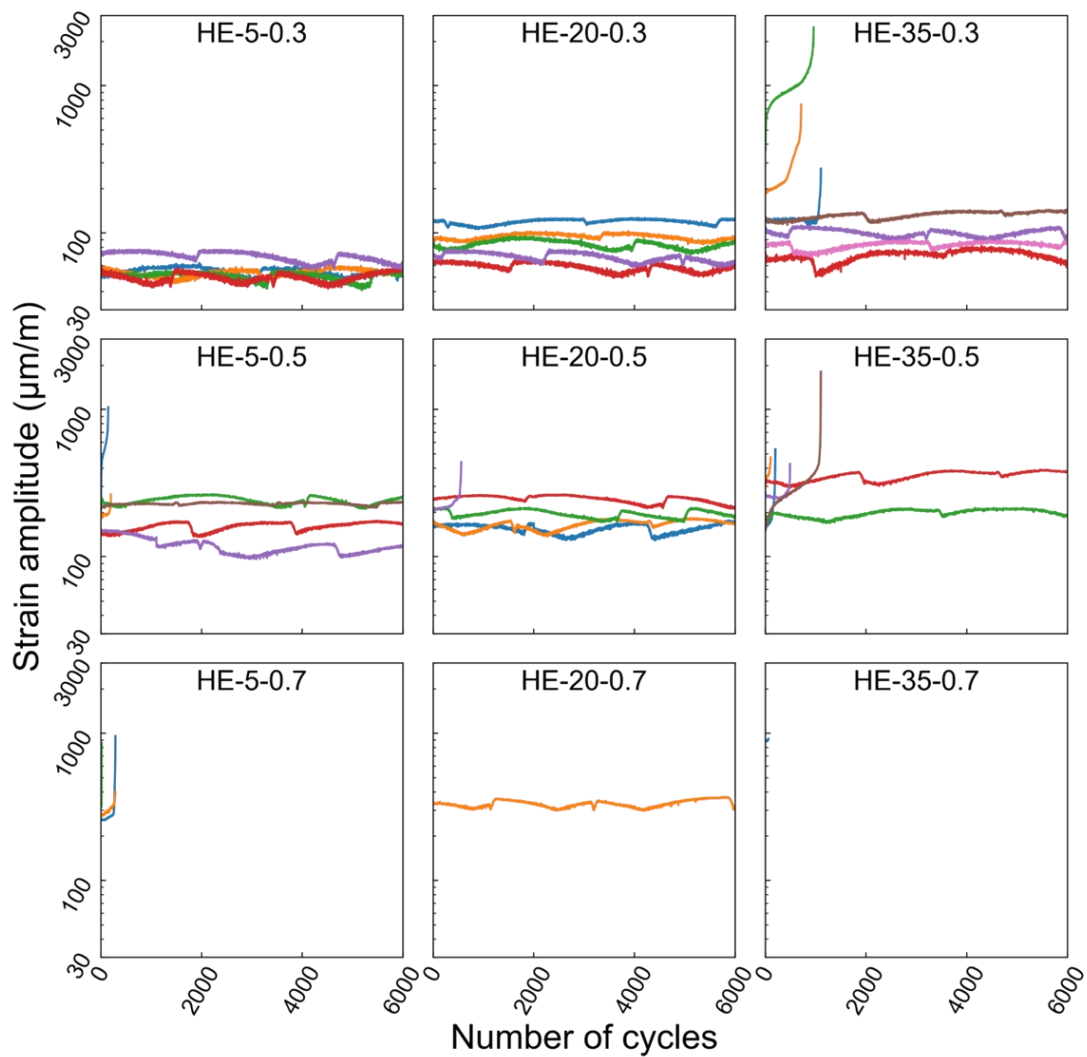For HE specimens, under the same movement conditions, the strain amplitude becomes larger as the temperature of the experimental environment increases. This can be explained that as temperature increases, the Young's modulus of HE becomes smaller and less able to resist the movement, thus tending to follow the movement and produce larger strain values. At the same temperature conditions, the greater the movement the greater the strain amplitude. And the specimens tend to fracture very early. (Referring to **Figure 4–50(a)**, all the HE specimens fractured before 61 cycles at 0.7 mm movement.)

For SE specimens, under the same movement conditions, the higher the temperature, the higher the amplitude, especially at 35°C. When the experimental ambient temperature is the same, the greater the movement the greater the amplitude. It is noted that almost all specimens in the 5°C-0.7 mm group could resist fatigue damage, but none of the specimens in the 35°C-0.7 mm group could. This indicates that SE is very sensitive to temperature during fatigue movements.

For SCA specimens, when the movement conditions are the same, the higher the temperature, the lower the strain amplitude, which is the opposite of the injection method. This may be caused by the strain gauges being set on the surface of the coating. The temperature rises, the thermal movement of

the molecules increases and the coating film softens. The movement at the bottom of the coating does not fully transfer to the surface layer, resulting in small strain measurements. In addition, the greater the movement at the same temperature, the greater the strain amplitude and the standard deviation of the amplitude becomes significantly larger. The reason is that the location of the coating degradation occurs randomly. Whether the position of the strain gauges of each specimen is covered within the degradation area causes intra-group errors. Moreover, the decreasing strain values in the SCA-35-0.7 group are caused by the peeling of the coating along the strain gauges.

For SCB, the trend of strain amplitude variation of the specimens is basically the same as that of SCA, except that the overall is smaller because SCB has an additional crack bridging coating than SCA. In addition, although there are also sharp increasing strain amplitude curves in the SCB group, these are only surface cracking degradation and not hole damage.

(5) Air leakage test results

The air leakage test method described in Chapter 3 can be used to quantitatively discriminate the harmfulness of cracks. In this experiment, air leakage experiments were performed on SCA-0.7 specimens to compare the deterioration of the specimens at each temperature condition. Data for the 30th s of the air leakage experiment were used for discussion, for which the β indicator was proposed. *β* values were calculated as follows:

$$\beta = \frac{P(t)}{P_0} \qquad\qquad (4-1)$$

where *P(t)* is the value of air pressure in the negative pressure chamber at time *t* in the unit of kPa. *p_0* is the value of air pressure in the negative pressure chamber at the initial moment in the unit of kPa. In this experiment, *t* was taken as 30 s, and *P_0* was approximately –60 kPa relative to the standard atmospheric pressure. A *β* value of 1 means that the air pressure remains unchanged for a certain time, i.e., there is no air leakage. A *β* value of 0 means that the air pressure returns to standard atmospheric pressure for a certain time. The smaller the *β* value, the higher the degree of deterioration.

The mean results of the specimens from the SCA-0.7 experimental group at each temperature and cycle condition are shown in **Figure 4–61**. In the figure, the higher the number of cycles, the higher the degree of deterioration of the specimens. Most of the specimens underwent hole deterioration under the movement of 0.7 mm, thus the tensile strength of the coating membrane dominated the degree of deterioration. The tensile strength of the coating is highest at 5°C, thus the degree of deterioration is probably the lightest. In the interval between 20°C and 35°C, the strength of the coating film does not change significantly, thus the degree of deterioration is also relatively close.
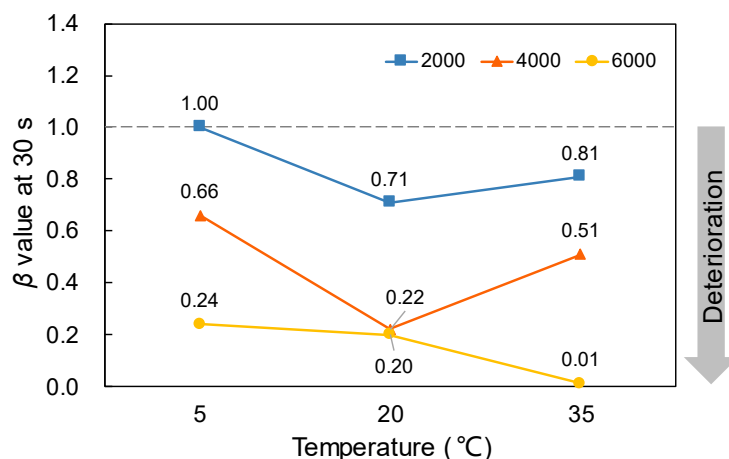
Figure 4–61 Average results of the SCA-0.7 experimental group at 30 s of the air leakage experiment.

4.4. Conclusions

The purpose of this Chapter 4 is to evaluate the durability of various repair methods under crack movement. The evaluation methods involved are the reproduction experimental method and the fatigue test method proposed in Chapter 3. The main conclusions are as follows:

1. In the reproduction experiments, when the injection method was applied, hard epoxy (HE) and polymer cement (PC) injection materials caused the repaired indoor and outdoor cracks to show a movement pattern that was both closed. In the case of soft resin (SE) with a smaller Young's modulus as the injection material and in the case of the U-groove routing sealing method (UC), the cracks were in reversed bending-like movement. When surface coatings A (SCA) and B (SCB) were applied, the crack movement pattern was not changed, i.e., it was still a bending-like movement. Surface coating C (SCC) caused a reverse bending-like movement similar to UC because it flowed inside the crack during the coating process. Moreover, the decrease in initial ambient temperature resulted in a decrease in the extreme values of movement for most specimens.

2. The repair solutions in the reproduction experiments maintained good durability for materials other than PC, and no signs of deterioration were observed during the tests. The PC specimen was likely to develop drying shrinkage cracks, which were worsened by thermal loading and movement cycles. The 30 s air leakage test result after 240 cycles was about 0.

3. Heat-flow sensors can be used to detect the defective parts of the wall. The heat-flow density at the cracks was less than at the mortar because the cracks were equivalent to a thin air insulation layer. After repair, epoxy, a repair material with less thermal conductivity than mortar, can also be detected. However, the data accuracy is not enough, thus a large number of samples is needed.

4. Numerical simulations demonstrated that different repair solutions in the reproduction experiments caused different movement patterns of the repaired cracks. For the injection method, changes in the coefficient of thermal expansion and Young's modulus of the material can cause various forms of crack movement. The U-groove routing and sealing method caused reverse bending-like movement probably because it was filled only on the outdoor side of the specimen. The surface coating method does not change the crack movement pattern because the coating has a very low Young's modulus relative to the mortar.

5. In the fatigue tests, brittle fracture occurred in all HE specimens, and the number of cycles at damage decreased with increasing temperature. The smallest strain at the crack was 56 for 0.3 mm movement at 5 °C. The largest strain at the crack was 737 for 0.7 mm movement at 35 °C. For SE specimens, the strain increased substantially with increasing temperature. The strains for all test groups ranged from 127 to 5098. At high temperatures, even though the elongation of SE was strong, the loss of adhesion still resulted in an extremely high rate of damage.

6. For the surface coating method in fatigue test, the SCA specimen could guarantee the repair effect when the movement of the apparatus was 0.3 mm. However, when the movement increased, SCA generated surface cracks and hole damage. As the temperature increased, the strain measured on the surface became smaller because the coating became softer, and the underlying motion was not transmitted to the surface. In addition, under small movements, the higher the elongation of the coating, the lower the damage rate. Under large movements, the tensile strength of the coating dominates the degree of damage, and the higher the strength, the lighter the deterioration. For SCB, crack repair is guaranteed at each temperature even with 0.7 mm movement.

7. The limitation of this chapter is the lack of measurement data of actual buildings and numerical simulations of full-size building models. In addition, the number of cycles and the apparatus movements in the fatigue test corresponding to the realistic situation are not clear. Furthermore, specimens with the surface left as cast are used to simulate cracks would underestimate the repair effect of the injection method.

Chapter 5

A simple test method for evaluating the thermal insulation performance of building envelopes

5.1. Purpose

Existing insulation performance evaluation methods may suffer from difficulties in equipment control and long testing time. To this end, a simple laboratory-scale method was designed in this chapter to evaluate the insulation performance of building elements. Two specimens of roof panels with different insulation levels were used. Static and dynamic heat-transfer experiments were conducted using an environmental simulation chamber and heat-flow sensor sensors. When the boundary conditions are the same, a larger absolute value of this heat-flow sensor means better insulation performance. The user can quickly compare the effectiveness of the insulation construction and the thermal transmittance value (U-value) of the building elements.

5.2. Materials and Methods

5.2.1. Environmental Simulation Chamber

The experiment involved in this chapter used an environmental simulation apparatus with independently controlled dual chambers, as shown in **Figure 5–1(a)**. The apparatus had effective insulation properties and a sensitive control system. Both chambers had the same dimensions: a width of 955 mm, height of 1100 mm, and depth of 1100 mm. The chambers were equipped with semi-enclosed environmentally controlled accessories, including sensors, blowers, and chillers. Aluminum alloy sheets formed the inner walls of the chambers. The temperature of the outdoor chamber could be controlled in the range of −20 to 40 °C, and its relative humidity could be controlled from 40% to 90%. The outdoor chamber was also equipped with an infrared lamp-based radiant heating function and a simulated precipitation function. The controllable temperature range of the indoor chamber was 4 °C to 40 °C, and the relative humidity ranged from 40% to 90%. The experimental setup is illustrated in **Figure 5–1(b)**.

(a) appearance of the simulation chamber

(b) heat-transfer experimental setup
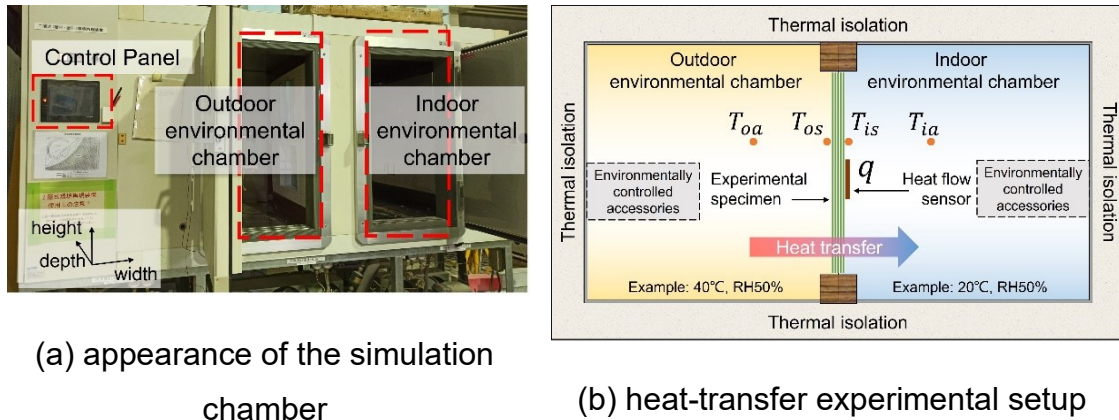
Figure 5–1 Environmental simulation chamber.

5.2.2. Heat-Flow Sensors

Details pertaining to the heat-flow sensors used in the experiments are listed in **Table 5–1**. The surface temperatures and heat-flow densities were measured by connecting a heat-flow sensor to the surface of the specimens. A specialized thermally conductive double-sided adhesive tape was used to attach the sensors while preventing the adherence of foreign objects or the formation of air layers. In addition to the increase or decrease in temperatures, the heat-flow sensors also measured the direction of heat transfer. As depicted in **Figure 5–2**, the measured value was positive when the heat-flow sensor was placed on the low-temperature side and negative when it was placed on the high-temperature side. The smaller the absolute value of the heat-flow density, the better the insulation performance of the test specimen.

Figure 5–2 Heat-flow sensor usage.

Table 5–1 Heat-flow sensor specifications.

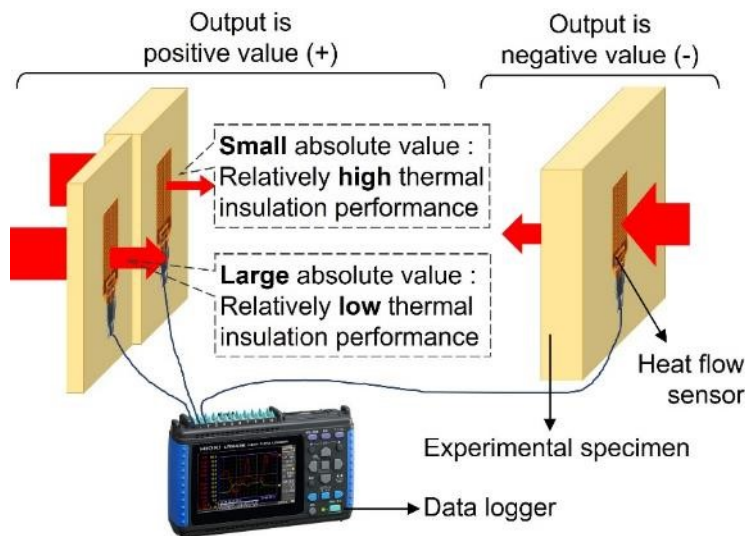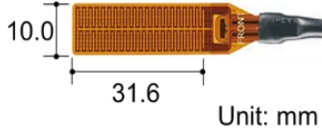| Heat-flow sensor dimensions (Approx.) Width = 10.0 mm	Width = 10.0 mm	Heat-Flow Sensor
	Length = 31.6 mm	
	Thickness = 0.25 mm	
Typical sensitivity	0.04 mV/W·m^{-2}	
Operating temperature	−40 ℃ to 150 ℃	
Liquid ingress protection (Except tip)	IP06, IP07 (EN60529)	
Internal resistance (Incl. cable)	3 Ω to 1000 Ω	
Min. curvature radius	30 mm	
Compression strength	4 MPa	
Thermal resistance	1.3 × 10^{-3} (m^2·K/W)	
Repeatable precision	± 2%	
Responsivity	Up to 0.4 s	

5.3. Two patterns of Heat-Transfer Performance Experiment

5.3.1.Experimental Specimen

The specimens used in the experiment had a width of 765 mm and height of 800 mm. The specimens were prepared using 0.8 mm-thick metal slabs as the substrates to simulate factory roofs, as illustrated in **Figure 5–3**. To mount the specimen slabs in the environmental simulation chamber, they were fitted using 30 mm × 45 mm foam frame strips. Therefore, in the experiment, the actual working area of the specimen had a width of 710 mm and height of 675 mm. Only a silicone acrylic coating was applied to specimen A1, as indicated in **Table 5–2**, whereas specimen A2 was subjected to a waterproof coating and a heat insulation layer.
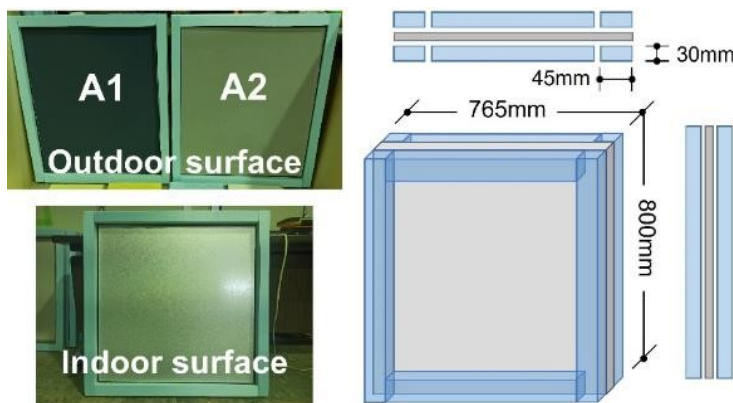

Figure 5–3 Metal substrate experimental specimens.

Table 5–2 Details of the metal substrate experimental specimens.

Specimen		Details of each layer
A1	Outdoor	1 kg silicone acrylic coating
		0.8 mm metal roof panel
	Indoor	
A2	Outdoor	1 kg silicone acrylic coating
		10 mm sprayed polyurethane foam
	Indoor	0.8 mm metal roof panel

5.3.2. Heat-Transfer Procedure and Setup

The heat-transfer process is shown in **Figure 5–4**. In **Figure 5–4(a)**, heat-transfer Pattern 1 simulates static heat transfer. At the beginning, the temperatures of both the outdoor and indoor chambers were set to 20 °C. The temperature of the indoor chamber was then held constant, and the outdoor chamber temperature was raised to 40 °C within the shortest possible duration. Over the next 10 h, a temperature difference of 20 °C was maintained between the two chambers. This temperature difference was large enough to reliably estimate the heat-transfer performance of the components. In **Figure 5–4(b)**, heat-transfer Pattern 2 simulated a dynamic heat transfer. The temperatures of the outdoor chamber and the indoor chamber were set to 40 °C and 20 °C, respectively. After reaching the balanced state, the power to the indoor chamber was individually turned off. This can simulate the situation of turning off the indoor air conditioner in real summer life. The temperature change in the indoor chamber was recorded while the outdoor temperature was maintained at 40 °C. A small air-circulation fan was used to minimize the air temperature differential in the indoor chamber after the power was turned off. However, as high-velocity winds can affect the results of heat-flow sensors, air was circulated in the chamber at a speed of less than 0.5 m/s. Further, data analysis was performed depending on the time at which the power was turned off. This was used as the initial time ($t = 0$). In addition, because the effect of humidity was not the focus of our discussion, the relative humidity of the chamber was set to 50% in all the experiments.
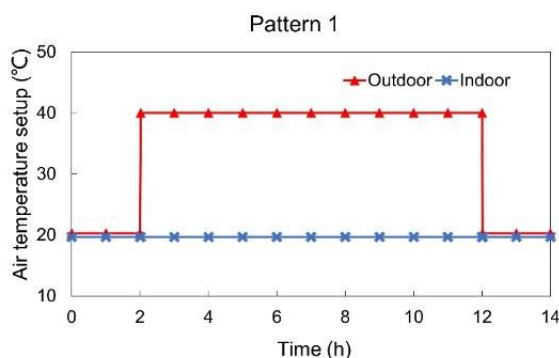
(a) Pattern 1 (static heat transfer)
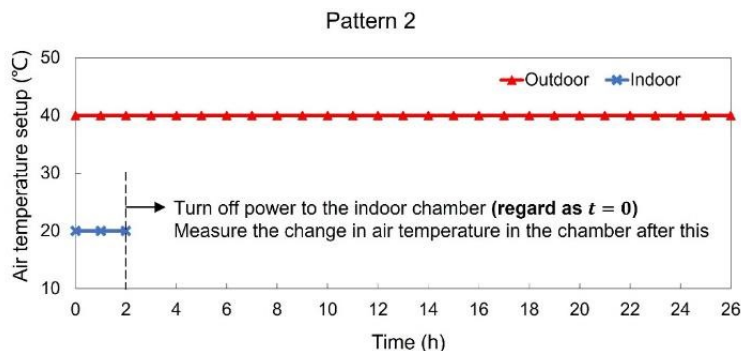
(b) Pattern 2 (dynamic heat transfer)

Figure 5–4 Air temperature settings for the environmental simulation chambers in the heat-transfer experiments.

During the experiments, data were recorded at 30 s intervals. In the preparation phase of the experiment, the positions of 10 heat-flow density and 29 temperature measurement points were calibrated (**Figure 5–5**). The results indicated that measurement points located at the geometric center could represent the average values of the corresponding space. Therefore, the measurement points for the heat-flow density and temperature in this experiment were set according to the configuration of black circles depicted in **Figure 5–5**.
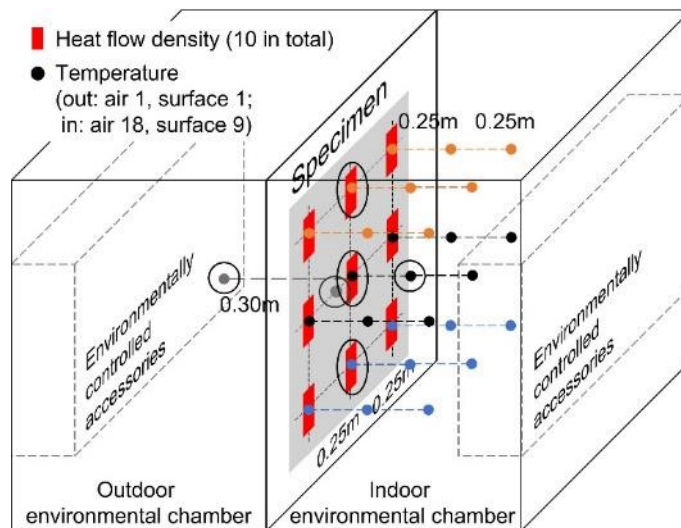
Figure 5–5 Settings of measurement points.

5.3.3. Results and Discussions

For heat-transfer Pattern 1, the results of the temperature and heat-flow density are shown in **Figure**

5–6 and **Figure 5–7**, respectively. The thermal transmittance (U-value) was calculated using **Equation (5–1)**:

$$U(t) = \frac{q(t)}{|T_{ia}(t) - T_{oa}(t)|} \qquad (5-1)$$
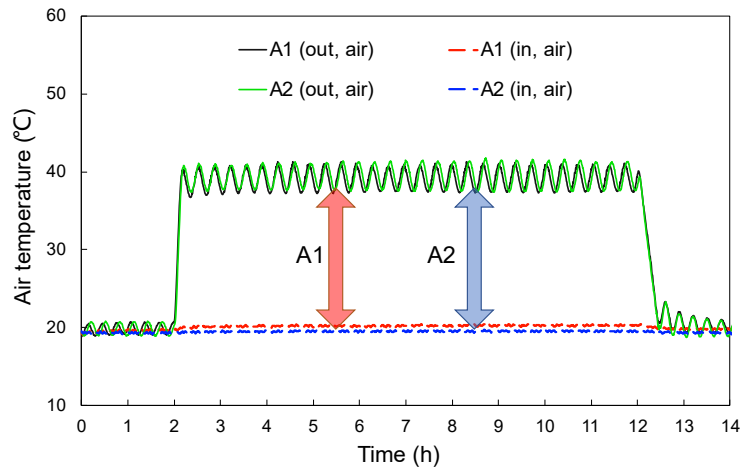
(a) Chamber air temperature results
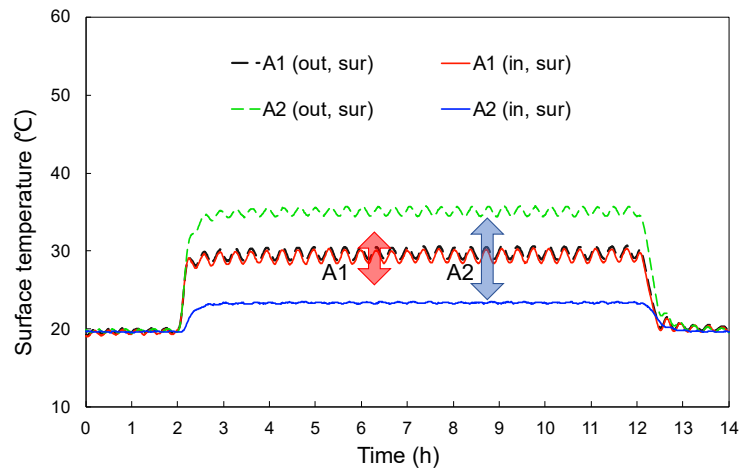
(b) Specimen surface temperature results

Figure 5–6 Temperature results for specimens A1 and A2 in heat-transfer Pattern 1.
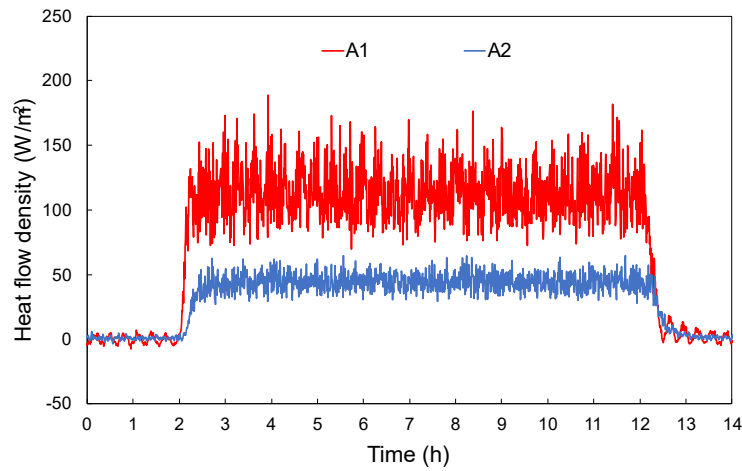
Figure 5–7 Heat-flow density results for specimens A1 and A2 in heat-transfer Pattern 1.

The results are shown in **Figure 5–8**. In **Equation (5–1)**, $U(t)$ and $q(t)$ indicate the U-value (W/(m^2 °C)) and heat-flow density (W/m^2) of the specimen, respectively. T_{oa} and T_{ia} denote air temperatures in the outdoor and indoor chambers, respectively. In heat-transfer Pattern 1, the middle 8 h, that is, 3–11 h of the experimental procedure, were considered to indicate a true steady state. The mean values and standard deviations (σ) of the experimental data for this period are listed in **Table 5–3**.
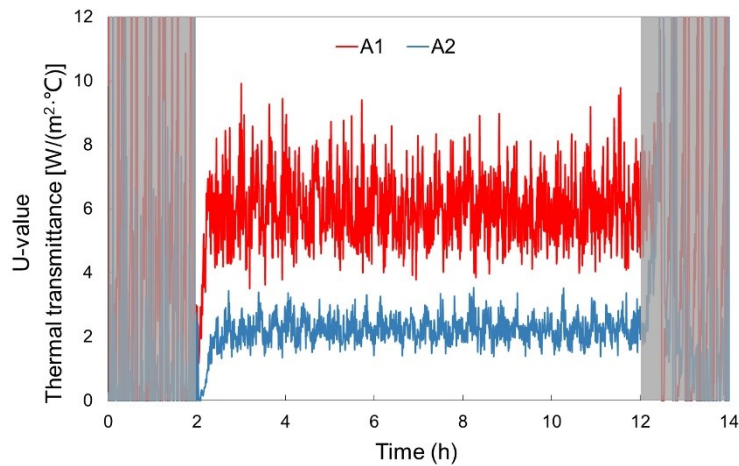
Figure 5–8 Thermal transmittance (U-value) results for specimens A1 and A2 in heat-transfer Pattern 1.

Table 5–3 Mean and standard deviations of the results for specimens A1 and A2 in heat-transfer Pattern 1.

Specimen	T_{oa} (σ) [°C]	T_{os} (σ) [°C]	T_{is} (σ) [°C]	T_{ia} (σ) [°C]	$\|T_{ia} - T_{oa}\|$ (σ) [°C]	$\|T_{is} - T_{os}\|$ (σ) [°C]	q (σ) [W/m^2]	U (σ) [W/(m^2·°C)]
A1	39.1	29.7	29.3	20.2	18.9	0.4	113.4	6.0
	(1.3)	(0.6)	(0.6)	(0.1)	(1.2)	(0.1)	(19.7)	(1.0)
A2	39.4	35.0	23.3	19.5	19.9	11.7	44.4	2.2
	(1.3)	(0.4)	(0.1)	(0.1)	(1.3)	(0.4)	(6.7)	(0.4)

In **Figure 5–6(a)**, during the first 2 h, the air temperature in both chambers was 20 °C, and almost no temperature difference was noted. Following this, the outdoor chamber temperature was set to increase rapidly while the indoor chamber temperature was maintained constant. During the heat-transfer process, the temperatures of both the indoor and outdoor chambers fluctuated around approximately 40 ± 2.2 and 20 ± 0.7 °C, respectively, which roughly satisfied the preset environmental conditions. In addition, the air temperature difference ($\|T_{ia} - T_{oa}\|$) for specimen A1 was approximately 1.0 °C greater than that for specimen A2. This difference could be explained by the poor insulation properties of specimen A1, which was extremely thin. As shown in **Figure 5–6(b)**, specimen A1 produced only a small difference between the indoor and outdoor surface temperatures ($\|T_{is} - T_{os}\|$), which was approximately 0.4 °C. In contrast, specimen A2 produced both a higher outdoor surface temperature ($T_{os} = 35.0$ °C) and lower indoor surface temperature ($T_{is} = 23.3$ °C). This difference in temperature between the two surfaces ($\|T_{is} - T_{os}\|$) of specimen A2 was significant at approximately 11.7 °C. This indicates that the application of an insulation material to a metal slab can effectively increase the thermal resistance of the element to achieve thermal insulation.

Figure 5–7 illustrates the heat-flow density results for heat-transfer Pattern 1. The corresponding data were acquired using the heat-flow sensor placed at the central position, as indicated in **Figure 5–5**. During the first 2 h, no heat transfer was noted, and the heat-flow density fluctuated around zero. After the first 2 h, the heat-flow density of specimen A1 rapidly increased to approximately 113.4 W/m^2. Conversely, the heat-flow density of specimen A2 increased at a slower rate and fluctuated at approximately 44.4 W/m^2. Thus, the insulating material reduced the heat transfer by more than half.

In **Figure 5–8**, which depicts the thermal transmittance results, the U-values fluctuated considerably for the 2 h during which almost no temperature difference was noted between the indoor and outdoor environments. Because heat transfer was almost absent during such periods, the data could not be used to calculate the U-values. During the middle 8 h of static heat transfer, specimen A1 exhibited a larger U-value of approximately 6.0 W/(m^2·°C). Under the same conditions, the U-value of specimen A2 was

significantly reduced at approximately 2.2 W/(m²·°C), and the thermal insulation performance of the element improved.

In heat-transfer Pattern 2, the time point ($t = 0$) at which the power to the indoor chamber was turned off, depicted in **Figure 5–4(b)**, was used as the starting point for data collection. The indoor surface heat-flow density and indoor chamber temperature results for the specimen are presented in **Figure 5–9**. Notably, because the wiring of the heat-flow sensor at the central position (**Figure 5–5**) had some flaws, the average values measured by the other two heat-flow sensors are presented here. Initially, the temperature difference between the indoor and outdoor chambers was the highest; thus, the heat transfer was the most intense. As the temperature difference decreased over time, heat transfer slowed. For specimen A1, the heat-flow density decreased rapidly from >100 W/m² to zero. After approximately 13 h, the chamber air temperature almost stopped increasing, implying the end of dynamic heat transfer. For specimen A2, the heat-transfer reduction process was slightly slower. The initial heat-flow density was about 50 W/m², which required about 24 h to gradually approach zero. A similar conclusion can be drawn from the temperature results, wherein, after 24 h, the dynamic heat-transfer process was almost complete. It is worth noting that, during the first 10 min, a rapid decrease in heat-flow density occurred. This could be attributed to the heating mechanism of the environmental simulation chamber. Note that the outdoor chamber temperature was not maintained constant at 40 °C but rather fluctuated in small ranges, and heating to target temperature was only reinitiated when the lower temperature limit of the system was reached. The decrease in heat-flow density was the combined result of a decrease in the outdoor chamber temperature and a reduction in heat transfer.
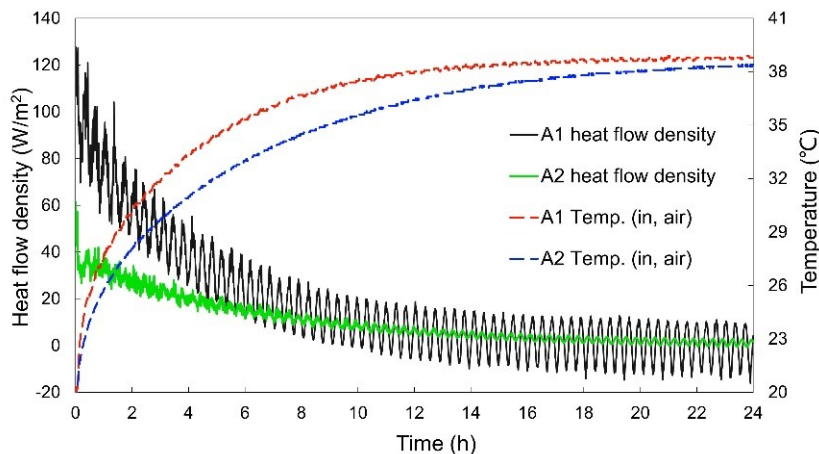
Figure 5–9 Results of specimen A1 and A2 for heat-transfer Pattern 2.

The relationship between the heat-flow density and air temperature difference at each moment for heat-transfer Pattern 2 is shown in **Figure 5–10**. A linear relationship with a coefficient of determination of 0.92 or more was obtained for both specimens. According to the implications of physical quantities of the data, the slope of the approximation curve denotes the U-value of the

specimen. Comparing these results with those of heat-transfer Pattern 1 (**Table 5–3**), it was observed that the U-values obtained for these two sets of experiments were almost the same. This indicates that the U-value of the specimen can also be obtained from this dynamic heat-transfer experiment.
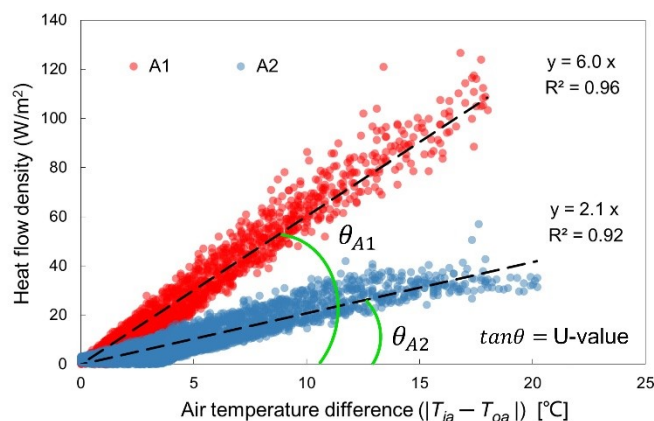

Figure 5–10 Relationship between the heat-flow density and temperature difference in heat-transfer Pattern 2.

5.4. Conclusions

In this chapter, a set of simple heat-transfer experiments was designed to evaluate the thermal insulation performance of building elements. The main conclusions of this chapter are as follows:

1. Using the environmental simulation chamber and the heat-flow sensor, two patterns of heat transfer experiments were designed in this chapter. Patterns 1 and 2 simulated steady-state heat transfer and dynamic heat transfer, respectively. The results showed that the thermal insulation performance of the experimental specimens could be determined by comparing the values measured by the heat-flow sensor under the same boundary conditions. The smaller absolute value of heat-flow density indicated the better thermal insulation performance.

2. In the steady-state heat transfer process with an ambient temperature difference of 20 °C, the difference between the indoor and outdoor surfaces of the metal roof panel specimen was only 0.4 °C, and the heat-flow density through the surface was 113.4 W/m^2. In contrast, the specimen with insulation increased this temperature difference to 11.7 °C and reduced the heat-flow value to 44.4 W/m^2. The insulation material achieved the function of heat insulation by increasing the temperature gradient inside itself.

3. In the dynamic heat-transfer, it was demonstrated that the thermal insulation performance of the experimental specimens could also be determined by the rate of change of heat-flow density. Moreover, the U-values obtained in the dynamic experiments were very close to the results of the previous static experiments, and it may be possible to reduce the U-values of the roof elements from 6 W/(m^2·°C) to about 2 W/(m^2·°C) by applying a thermal insulation layer.

Chapter 6

Thermal insulation method performance evaluation

6.1. Purpose

The purpose of this chapter was to establish a relationship between heat-flow values and temperature for evaluating the thermal insulation performance of building elements. To that end, static and dynamic heat-transfer experiments were conducted on two factory roof slab specimens using an environmental simulation chamber and heat-flow sensors. A relationship between heat-flow density and time has been established, and it can evaluate the insulation performance in the field in the case of using heat-flow sensors. Six simulation cases were analyzed by determining the relationship between the heat-flow density and temperature increase in an indoor space using a simple full-scale building model. In addition, the insulation performance of 14 experimental specimens was evaluated under steady-state heat-transfer conditions, including self-developed and commercially available insulation materials and construction methods for factory roof slabs.

6.2. Proposal for Simulating Building Thermal Insulation Performance

During the warmest seasons, improving the insulating performance of a roof can be highly effective in reducing the total energy penetrating a building. Notably, temperature is a better understood concept than heat. This is because temperature is a physical quantity that is commonly used by the public in their daily lives. However, the conversion of heat to temperature often requires specialized and complex models. This conversion is not conveniently achievable for owners with daily sensor usage. Therefore, in this section, we propose a relationship between the change in heat-flow density and time. This relationship can be used to help owners better establish a correlation between the heat-flow density and temperature when using heat-flow sensors by predicting the indoor temperature increase.

6.2.1. Simulation Formula for the Heat-Flow Density

Our proposal can be used to simulate a situation wherein the outdoor temperature is higher than the indoor temperature, as is often the case in summers. Notably, indoor temperature increases when cooling air conditioners in the building are turned off. The proposed method can roughly predict the heat-flow density in a building during this process. This corresponds exactly to the dynamic heat transfer described by Pattern 2 in Chapter 5. This proposal assumes that the variation law of heat-flow

136

density with time conforms to an exponential function. To simplify this model, we use only two variables, q_0 and α, as presented in **Equation (6–1)**:

$$q_{Simu.}(t) = q_0 \cdot e^{\alpha t} \qquad\qquad (6-1)$$

In this equation, q_0 denotes the average of several heat-flow densities obtained during static heat transfer. The data in Chapter 5 are referenced in this calculation; thus, the q_0 values for specimens A1 and A2 were 113.4 W/m^2 and 44.4 W/m^2, respectively. However, in case of field limitations, q_0 can also refer to the heat-flow density at any point when the air conditioner is turned off ($t = 0$). It should be noted that the calculated temperature result will be greater when the employed q_0 is larger than the actual average heat-flow density, and vice versa. The other symbol α is a dimensionless quantity that indicates the rate of heat-flow density change with time. The larger the absolute value of α, the faster the change in the heat-flow density. The α value is calculated inversely based on the time corresponding to the end of the heat-transfer process (t_{end}). According to the respective physical meanings, at moment t_{end}, $q(t)$ should be minimal. Because the exponential function can only be infinitely close to, but not equal to, zero, the value of $q_{simu.}(t_{end})$ is simplified to 1.0. Therefore, the formula for α is expressed by **Equation (6–2)**:

$$\alpha = \ln (1/q_0)/t_{end} \qquad\qquad (6-2)$$

According to Chapter 5, the approximate values of t_{end} for specimens A1 and A2 were considered as 13 and 24, respectively, as the temperature change of the corresponding experimental specimen in that hour was only 0.1 °C.

Subsequently, the rise in temperature was calculated. For dynamic heat transfer, the outdoor chamber temperature was held at approximately 40 °C after the power was turned off in the indoor chamber. The quantity of heat (Q) continuously penetrating the indoor chamber through the specimen was calculated using **Equation (6–3)**:

$$Q_{tot}(t) = \int_0^t q_{Simu.}(t)\, dt \cdot A \qquad\qquad (6-3)$$

where the area A had a heat inflow of approximately 0.048 m^2 in this experiment. During the heat-transfer process, the air, aluminum alloy inner wall, and other accessories in the indoor chamber were heated at the same rate. The relationship between the quantity of heat (Q) absorbed and the temperature increase (ΔT) is presented in **Equation (6–4)** and **Equation (6–5)**, respectively:

$$Q_a(t) = m_a \cdot c_a \cdot \Delta T(t) \qquad\qquad (6-4)$$

$$Q_{Al}(t) = m_{Al} \cdot c_{Al} \cdot \Delta T(t) \qquad\qquad (6-5)$$

where the air specifically refers to the air in the volume of the indoor chamber. The mass m_a and

specific heat capacity c_a of air were 1.40 kg and 1007 J/(kg·°C), respectively. The corresponding quantities for the aluminum alloy inner wall and environmental controlling accessories were estimated using the measurable surface area and thickness of the aluminum alloy. Thus, the m_{Al} and c_{Al} values were 25 kg and 900 J/(kg·°C), respectively. In addition, heat loss primarily comprised the loss caused by the chamber wall and the flanking loss of the specimen slab, which was calculated according to **Equation (6–6)**:

$$Q_l(t) = (1 - \eta) \cdot Q_{tot}(t) \qquad (6-6)$$

The smaller the specimen thickness, the greater the flanking loss, and the lower the heating efficiency [135][136]. The efficiency η values for specimens A1 and A2 were considered as constants with values of 85% and 95%, respectively. The heat-transfer process followed the law of conservation of energy with **Equation (6–7)**:

$$Q_{tot}(t) = Q_a(t) + Q_{Al}(t) + Q_l(t) \qquad (6-7)$$

and the temperature variation curve for the indoor chamber air could be obtained using **Equation (6–8)**:

$$T_{ia}(t) = T_{ia}(t = 0) + \Delta T(t) \qquad (6-8)$$

where the initial value of the indoor chamber air temperature (T_{ia} (t = 0)) was 20 °C.

The experimental data were plotted against the simulation results, as in **Figure 6–1**. To clearly present the data points, unlike in Chapter 5, the time interval for the experimental data scatter was decreased to one per hour. As can be seen, the trend of heat-flow density decreasing with time is well-fitted in **Figure 6–1**. For specimen A1, the fluctuations in the experimental data after 8 h were caused by high-frequency changes in the outdoor chamber temperature. However, this was an experiment-specific deviation that did not need to be filtered. Moreover, for the quantity of heat, this fluctuation did not have a significant effect on the indoor temperature change. Notably, the quantity of heat refers to the area between the heat-flow density curve and horizontal time axis curve. The temperature-change curve was determined using the simulated heat-flow density curve. This curve also exhibited a trend similar to that of the experimental data. This implies that the heat-flow simulation formula can be used to roughly estimate the rise in the indoor space temperature.
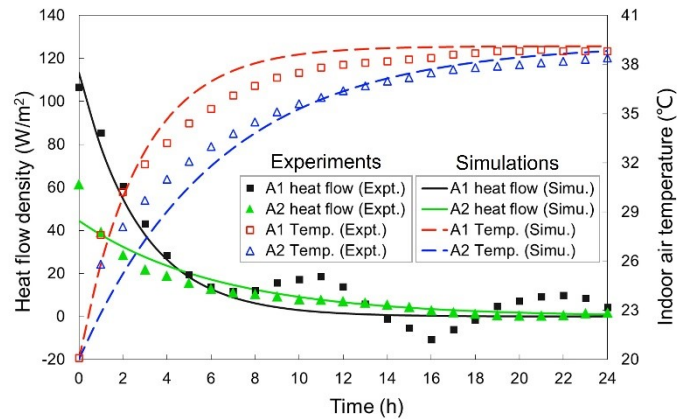
Figure 6–1 Comparison of experimental data with simulation results.

6.2.2.Simple Full-Scale Building Model

Further, in our analysis, simplified heat-transfer simulations were performed on a full-scale factory building model using **Equation (6–1)**. Note that the scope of the following discussion encompasses the heat-transfer process that occurs during summers. The initial state ($t = 0$) indicates the time at which the indoor air conditioner is turned off. Heat is continuously transferred from the outdoor environment to the indoor environment through roofs. The heat-transfer process is considered complete ($t = t_{end}$) when the indoor air temperature reaches the same level as the outdoor temperature. The dimensions of the adopted building model are depicted in **Figure 6–2**.
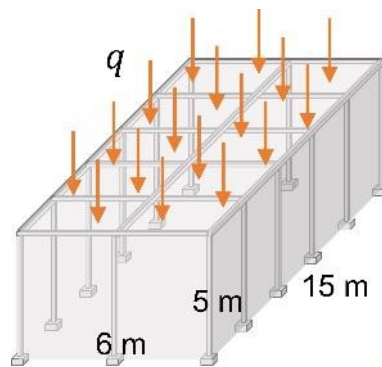

Figure 6–2 Factory building model.

Note that five cases are discussed in this section, and the corresponding details are listed in **Table 6–1**. In Cases 1 to 3, the roofs had the same thermal transmittance (1.0 W/m²·°C) and different initial indoor–outdoor temperature differences. The purpose was to discuss the effect of the initial indoor–outdoor temperature difference on the overall temperature rise. In Cases 3 to 5, the indoor–outdoor temperature difference was the same (15.0 °C), whereas the thermal transmittances of the roofs were varied. The purpose was to discuss the effect of the thermal transmittance of roofs on the indoor

temperature rise.

Table 6–1 Case details.

	Thermal transmittance ($U(t = 0)$) [W/m²·°C]	Temperature Difference ($|T_{ia}(t = 0) - T_{oa}(t = 0)|$) [°C]	Hear flow density ($q_0 = q(t = 0)$) [W/m²]
Case 1	1.0	5.0	5.0
Case 2	1.0	10.0	10.0
Case 3	1.0	15.0	15.0
Case 4	2.0	15.0	30.0
Case 5	0.5	15.0	7.5

The assumptions of the model calculations are presented below:

1. Only heat entering the building from the roof is considered;

2. In all cases, the effective quantity of heat (Q_e) entering the building within 24 h heats the indoor air to a preset outdoor air temperature;

3. The effective quantity of heat (Q_e) denotes the amount of heat used to heat the air, which is 30% of the total quantity of heat (Q_{tot}). The remaining heat is assumed to be absorbed by factory machinery or lost via ventilation.

The variation in the heat-flow density with time was obtained using **Equation (6–1)**. The q_0 value in each case was calculated according to **Equation (5–1)** in chapter 5 using the U-value and the indoor–outdoor temperature difference at $t = 0$. The α value was calculated inversely based on the end-time of the heat transfer (t_{end}) using **Equation (6–2)**. Here, t_{end} was determined according to the second assumption and was obtained, as shown in the following **Equation (6–9)**:

$$
\begin{cases}
Q_e(t = 24h) = m_a \cdot c_a \cdot \Delta T(t = t_{end}) \\
Q_e(t) = \eta \cdot Q_{tot}(t) \\
Q_{tot}(t) = \int_0^t q_{Simu.}(t) \, dt \cdot A \\
\Delta T(t = t_{end}) = |T_{ia}(t = 0) - T_{oa}(t = 0)|
\end{cases}
\tag{6 - 9}
$$

where the mass m_a and specific heat capacity c_a of air in the factory were assumed to be 541.8 kg and 1007 J/(kg·°C), respectively. The value of η was considered as 30% according to the third assumption. Here, the working area A refers to a roof area of 90 m².

The simulation results for the indoor temperature increase in 24 h (assumption 2) are illustrated in **Figure 6–3**. The data for the 6th h in the figure are labeled while considering the realistic duration of the high-temperature period during daytime. In **Figure 6–3(a)**, for the same insulation performance of the roof, the temperature difference between the indoor and outdoor environments plays a decisive

role in the level of indoor temperature rise. For equivalent time periods, the higher the initial temperature difference, the higher the increase in temperature. Particularly in the first few hours, the temperature in Case 1 increased by 9.9 °C at 6 h. **Figure 6–3(b)** indicates that the insulation performance of the roof exerted a significant effect on the temperature change in the building. Moreover, in the first few hours, the temperature in Case 4, which involved a relatively poor insulation (U = 2.0 W/m²·°C), increased rapidly. Thus, heat from the outside was quickly transferred to the building. Conversely, the temperature in Case 5, which had better insulation (U = 0.5 W/m²·°C), increased at a much slower and more uniform rate. At the 6th h, the temperature rise in Case 5 (6.5 °C) was less than half of that in Case 4 (13.2 °C). This implies that a well-insulated roof can reduce indoor temperatures by decreasing the rate of heat influx into the building.
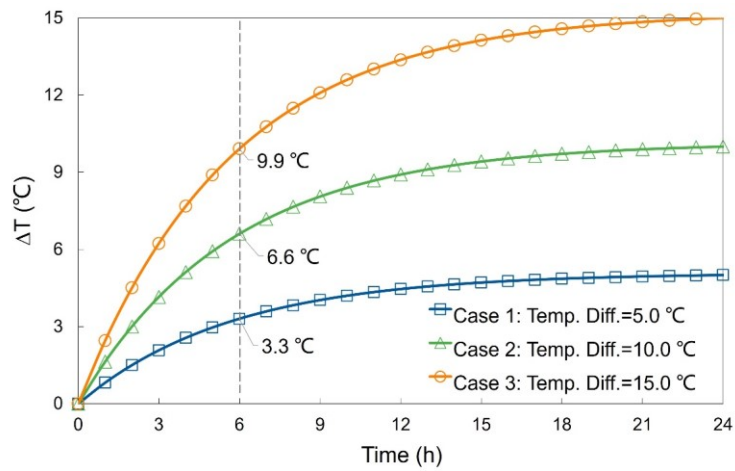
(a) effect of indoor–outdoor temperature difference on temperature rise
(Cases 1 to 3)
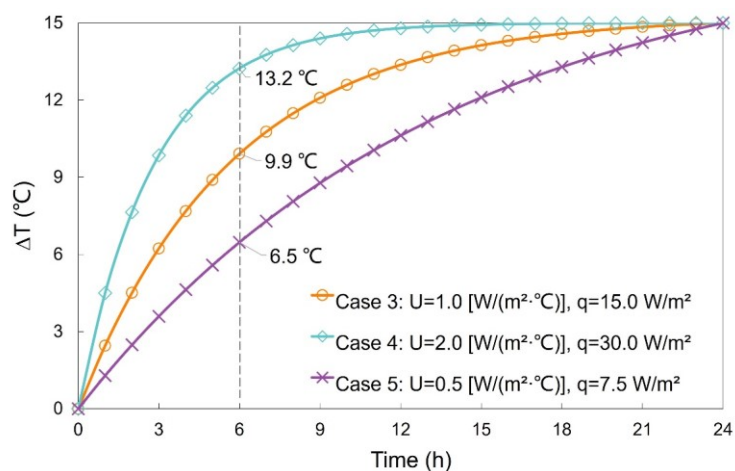
(b) effect of heat transmittance of the roof on temperature rise (Cases 3 to 5)

Figure 6–3 Simulations of indoor temperature rise.

6.3. Evaluating the Thermal Insulation Performance of Various Roof Slabs

Improving the thermal insulation performance of a roof is important to provide a more comfortable indoor environment during warmer seasons. This is particularly true for buildings such as factories, which often possess large roof surface areas for equivalent building spaces. Therefore, balancing the heat entering through the roof results in considerable power consumption of cooling equipment. From this perspective, the better the insulation performance of roof slab elements, the greater the achievable energy savings. In this section, static heat-transfer experiments were conducted on specimens of commercially available insulation materials, self-developed insulation materials, and common construction methods. The thermal insulation performance of these roof slabs was evaluated using simple experiments and simulations.

6.3.1. Specimens and Experiment

The specimens involved in this section were square slabs with side lengths of 30 mm, as shown in **Figure 6–4**. The specimens were constructed using a fiber-reinforced concrete board as the substrate, and on top of this, waterproof or thermal insulation was applied. Details pertaining to each layer are listed in **Table 6–2**.
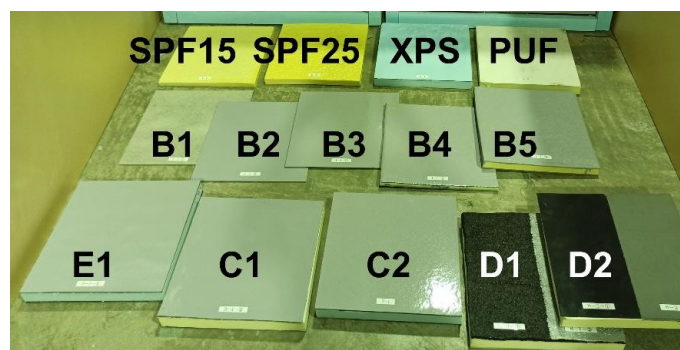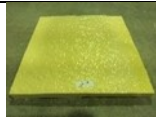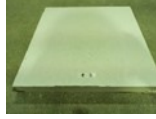

Figure 6–4 Appearance of the specimens.
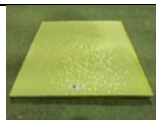
Table 6–2 Details of specimen layers.

Specimen	Details of Each Layer		Photo
SPF15		15 mm sprayed polyurethane foam	
SPF25		25 mm sprayed polyurethane foam	

XPS		30 mm extruded polystyrene foam	
PUF		30 mm rigid polyurethane foam	
B1		3 mm fiber-reinforced cement board	
B2		18 g acrylic-urethane topcoat 3 mm fiber-reinforced cement board	
B3		18 g acrylic-urethane topcoat 1.5 mm polyurethane waterproof 3 mm fiber-reinforced cement board	
B4		18 g acrylic-urethane topcoat 1.5 mm polyurethane waterproof 10 mm sprayed polyurethane foam (SPF) 3 mm fiber-reinforced cement board	
B5		18 g acrylic-urethane topcoat 1.5 mm polyurethane waterproof 20 mm sprayed polyurethane foam (SPF) 3 mm fiber-reinforced cement board	
C1 C2		18 g acrylic-urethane topcoat 2 mm polyurethane waterproof 1.1 mm self-adhesive asphalt sheet 30 mm thermal insulation layer* 1.5 mm butyl adhesive sheet 3 mm fiber-reinforced cement board *C1: extruded polystyrene foam (XPS) *C2: rigid polyurethane foam (PUF)	
D1		6 mm asphalt waterproof 30 mm rigid polyurethane foam (PUF) 3 mm fiber-reinforced cement board	
D2		1.7 mm rubber sheet waterproof 30 mm rigid polyurethane foam (PUF) 3 mm fiber-reinforced cement board	
E1		18 g acrylic-urethane topcoat 2 mm polyurethane waterproof 1.3 mm modified asphalt sheet 30 mm extruded polystyrene foam (XPS) 3 mm fiber-reinforced cement board	

In **Table 6–2**, the listed sprayed polyurethane foam (SPF) specimen is a self-developed specimen sprayed with polyurethane foam insulation with a ten-fold expansion rate. The extruded polystyrene

foam (XPS) is a molded thermal insulation material with a thermal conductivity of 0.028 W/m·°C (JIS A 9521). The rigid polyurethane foam (PUF) is a molded thermal insulation material with a thermal conductivity of 0.023 W/m·°C (JIS A 9521). All three types of insulation are highly durable, high-performance materials that resist moisture and prevent condensation. According to the type of material, SPF and PUF are both polyurethane insulations, while XPS is polystyrene insulation. The former has better insulation properties, while the latter is cheaper and less sensitive to moisture. According to the molding process, SPF is molded in situ by spraying and making it foam at the same time, while XPF and PUF are made into boards at the plant and cut into various sizes in situ as needed. The spraying process ensures the adhesion and fixation of the insulation to the substrate. It is not only limited to flat construction surfaces but also suitable for wave panels or metal-profiled cladding sheets. However, weather conditions such as natural winds for spraying operations should be regulated to take full account of their impact on the surrounding area. The molded thermal insulation is applicable to flat surfaces only and not suitable for small or cornered areas. The cutting and assembling part of the molded board tends to lose its insulation and airtightness [137], thus requiring additional treatment attention. However, the use of molded insulation requires less technology and has economic advantages.

Specimens B1 through B5 were SPF insulation systems that could be used to elucidate the effects of each layer on the insulation performance. Specimen B3 was coated with a rapid-spray polyurethane seal for waterproofing. Specimen B4 had a standard construction with a 10 mm-thick SPF insulation system. The 20 mm-thick specimen (B5) was used for special construction in individual regions.

Specimens C1 through E1 were based on various waterproofing and thermal insulation constructions specified in JASS 8 [138]. Among them, specimens C1 and C2 were typified by adhesive waterproofing and insulation methods that could be used for flat concrete roofs. The two-sided adhesive butyl system allows the insulation to be bonded to the substrate, eliminating the need for anchors, and thus avoiding thermal bridging. Moreover, the butyl sheet is waterproof, making the system unaffected by the moisture of the substrate; thus, the insulation layer can be either polyurethane or polystyrene. Specimens D1 and D2 were asphalt waterproofing and rubber sheet waterproofing constructions, respectively. Asphalt waterproofing has been widely used since very early on, with excellent waterproofing performance and a high degree of reliability. However, it is difficult to remove it during the renovation, and in some cases the construction process is not environmentally friendly. The rubber sheet waterproof has good ductility and can follow the movement of the roof slab joints without breaking. In the case of renovation, it can be directly covered on the uppermost layer of the existing structure with simple construction and short construction period. However, the thickness of the rubber sheet waterproof is small; thus, it is sensitive to UV and impact, and in addition, the cost is high. Specimen E1 was a modified asphalt waterproofing construction used for mechanical fixation systems. This specimen refers to the waterproofing and insulation constructions of concrete flat roofs

using metal anchors. Notably, the small specimen used butyl adhesive sheets instead of anchors to bond the layers. Mechanical fixation systems require less surface treatment of the substrate; however, since the insulation layer is in direct contact with the substrate, only insulation materials with low water absorption should be used.

All specimens were subjected to heat-transfer Pattern 1, as described in Chapter 5. The temperature difference between the indoor and outdoor air was 20 °C. The experimental setup is shown in **Figure 6–5**. A heat-flow sensor was set at the geometric center of the indoor surface of the specimen. The time interval for data recording was set to 5 min.
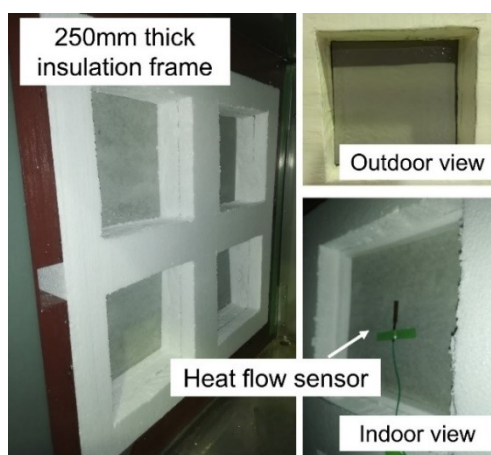
Figure 6–5 Heat-transfer experimental setup.

6.3.2. Results and Discussions

The heat-flow density results for each specimen listed in **Table 6–2** are presented in **Figure 6–6**. At the beginning of data recording, the heat flow was negative for some of the specimens. This was because the surface temperature of the specimens was below 20 °C at the beginning, owing to which heat flowed into the specimens from the indoor chamber. Within the first 2 h, the heat-flow density values for all specimens reached near zero. This indicates that no heat transfer occurred within the specimens and that both chambers had reached the preset temperature of 20 °C. After the 2nd h, the outdoor chamber temperature was set to rise rapidly, resulting in a significant increase in the heat-flow density values of the specimens. Subsequently, the whole system gradually reached a steady state of heat transfer, with the heat-flow density fluctuating around a specific value. At the 12th h, the temperature difference between the two chambers disappeared, and the heat-flow density through the specimen then decreased rapidly. At the end of the experiment, there was no heat transfer; that is, the heat-flow density was zero. The calculation of the U-value requires experimental data of steady-state heat transfer at large temperature differences to evaluate the thermal insulation performance. The middle 8 h of the experiment were regarded to correspond to the true static heat transfer. Thus, the

data from 3–11 h were averaged to evaluate the performance of the specimens.
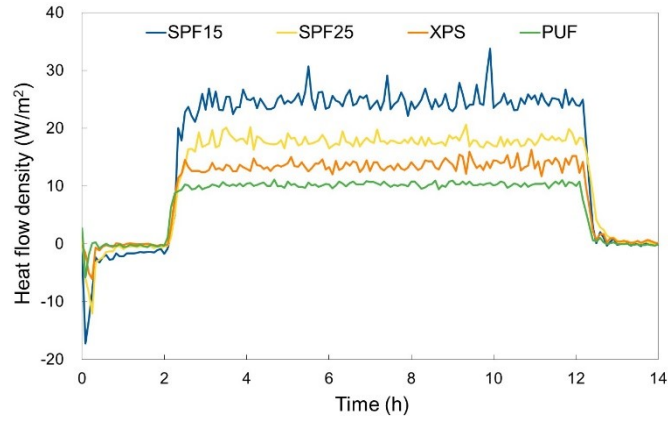
(a) insulation material specimens
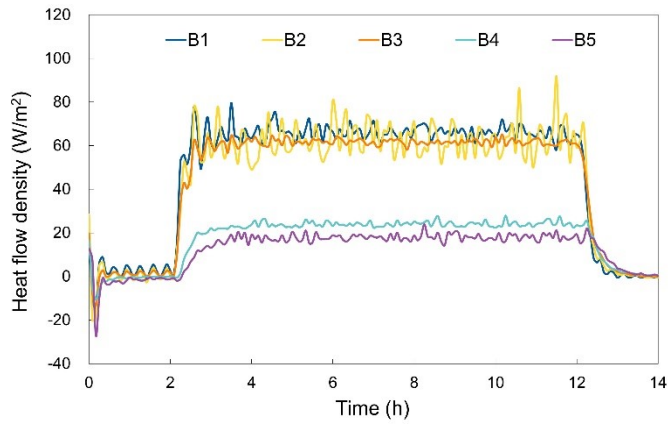
(b) specimens B1 to B5
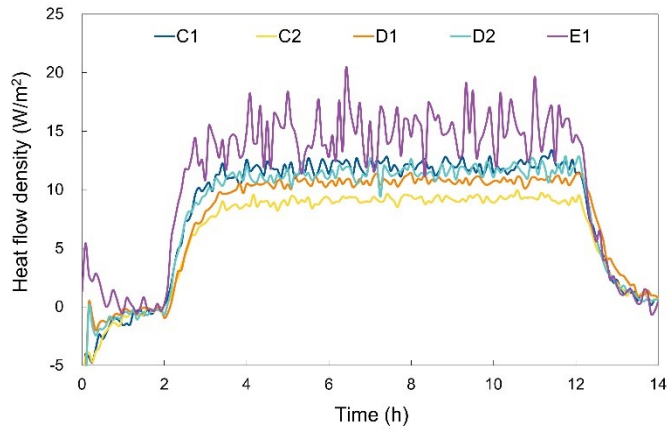
(c) specimens C1 to E1

Figure 6–6 Heat-flow density results in heat-transfer Pattern 1 for the
specimens listed in Table 5–5.

In **Figure 6–6(a)**, the insulation properties of various insulation materials are clearly compared. Note that lower heat-flow density values indicate better thermal insulation performance. Among the specimens, the PUF specimen with a thickness of 30 mm demonstrated optimal thermal insulation performance. The average heat-flow density from the surface of the specimen to the indoor chamber was approximately 10.3 W/m^2. In addition, the SPF insulation material exhibited an excellent insulation ability. The average heat-flow density of the SPF specimen with a thickness of 25 mm was approximately 17.8 W/m^2.

As shown in **Figure 6–6(b)**, the specimens with more complete construction procedures demonstrated lower heat-flow densities and better thermal insulation performance. The average heat-flow density of the specimens without insulation layers (B1, B2, and B3) was about 60 W/m^2, whereas that of specimens with insulation layers (B4 and B5) was about 20 W/m^2. The difference between the two groups was evident, with a heat-transfer difference of approximately three times. The average heat-flow densities of specimens B1, B2, and B3 were 66.2 W/m^2, 62.2 W/m^2, and 61.7 W/m^2, respectively. Therefore, it could be determined that the top coating and waterproofing layers also had certain insulation capacities. The data for specimen B2 fluctuated considerably, which can be explained since the experimental specimen was too thin and, therefore, particularly sensitive to temperature changes. The average heat-flow densities of specimens B4 and B5 were 23.8 W/m^2 and 17.8 W/m^2, respectively. The 10 mm-thick SPF insulation material demonstrated a good insulation effect, and the 20 mm-thick SPF insulation material further reduced the heat-flow density. However, in terms of efficiency per unit thickness, the 10 mm SPF may be more efficient. This implies that, for most building insulation constructions, selecting materials with excessive thicknesses is not essential; alternatively, striking a balance between the efficiency and economic benefits appears more reasonable.

Figure 6–6(c) indicates that the heat-flow densities of all the specimens were between 10 W/m^2 and 15 W/m^2, with minimal variation. The large fluctuations in the heat-flow density of specimen E1 could be explained by the effect of wind on the heat-flow sensor in the chamber during the experiment. This may also be attributed to the insufficient adhesion of the heat-flow sensor onto the surface of the specimen. The difference between different insulation materials for the same construction method can be determined by comparing specimens C1 and C2. The trend followed by the results for this group of experiments was the same as that depicted in **Figure 6–6(a)**; that is, the PUF insulation slightly outperformed the XPS insulation for the same thickness. By comparing specimens D1 and D2, the insulation effects of different waterproofing methods can be ascertained. Asphalt waterproofing may provide better insulation performance than rubber sheet waterproofing. The differences in the insulation fixation techniques can be obtained by comparing specimens C1 and E1. Evidently, the adhesion method results in better insulation than the mechanical fixation method. This could be related to the construction method itself, which increases the number of layers and the thickness of the specimen. It is worth noting that the adhesion method can also avoid thermal bridging resulting from

the mechanical fixation method in actual constructions. In general, the difference in insulation performance between the specimens can be conveniently compared using a heat-flow sensor when the boundary conditions of heat transfer are the same.

The results of the average values of the heat-flow density and calculated heat transmittance for all specimens are summarized in **Figure 6–7**. The smaller the U-value, the better the thermal insulation of the specimens. The chamber temperature was the same in these experiments, which means that the boundary conditions of the specimens were the same. In this case, the trend of U-value and heat-flow density values should be the same for various specimens. In addition, insulating materials perform the insulation function by increasing the temperature gradient inside themselves. This means that excellent thermal insulations reduce the heat exchange between the entire specimen and the chamber environment. Thus, the specimens with better thermal insulation may have smaller heat-flow density values. However, the heat-flow density of specimen E1 was greater than that of the insulation material alone (XPS), which may be explained based on the disparate vertical position of the specimen in the environmental simulation chamber (**Figure 6–5**). Because hot air tends to move upward, the temperature in the upper part of the chamber may be slightly higher than that in the lower part. Specimen E1, which was placed in the upper part, exhibited an elevated temperature and high heat-flow density. In addition, the heat-flow densities of specimens D1 and D2 were also slightly higher than those of the corresponding individual insulating materials (PUF). This may be attributed to the specimen size. As presented in **Figure 6–4**, specimens D1 and D2 were divided into left and right parts. Among these, the left half was the object of the measurements in this experiment, and the right half was superimposed with a highly reflective coating on top of the left half for other experiments. Notably, the thermal bridge effect could have been caused by the difference in thickness between the left and right halves, as well as the small size of the specimens. More heat could be transferred into the indoor chamber through the left half, and this led to the large values of the heat flow measured in specimens D1 and D2.
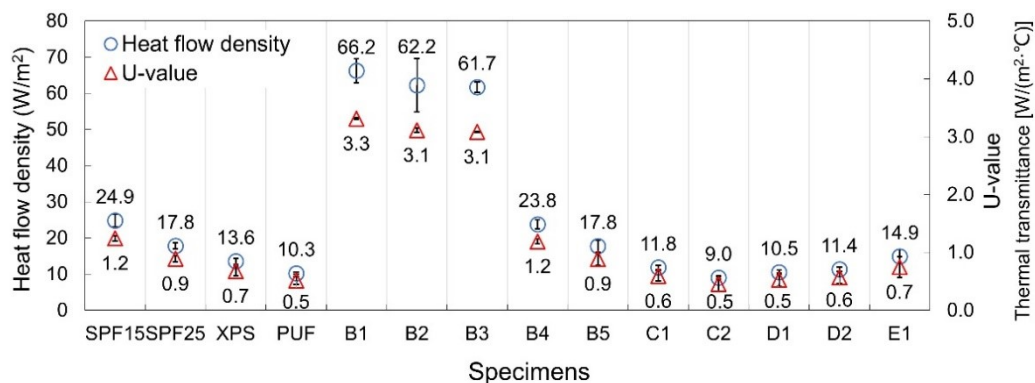
Figure 6–7 Mean values of the heat-flow density and U-value for each specimen.

Generally, the thermal insulation performance of building elements can be evaluated using heat-flow sensors. A heat-flow sensor can provide reference data for evaluating the effectiveness of various constructions or renovations of the building thermal insulation. In fine evaluations, extra care must be dedicated to set up such sensors to reduce errors. Heat-flow sensors should be tightly adhered onto the measurement surfaces, and the use of excessively small specimens should be avoided. This is because small specimens may lead to heat transfer in a direction parallel to the sensor or the thermal bridge, which can affect the measured value. The heat-flow sensor itself should also avoid direct- or variable-speed winds, which can cause fluctuations in the heat-flow density by altering the temperature.

Temperature simulations of the full-scale building were also performed for the specimens in this section using the heat-flow density calculation equation presented in **Section 6.2.1**. The equations and assumptions involved in the calculation process were the same as those described in **Section 6.2.2**. To simulate hot summer conditions, the difference between indoor and outdoor temperatures was set to 12 °C. Similarly, the 6th h of the heat-transfer process was considered as the subject of our discussion, considering the duration of high temperatures during daytime. The temperature increases inside the factory after turning off the indoor cooling equipment are depicted in **Figure 6–8**. The indoor temperature of the roof slab specimens B1 to B3 (without insulation) increased by an average of 11.7 °C after 6 h. In contrast, for roofs constructed based on various waterproofing and insulation construction methods specified in JASS 8, such as specimens C1 to E1, the average temperature rise after 6 h was around 6.1 °C, which was only 52% of the former. Thus, roof slabs with excellent thermal insulation can effectively reduce the temperature increase inside buildings, and smaller temperature increments can result in economic benefits by reducing the cooling power requirements of factories during summers. Certainly, the initial cost of applying thermal insulation should not be underestimated; thus, more grants such as the thermal insulation retrofit program are recommended.
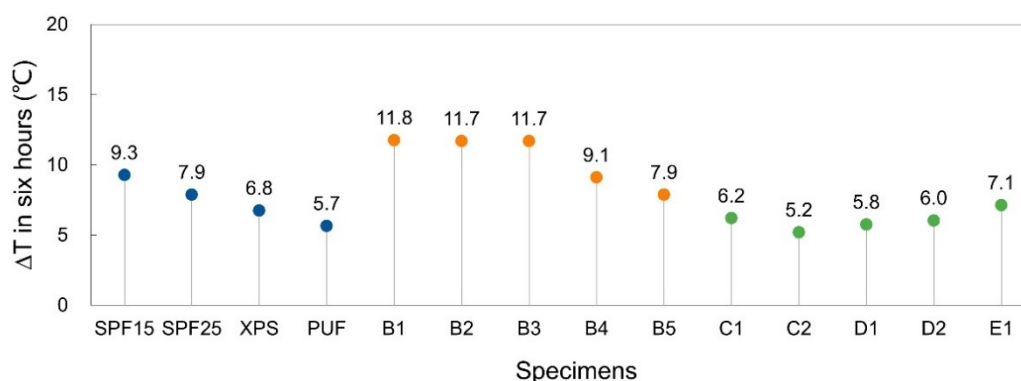
Figure 6–8 Temperature increments in 6 h for buildings with various roof slabs in the simulation.

6.4. Conclusions

This chapter attempted to connect specialized evaluation indicators to the temperature, a common physical quantity. The main conclusions of this chapter are as follows:

1. A simplified equation for the variation in heat-flow density with time was established. This equation could be used to approximate the temperature rise in an indoor space. The simulation results agreed well with the experimental results. Notably, temperature is a quantity easily understood by laymen; thus, it can improve the communication efficiency between owners, thereby aiding in the mitigation of environmental problems.

2. A better-insulated roof can achieve a lower interior temperature in summers by increasing the temperature gradient within it. In steady-state heat-transfer experiments, the heat-flow density values and heat transmittance values (U-values) of various specimens ranged from 9.0 W/m^2 to 113.4 W/m^2 and from 0.5 W/m^2·°C to 6.0 W/m^2·°C, respectively. Better-insulated specimens have lower heat-flow densities and U-values under the same boundary conditions. During dynamic heat transfer, better-insulated specimens reduce the rate of heat transfer, resulting in a smaller temperature rise in the same amount of time.

3. During our simulations on a full-scale building model, the indoor–outdoor temperature difference was a key factor in determining the degree of indoor temperature increase inside the building. An extra 5.0 °C increase in temperature difference may result in an extra 3.3 °C temperature rise after 6 h. In addition, buildings with a small U-value for the roof were found to be capable of efficiently improving the indoor thermal environment, particularly in the first few hours. At the 6th h, the average indoor temperature rise for buildings with insulated roof slabs was approximately 52% of that without insulation.

4. To ensure the simplicity of the structure, the current prediction model is only applicable under certain conditions. Since uniform thermal radiation based on infrared lamps had not been realized on the specimen surface in the laboratory, the scope of this paper does not address the effect of solar radiation on thermal insulation performance. The primary limitations may arise from the definition of the end-time of the heat-transfer process and the heating efficiency. In future, establishing a relationship between these variables and the heat-flow density may be a feasible solution. In addition, obtaining measurement data from actual physical buildings could also provide a reference for accurate building models.

Chapter 7 Conclusions and Prospects

7.1. Conclusions

To extend the service life of buildings, this paper studied the effectiveness of crack repair and thermal insulation performance in building envelopes, and the main conclusions drawn are as follows:

Chapter 1

Chapter 1 investigated the processes and difficulties of sustainable development in the construction industry. It was found that extending the service life of existing buildings is a priority to improve the current situation. In addition, energy use for space cooling is one of the main causes of climate change. To this end, improving the thermal insulation of buildings and raising public awareness seem to be effective methods. In fact, the building envelope is an important element that separates the internal and external spaces, which determines the characteristic that it is the part most prone to deterioration. Surveys revealed that occupants were most distressed by the exterior wall as an element and by cracks as a form of deterioration. In this chapter, the research objects were selected from the perspective of sustainable development for exterior wall crack repair and thermal insulation renovation.

Chapter 2

(1)   Crack repair effectiveness

In Chapter 2, through literature survey and actual measurements, it is found that cracks accelerate the deterioration of buildings and may also cause abnormal vibration of buildings. The crack width and leakage condition are the main selection criteria for the current crack repair solutions. However, repair failures still occur, and one possible reason for this may be that crack movement is not adequately considered. Crack movement refers to the change in concrete crack width caused by daily temperature changes. To address this issue, after combing the studies on crack movement, it was found that the daily cycle of concrete cracks has a movement of about 0.02 mm to 0.2 mm. Moreover, the movement decreases after repair, but it still exists. Starting with the most harmful through-thickness cracks, measurement data from various locations in Japan indicate that such cracks are likely to produce bending-like movement. In other words, when the outdoor surface temperature rises, the outdoor cracks close and the indoor cracks open.

To clarify the evaluation method for the durability of the repaired cracks under this movement, a literature survey of existing methods was conducted. These methods include filling conditions, physical strength, chemical resistance, etc. Experiments with multiple degradation conditions coupled usually include temperature conditions, hydrostatic pressure, etc. Therefore, Chapter 2 clarified that there is no experimental method about the degradation conditions to simulate the bending-like cyclic

151

movement.

(2) Insulation performance

After a survey of building insulation solutions, it was found that insulation materials are popular owing to their lack of site restrictions and versatility. Regarding thermal insulation performance, evaluation indicators generally include thermal conductivity (K-value) and thermal resistance (R-value). In the field, the total thermal resistance and thermal conductivity (U-value) are most often chosen. In the specifications, these indicators of insulation performance are clearly defined and measured. However, in the laboratory, huge equipment and complex calibration processes are the main difficulties. In field measurements, long periods of monitoring must be experienced. In this chapter it was found that when communicating the effectiveness of insulation systems, commonly used physical quantities rather than specialized metrics may improve the efficiency of communication with building owners.

Chapter 3

To accumulate data, this chapter monitored cracks in buildings on campus. The results agreed with previous studies and found that exterior wall through-thickness cracks are subject to bending-like movement: when the temperature changes, cracks on the high-temperature side close and cracks on the low-temperature side open. There are no experimental methods available to produce this form of degradation in the repair area, therefore two laboratory-scale simulation methods are presented in this chapter.

(1) Reproduction experimental method

To ensure the validity of the reproduction experiments, the available data on through-thickness cracks were compiled. It was found that the daily movement of through-thickness cracks was directly proportional to the wall section temperature gradient, inversely proportional to constraint strength, and not significantly related to the initial crack width. Moreover, the bending-like movement is a combined deterioration of temperature and mechanical loading that acts on the crack repair area almost every day. These are the conditions that need to be met for the reproduction experiment.

Numerical simulations of the three constraint schemes of the mortar specimen by the finite element method revealed that the bending-like movement could be reproduced in the asymmetric constraint scheme. It was verified that the proposed experimental method can satisfy the conditions mentioned above. In addition, the method can also achieve a variety of experimental groups by adjusting parameters such as infrared lamp intensity, wrench torque and initial crack width.

(2) Fatigue test method

Thermal loading is an essential deterioration condition when evaluating the effectiveness of a repair, however, the heating-cooling cycle usually takes a lot of test time. For this reason, distinguishing the

mechanical load from the ambient temperature can shorten the test cycle. The fatigue test proposed in this chapter is an efficient device for simulating bending-like movement. This method can simulate the mechanical fatigue in the repair area, and combined with the constant temperature and humidity chamber can also simulate the fatigue evaluation under a variety of climatic conditions. Its advantages are controllable movement and period, easy to increase the experimental variables, accelerate the degradation process and shorten the test period. Meanwhile, the results of the digital image correction method showed that the specimens used for this experiment need to meet the condition of geometric symmetry of the upper and lower halves. This allows for a half-tensioned and half-compressed state of force.

Chapter 4

Chapter 4 focuses on the durability evaluation of common crack repair solutions for crack movement using the reproduction experimental method and fatigue test method proposed in Chapter 3. Methods covered are injection method, U-groove routing and sealing method, and surface coating method. The materials used include mainly epoxy resins, polymer cement and water-based acrylic waterproofing coatings. The results of the two experiments are combined and summarized here according to the distinction of each repair material.

(1) Hard epoxy resin (HE)

In the reproduction experiment, the crack movement pattern changed after HE injection repair. With the increase of outdoor temperature, the movement from indoor-opening outdoor-closing bending-like movement became closed on both sides. It suppresses the crack movement better than most repair methods. When the initial temperature decreases, the movement amplitude of the HE specimen decreases, and the movement pattern remains unchanged. The closing movement resulted in the HE is compressed stress state, and it can be presumed that its durability may be excellent. Because compression is less likely to cause bond failure, it is more durable than tension.

However, in the fatigue test, HE proved to be suitable only for cracks with small amplitude movement. Once the crack movement becomes large, HE undergoes brittle fracture. In addition, the ambient temperature also influenced the durability of HE, and brittle fracture occurred in the experimental group with small movement at 35 °C.

In general, HE is one of the repair materials with high Young's modulus. It is assumed that HE can obtain durability by suppressing crack movement. The most suitable conditions of application for HE used in this study may be to repair cracks with small movements. Moreover, it is preferable to use it in winter or cold place, where a longer service time can be obtained in a compressed condition.

(2) Soft epoxy resin (SE)

In the reproduction experiments with an initial ambient temperature of 20 °C, the specimens generated a reverse bending-like crack movement after SE injection. That is, when the outdoor

temperature increased, the outdoor cracks opened, and the indoor cracks closed. In the reproduction experiment with an initial ambient temperature of 5 °C, the SE specimens showed the same bilaterally closed movement as the HE specimen. The different initial ambient temperatures may have influenced the movement patterns by changing the thermal expansion coefficient and Young's modulus of SE. Numerical simulations of the finite element method for the reproduction experiments also support this idea.

In fatigue experiments, the SE is highly sensitive to temperature. 35 °C fatigue tests in which the SE fails to repair with very little movement. At high temperatures the Young's modulus of SE becomes smaller, the material becomes more ductile, and the ability to follow deformation becomes better. However, the bond failure at the mortar-resin interface prevents all these properties from being realized. In other words, the soft injection material can follow the deformation of the crack movement, but only if sufficient bonding capacity is guaranteed.

In general, the SE used in this study can repair cracks with a wide range of movements and ensure good repair durability. However, it is only suitable for use in cold regions or winter. The compressed state of force in low temperature environment can ensure that SE does not fail in bonding. Under high temperature environment, SE is not only the state of being tensioned at outdoor surface but also must bear the effect of low bonding brought by high temperature, which is an unfriendly state.

(3) Polymer cement (PC)

The polymer cement injection repair was the only specimen that showed significant deterioration in the reproduction experiments. The crack movement pattern after repair was closed both indoors and outdoors. The main cause of deterioration was early drying shrinkage cracks. In the combined thermal and mechanical load deterioration mode, the apex of the drying shrinkage cracks kept getting longer and wider. 30 s air leakage test results at 240 cycles showed that all the air in the negative pressure air chamber was exhausted. Therefore, cement-based materials may not be suitable for repairing the crack of movement.

(4) U-groove routing and sealing method (UC)

The movement of UC specimens at the crack after repair may be a reverse bending-like movement with indoor closing and outdoor opening. The possibility of generating such movement was also demonstrated by numerical simulations with the finite element method. The reason for this movement may be that the repair method was filled only outdoors, and the stresses originally concentrated in the cracks were dispersed by the filling material and the specimens expanded in the out-of-plane direction. Presumably, the repair solution is durable as long as the flexible epoxy resin used can follow the deformation at the crack and ensure sufficient bonding strength.

(5) Surface Coating Method (SCA, SCB and SCC)

After SCA and SCB were coated on the cracks, the specimens produced still bending-like

movements when the temperature of the assumed outdoor surface increased. This may be because the coatings were applied only to the outdoor surface and the Young's modulus of the layers was too small compared to that of the mortar, insufficient to affect the crack movement pattern. The use of SCC caused a reverse bending-like movement similar to that of UC. This may be related to the fact that it flowed inside the cracks during the coating process.

In the fatigue tests, SCA ensured the repair for cracks with small movements. However, when the movement increased, the specimens produced surface cracks or hole damage. If additional crack bridging functional layer, i.e., SCB solution, is added, the repair effect can be guaranteed for cracks with large movements. At small movements, the specimen damage rate may be dominated by the elongation of the coating. The lower the elongation the more likely the repair failure. At large movements, the degree of specimen damage may be dominated by the tensile strength of the coating. The higher the tensile strength, the lower the degree of damage. Moreover, as the temperature of the experimental environment increases, the molecular kinetic energy within the coating becomes larger and the interlayer mobility becomes better. This means that the crack movement decreases gradually during the transfer from the substrate to the surface. This reduces the risk of cracking of the surface layer of the coating. This means that the crack movement decreases gradually during the transfer from the substrate to the surface. This reduces the risk of cracking of the surface layer of the coating.

In general, the water-based acrylic waterproofing coating used in this paper can be used for repairs where crack movement exists. It can reduce crack movement by reducing the driving force of temperature gradients through thermal insulation properties. It can also perform its soft properties to follow the deformation and thus ensure the effectiveness of the repair. Compared to epoxy injection methods, the surface coating is not sensitive to application temperature and can be used in most seasons and regions. It should be used in conjunction with a crack bridging layer when the crack movement is large.

Chapter 5

Chapter 5 designed a set of simple heat transfer experiments based on an environmental simulation chamber and a heat-flow sensor to evaluate the thermal insulation performance of building components. The results of both static and dynamic heat transfer experiments showed that the heat-flow sensor can be used to quantitatively evaluate the thermal insulation performance. The smaller the absolute value of heat-flow density under the same boundary conditions, the better the thermal insulation performance is indicated. In static heat transfer experiments at 40°C outdoors and 20°C indoors, the application of an insulation layer to a metal roof slab specimen reduced the surface heat-flow density from 113.4 W/m^2 to 44.4 W/m^2. In dynamic heat transfer experiments, it was possible to reduce the U-value of the roof element from 6 W/(m^2·°C) to about 2 W/(m^2·°C) by applying an insulation layer.

Chapter 6

Temperature is a physical quantity that is easily understood by the general public and using it as an evaluation criterion can improve the efficiency of communication with homeowners, thus helping to mitigate environmental problems. To this end, this chapter established a relationship between professional evaluation metrics and temperature, a common physical quantity. A simplified equation for the variation of heat-flow density with time is first established. This equation is then used to approximate the temperature increment in an indoor space. The calculated results are in good agreement with the experimental ones. Subsequently, in a simulation of a full-scale building model, it was found that buildings with small roof U-values were effective in improving the indoor thermal environment, especially during the first few hours when the cooling equipment was turned off. At the 6th hour, the average indoor temperature increment of the building with insulated roof panels was reduced by approximately 48%.

7.2. Prospects

The items to be refined and conducted in future studies are as follows:

1. This study only involved the bending-like movement of through-thickness cracks. Monitoring and experiments of other kinds of cracks and other movement patterns also need to be performed if a complete crack repair solution selection system is to be proposed. In addition, the various initial widths of cracks should also be included as variables in the evaluation.

2. The current reproduction experiments are inefficient, with slow deterioration of the solution and long test periods. In the future, attempts could be made to minimize the specimen size or improve the constraint methods.

3. The current discussion about the crack movement patterns after the application of various repair solutions can only revolve around the results of reproduction experiments and its numerical simulation by finite element methods. To obtain more convincing conclusions, measurement data of the actual building are essential. Numerical analysis of full-size building models should also be performed.

4. In the fatigue experiments, the crack cross section of the injection method specimens is left as cast. This can lead to an underestimation of the durability of the injection method. Therefore, the conclusions of this experiment can currently only be used for the evaluation of the same material under different conditions, and not for the evaluation of comparing different repair method. In the future, the influence of cross-section factors on durability can be clarified by making specimens with natural cross-section cracks. Moreover, the relationship between the number of cycles of crack movement in the experiment and the realistic length of service needs to be clarified. The correspondence between the movement of the fatigue device corresponding to the movement of the actual building also needs to be investigated.

5. Regarding the predictive equation of heat flow over time proposed in this paper, the simplicity of the structure has led to the possibility that the current predictive model may not be applicable in some cases. The main limitation may come from the definition of the end time of the heat transfer process and the heating efficiency. In the future, relating these variables to the heat-flow density may be a feasible solution. Furthermore, incorporating empirical data obtained from real buildings could serve as a valuable point of reference, enhancing the precision of future predictive equations.

References

[1]   UNEP, 2021 Global Status Report for Buildings and Construction, United Nations Environment Programme, 2021.

[2]   UNEP, 2022 Building Construction Global Status Report, United Nations Environment Programme, 2022.

[3]   Housing Consultation Statistics Annual Report 2022 (in Japanese), Dispute Resolution Support Center and Home Renovation (Public Interest Incorporated Foundation), 2022.

[4]   2021 Global Status Report for Buildings and Construction: Towards a Zero-emission, Efficient and Resilient Buildings and Construction Sector, 2021.

[5]   Construction Industry Handbook 2020 - Part III - Current state of the construction market (in Japanese), Japan federation of construction contractors, 2020.

[6]   W.J. Weiss, W. Yang, S.P. Shah, Shrinkage Cracking of Restrained Concrete Slabs, J. Eng. Mech. 124 (1998) 765–774. https://doi.org/10.1061/(asce)0733-9399(1998)124:7(765).

[7]   W.J. Weiss, S.P. Shah, Restrained shrinkage cracking: The role of shrinkage reducing admixtures and specimen geometry, Mater. Struct. Constr. 34 (2002) 85–91. https://doi.org/10.1007/bf02482106.

[8]   H. Zhu, Y. Hu, R. Ma, J. Wang, Q. Li, Concrete thermal failure criteria, test method, and mechanism: A review, Constr. Build. Mater. 283 (2021). https://doi.org/10.1016/j.conbuildmat.2021.122762.

[9]   B. Fournier, M.-A. Bérubé, K.J. Folliard, M. Thomas, Report on the Diagnosis, Prognosis, and Mitigation of Alkali-Silica Reaction (ASR) in Transportation Structures, 2010.

[10]   M.D.A. Thomas, B. Fournier, K.J. Folliard, Y.A. Resendez, Alkali-Silica Reactivity Field Identification Handbook, Fed. Highw. Adm. (FHWA), U.S. Dept Transp. FHWA-HIF-12-022. (2011) 80.

[11]   Practical Guidelines for Investigation, Repair and Strengthening of Cracked Concrete Structures -2013- (in Japanese), Japan Concrete Institute (JCI), 2013.

[12]   K. Wardhana, F.C. Hadipriono, Study of Recent Building Failures in the United States, J. Perform. Constr. Facil. 17 (2003) 151–158. https://doi.org/10.1061/(ASCE)0887-3828(2003)17:3(151).

[13]   N. Delatte, Failure, distress and repair of concrete structures, Woodhead Publishing Limited, 2009. https://doi.org/10.1533/9781845697037.

[14]   ISO 15686-1: 2011 - Buildings and constructed assets - Service life planning Part 1: General principles and framework, International Standard ISO 15686, 2011.

[15]   Concrete Society., Non-Structural Cracks in Concrete, A cement and concrete industry publication, 1992.

[16]   R. Talib, D. Boyd, S. Hayhow, A.G. Ahmad, M. Sulieman, Investigating Effective Waterproofing Materials in Preventing Roof Leaking; Initial Comparative Study: Malaysia, U.K., Procedia Manuf. 2 (2015) 419–427. https://doi.org/10.1016/j.promfg.2015.07.074.

[17]   E. Ahn, M. Shin, J.S. Popovics, Air-coupled ultrasonic diffuse-wave techniques to evaluate distributed cracking damage in concrete, Ultrasonics. 125 (2022) 106800. https://doi.org/10.1016/j.ultras.2022.106800.

[18]   M. Ohtsu, Elastic wave methods for NDE in concrete based on generalized theory of acoustic emission, Constr. Build. Mater. 122 (2016) 845–854. https://doi.org/10.1016/j.conbuildmat.2015.12.137.

[19]   A. Behnia, H.K. Chai, T. Shiotani, Advanced structural health monitoring of concrete structures with the aid of acoustic emission, Constr. Build. Mater. 65 (2014) 282–302. https://doi.org/10.1016/j.conbuildmat.2014.04.103.

[20]   N. Pal Kaur, J. Kumar Shah, S. Majhi, A. Mukherjee, Healing and simultaneous ultrasonic monitoring of cracks in concrete, Mater. Today Commun. 18 (2019) 87–99. https://doi.org/10.1016/j.mtcomm.2018.10.022.

[21]   M. Alsharqawi, T. Dawood, S. Abdelkhalek, M. Abouhamad, T. Zayed, Condition assessment of concrete-made structures using ground penetrating radar, Autom. Constr. 144 (2022) 104627. https://doi.org/10.1016/j.autcon.2022.104627.

[22]   S.T. Kuchipudi, D. Ghosh, H. Gupta, Automated Assessment of Reinforced Concrete Elements using Ground Penetrating Radar, Autom. Constr. 140 (2022) 104378. https://doi.org/10.1016/j.autcon.2022.104378.

[23]   S. Bagavathiappan, B.B. Lahiri, T. Saravanan, J. Philip, T. Jayakumar, Infrared thermography for condition monitoring - A review, Infrared Phys. Technol. 60 (2013) 35–55. https://doi.org/10.1016/j.infrared.2013.03.006.

[24]   T.C. Su, Assessment of cracking widths in a concrete wall based on tir radiances of cracking, Sensors (Switzerland). 20 (2020) 1–21. https://doi.org/10.3390/s20174980.

[25]   C. Bernstone, A. Heyden, Image analysis for monitoring of crack growth in hydropower concrete structures, Measurement. 42 (2009) 878–893. https://doi.org/10.1016/j.measurement.2009.01.007.

[26]   H.J. Oh, Y.K. Cho, S.-M. Kim, Experimental evaluation of crack width movement of continuously reinforced concrete pavement under environmental load, Constr. Build. Mater. 137 (2017) 85–95. https://doi.org/10.1016/j.conbuildmat.2017.01.080.

[27]   M.O. Kim, A.C. Bordelon, N.K. Lee, Early-age crack widths of thin fiber reinforced concrete overlays subjected to temperature gradients, Constr. Build. Mater. 148 (2017) 492–503. https://doi.org/10.1016/j.conbuildmat.2017.05.099.

[28]   Y.K. Cho, S.-M. Kim, Experimental analysis of crack width movement of continuously

reinforced concrete railway track, Eng. Struct. 194 (2019) 262–273. https://doi.org/10.1016/j.engstruct.2019.05.075.

[29]   K. Tanaka, H. Shin, N. Ando, Test Method for Evaluating Fatigue Resistance of Crack Repaired Zone in Concrete and Mortar by Injecting Epoxy Resin, J. Struct. Constr. Eng. (Transactions AIJ). 67 (2002) 21–27. https://doi.org/10.3130/aijs.67.21_2.

[30]   K. Toda, A. Teramoto, T. Kanazawa, T. Ohkubo, A Study on the Crack Opening and Closing Behavior of Real Structures at Subzero Temperatures (in Japanese), Proc. Japan Concr. Inst. 42 (2020) 335–340.

[31]   H. Shin, H. Miyauchi, K. Tanaka, An experimental study of fatigue resistance in epoxy injection for cracked mortar and concrete considering the temperature effect, Constr. Build. Mater. 25 (2011) 1316–1324. https://doi.org/10.1016/j.conbuildmat.2010.09.013.

[32]   Standard specifications for concrete structures - 2007: Maintenance, Japan Society of Civil Engineers (JSCE), 2010.

[33]   L. Czarnecki, R. Geryło, K. Kuczyński, Concrete Repair Durability, Materials (Basel). 13 (2020) 4535. https://doi.org/10.3390/ma13204535.

[34]   A.M. Vaysburd, P.H. Emmons, N.P. Mailvaganam, J.E. McDonald, B. Bissonnette, Concrete repair technology - a revised approach is needed, Concr. Int. 26 (2004) 59–65.

[35]   C.S. Suryawanshi, Structural concrete repair - A durability based revised approach is needed, Indian Concr. J. 86 (2012) 37–42.

[36]   M.Y. Al-Mandil, H.S. Khalil, M.H. Baluch, A.K. Azad, Performance of epoxy-repaired concrete under thermal cycling, Cem. Concr. Compos. 12 (1990) 47–52. https://doi.org/10.1016/0958-9465(90)90035-V.

[37]   Y. Ryuuda, T. Ohkubo, Y. Takase, T. Yonei, Dependence of Building Component Temperature on the Mechanical Properties of Polymeric Materials for Crack Repair, J. Struct. Constr. Eng. (Transactions AIJ). 78 (2013) 419–426. https://doi.org/10.3130/aijs.78.419.

[38]   U. Tamon, K. Rashid, Y. Qian, Z. Dawei, Effects of Temperature and Moisture on Concrete-PCM Interface Performance, Procedia Eng. 171 (2017) 71–79. https://doi.org/10.1016/j.proeng.2017.01.311.

[39]   K. Al-Lami, P. Colombi, T. D'Antino, Influence of hygrothermal ageing on the mechanical properties of CFRP-concrete joints and of their components, Compos. Struct. 238 (2020) 111947. https://doi.org/10.1016/j.compstruct.2020.111947.

[40]   T. OhkuboO, N. Morihama, Y. Ryuuda, T. Hasegawa, S. Fujimoto, A Study on the Investigation for Choosing the Crack Repair Method Based on Actual Movements of Cracks Occurred in the Building Walls, J. Struct. Constr. Eng. (Transactions AIJ). 76 (2011) 737–744. https://doi.org/10.3130/aijs.76.737.

[41]   Y. Li, T. Ohkubo, A. Teramoto, K. Saga, Y. Kawashima, Lab-scale reproduction test method

for temperature-driven movement of through-thickness cracks in concrete exterior walls for crack repair evaluation, Constr. Build. Mater. 331 (2022) 127169. https://doi.org/10.1016/j.conbuildmat.2022.127169.

[42]   Z. Yulu, A. Teramoto, T. Kanazawa, T. Ohkubo, A Study on the Effects of Wall Temperature and Member Constraint Conditions on the Opening and Closing Behavior of Drying Shrinkage Cracks (in Japanese), Proc. Japan Concr. Inst. 41 (2019) 425–430.

[43]   ACI 224.1R-07 Causes, Evaluation, and Repair of Cracks in Concrete Structures, American Concrete Institute (ACI), 2003.

[44]   Manual for Repair of Concrete Structures (Draft) (in Japanese), Public Works Research Institute (PWRI), 2016.

[45]   ACI 546R-14: Guide to Concrete Repair, American Concrete Institute (ACI), 2014.

[46]   M. Sánchez, P. Faria, L. Ferrara, E. Horszczaruk, H.M. Jonkers, A. Kwiecień, J. Mosa, A. Peled, A.S. Pereira, D. Snoeck, M. Stefanidou, T. Stryszewska, B. Zając, External treatments for the preventive repair of existing constructions: A review, Constr. Build. Mater. 193 (2018) 435–452. https://doi.org/10.1016/j.conbuildmat.2018.10.173.

[47]   A. Parghi, M. Shahria Alam, Effects of curing regimes on the mechanical properties and durability of polymer-modified mortars – an experimental investigation, J. Sustain. Cem. Mater. 5 (2016) 324–347. https://doi.org/10.1080/21650373.2015.1124812.

[48]   N. Su, L. Lou, A. Amirkhanian, S.N. Amirkhanian, F. Xiao, Assessment of effective patching material for concrete bridge deck -A review, Constr. Build. Mater. 293 (2021) 123520. https://doi.org/10.1016/j.conbuildmat.2021.123520.

[49]   J.T. San-José, I.J. Vegas, Moisés Frías, Mechanical expectations of a high performance concrete based on a polymer binder and reinforced with non-metallic rebars, Constr. Build. Mater. 22 (2008) 2031–2041. https://doi.org/10.1016/j.conbuildmat.2007.08.001.

[50]   K. Somna, C. Jaturapitakkul, P. Kajitvichyanukul, P. Chindaprasirt, NaOH-activated ground fly ash geopolymer cured at ambient temperature, Fuel. 90 (2011) 2118–2124. https://doi.org/10.1016/j.fuel.2011.01.018.

[51]   G. Fahim Huseien, J. Mirza, M. Ismail, S.K. Ghoshal, A. Abdulameer Hussein, Geopolymer mortars as sustainable repair material: A comprehensive review, Renew. Sustain. Energy Rev. 80 (2017) 54–74. https://doi.org/10.1016/j.rser.2017.05.076.

[52]   S. Hu, H. Wang, G. Zhang, Q. Ding, Bonding and abrasion resistance of geopolymeric repair material made with steel slag, Cem. Concr. Compos. 30 (2008) 239–244. https://doi.org/10.1016/j.cemconcomp.2007.04.004.

[53]   S. Navaratnam, K. Selvaranjan, D. Jayasooriya, P. Rajeev, J. Sanjayan, Applications of natural and synthetic fiber reinforced polymer in infrastructure: A suitability assessment, J. Build. Eng. 66 (2023) 105835. https://doi.org/10.1016/j.jobe.2023.105835.

[54]   ISO 16311-3: Maintenance and repair of concrete structures - Part 3: Design of repairs and prevention, International standard ISO 16311, 2014.

[55]   T. Muranaka, I. Naitoh, A. Shimata, Survey on selection of crack repair method and actual construction (in Japanese), 2013.

[56]   S. Matthews, CONREPNET: Performance-based approach to the remediation of reinforced concrete structures: Achieving durable repaired concrete structures, J. Build. Apprais. 3 (2007) 6–20. https://doi.org/10.1057/palgrave.jba.2950063.

[57]   G. Tilly, The Durability of Repaired Concrete Structures, in: IABSE Symp. Weimar 2007 Improv. Infrastruct. Worldw., International Association for Bridge and Structural Engineering (IABSE), Zurich, Switzerland, 2007: pp. 146–147. https://doi.org/10.2749/222137807796120030.

[58]   T. Shiotani, T. Nishida, K. Kawaai, H. Hamasaki, Technical Committee on Crack Repair Evaluation in Concrete by Means of Non-Destructive Testing, 2018.

[59]   D.G. Aggelis, T. Shiotani, D. Polyzos, Characterization of surface crack depth and repair evaluation using Rayleigh waves, Cem. Concr. Compos. 31 (2009) 77–83. https://doi.org/10.1016/j.cemconcomp.2008.09.008.

[60]   W. Wang, W. Zhao, J. Zhang, J. Zhou, Epoxy-based grouting materials with super-low viscosities and improved toughness, Constr. Build. Mater. 267 (2021) 121104. https://doi.org/10.1016/j.conbuildmat.2020.121104.

[61]   C.A. Issa, P. Debs, Experimental study of epoxy repairing of cracks in concrete, Constr. Build. Mater. 21 (2007) 157–163. https://doi.org/10.1016/j.conbuildmat.2005.06.030.

[62]   Y. Wang, J. Ye, Y. Liu, X. Qiang, L. Feng, Influence of freeze-thaw cycles on properties of asphalt-modified epoxy repair materials, Constr. Build. Mater. 41 (2013) 580–585. https://doi.org/10.1016/j.conbuildmat.2012.12.056.

[63]   S. Ahmad, A. Elahi, S. Barbhuiya, Y. Farooqi, Repair of cracks in simply supported beams using epoxy injection technique, Mater. Struct. Constr. 46 (2013) 1547–1559. https://doi.org/10.1617/s11527-012-9996-x.

[64]   J. Liu, C. Vipulanandan, Tensile bonding strength of epoxy coatings to concrete substrate, Cem. Concr. Res. 35 (2005) 1412–1419. https://doi.org/10.1016/j.cemconres.2004.06.035.

[65]   S.Y. Guo, X. Zhang, J.Z. Chen, B. Mou, H.S. Shang, P. Wang, L. Zhang, J. Ren, Mechanical and interface bonding properties of epoxy resin reinforced Portland cement repairing mortar, Constr. Build. Mater. 264 (2020) 120715. https://doi.org/10.1016/j.conbuildmat.2020.120715.

[66]   L.A. Modesti, A.S. de Vargas, E.L. Schneider, Repairing concrete with epoxy adhesives, Int. J. Adhes. Adhes. 101 (2020) 102645. https://doi.org/10.1016/j.ijadhadh.2020.102645.

[67]   J. Mirza, C. Abesque, M.-A. Bérubé, Evaluation of surface sealers for concrete hydraulic structures exposed to low temperatures, Mater. Struct. 44 (2011) 5–12. https://doi.org/10.1617/s11527-010-9604-x.

[68]   M.A. Safan, Z.A. Etman, A. Konswa, Evaluation of polyurethane resin injection for concrete leak repair, Case Stud. Constr. Mater. 11 (2019) e00307. https://doi.org/10.1016/j.cscm.2019.e00307.

[69]   X. Pan, Z. Shi, C. Shi, T.-C. Ling, N. Li, A review on concrete surface treatment Part I: Types and mechanisms, Constr. Build. Mater. 132 (2017) 578–590. https://doi.org/10.1016/j.conbuildmat.2016.12.025.

[70]   T.K. Kim, J.S. Park, Performance evaluation of concrete structures using crack repair methods, Sustain. 13 (2021) 3217. https://doi.org/10.3390/su13063217.

[71]   A. Manawadu, P. Qiao, H. Wen, Characterization of Substrate-to-Overlay Interface Bond in Concrete Repairs: A Review, Constr. Build. Mater. 373 (2023) 130828. https://doi.org/10.1016/j.conbuildmat.2023.130828.

[72]   B. Jiang, K.H. Oh, S.Y. Kim, X. He, S.K. Oh, Technical evaluation method for physical property changes due to environmental degradation of grout-injection repair materials for water-leakage cracks, Appl. Sci. 9 (2019) 1740. https://doi.org/10.3390/app9091740.

[73]   K. Rashid, T. Ueda, D. Zhang, K. Miyaguchi, H. Nakai, Experimental and analytical investigations on the behavior of interface between concrete and polymer cement mortar under hygrothermal conditions, Constr. Build. Mater. 94 (2015) 414–425. https://doi.org/10.1016/j.conbuildmat.2015.07.035.

[74]   K. Rashid, Y. Wang, T. Ueda, Influence of continuous and cyclic temperature durations on the performance of polymer cement mortar and its composite with concrete, Compos. Struct. 215 (2019) 214–225. https://doi.org/10.1016/j.compstruct.2019.02.057.

[75]   BS EN 1062-7: Paints and varnishes - Coating materials and coating systems for exterior masonry and concrete - Part 7: Determination of crack bridging properties, British Standards Institution (BSI), 2004.

[76]   M. Delucchi, G. Cerisola, Influence of temperature on crack-bridging ability of coatings for concrete, Prog. Org. Coatings. 75 (2012) 253–258. https://doi.org/10.1016/j.porgcoat.2012.05.006.

[77]   H. Shin, H. Miyauchi, K. Tanaka, Effect of Weathering on Fatigue Resistance of Crack Repaired Area by Epoxy Resin Injection, J. Struct. Constr. Eng. (Transactions AIJ). 69 (2004) 29–34. https://doi.org/10.3130/aijs.69.29_2.

[78]   H. Shin, K. Tanaka, H. Miyauchi, Effects of Movement and Temperature on Fatigue Resistance of Crack Repaired Zone by Injecting Epoxy Resin, J. Struct. Constr. Eng. (Transactions AIJ). 68 (2003) 37–44. https://doi.org/10.3130/aijs.68.37_5.

[79]   K. Çomakli, B. Yüksel, Environmental impact of thermal insulation thickness in buildings, Appl. Therm. Eng. 24 (2004) 933–940. https://doi.org/10.1016/j.applthermaleng.2003.10.020.

[80]   S. Schiavoni, F. D'Alessandro, F. Bianchi, F. Asdrubali, Insulation materials for the building sector: A review and comparative analysis, Renew. Sustain. Energy Rev. 62 (2016) 988–1011.

https://doi.org/10.1016/j.rser.2016.05.045.

[81]   Y. Li, T. Ohkubo, A. Teramoto, K. Saga, Y. Kawashima, Lab-scale reproduction test method for temperature-driven movement of through-thickness cracks in concrete exterior walls for crack repair   evaluation,   Constr.   Build.   Mater.   331   (2022)   127169. https://doi.org/10.1016/j.conbuildmat.2022.127169.

[82]   N.M. Nahar, P. Sharma, M.M. Purohit, Performance of different passive techniques for cooling   of   buildings   in   arid   regions,   Build.   Environ.   38   (2003)   109–116. https://doi.org/10.1016/S0360-1323(02)00029-X.

[83]   K.C.K. Vijaykumar, P.S.S. Srinivasan, S. Dhandapani, A performance of hollow clay tile (HCT) laid reinforced cement concrete (RCC) roof for tropical summer climates, Energy Build. 39 (2007) 886–892. https://doi.org/10.1016/j.enbuild.2006.05.009.

[84]   M. Rawat, R.N. Singh, A study on the comparative review of cool roof thermal performance in   various   regions,   Energy   Built   Environ.   3   (2022)   327–347. https://doi.org/10.1016/j.enbenv.2021.03.001.

[85]   B. Raji, M.J. Tenpierik, A. Van Den Dobbelsteen, The impact of greening systems on building energy performance: A literature review, Renew. Sustain. Energy Rev. 45 (2015) 610–623. https://doi.org/10.1016/j.rser.2015.02.011.

[86]   A.B. Besir, E. Cuce, Green roofs and facades: A comprehensive review, Renew. Sustain. Energy Rev. 82 (2018) 915–939. https://doi.org/10.1016/j.rser.2017.09.106.

[87]   E. Jamei, H.W. Chau, M. Seyedmahmoudian, A. Stojcevski, Review on the cooling potential of   green   roofs   in   different   climates,   Sci.   Total   Environ.   791   (2021)   148407. https://doi.org/10.1016/j.scitotenv.2021.148407.

[88]   T.P. Scolaro, E. Ghisi, Life cycle assessment of green roofs: A literature review of layers materials   and   purposes,   Sci.   Total   Environ.   829   (2022)   154650. https://doi.org/10.1016/j.scitotenv.2022.154650.

[89]   S.W. Lee, C.H. Lim, E.@. I. Bin Salleh, Reflective thermal insulation systems in building: A review on radiant barrier and reflective insulation, Renew. Sustain. Energy Rev. 65 (2016) 643–661. https://doi.org/10.1016/j.rser.2016.07.002.

[90]   A. Rosati, M. Fedel, S. Rossi, NIR reflective pigments for cool roof applications: A comprehensive   review,   J.   Clean.   Prod.   313   (2021)   127826. https://doi.org/10.1016/j.jclepro.2021.127826.

[91]   M.Z. Mohd Ashhar, L.C. Haw, Recent research and development on the use of reflective technology   in   buildings   –   A   review,   J.   Build.   Eng.   45   (2022)   103552. https://doi.org/10.1016/j.jobe.2021.103552.

[92]   M.A. Medina, On the performance of radiant barriers in combination with different attic insulation levels, Energy Build. 33 (2000) 31–40. https://doi.org/10.1016/S0378-7788(00)00065-7.

[93]   C. Michels, R. Lamberts, S. Güths, Evaluation of heat flux reduction provided by the use of radiant barriers in clay tile roofs, Energy Build. 40 (2008) 445–451. https://doi.org/10.1016/j.enbuild.2007.03.013.

[94]   H. Schreiber, Z. Jandaghian, B. Baskaran, Energy performance of residential roofs in Canada – Identification of missing links for future research opportunities, Energy Build. 251 (2021) 111382. https://doi.org/10.1016/j.enbuild.2021.111382.

[95]   T.C. Quevedo, A.P. Melo, R. Lamberts, Assessing cooling loads from roofs with attics: Modeling versus field experiments, Energy Build. 262 (2022) 112003. https://doi.org/10.1016/j.enbuild.2022.112003.

[96]   A.M. Papadopoulos, State of the art in thermal insulation materials and aims for future developments, Energy Build. 37 (2005) 77–86. https://doi.org/10.1016/j.enbuild.2004.05.006.

[97]   L. Aditya, T.M.I. Mahlia, B. Rismanchi, H.M. Ng, M.H. Hasan, H.S.C. Metselaar, O. Muraza, H.B. Aditiya, A review on insulation materials for energy conservation in buildings, Renew. Sustain. Energy Rev. 73 (2017) 1352–1365. https://doi.org/10.1016/j.rser.2017.02.034.

[98]   J.-W. Wu, W.-F. Sung, H.-S. Chu, Thermal conductivity of polyurethane¨ foam - best performance, Int. J. Heat Mass Transf. 42 (1999) 2211–2217.

[99]   C. V. Vo, F. Bunge, J. Duffy, L. Hood, Advances in thermal insulation of extruded polystyrene foams, Cell. Polym. 30 (2011). https://doi.org/10.1177/026248931103000303.

[100]   Á. Lakatos, F. Kalmár, Analysis of water sorption and thermal conductivity of expanded polystyrene insulation materials, Build. Serv. Eng. Res. Technol. 34 (2013) 407–416. https://doi.org/10.1177/0143624412462043.

[101]   ISO 8301 Thermal insulation - Determination of steady state thermal resistance and related properties - Heat flow meter apparatus, International Organization for Standardization, 1991.

[102]   C. Brischke, M. Humar, Performance of the bio-based materials, in: Perform. Bio-Based Build. Mater., Elsevier Inc., 2017: pp. 249–333. https://doi.org/10.1016/B978-0-08-100982-6.00005-7.

[103]   ISO 8302 Thermal insulation - Determination of steady - state thermal resistance and related properties - Guarded hot plate apparatus, International Organization for Standardization, 1991.

[104]   ISO 6946 Building components and building elements - Thermal resistance and thermal transmittance - Calculation methods, International Organization for Standardization, 2017.

[105]   ISO 8990 Thermal insulation-Determination of steady - state thermal transmission properties - Calibrated and guarded hot box, International Organization for Standardization, 1994.

[106]   ISO 9869-1 Thermal insulation-Building elements - In-situ measurement of thermal resistance and thermal transmittance — Part 1: Heat flow meter method, International Organization for Standardization, 2014.

[107]   D. Bienvenido-Huertas, J. Moyano, D. Marín, R. Fresco-Contreras, Review of in situ

methods for assessing the thermal transmittance of walls, Renew. Sustain. Energy Rev. 102 (2019) 356–371. https://doi.org/10.1016/j.rser.2018.12.016.

[108]   I. Nardi, E. Lucchi, T. de Rubeis, D. Ambrosini, Quantification of heat energy losses through the building envelope: A state-of-the-art analysis with critical and comprehensive review on infrared thermography, Build. Environ. 146 (2018) 190–205. https://doi.org/10.1016/j.buildenv.2018.09.050.

[109]   C. Peng, Z. Wu, In situ measuring and evaluating the thermal resistance of building construction, Energy Build. 40 (2008) 2076–2082. https://doi.org/10.1016/j.enbuild.2008.05.012.

[110]   S.H. Kim, J.H. Kim, H.G. Jeong, K.D. Song, Reliability field test of the air-surface temperature ratio method for in situ measurement of U-values, Energies. 11 (2018) 1–15. https://doi.org/10.3390/en11040803.

[111]   N. Soares, C. Martins, M. Gonçalves, P. Santos, L.S. da Silva, J.J. Costa, Laboratory and in-situ non-destructive methods to evaluate the thermal transmittance and behavior of walls, windows, and construction elements with innovative materials: A review, Energy Build. 182 (2019) 88–110. https://doi.org/10.1016/j.enbuild.2018.10.021.

[112]   D. Bienvenido-Huertas, R. Rodríguez-Álvaro, J.J. Moyano, F. Rico, D. Marín, Determining the U-Value of fa ades using the thermometric method: Potentials and limitations, Energies. 11 (2018). https://doi.org/10.3390/en11020360.

[113]   C. Peng, Z. Wu, Thermoelectricity analogy method for computing the periodic heat transfer in external building envelopes, Appl. Energy. 85 (2008) 735–754. https://doi.org/10.1016/j.apenergy.2008.02.003.

[114]   K. Martín, I. Flores, C. Escudero, A. Apaolaza, J.M. Sala, Methodology for the calculation of response factors through experimental tests and validation with simulation, Energy Build. 42 (2010) 461–467. https://doi.org/10.1016/j.enbuild.2009.10.015.

[115]   A.H. Deconinck, S. Roels, Comparison of characterisation methods determining the thermal resistance of building components from onsite measurements, Energy Build. 130 (2016) 309–320. https://doi.org/10.1016/j.enbuild.2016.08.061.

[116]   M. Teni, H. Krstić, P. Kosiński, Review and comparison of current experimental approaches for in-situ measurements of building walls thermal transmittance, Energy Build. 203 (2019). https://doi.org/10.1016/j.enbuild.2019.109417.

[117]   R. Ponechal, P. Juras, Selected Problems of Heat Transfer Measuring by Hotbox Apparatus in Climate Chambers, IOP Conf. Ser. Mater. Sci. Eng. 661 (2019). https://doi.org/10.1088/1757-899X/661/1/012079.

[118]   B. Su, T. Zhang, S. Chen, J. Hao, R. Zhang, Thermal properties of novel sandwich roof panel made of basalt fiber reinforced plastic material, J. Build. Eng. 52 (2022). https://doi.org/10.1016/j.jobe.2022.104478.

[119]   F. Geoola, Y. Kashti, A. Levi, R. Brickman, A study of the overall heat transfer coefficient

of greenhouse cladding materials with thermal screens using the hot box method, Polym. Test. 28 (2009) 470–474. https://doi.org/10.1016/j.polymertesting.2009.02.006.

[120]   A. Pasupathy, L. Athanasius, R. Velraj, R. V. Seeniraj, Experimental investigation and numerical simulation analysis on the thermal performance of a building roof incorporating phase change material (PCM) for thermal management, Appl. Therm. Eng. 28 (2008) 556–565. https://doi.org/10.1016/j.applthermaleng.2007.04.016.

[121]   D. Prakash, P. Ravikumar, Transient analysis of heat transfer across the residential building roof with PCM and wood wool- A case study by numerical simulation approach, Arch. Civ. Eng. 59 (2013) 483–497. https://doi.org/10.2478/ace-2013-0026.

[122]   G. Costantine, C. Maalouf, T. Moussa, G. Polidori, Experimental and numerical investigations of thermal performance of a Hemp Lime external building insulation, Build. Environ. 131 (2018) 140–153. https://doi.org/10.1016/j.buildenv.2017.12.037.

[123]   T. Rahman, K. Nagano, J. Togawa, Study on building surface and indoor temperature reducing effect of the natural meso-porous material to moderate the indoor thermal environment, Energy Build. 191 (2019) 59–71. https://doi.org/10.1016/j.enbuild.2019.03.014.

[124]   M. Altin, G.Ş. Yildirim, Investigation of usability of boron doped sheep wool as insulation material and comparison with existing insulation materials, Constr. Build. Mater. 331 (2022). https://doi.org/10.1016/j.conbuildmat.2022.127303.

[125]   Y. Yin, Y. Song, W. Chen, Y. Yan, X. Wang, J. Hu, B. Zhao, S. Ren, Thermal environment analysis of enclosed dome with double-layered PTFE fabric roof integrated with aerogel-glass wool insulation mats: On-site test and numerical simulation, Energy Build. 254 (2022) 111621. https://doi.org/10.1016/j.enbuild.2021.111621.

[126]   A.S. Hasan, O.M. Ali, A.A. Hussein, Comparative study of the different materials combinations used for roof insulation in Iraq, Mater. Today Proc. 42 (2021) 2285–2289. https://doi.org/10.1016/j.matpr.2020.12.317.

[127]   A. Kumar, B.M. Suman, Experimental evaluation of insulation materials for walls and roofs and their impact on indoor thermal comfort under composite climate, Build. Environ. 59 (2013) 635–643. https://doi.org/10.1016/j.buildenv.2012.09.023.

[128]   J. Zhao, S. Li, Life cycle cost assessment and multi-criteria decision analysis of environment-friendly building insulation materials - A review, Energy Build. 254 (2022) 111582. https://doi.org/10.1016/j.enbuild.2021.111582.

[129]   M.S. Al-Homoud, Performance characteristics and practical applications of common building thermal insulation materials, Build. Environ. 40 (2005) 353–366. https://doi.org/10.1016/j.buildenv.2004.05.013.

[130]   R.U. Halwatura, M.T.R. Jayasinghe, Influence of insulated roof slabs on air conditioned spaces in tropical climatic conditions-A life cycle cost approach, Energy Build. 41 (2009) 678–686.

https://doi.org/10.1016/j.enbuild.2009.01.005.

[131] Y. Huang, B. Yuan, L. Xiao, Y. Liu, Studies on the wet expansion deformation of hydraulic concrete with fly ash under non-standard temperatures, Case Stud. Constr. Mater. 8 (2018) 392–400. https://doi.org/10.1016/j.cscm.2018.03.003.

[132] S. Tang, D. Huang, Z. He, A review of autogenous shrinkage models of concrete, J. Build. Eng. 44 (2021) 103412. https://doi.org/10.1016/j.jobe.2021.103412.

[133] S. Asamoto, A. Ohtsuka, Y. Kuwahara, C. Miura, Study on effects of solar radiation and rain on shrinkage, shrinkage cracking and creep of concrete, Cem. Concr. Res. 41 (2011) 590–601. https://doi.org/10.1016/j.cemconres.2011.03.003.

[134] G.M. Moelich, J.E. van Zyl, N. Rabie, R. Combrinck, The influence of solar radiation on plastic shrinkage cracking in concrete, Cem. Concr. Compos. 123 (2021) 104182. https://doi.org/10.1016/j.cemconcomp.2021.104182.

[135] R.J. Onega, P.J. Burns, Thermal Flanking Loss Calculations for the National Bureau of Standards Calibrated Hot Box, 1985.

[136] C.J. Schumacher, D.G. Ober, J.F. Straube, A.P. Grin, Development of a New Hot Box Apparatus to Measure Building Enclosure Thermal Performance, in: Therm. Perform. Exter. Envel. Whole Build. XII Int. Conf., Clearwater, Florida, USA., Held 1-5 December, 2013.

[137] J. Hallik, P. Klõšeiko, R. Piir, T. Kalamees, Numerical analysis of additional heat loss induced by air cavities between insulation boards due to non-ideality, J. Build. Eng. 60 (2022) 1–15. https://doi.org/10.1016/j.jobe.2022.105221.

[138] Japanese Architectural Standard Specification JASS 8 Waterproofing and Sealing, 2014.

Acknowledgements